

Analysis of the reaction of a one-neutron halo nucleus on a heavy target at energies around the Coulomb barrier. The case of ^{11}Be on ^{197}Au .

Análisis de la reacción de un núcleo halo de un neutrón contra un blanco pesado a energías alrededor de la barrera coulombiana. El caso de ^{11}Be contra ^{197}Au .

Vicente Pseudo Fortes

PhD. Thesis

Supervisors:

Prof. María José García Borge
Instituto de Estructura de la Materia (CSIC)

Dr. Antonio Matías Moro Muñoz
Universidad de Sevilla

A la meua família

Acknowledgements

In my opinion, this should probably be the largest chapter of this thesis. The number of persons that have contributed to this work is extremely large and, probably, the number of persons that have put up with me, that have saved me a lot of money in psychiatrists and have cost me a lot of money in beers, is even larger.

Firstly, I want to thank María José. Thanks for the opportunity that you offered me and that made all this happen. Being involved in this work has given me the chance of taking the first steps in my career in difficult times for researching, particularly in Spain, and doing so in this group has offered me the chance to know a great bunch of wonderful people.

Thanks, Antonio, for being an example in so many things, for the patience in explaining the things as many times as necessary (in the faculty, in a Starbucks or in Triana), but mainly for transmitting a deep honest love to physics, which is necessarily contagious.

Thanks, Olof. I hated cables and modules until your appearance, so it is straightforward to infer the large weight you have had in my becoming an experimentalist. Thanks for saying so many things with so few words and for being so authentic regardless the context.

Thanks to the people from Sevilla, Aarhus, Huelva, TIGRESS, Catania, Colorado, Louisiana and Goteborg for all the things shared during the different experiments.

Thanks to Mariano, Guille, Briz, Mario, Andrés, Ale, Jan and Irene for trespassing the border from colleagues to friends and for all the discussions about every single possible topic in the Universe. We have not solved a single one among the many problems of the world, but at least I expect you to have a clear idea of what is and what is not a paella. Thanks, Ángel, for the always interesting point of view, for the music we have learned from each other, and for being there when needed.

Thanks to Kike. Without you, I doubt if I would have written this thesis. Thanks for having a rationalism so overwhelming that it seems irrational. Thanks for sharing all your knowledge with such modesty and for saying I don't know when you didn't know. Thanks

Riccardo, for asking the uncomfortable questions when they had to be asked, for encouraging me always and for your enthusiasm; for the funny extreme negativism when something annoyed you, but specially for the crushing positivism under the rest of circumstances and your love towards every tiny detail in life. Thanks to the *Intocantes*, for those good moments and for taking their name so seriously.

Thanks to all my friends from Vila-real, Barcelona, Madrid and elsewhere, for being patient with me, specially in this last stage when I did not answer their messages or calls.

Thanks, Eli. Thanks for loving every living species and for having a preferential space in your loving for me.

Gràcies a la meua família. Arquímedes, en l'any 340, va escriure "Doneu-me un punt de suport i mouré el món". No sé si mouré el món (falta li fa), però tinc clar que tinc els tres punts de suport més sòlids que se poden tindre.

Contents

Index	ii
List of figures	vi
List of tables	x
1 Introduction	2
1.1 Nuclear Physics overview	3
1.2 The halo structure	6
1.3 The ^{11}Be case	7
1.4 The Coulomb barrier	9
1.5 The role of nuclear reactions	12
1.6 Motivation	16
2 Direct reaction theory	18
2.1 Quantum scattering	20
2.2 Model space	22
2.3 Optical Model	23
2.3.1 Partial wave expansion	24
2.4 Coupled channels formalism	26
2.4.1 Distorted Wave Born Approximation (DWBA)	27
2.4.2 Continuum-Discretized Coupled Channels (CDCC)	28
2.4.3 Transfer to the Continuum of the target (TC)	30
2.4.4 CDCC including core excitation: XCDCC	31
2.5 A semiclassical formalism. The Equivalent Photon Method	31
3 The S1202 experiment	34
3.1 Experiments with radioactive beams	35
3.2 TRIUMF and ISAC. Facility and beam production	35
3.3 Experimental setup	36
3.4 Detectors	38
3.4.1 Silicon detectors	38

3.4.1.1	Double-Sided Silicon Strip Detectors (DSSSDs)	41
3.4.1.2	SSSSD	41
3.4.1.3	PAD	41
3.4.2	Telescope configuration	42
3.4.3	Plastic Detector	42
3.4.4	Germanium detectors	43
3.5	Printed circuit board	43
3.6	Target	44
3.7	The chamber design	46
3.8	TIGRESS	47
3.9	Electronic chain	48
3.9.1	Trigger and data acquisition system	50
4	Analysis of the data	52
4.1	Data preparation	52
4.1.1	Energy calibration of the Si detectors	53
4.1.2	Thickness determination	57
4.1.3	Position optimization	59
4.1.4	Efficiency calibration of TIGRESS	65
4.1.5	Doppler correction and γ gating	67
4.1.6	Data selection	69
4.1.7	Examples of spectra	72
4.2	Data analysis	73
4.2.1	Identification of breakup channel	73
4.2.1.1	Angular binning	78
4.2.1.2	Angular distribution of breakup probability	79
4.2.2	Identification of the inelastic channel	79
4.2.3	Identification of the elastic channel	83
4.2.4	Calculation of absolute cross sections	83
5	Analysis of the results and discussion	90
5.1	Analysis within the optical model	91
5.2	Analysis within the EPM	97
5.3	Analysis within a CDCC formalism	101
5.4	Analysis within the TC formalism	112
5.5	Analysis within an XCDCC formalism	114
6	Summary and conclusions	124
	Appendices	128
A	Cross sections and probabilities	130
B	Thickness of SSSSD4	138

C Summary	140
C.1 Introduction	140
C.2 Objectives	145
C.3 Direct reaction theory	146
C.4 Experiment and setup	147
C.4.1 Calibrations	150
C.5 Results	151
C.5.1 Discussion	152
C.6 Conclusions	156
D Resumen	158
D.1 Introducción	158
D.2 Objetivos	163
D.3 Teoría de reacciones directas	164
D.4 Experimento y montaje	166
D.4.1 Calibraciones	168
D.5 Resultados	170
D.5.1 Discusión	171
D.6 Conclusiones	175
Bibliography	177

List of Figures

1.1	Scatter of ^{11}Be on ^{208}Pb	3
1.2	Nuclide chart	5
1.3	^{11}Be density	7
1.4	Standard shell model	8
1.5	^{11}Be level scheme	10
1.6	Potentials	11
1.7	Angular distribution of ^4He arising from $^6\text{He}+^{208}\text{Pb}$	14
1.8	Angular distribution of the $^{11}\text{Li}+^{208}\text{Pb}$ elastic scattering.	15
1.9	Reduced breakup probability for $^{11}\text{Li}+^{208}\text{Pb}$	16
2.1	Direct reaction	18
2.2	Space coordinates	21
2.3	Model space	22
2.4	Woods-Saxon parameters	24
2.5	Destructive interference	29
2.6	Coordinates	30
3.1	Triumf layout	37
3.2	Studies for detectors positioning	38
3.3	Detectors position	39
3.4	pn junction	40
3.5	DSSSD schematic representation	41
3.6	Printed Circuit Board	44
3.7	Target wheel	45
3.8	Target shade	46
3.9	Reaction chamber and experimental setup	46
3.10	TIGRESS	47
3.11	Reaction Chamber	48
3.12	CFD signal	49
4.1	Alpha spectrum	54

4.2	Beginning and ending calibration runs	56
4.3	Irregular thickness in SSSSD4	57
4.4	Thickness test	58
4.5	Thickness2	58
4.6	Change of coordinate system	60
4.7	Position optimization	61
4.8	Position optimization of ^{11}Be	62
4.9	Position optimization	63
4.10	^{12}C - ^{208}Pb angular distribution around the Coulomb barrier	64
4.11	^{12}C - ^{197}Au angular distribution around the Coulomb barrier	65
4.12	TIGRESS Efficiency	66
4.13	Gamma Spectra	68
4.14	Gamma Gate	69
4.15	Gamma spectra with identified gamma lines	69
4.16	Ediff	71
4.17	Multiplicity one events	72
4.18	$\Delta E - E$ plots for ^{12}C on ^{197}Au	72
4.19	$\Delta E - E$ plots for ^{11}Be on ^{197}Au around the Coulomb barrier	73
4.20	$\Delta E - E$ plots for ^{12}C on ^{197}Au	73
4.21	$\Delta E - E$ plots for ^{11}Be on ^{197}Au below the Coulomb barrier	73
4.22	$\Delta E - E$ plots for pixels at significantly different angle ($E_{lab} = 2.9 \text{ MeV/u}$)	74
4.23	$\Delta E - E_{back}$ versus $\Delta E - E_{tot}$ plot	74
4.24	Identification of ^{10}Be and ^{11}Be fragments.	75
4.25	Intersection area between ^{10}Be and ^{11}Be fragments	76
4.26	$\Delta E - E$ plots for pixels at significantly different angle ($E_{lab} = 3.6 \text{ MeV/u}$)	77
4.27	$\Delta E - E$ plots with and without corrections	79
4.28	Experimental breakup probability	80
4.29	$\Delta E - E$ plots in coincidence with 320 keV gamma	81
4.30	Experimental inelastic scattering probability	82
4.31	Experimental elastic scattering probability	84
4.32	Experimental inelastic scattering cross section	85
4.33	Experimental inelastic scattering cross section	86
4.34	Energy distribution of ^{10}Be fragments	88
4.35	Energy distribution of ^{11}Be fragments	88
5.1	Elastic scattering cross section	92
5.2	Elastic scattering cross section	94
5.3	Elastic scattering cross section	94
5.4	Elastic scattering cross section	95
5.5	Study of the sensitivity radius	96
5.6	Optimization of the imaginary diffuseness a_i	97
5.7	$\mathcal{B}(E1)$ distribution of the ^{11}Be	98
5.8	Inelastic scattering probability, EPM	100
5.9	Second order processes	101
5.10	Breakup probability, EPM	102
5.11	Breakup probability in a CDCC approach	106
5.12	Inelastic scattering probability in a CDCC approach	107

5.13	Elastic scattering probability in a CDCC approach	109
5.14	Quasielastic scattering probability in a CDCC approach	110
5.15	Neutron single-particle states of ^{198}Au	113
5.16	Breakup probability in a TC approach	115
5.17	Coordinates in the particle-rotor model	116
5.18	Breakup probability for the XCDCC formalism	118
5.19	Elastic scattering cross section for the XCDCC formalism	120
5.20	Inelastic scattering probability for the XCDCC formalism	121
5.21	Measured reaction cross sections compared to CDCC and XCDCC	122
C.1	Scatter of ^{11}Be on ^{208}Pb	141
C.2	^{11}Be level scheme	144
C.3	Detectors position	148
C.4	TIGRESS	149
C.5	^{12}C - ^{197}Au angular distribution around the Coulomb barrier	150
C.6	$\Delta E - E$ plots for ^{11}Be on ^{197}Au below the Coulomb barrier	152
C.7	Two-dimensional $\Delta E - E$ plots in coincidence with 320 keV gamma	153
C.8	Elastic scattering cross section	153
C.9	Inelastic scattering and breakup probability, EPM	154
C.10	Probabilities in a CDCC approach	155
C.11	Probabilities within an XCDCC formalism	156
C.12	Breakup probability in a TC approach	156
D.1	Dispersión de ^{11}Be con ^{197}Au	159
D.2	Esquema de niveles del ^{11}Be	162
D.3	Posición de los detectores	167
D.4	Imágen de TIGRESS	168
D.5	Sección eficaz diferencial de la dispersión elástica de ^{12}C - ^{197}Au respecto a Rutherford a energías alrededor de la barrera de Coulomb	169
D.6	Gráficos bidimensionales $\Delta E - E$ de la dispersión de ^{11}Be en ^{197}Au a energías por debajo de la barrera de Coulomb	171
D.7	Gráfico bidimensional $\Delta E - E$ en coincidencia con una gamma a 320 keV	172
D.8	Sección eficaz de dispersión elástica	172
D.9	Probabilidad de dispersión inelástica y de breakup, EPM	173
D.10	Probabilidades calculadas con el método CDCC	174
D.11	Probabilidades calculadas con el método XCDCC	175
D.12	Probabilidad de breakup obtenida con un cálculo de transfer	176

List of Tables

3.1	Ion beams produced for the S1202 experiment	37
3.2	Silicon detectors used in the S1202 experiment	39
4.1	Energy and range of the alpha sources	53
4.2	FWHM of peaks in SSSSD4	56
4.3	Lines identified in the gamma spectrum.	70
5.1	Optical model parameters for $^{11}\text{Be}+^{197}\text{Au}$	93
5.2	Parameters for the calculation of the $\mathcal{B}(E1)$	99
5.3	Parameters of the potentials used in the CDCC calculation	103
5.4	Parameters for the XCDCC calculation	116
A.1	Elastic scattering cross section. $E_{lab} = 39.6$ MeV	130
A.2	Elastic scattering cross section. $E_{lab} = 31.9$ MeV	131
A.3	Inelastic scattering probability at $E_{lab} = 39.6$ MeV	132
A.4	Inelastic scattering probability at $E_{lab} = 31.9$ MeV	133
A.5	Breakup probability at $E_{lab} = 39.6$ MeV	134
A.6	Breakup probability at $E_{lab} = 31.9$ MeV	135
A.7	Inelastic scattering cross section. $E_{lab} = 39.6$ MeV	135
A.8	Inelastic scattering cross section. $E_{lab} = 31.9$ MeV	136
A.9	Breakup cross section. $E_{lab} = 39.6$ MeV	136
A.10	Breakup cross section. $E_{lab} = 31.9$ MeV	137
B.1	Minimum thickness of the SSSSD used in telescope 4	138
B.2	Maximum thickness of the SSSSD used in telescope 4	139
C.1	Ion beams produced for the S1202 experiment	147
C.2	Silicon detectors used in the S1202 experiment	148
D.1	Haces de iones producidos en el experimento S1202 en TRIUMF	166
D.2	Características de los detectores de silicio utilizados en el experimento S1202	167

This work is part of a series of experiments performed by an international collaboration led by the nuclear physics groups at the IEM-CSIC (Madrid) and the Universities of Seville and Huelva. The global aim of these experiments is the understanding of the dynamics of the collisions of weakly-bound light nuclei on heavy targets at Coulomb barrier energies. Previous to the present work, this collaboration had measured the reactions ${}^6\text{He}+{}^{208}\text{Pb}$ (at Louvain-la-Neuve), ${}^{11}\text{Be}+{}^{120}\text{Sn}$ (CERN-ISOLDE) and ${}^{11}\text{Li}+{}^{208}\text{Pb}$ (TRIUMF).

Along the same lines, in this thesis we have studied the reaction of ${}^{11}\text{Be}$ on a gold (${}^{197}\text{Au}$) target at two incident energies, 31.9 MeV and 39.6 MeV, which are below and around the Coulomb barrier ($V_b \sim 40$ MeV), respectively. These experimental data, together with a proper interpretation using different theoretical calculations, contributes to the understanding of how the halo structure, observed in some nuclei close to the neutron and proton driplines, influences the dynamics of the reaction around and below the Coulomb barrier, where nuclear effects should be of minor relevance. The data analysed as part of this PhD work were acquired in the S1202 experiment performed at TRIUMF in July of 2012 and June of 2013, which will be thoroughly described along the text.

The ${}^{11}\text{Be}$ nucleus is a one-neutron-halo nucleus. Halo nuclei are weakly bound systems, close to the neutron or proton driplines, in which one or two nucleons have a large probability of being at large distances of the center of the nucleus, well beyond the range of the nuclear potential. The major source of information of these nuclei are nuclear reactions. Being unstable systems (for example ${}^{11}\text{Be}$ decays in 13.76(7) s by beta emission to ${}^{11}\text{B}$), these reactions require a mechanism to produce these unstable nuclei and to accelerate them, using them as projectiles that bombard a stable target nucleus.

A reaction on heavy nuclei was chosen for this study. Heavy nuclei have a large amount of protons, translating into a strong electrostatic repulsion felt by the projectile. In a very simplistic representation, the reaction ${}^{11}\text{Be}+{}^{197}\text{Au}$ can be imagined as the neutron in the halo not feeling the field while the core is pushed away, being easily broken apart. This process is known as Coulomb breakup and previous works in other energy regimes or for similar reactions [Sá08, Esc07, Fer13, Cub12, Nak97, Aum00, Fuk04, Pal03] concluded that it has a major contribution in reactions with halo nuclei. The importance of this particular process in this case and what are the other contributions to the total reaction cross section (inelastic

scattering and breakup considering nuclear effects are two examples) will be reported here.

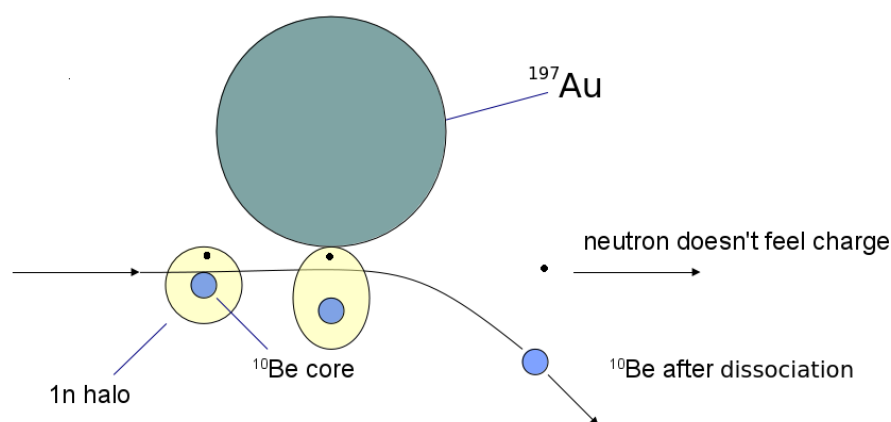


Figure 1.1: *Simplistic representation of the breakup process that the ^{11}Be on the heavy target may undergo.*

Since the ^{11}Be nucleus is unstable, this experiment requires a facility capable of producing radioactive beams. The high quality of the ^{11}Be beam (continuous, with a high yield and low contamination) produced at TRIUMF (Vancouver, Canada) and the possibility of using the HPGe array TIGRESS for detecting the gamma radiation produced in the reaction were the reasons for choosing that facility.

In this chapter, the departure point of this work will be presented, focusing on the main concepts that will be used along this text, the known features of the ^{11}Be nucleus and information that can be extracted from reactions with halo nuclei.

1.1 Nuclear Physics overview

A nucleus is a very compact system formed by protons and neutrons, which are generically referred to as nucleons, as they behave equally under the strong force. In fact, nuclei are the most dense structures in Universe (other than black holes). To have a scaled example that helps our classical brain to understand their density, we can look at their macroscopic extension, the neutron stars, which may have the mass of the sun within a 10 km diameter sphere. An even more tangible example may be that 1 mm^3 of nuclear matter weighs more than 10000 tonnes.

In order to assimilate the jump from nuclear to atomic magnitudes another scaling exercise may help our macroscopically educated brain. The nuclear radius is of the order of a few *fermi* ($1\text{ fm} = 10^{-15}\text{ m}$), while the atomic radius has a value that oscillates around the *Ångstrom* scale ($1\text{ Å} = 10^{-10}\text{ m}$). This means that if a nucleus had a 1 cm radius, the space occupied by the electrons around it would be a sphere with a radius of 1 km, and the distance to the next nucleus another km. This tiny sphere constitutes more than the 99% of the mass of the atom so, the rest of the space, i.e. most of our body itself, is vacuum. The low probability of hitting that 1 cm sphere with another 1 cm sphere thrown from several km of distance can provide a first idea of the difficulty of experimental nuclear physics. This low probability is what was

first noticed in the experiments performed between 1908 and 1913 by H. Geiger and E. Marsden and directed by E. Rutherford. It consisted on a collimated beam of ${}^4\text{He}$ ions thrown on a gold foil. In addition to the low interacting probability, it was observed that some particles were deviated to large, backward angles. This entailed the discovery of a dense positively charged nucleus in the center of the atom concentrating most of its mass, and the birth of nuclear physics.

Studying the physics of such a new object opened a new horizon to knowledge which, as this thesis proves, is still open. The non-linear relation between the mass and the charge of the nuclei became the hot topic in the 20s, until the experimental discovery of the neutron by J. Chadwick in 1932, completing the atomic model.

After the first nuclear scattering experiments, the first documented nuclear reactions were performed by E. Rutherford, as well, in 1919 (${}^4\text{He} + {}^{14}\text{Ni} \rightarrow {}^1\text{H} + {}^{17}\text{O}$). What is the preferred ratio of protons and neutrons? Why are some reactions more likely than others? The more questions wanted to be answered, the more questions arose. (And many of them could be answered in a laboratory at home. What a glorious time for being an experimental physicist!)

On Earth, only in the outer layers of the atmosphere can happen some natural processes able to produce nuclear reactions. Besides those isotopes of species present in the atmosphere, only the stable isotopes and the primordial nuclides (unstable nuclei which have half-lives larger or around our planet's age, 4.5×10^9 years) can be found. For this reason, the first experiments were performed with this natural radioactive material as their source of radiation. Soon, this *crescendo* of questions to be answered lead to the development of new devices that allowed for reactions at higher energies: the particle accelerators. J.D. Cockcroft and E.T.S. Walton devised the way of creating a high DC field from a low voltage AC input and used it for accelerating particles, performing the first successful nuclear transmutation induced by artificially accelerated particles in history in 1932 [Kle73], using a proton beam on a lithium target and observing the two outgoing alpha particles ($p + {}^7\text{Li} \rightarrow {}^8\text{Be}^* \rightarrow {}^4\text{He} + {}^4\text{He}$).

The accelerators have gradually become more sophisticated and powerful. In the following 40 years, besides the 300 stable nuclear species, 1300 radioisotopes were produced, identified and studied (see figure 1.2). Most of this knowledge, and most of the knowledge acquired until now in the field of nuclear physics, has been obtained through nuclear reactions. Currently, the accelerators can accelerate particles to energies so high that a new field in physics has split from the former nuclear physics to treat subnuclear processes specifically .

Delving into the unstable newly produced species, some interesting features were found out, keeping the initial interest in the field intact. One example is the discovery of magic numbers. If a nucleus has a magic number of protons or neutrons it is more stable than other neighboring nuclei. In a shell model picture, these numbers correspond to the amount of nucleons necessary for closing a shell. A shell is said to be closed if it is full and has a large gap to the energy level above it. Nuclei can have a magic number of protons, a magic number of neutrons or both (the doubly magic nuclei). The energy needed for exciting these nuclei, or for producing a nuclear reaction with them, is high, so double magic nuclei can be understood as

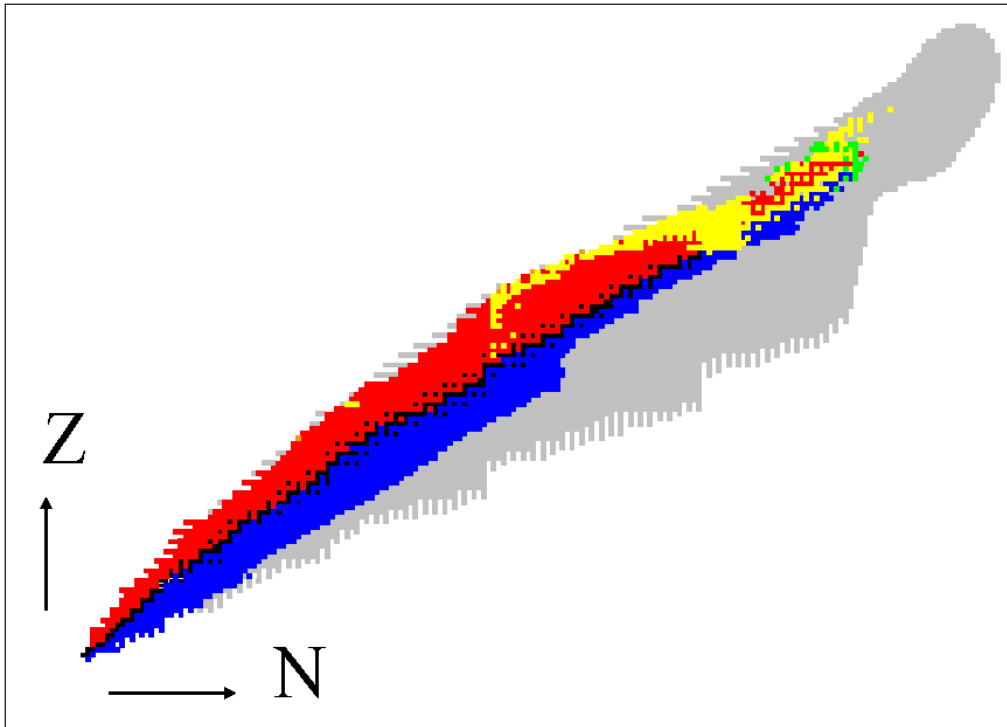


Figure 1.2: Nuclide chart. In black the stable isotopes, forming what is called the valley of stability. In red the nuclei decaying by β^+ and in blue the nuclei decaying by β^- processes. The line that separates the (coloured) unstable nuclei from the unbound ones is called the dripline.

the nuclear counterpart of the noble gases in chemistry.

In the late XX century, a crucial step forward was taken. Until then, beams and targets made of stable matter were used for producing unstable species. In 1985, at the Lawrence Berkeley Laboratory, I. Tanihata and his collaborators performed the first experiment using a beam of a radioactive ion [Tan85]. This experiment consisted on beams of Li and Be isotopes impinging on Be, C and Al targets at energies of 790 MeV/u. In this high energy regime, the interaction cross section (σ_I) is approximately equal to the area calculated from the sum of the nuclear radius of target (R_t) and projectile (R_p),

$$\sigma_I = \pi(R_t + R_p)^2. \quad (1.1)$$

“The nucleus ^{11}Li showed a remarkably large radius, suggesting a large deformation or a long tail in the matter distribution”. These were the first words pointing to a new structure, which later was labeled as halo.

After the success of the very first experiment performed with radioactive ion beams (RIBs), the interest in the field was renewed. Physicists could explore further the nuclide chart, discovering more interesting behaviors as nuclei closer and closer to the driplines were studied. An example, which will be relevant for this study, is that magic numbers are not that *magic*, and they change for nuclei far from stability, where the proton to neutron ratio is very

different from the one of stable nuclei.

1.2 The halo structure

The term *halo* was first coined by P.G Hansen and B. Jonson in 1987 [Han87]. They ruled out the possibility of a nuclear deformation of ^{11}Li and calculated, considering a two body structure with ^9Li and ^2n , that the decay length of the ^2n wavefunction was $\rho = 8.2$ fm,

$$\rho = \frac{\hbar}{(2\mu B)^{1/2}}, \quad (1.2)$$

with μ the reduced mass and B the binding energy. The “long tail in the matter distribution” suspected by Tanihata and collaborators was called *neutron halo* and other nuclei with similar properties were found later. Examples of halo nuclei are ^6He , ^{11}Li (which are two-neutron halo nuclei), ^{11}Be , ^{19}C (which are one-neutron halo nuclei), or ^8B (which is a candidate for a proton halo nucleus).

In general, a halo nucleus is a system composed of a compact core, formed by most of its nucleons, and a diffuse halo formed by one or two weakly bound nucleons. In principle both, proton and neutron, can form a halo. However, in the case of protons, the Coulomb barrier tends to confine the nucleons inside the nucleus, thus hindering the development of a halo structure. Such structures are observed close to the driplines, where there is an excess of either protons or neutrons that still can be bound to the nucleus but with very low binding energy. Since the core attraction is faint, these nucleons can be found at large distances of the center of the nucleus. In particular, when the last nucleon is in an *s*-orbit, it has no centrifugal barrier and, hence, it may be found particularly far. Saying it with quantum mechanics correctness, the wavefunction of these particles has a long tail, i.e. their density is not negligible up to abnormally large radii, compared to other nuclei with the same mass.

A suitable representation of the nuclear density is given by the Fermi-Dirac distribution:

$$\rho = \frac{\rho_0}{1 + \exp \frac{r-R}{a}}, \quad (1.3)$$

where r is the radius from the center of the nucleus, $R = r_v \times A^{1/3}$, being r_v a constant between 1.2 and 1.44 fm, A the mass number of the nucleus and a the diffuseness, that models the sharpness of the density fall, which can also be understood as a measure of the thickness of the surface. Large radius and diffuseness parameters can be used for describing the densities of halo nuclei. This kind of collective approaches are useful for describing macroscopically the density profile of halo nuclei, however, more fundamental interpretation of the density distribution can be obtained using microscopic approaches like those shown in figure 1.3.

The characteristic tail of a halo wavefunction is represented in figure 1.3, comparing the shape of the proton and neutron density of an ordinary nucleus like ^{10}Be with the density of a nucleus with a neutron halo.

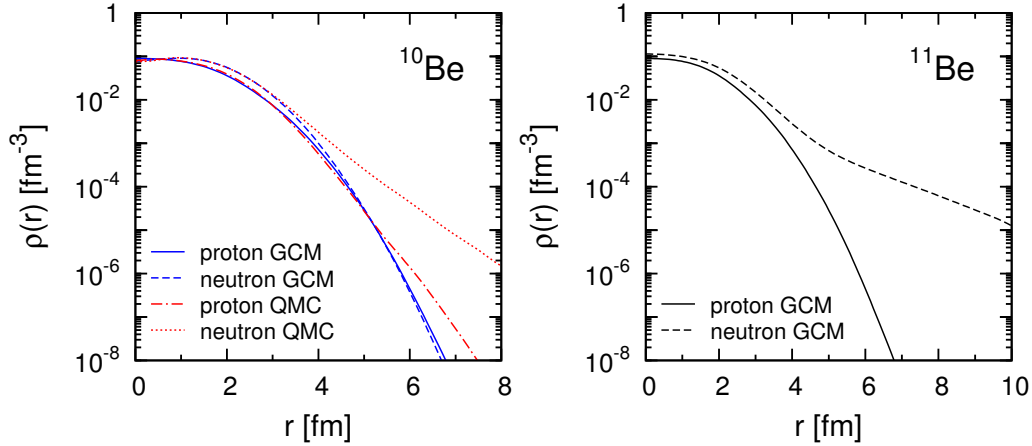


Figure 1.3: Proton and neutron densities calculated with the Quantum Montecarlo Method [Luk15] and the Generator Coordinate Method [Des97].

1.3 The ^{11}Be case

Berillium is the fourth element in the periodic table, what in turn means that it has 4 protons. The ^{11}Be isotope has, as its name indicates, 11 nucleons, the 4 protons plus 7 neutrons. The only stable isotope of berillium is ^9Be , which has an structure that may be thought of as two alpha particles bound together by a neutron. That neutron plays a role comparable to that of the electron in a covalent bond. Adding another neutron ^{10}Be is obtained, which has the same structure, but with two neutrons making this kind of covalent binding. The ^{10}Be nucleus ($j^\pi = 0^+$) decays through β^- to ^{10}B ($j^\pi = 3^+$) with a half-life of $t_{1/2} = 1.6 \times 10^6$ years. The addition of an extra neutron brings a completely different structure to the stage. The half-life of ^{11}Be ($j^\pi = 1/2^+$), decaying through β^- to ^{11}B ($j^\pi = 3/2^-$), is $t_{1/2} = 13.76(7)$ s (10^{12} times lower) [Kel12], so the experimental requirements to study this nucleus will be more challenging.

It is a presently well-established that magic numbers are not immovable at all. Far from stability the gaps between shells are altered and even their ordering may change. This peculiarity is necessary for explaining the spin, parity and structure of ^{11}Be . According to the standart level ordering (see figure 1.4a), as the ^{10}Be ($Z=4$, $N=6$, $J^\pi = 0^+$) does not present a closed shell structure, the ground state of ^{11}Be would be formed by adding a neutron to the close-in-energy $p_{1/2}$ orbit, as it happens in ^{15}O . However, as it is observed in figure 1.4b, this is not what happens. Due to an anomalous inversion of the $2s_{1/2}$ and the $1p_{1/2}$ levels, neutron occupies the $2s_{1/2}$, thus giving rise to a $J^\pi = 1/2^+$ state. In addition to that, as protons are removed from ^{15}O (keeping the number of neutrons in $N = 7$), the gap typically found at $N=8$ becomes smaller. Instead, as the $p_{1/2}$ orbit goes higher in energy, the gap appears at $N=6$, giving the so-called closed shell structure to ^{10}Be . The comparison of the energy needed for exciting the ^{10}Be (3368 keV) compared to the energy of the first excited states of ^{11}Be (320 keV) and ^{12}Be (2101 keV) reinforces the statement that the shell is closed at $N = 6$. The closed shell of the ^{10}Be nucleus, the s -orbit of the last neutron and the low binding energy, all together sum up into becoming the ^{11}Be a weakly bound one-neutron halo nucleus with a ^{10}Be core. Schematically, the wavefunction of the ground state of ^{11}Be can be written as

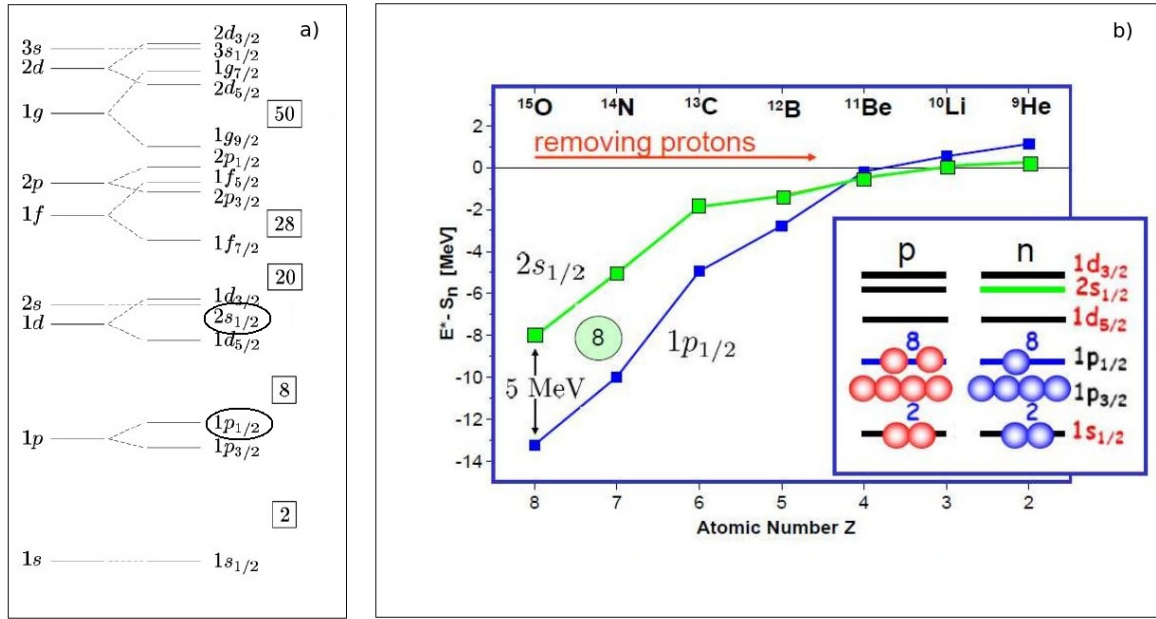


Figure 1.4: a) Shell distribution and gaps between them following the Standard Nuclear Shell Model. b) Energy difference between the $p_{1/2}$ and the $s_{1/2}$ shells for $N = 7$ as the number of protons is reduced. Plot from P.G. Hansen and J.A. Tostevin [Han01]

$$|^{11}\text{Be}(\text{g.s.})\rangle_{1/2^+} = |^{10}\text{Be}(0^+) \otimes \nu(s_{1/2})\rangle_{1/2^+}. \quad (1.4)$$

The neutron separation energy is $S_n = 501.6$ keV. Despite being low, it is high enough for the inverted p -orbit to be below the threshold, so there is one bound excited state ($J^\pi = 1/2^-$), which lies at $E_x = 320.04(10)$ keV above the ground state ($S_n = 181.6$ keV),

$$|^{11}\text{Be}^*\rangle_{1/2^-} = |^{10}\text{Be}(0^+) \otimes \nu(p_{1/2})\rangle_{1/2^-}. \quad (1.5)$$

It is possible to populate this state through an $E1$ transition from the ground state, and it is remarkable that with a strength of $\mathcal{B}(E1) = 0.116 \pm 0.012 e^2 fm^2$ [Mil83], it is the strongest $\mathcal{B}(E1)$ measured between bound states.

The pure simple-particle approach leading to eq. 1.4 and eq. 1.5 is useful, but is a functional simplification of an underlying more complicated system. The ^{11}Be states are known to contain significant admixtures of excited components of ^{10}Be . Including these components (and maintaining the description in terms of a ^{10}Be core and a valence neutron),

$$\begin{aligned} |^{11}\text{Be}(\text{g.s.})\rangle_{1/2^+} = & \alpha |^{10}\text{Be}(0^+) \otimes \nu(s_{1/2})\rangle_{1/2^+} \\ & + \beta |^{10}\text{Be}(2^+) \otimes \nu(d_{5/2})\rangle_{1/2^+} \\ & + \gamma |^{10}\text{Be}(2^+) \otimes \nu(d_{3/2})\rangle_{1/2^+} \\ & + \dots \end{aligned} \quad (1.6)$$

with spectroscopic factors $\alpha^2 \sim 0.86$, $\beta^2 \sim 0.12$ and $\gamma^2 \sim 0.02$ quoted from [Lay12b] (using the model in [Nun96], and consistent with the experimental values in [Zwi79, For99, Win01, Sch12]). In the same picture, the bound excited state is better described in the following form:

$$\begin{aligned}
 |^{11}\text{Be}^*\rangle_{1/2^-} = & a |^{10}\text{Be}(0^+) \otimes \nu(p1/2)\rangle_{1/2^-} \\
 & + b |^{10}\text{Be}(2^+) \otimes \nu(f5/2)\rangle_{1/2^-} \\
 & + c |^{10}\text{Be}(2^+) \otimes \nu(p3/2)\rangle_{1/2^-} \\
 & + \dots
 \end{aligned} \tag{1.7}$$

with spectroscopic factors $a^2 \sim 0.79$, $b^2 \sim 0.21$ and $c^2 \sim 0.004$ extracted from [Lay12a], using the same model that for the ground state [Nun96], and compatible with the experimental values measured by Schmitt [Sch12]. In [Nun96], the extra configurations resulting from the coupling of excited states of the core with the valence particle, have been interpreted within the particle-rotor model, assuming a permanent deformation of the ^{10}Be nucleus ($\beta = 0.67$). Other works [Gor04, Vin95], use a particle-vibrator model, treating the excitation as a result of surface excitations of the ^{10}Be core. Independently of the model, all these calculations suggest a large probability of the neutron for being in a d-orbit, so they are not halo configurations (halos are only observed in s and p orbits). In the ground state, the halo structure is only due to the first and main term $|^{10}\text{Be}(0^+) \otimes \nu(s1/2)\rangle_{1/2^+}$, which will determine in a large extent the dynamics of the reaction.

Above the neutron separation energy, many other states have been identified (see [Kel12] for a recent review). Among them, we note here the two narrow resonances observed in the experiment of Fukuda et al, one at 1.78 MeV ($J^\pi = 5/2^+$) and one at 3.41 MeV ($J^\pi = 3/2^+$) [Fuk04].

1.4 The Coulomb barrier

A recurrent concept along the text is the Coulomb barrier. It is an energy threshold associated with the electrostatic repulsion of positive charges, which has to be exceeded for nuclear effects to be seen.

The Coulomb barrier can be defined in different ways. The most common definition is the maximum positive value of the real potential, obtained adding the electrostatic potential and the bare part of the nuclear potential. It arises naturally due to the long range of the electromagnetic interaction compared to the short range of the nuclear force. As the distance between the colliding nuclei increases, the nuclear potential tends to zero within a few fermi (10^{-15} m), where the repulsive Coulomb potential still has non-negligible values, becoming the dominant force. This creates a (positive) maximum in the potential at a certain radius. Classically, if the energy of the reaction is below this threshold, the projectile cannot penetrate in the potential and the interaction would be purely electromagnetic. Within this picture, a reasonable estimate of the value of the Coulomb barrier is given by

$$V_b = \frac{1}{4\pi\epsilon_0} \frac{Z_p Z_t e^2}{R_b} \tag{1.8}$$

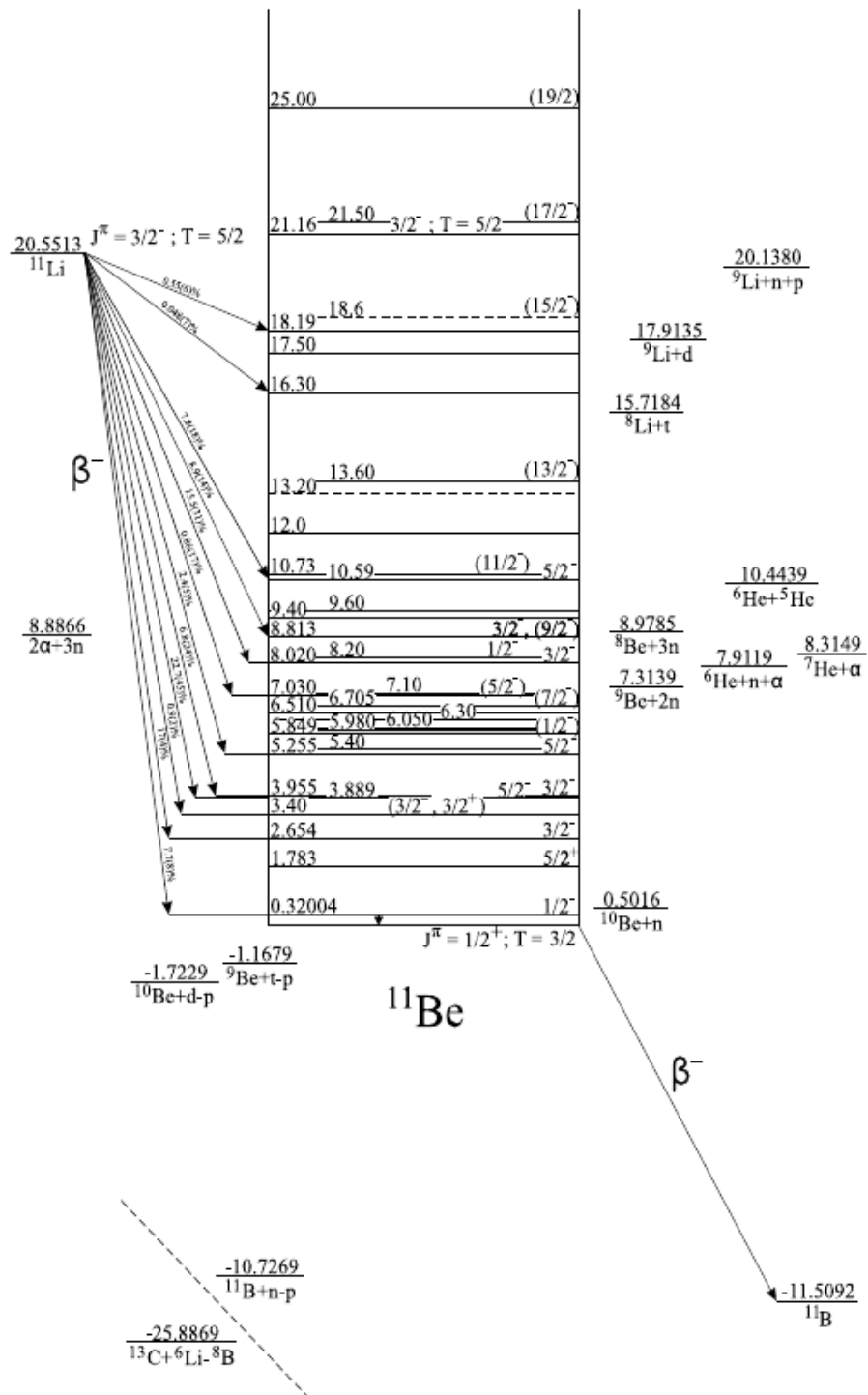


Figure 1.5: ^{11}Be level scheme obtained from β -decay and reaction studies [Kel12].

with R_b the interaction radius defined from the mass numbers A : $R_b = 1.44 \times (A_t^{1/3} + A_p^{1/3})$ fm.

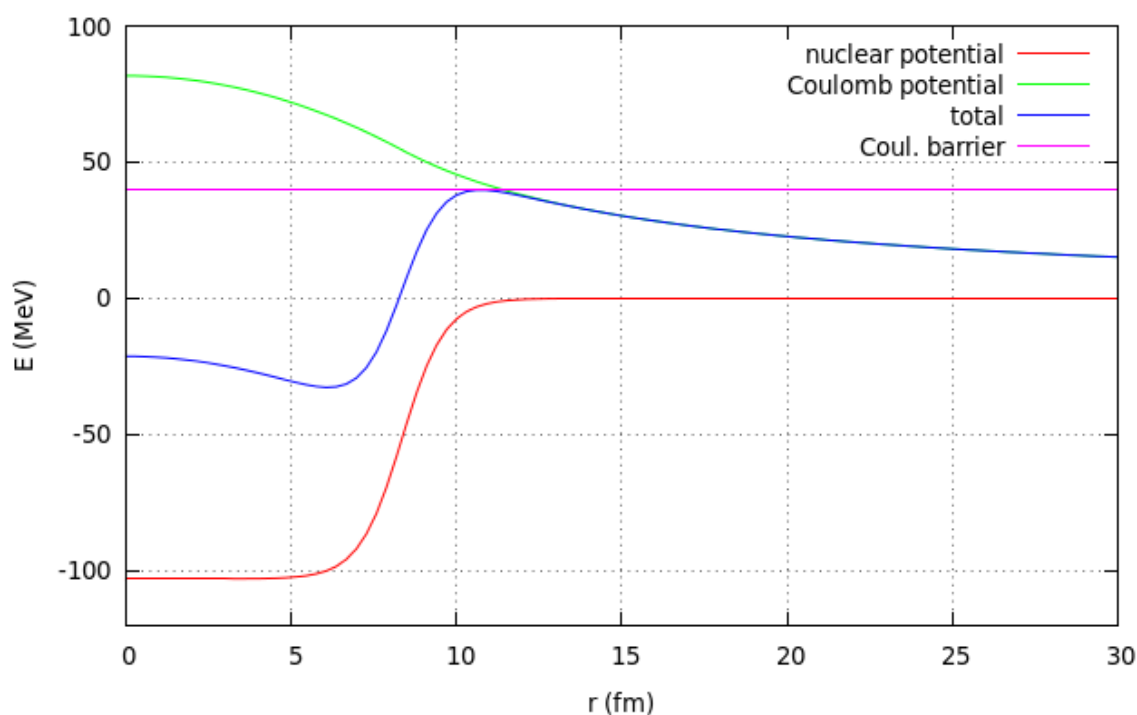


Figure 1.6: Coulomb and nuclear contributions to the potential between ^{10}Be and ^{197}Au , total potential and position of the Coulomb barrier.

This definition is appropriate for ordinary compact nuclei. When one of the colliding nuclei is a halo nucleus the definition is less clear. The low binding energy translates into reaction channels other than Rutherford elastic scattering opened at energies much lower than the barrier defined this way.

It is not trivial to adopt a rigorous definition of the Coulomb barrier for halo nuclei. If we base the definition on the constraint that only Rutherford scattering is observable, the Coulomb barrier would be at extremely low energies. If we base the definition on the maximum of the potential, this actual does not reflect the ordinary energy barrier in the system. A compromise often used in nuclei with neutron haloes, for being consequent with the ordinary definition, is considering as the Coulomb barrier of the halo nucleus such of the core (which will have the same Coulomb repulsion).

Independently of the definition chosen for the Coulomb barrier, the adopted value will be within the *low energy* range, and reactions at energies around the barrier are considered low energy experiments. In particular, when impinging on heavy targets, the interaction is clearly dominated by the Coulomb potential, which extends to very large distances (hundreds of fm). Even when the projectile incides with a large impact parameter it will feel this repulsion and may undergo breakup which will be detected in a vast angular range. As a matter of fact, in our work the breakup cross section will be measured in all the angular range and, in particular, at forward angles it will be dominated by Coulomb breakup.

1.5 The role of nuclear reactions

The energies used for studying nuclear reactions range from the few keV to hundreds of GeV. The different energy regimes are used for exploring different features of the nuclei and for exploring different areas of the nuclide chart. The higher the energy, the more reaction channels will be opened and the deeper the structure can be digged in. On the other hand, reactions at low energies are useful for studying low-lying excited states, the shell structure (by means of transfer reactions, for instance) and dynamic phenomena, like the Coulomb-nuclear interplay. This is the case of reactions at energies around the Coulomb barrier.

The energy of the reaction is not the only parameter to take into account in nuclear reactions. Different experiments may explore different features of the nuclei focusing on different reaction channels. In the case of loosely bound nuclei, the assortment of experiments that can provide relevant data is extense. Some examples of experiments that studied ^{11}Be have been selected from [Kel12] to illustrate the information on the structure and the reaction dynamics that can be extracted from experiments of different nature.

- $^{11}\text{Be}(p,p)^{11}\text{Be}$, $^{11}\text{Be}(p,p')^{11}\text{Be}$: The elastic and inelastic scattering with protons, usually referred to as (p,p) and (p,p') reactions, respectively, has been studied in inverse kinematics at $E(^{11}\text{Be}) = 63 \text{ MeV}/A$, $^1\text{H}(^{11}\text{Be},^{11}\text{Be})^1\text{H}$, $^1\text{H}(^{11}\text{Be},^{11}\text{Be}')^1\text{H}$ [Shr04]. With this experiment the bound states in ^{11}Be could not be resolved, but the resonance at $E_x = 1.78 \text{ MeV}$ ($J^\pi = 5/2^+$) was observed. Other resonances at higher energies were not resolved either. The CDCC calculations underpredict the breakup, and this mismatch was attributed to the role of the core deformation and excitations.
- $^{10}\text{Be}(d,p)^{11}\text{Be}$: Since the structure of the deuteron is well known and it is loosely bound, it is often used for neutron transfer reactions. For instance, using a deuteron beam of $E_d = 12 \text{ MeV}$ on a ^{10}Be target, the spectroscopic factor of the components with the core in the ground state was extracted for different ^{11}Be states: $S(^{11}\text{Be}_{gs}) = 0.73 \pm 0.06$ and $S(^{11}\text{Be}_{320}) = 0.63 \pm 0.15$ [Aut70].
- $^9\text{Be}(t,p)^{11}\text{Be}$: The protons detected after the two-neutron transfer to a ^9Be target give information on the states of the ^{11}Be populated. Measuring the gamma rays emitted after the population of the bound excited state, the energy and the lifetime were determined to be $E_x = 320.04 \pm 0.10 \text{ keV}$, $\tau_m = 116 \pm 15 \text{ fs}$, respectively. From this lifetime measurement the extracted strength is $\mathcal{B}(E1) = 0.116 \pm 0.012 \text{ e}^2\text{fm}^2$ [Mil83].
- $^{11}\text{B}(t,^3\text{He})^{11}\text{Be}$: With an energy in tritium beam of $E_t = 127 \text{ MeV}$, the cross sections for populating $^{10}\text{Be}^*$ states at $E_x = 320 \text{ keV}$, 2.69 MeV , 3.89 MeV and 8.94 MeV were measured at $\theta = 0^\circ$, extracting the $\mathcal{B}(GT)$ for the three low lying negative-parity states. This is a charge-exchange reaction, commonly used for the simple structure of both ^3H and ^3He [Dai98].
- $^{11}\text{B}(^7\text{Li},^7\text{Be})^{11}\text{Be}$: This is a charge-exchange reaction involving heavier species. An experiment of this nature provided accurate information on the position of the resonances and their widths [Cap04b].
- $^{208}\text{Pb}(^{11}\text{Be}, ^{10}\text{Be}+n)^{208}\text{Pb}$: Exclusive breakup measurements, in which the outgoing neutron and ^{10}Be are measured in coincidence, have been performed at RIKEN at energies

~ 70 MeV/u [Nak97, Fuk04] and at GSI at energies ~ 520 MeV/u [Pal03]. At very small scattering angles, the breakup cross sections measured in these experiments are mostly due to a direct $E1$ mechanism. Therefore, these kind of measurements have been used to infer the $\mathcal{B}(E1)$ probability to the continuum, by comparing the forward-angle breakup data with a suitable reaction model. Although the extracted $\mathcal{B}(E1)$ distributions differ quantitatively among the different experiments, they all predict a large $\mathcal{B}(E1)$ strength near the breakup threshold, as expected for a halo nucleus. These experiments also permitted the extraction of the spectroscopic factor for the $\nu 2s_{1/2} \otimes {}^{10}\text{Be}(0^+)$ configuration in the ${}^{11}\text{Be}$ ground state: $S = 0.61 \pm 0.05$ [Pal03] and $S = 0.72 \pm 0.04$ [Fuk04].

- ${}^{12}\text{C}({}^{11}\text{Be}, {}^{10}\text{Be}+n){}^{12}\text{C}$: The breakup measurements on light targets, in which nuclear effects are dominant, allowed the identification of low-lying resonances and their spin-parity assignment. In [Fuk04] the states at $E_x = 1.78$ MeV ($J^\pi = 5/2^+$) and $E_x = 3.41$ MeV ($J^\pi = 3/2^+$) are observed.
- ${}^{64}\text{Zn}({}^{11}\text{Be}, {}^{11}\text{Be}){}^{64}\text{Zn}$ [Pie13] and ${}^{120}\text{Sn}({}^{11}\text{Be}, {}^{11}\text{Be}){}^{120}\text{Sn}$ [Aco11]: These experiments at CERN-ISOLDE showed the differences of the reactions using several Be isotopes (${}^9, {}^{10}, {}^{11}\text{Be}$) on medium-mass targets at energies around the Coulomb barrier. For the ${}^{11}\text{Be}$ beam, a large absorption in the elastic channel was observed at all the measured angles. This absorption also produces the disappearance of the characteristic interference pattern at the grazing angle, where the projectile reaches the radius at which the Coulomb and nuclear potentials are of the same order. In the experiment with the Zn target, the resolution at forward angles was enough for separating the breakup fragments and they estimated an integrated cross section of $\sigma = 1100 \pm 150$ mb.

The reaction of halo nuclei on heavy targets at energies around the Coulomb barrier has been carried out for other species, namely ${}^6\text{He}$ [Esc07, Sá08] and ${}^{11}\text{Li}$ [Cub12, Fer13]. The knowledge acquired in those works is the cornerstone of this one, so it may be suitable to present here a more detailed overview of the results there obtained, where elastic scattering and breakup were observed for halo nuclei on heavy targets below the Coulomb barrier.

The first reaction studied by the collaboration was ${}^6\text{He}+{}^{208}\text{Pb}$. This was measured at the Louvain-la-Neuve facility (Belgium), at several incident energies ranging from 14 to 27 MeV (the Coulomb barrier in this case is approximately at 22 MeV). A large yield of alpha particles was observed even at energies below the Coulomb barrier, as shown in figure 1.7. The elastic angular distribution, as well as angular and energy distributions of these alpha particles, were obtained but, due to contamination with alpha particles produced by other processes, the angular distribution of these alpha particles could be only reliably obtained at large scattering angles. Optical model calculations [Kel03, San05] evidenced the need for a very diffuse imaginary potential in order to describe the data, thus suggesting the presence of long-range couplings. Later on, the data were compared with coupled channels calculations, based on a two-body description of the ${}^6\text{He}$ states (${}^4\text{He} + 2n$), including Coulomb and nuclear couplings to the breakup channels. These calculations described very well the elastic data, including the strong suppression of the cross sections, but underestimated largely the alpha cross sections. The latter could be reproduced, below the barrier, using an alternative model for breakup, the so-called transfer to the continuum method [Mor06], which includes transfer to bound and unbound states of the $2n$ -target and accounts for non-elastic breakup contributions. The most satisfactory calculations predicted two-neutron transfer as the most relevant mechanism at the

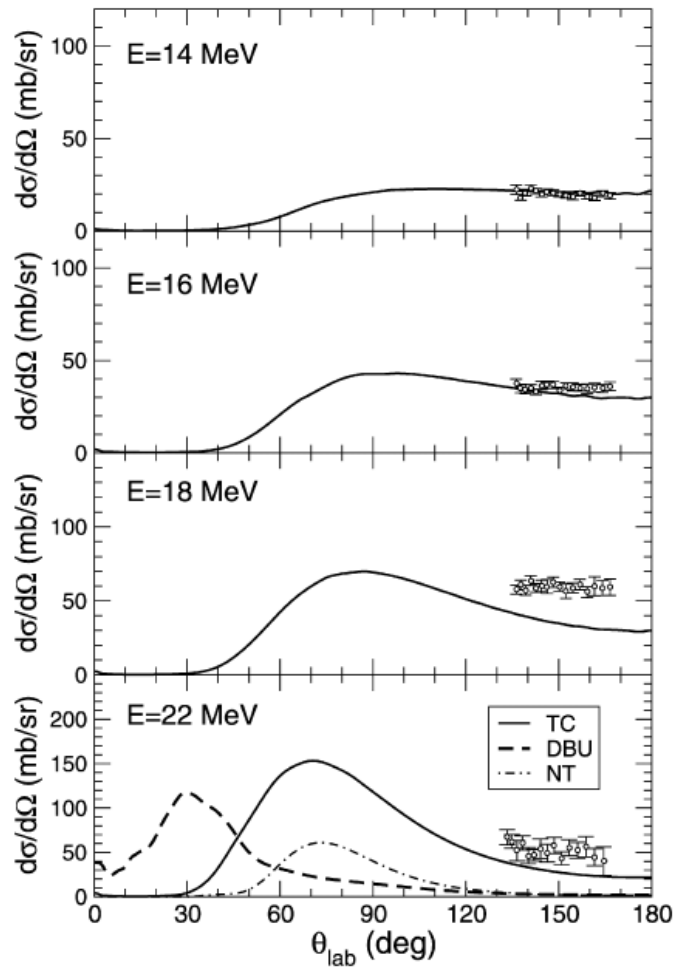


Figure 1.7: Angular distribution of ${}^4\text{He}$ arising from ${}^6\text{He}+{}^{208}\text{Pb}$ compared with three calculations: a direct breakup calculation performed within a CDCC approach (dashed line), a DWBA calculation for the one-neutron transfer to the continuum of the target (dot dashed), and a two-neutron transfer to the continuum of the target (solid) [Esc07]. It is observed that the two-neutron transfer dominates at backward scattering angles, but at energies around the barrier ($V_b \sim 22$ MeV is not enough for describing all the ${}^4\text{He}$ yield).

measured angles.

The contribution of the one-neutron transfer and the direct breakup were also studied. There was a lack of experimental data that did not allow for confirmation, but it was predicted that these processes were dominant at intermediate and small angles, respectively.

More refined CDCC calculations, based on a three-body model of the ${}^6\text{He}$ ($\alpha+n+n$) were performed later [Rod08, Rod09, RGM11]. These calculations reproduced very well the measured elastic angular distributions, but underestimated also the alpha yields at large angles, confirming that this result was not a byproduct of the limitation of the di-neutron model adopted in the original analysis.

Later on, the reactions ${}^9\text{Li}+{}^{208}\text{Pb}$ (at energies 24.1 MeV, 29.5 MeV and 33.1 MeV) and ${}^{11}\text{Li}+{}^{208}\text{Pb}$ (at 23.1 MeV and 28.3 MeV) were measured at TRIUMF (Vancouver, Canada). The case of ${}^{11}\text{Li}$ presents the same complications from the theoretical point of view, but the experiment, performed several years later, had several improvements that allowed for a larger angular range to be properly studied. The most forward angles were covered and valuable information could be extracted from it. The data were compared to Optical Model and CDCC calculations. The OM analysis revealed again the need for very large diffuseness parameter in the imaginary potential (which accounts for a long-range couplings to the continuum). The CDCC calculations confirmed the strong effect of the coupling to the breakup channels on the elastic cross sections and the indispensability of including those couplings for explaining the data.

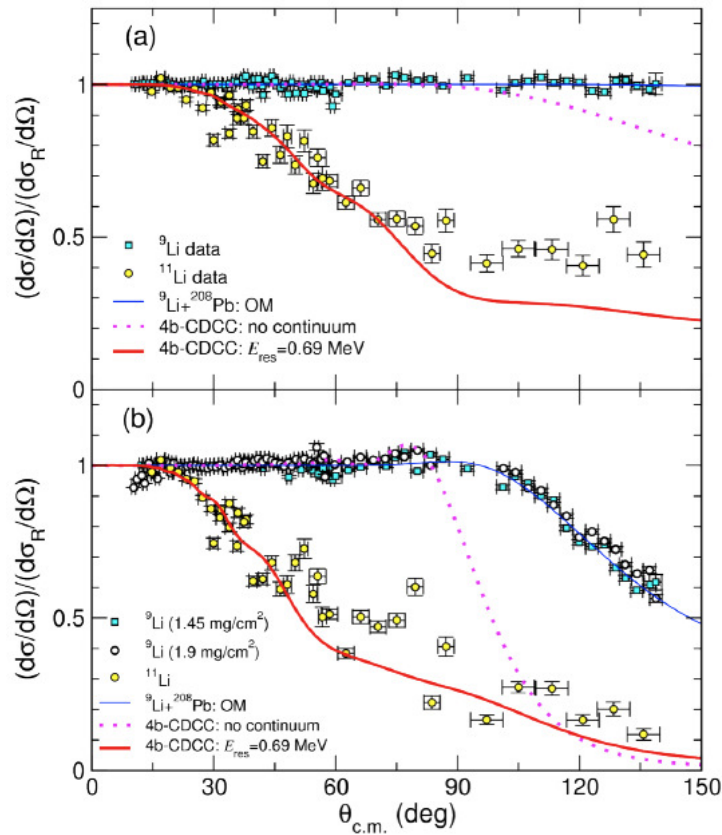


Figure 1.8: Angular distribution of the ${}^{11}\text{Li}+{}^{208}\text{Pb}$ elastic scattering compared with different calculations. It is evidenced that the inclusion of the channels in the continuum is essential for describing the elastic scattering. 4-body coupled-channel calculations including a soft dipole resonance at $E_x = 0.69$ MeV succeeded in reproducing the data.

The $\mathcal{B}(E1)$ to the continuum obtained with the model that better explained the data is significantly larger than the one obtained by T. Nakamura and collaborators in a high energy experiment at RIKEN [Nak06]. The apparent mismatch was argued to arise because the two experiments are sensitive to different ranges of the excitation energy (relative energy of the neutron with respect to the core). This work tries to deliver new data that tests this methodol-

ogy, using reactions around the Coulomb barrier, for extracting $\mathcal{B}(E1)$.

Assuming a one-step pure Coulomb excitation, the breakup cross section can be calculated within the Alder and Winther theory of Coulomb excitation [Ald75] at first order. It was shown that, if these breakup cross sections are expressed in terms of the so-called *collision time* (related to the scattering angle), one obtains a universal function, which depends only on the $\mathcal{B}(E1)$ distribution. The resulting breakup magnitude is independent of other dynamical quantities, such as as the collision energy, and the projectile and target charge. Considering that at very low excitation energies, the $\mathcal{B}(E1)$ can be approximated by a linear function of the excitation energy determined by an effective breakup energy ε_b and a slope parameter b , we may write:

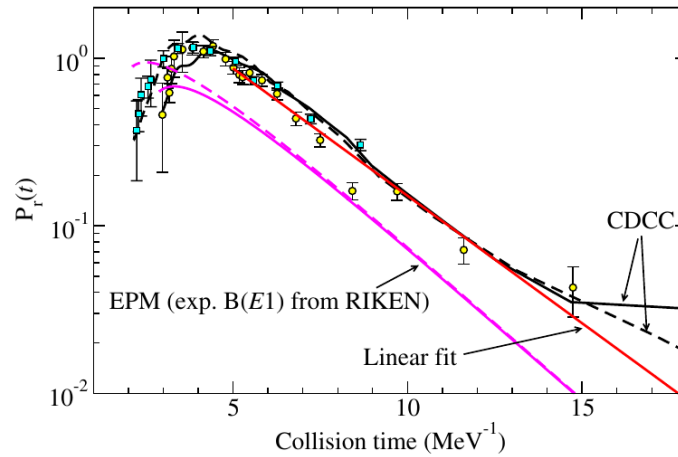


Figure 1.9: Reduced breakup probability for $^{11}\text{Li}+^{208}\text{Pb}$. Yellow circles and solid lines correspond to data and calculations at 24.3 MeV, and blue squares and dashed lines at 29.8 MeV, respectively.

$$\varepsilon \frac{d\mathcal{B}(E1, \varepsilon)}{d\varepsilon} \simeq b(\varepsilon - \varepsilon_b) \quad (1.9)$$

and the effective breakup energy can be extracted as the logarithmic derivative of the reduced breakup probability

$$P_r(t) \simeq b e^{-t\varepsilon_b}. \quad (1.10)$$

This is a method for obtaining the effective breakup energies of loosely bound nuclei from reactions in which the forward angle breakup is dominated by a $E1$ mechanism (large collision times).

1.6 Motivation

The motivation to undertake this study is manifold. Mainly, there was a research line of halo nuclei in the Experimental Nuclear Physics group at IEM-CSIC and our collaborators, which had performed studies on ^{11}Li and ^6He and provided the valuable results already discussed. Furthermore, there was a vacant amongst the results obtained from reactions using ^{11}Be beams.

The final goal of this work, as mentioned earlier, is to contribute to the understanding of the halo structure and its influence in the reaction dynamics. Such purpose can be tackled in many ways, so an explanation of the scope of this particular work may help the reader to have an idea of what he is going to find in the text.

The experimental data provided here are the energy and angle of the Be ejectiles after scattering on the ^{197}Au target, identifying the reaction channel associated to each detected particle (elastic, inelastic or breakup). With that, the angular and energy distribution for these three channels will be obtained and compared with calculations.

This work focuses on the simultaneous study of all of them, which are open at energies around and below the Coulomb barrier. Using Silicon and Germanium detectors with high granularity, high resolution charged-particle and gamma spectra could be obtained. The obtained angular distributions provided new experimental data which motivated some theoretical developments.

The energy of the beam used in this work is 20 times lower than the previous studies focused on the breakup, so the interaction mechanism is completely different. In the high energy regime, the interaction time is considerably shorter than the characteristic time of the electromagnetic interaction (the dominant one), so it is unlikely that the interaction happens in more than one step. In that framework, first-order calculations are a good approach to the problem. This approximation is also referred to as *sudden*, since beyond this *step*, there is no re-arrangement of the system during the reaction.

The interaction time can be approximated by the time that takes to the incoming particles to cross the distance of closest approach $2a_0$. In our case, this means $t_i \sim 1.21 \times 10^{-21}$ s and $t_i \sim 0.87 \times 10^{-21}$ s, at 2.9 and 3.6 MeV/u, respectively (the distance of closest approach is $2a_0 = 28.6$ fm for the low energy case and $2a_0 = 23.0$ fm for the other one). These times are of the same order than the characteristic time of the electromagnetic processes, so including high-order processes becomes essential for a correct description of the data. This gives information on how the systems minimizes its energy through the reaction dynamics.

Direct reaction theory

Nuclear reactions have been the major source of knowledge in the field of nuclear physics in general and in the field of halo nuclei in particular. A nuclear reaction is an interaction between two or more nuclei, forming a system which is brought to a different state than the initial one. The first nuclear reaction experiment was performed in 1909 by Geiger and Marsden without them being actually aware of it, when they studied the scattering of alpha particles from a gold target. A broad set of theories have been developed in order to explain the different measurements performed since then. The pioneer in this sense was Ernst Rutherford, when he inferred in 1911 that an atomic model with a small compact positively charged nucleus was more suitable for explaining the angular distribution obtained in the Geiger and Marsden experiment, instead of the previous description of the atom by J.J. Thomson. Nowadays, there are many theories available which describe different features of the nuclei. Unfortunately, the more accurate they are, the more complicated they usually become, so it is the task of the physicist to select the most suitable model depending on the needs in each case.

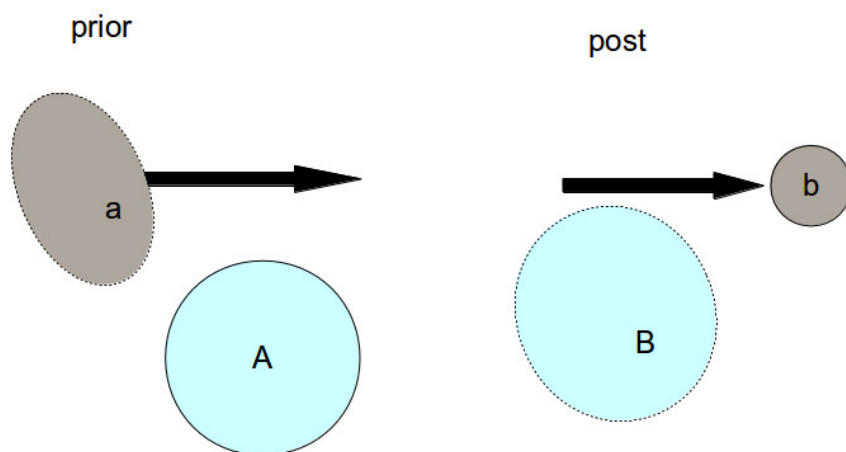


Figure 2.1: Post and prior representation of a direct reaction, where the projectile-like and the target-like products can be identified.

Direct reactions are those in which the projectile and the target maintain their identity, even when a few nucleons are broken apart or exchanged,

$$a + A \rightarrow b + B, \quad (2.1)$$

as depicted in figure 2.1. This is the case concerning this study. Due to the low energy of the beam and the low neutron separation energy of ^{11}Be one expects that the elastic, inelastic and breakup channels dominate over the compound nucleus formation. These are also called peripheral or surface processes. In this framework, the projectile and the target are identifiable through out the whole process. Due to this peripheral condition, the number of degrees of freedom involved is small, and theories that deal with the excitation of these few degrees of freedom are expected to be appropriate for describing the process.

The goal of scattering theory is to develop models that, containing relevant information of the colliding nuclei and the dynamics of the process, are able to generate outputs comparable to the measured observables. In this experiment, the measured observables are the angular distribution of the elastic and inelastic scattering cross sections and the angular and energy distributions of the breakup cross section. It is convenient to recall some common concepts used throughout this text:

- Differential cross section of particles scattering in some direction θ : Constant of proportionality between the flux of scattered particles through the area $dA = r^2 d\Omega$ in the direction of θ and the incident flux ([Gle04], p. 22). The differential cross section can be defined for an especific output channel $d\sigma_\beta/d\Omega$, or with respect to magnitudes other than the direction, like the energy of the ejectile $d\sigma/dE_b$.
- Elastic scattering: Scattering in which the resultant nuclei are the same as the initial ones, and they remain in their initial state after the collision.
- Inelastic scattering: Scattering in which either the projectile or the target populate an excited state. We will focus on the excitation of the ^{11}Be projectile, measuring the gamma radiation produced after the subsequent dexcitation.
- Breakup: Reaction in which the projectile, weakly bound, is broken up into two or more fragments due to the electrostatic or the nuclear field. In this case, the ^{11}Be nucleus can be easily broken up into ^{10}Be and a neutron.

Considering the low energy of the reaction, and the interacting nuclei, five different models were used:

- Optical model.
- Equivalent Photon Method (semiclassical calculation).
- Continuum Discretized Coupled-Channels Calculations (CDCC).
- Neutron-transfer to the bound and unbound states of the target.
- Continuum Discretized Coupled-Channels Calculations including core excitations (XCDCC).

Each of these calculations will be suitable for explaining different particular features of this study and, reciprocally, this study will show some advantages and limitations of the different models. All of them are quantum scattering theories except the Equivalent Photon Method, which relies on a semiclassical approach. The fundamentals of each method will be explained in this chapter.

2.1 Quantum scattering

In a time-independent description, the wavefunction of the system is given by the solution of the Schrödinger equation $H\psi = E\psi$, where E is the total energy of the system. Explicitly,

$$\left[-\frac{\hbar^2}{2\mu} \nabla_{\mathbf{R}}^2 + H_p(\xi_p) + H_t(\xi_t) + V(\mathbf{R}, \xi_p, \xi_t) \right] \psi(\mathbf{R}, \xi_p, \xi_t) = E\psi(\mathbf{R}, \xi_p, \xi_t) \quad (2.2)$$

where the first term corresponds to the kinetic energy for the relative motion of the nuclei, H_p (H_t) is the internal Hamiltonian of the projectile (target) depending on its internal degrees of freedom ξ_p (ξ_t), V is the interacting potential between the projectile and the target which, in general, depends on their internal degrees of freedom and their relative coordinate \mathbf{R} . In this case there is no polarization of the target or the beam, so there will be no privileged directions but the beam one. This means that there will be axial symmetry and we will be specially sensitive to the polar angle, θ (when we generically mention angle we will refer to θ unless explicitly stated otherwise), and that the dependence on the azimuthal angle, ϕ , will be limited to the inelastic scattering case, where the gamma ray emitted in the deexcitation may be emitted in any direction, and the breakup cases, in which the three resulting fragments ($^{10}\text{Be} + n + ^{197}\text{Au}$) may not be in the same plane. It has to be noted that in this experiment we will not be able to determine the breakup dependence on ϕ because we do not detect the neutron. A generic case is depicted in figure 2.2.

Equation (2.2) has many mathematical solutions. Among them, we must choose the solution that corresponds to our physical scattering process. The incoming beam can be represented by a plain wave¹ from which, after the collision with the target, a small part of the intensity will be emitted in a set of outgoing spherical waves. Most of the particles do not interact with any nucleus of the target and pass through it. These cases are included in the plain wave component of the wavefunction,

$$\psi(\mathbf{R}, \xi) \longrightarrow e^{i\mathbf{K}_0 \cdot \mathbf{R}} \Phi_0(\xi) + \text{outgoing spherical waves.} \quad (2.3)$$

Asymptotically, the target and the projectile do not interact anymore ($V \rightarrow 0$), so the hamiltonian is the sum of the internal hamiltonians and the kinetic energy term, $H = H_p + H_t + \hat{T}_{\mathbf{R}}$, and the wavefunction can be factorized in a part depending on the space coordinates and another part depending on the internal degrees of freedom $\Phi_0(\xi) = \Phi_p^{(0)}(\xi_p) \Phi_t^{(0)}(\xi_t)$. This original configuration in which both nuclei are in their ground state will be tagged as α . Excited states that respect the configuration (i.e. the states accessible via inelastic scattering) will be

¹When long range couplings are relevant a Coulomb wave has to be used instead of a plain wave, but for simplicity in the notation plain waves will be used in this explanation.

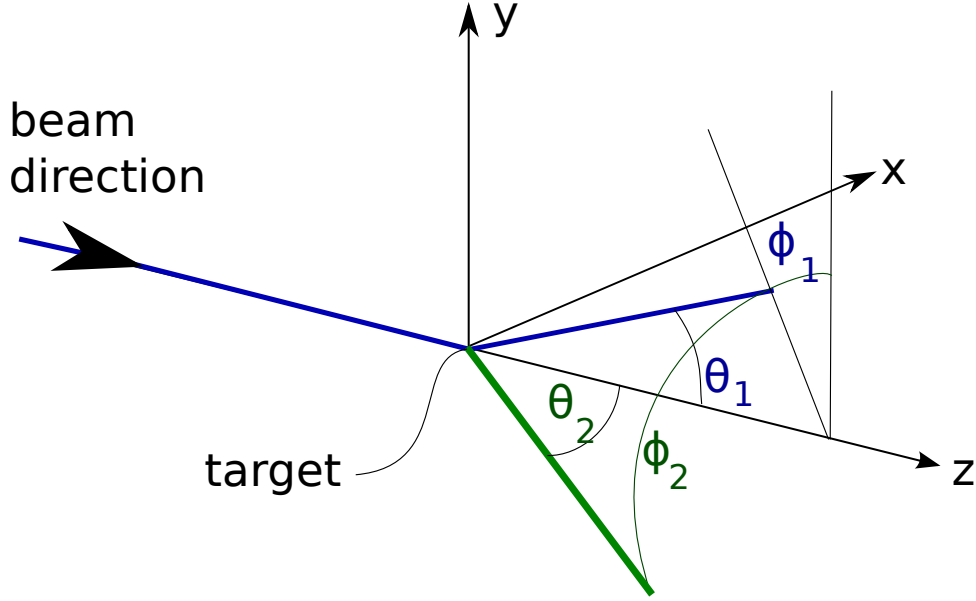


Figure 2.2: Spatial coordinates relevant for nuclear scattering, defined with respect to an origin of coordinates in the target position and z as the beam direction. This is a generic representation for two scattered particles (1 and 2). θ is the polar angle between the beam direction and the direction of the scattered particle. In our reaction it is the only relevant angle due to axial symmetry along z . ϕ is the angle between the plane in which the particle is emitted and the vertical plane.

called α' and configurations in which there is a rearrangement of nucleons will be called β . With this nomenclature, the complete wave function of the system should verify the following boundary conditions:

$$\begin{aligned} \psi(\mathbf{R}, \xi) &\xrightarrow{R_\alpha \gg} e^{i\mathbf{K}_\alpha \cdot \mathbf{R}_\alpha} \Phi_\alpha(\xi_\alpha) + f_{\alpha,\alpha}(\theta) \frac{e^{iK_\alpha R_\alpha}}{R_\alpha} \Phi_\alpha(\xi_\alpha) \\ &\quad + \sum_{\alpha' \neq \alpha} f_{\alpha,\alpha'}(\theta) \frac{e^{iK_{\alpha'} R_\alpha}}{R_\alpha} \Phi_{\alpha'}(\xi_\alpha), \\ \psi(\mathbf{R}, \xi) &\xrightarrow{R_\beta \gg} \sum_{\beta} f_{\alpha,\beta}(\theta) \frac{e^{iK_\beta R_\beta}}{R_\beta} \Phi_\beta(\xi_\beta), \end{aligned} \quad (2.4)$$

where θ is the angle between the incoming beam momentum and the direction in which the ejectile is detected. This wavefunction is compared to each of the measured differential cross sections through each of the amplitudes (f_{xy}) of the considered states:

$$\frac{d\sigma_\beta}{d\Omega} = \frac{v_\beta}{v_\alpha} |f_{\alpha,\beta}(\theta)|^2 \quad (2.5)$$

The factor v_β/v_α comes from the definition of the cross section as the constant of proportionality between the incident and measured **flux**, which is a magnitude that depends on the velocity of the fragments.

2.2 Model space

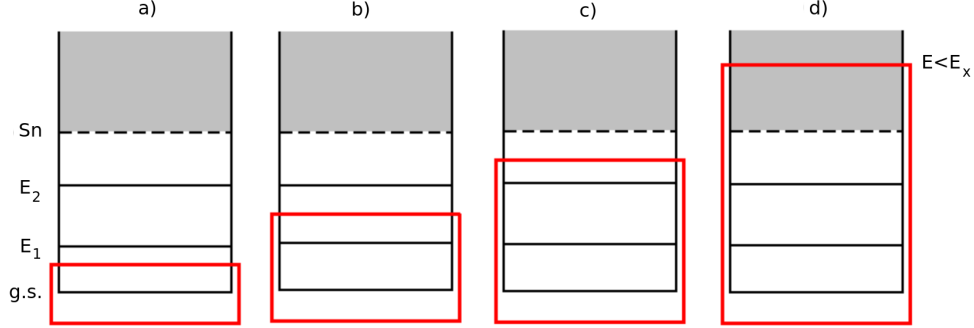


Figure 2.3: Graphical examples of model spaces. a) The model space is only the ground state, so only elastic scattering is explicitly included in the calculation. b) The model space is the ground state and the first excited state. c) All the bound states are included in the model space. d) The model space includes all the bound states and the states in the continuum up to a certain E_x .

The model space is an important concept that often is explained too vaguely. Every quantum system has an infinite number of states, and obviously it is not possible to include all of them explicitly in the calculations. A way of dealing with this limitation is dividing the space of states into two subspaces. The first subspace is the one that will be explicitly accounted for in the calculation and is what is called the model space or the P space. The other subspace, often called Q , is the set of all the states which are not explicitly described. For instance, in case we were only interested in describing explicitly the elastic scattering, the elastic channel would be the P space. The inelastic scattering and the breakup to all the accessible states of the continuum would be considered part the Q space. This is graphically explained in Fig. 2.3 a). The model space included in a typical continuum-discretized coupled-channels calculation, in which part of the states in the continuum are included, is depicted in figure 2.3 d).

Nevertheless, the existence of the states in the Q space is taken into account for the calculations as effective potentials, since there are terms in the potential V connecting all the states in the basis.

$$\psi = \psi_p + \psi_q \quad (2.6)$$

$$\langle \psi_p | H | \psi_p + \psi_q \rangle = H_{pp} + V_{pq} \quad (2.7)$$

The P and Q parts of the wavefunction verify the following set of coupled equations (see [Gle04] for more details):

$$(E - H_{pp})\psi_p = V_{pq}\psi_q, \quad (2.8)$$

$$(E - H_{qq})\psi_q = V_{qp}\psi_p. \quad (2.9)$$

Substituting ψ_q in eq. (2.8) from its form in eq. (2.9), an effective Hamiltonian of the following form can be obtained:

$$H_{eff} \xrightarrow{\epsilon \rightarrow 0^+} H_{pp} + V_{pq} \frac{1}{E - H_{qq} + i\epsilon} V_{qp} \quad (2.10)$$

with $i\epsilon$ an infinitesimal imaginary quantity added for avoiding the singularity when the operator is acting upon an eigenstate and ensuring the outgoing boundary condition. This effective Hamiltonian is extremely complicated (non-local, energy and angular momentum-dependent) and involves the coupling to all the channels in the basis, which cannot be evaluated in practice. Potentials determined phenomenologically are often used instead to model the interactions.

2.3 Optical Model

The optical model (name taken from the model for describing the scattering of light on an opaque glass sphere) is the simplest quantum scattering formalism between composite systems, in which only the elastic scattering is considered explicitly. This means that the internal degrees of freedom of the projectile and target are not considered and the interaction between them is described by an effective potential depending only on their relative coordinate (and, possibly, their spins). Since only the elastic channel is considered explicitly, the boundary conditions in eq. 2.4 are reduced to

$$\psi(\mathbf{K}, \mathbf{R}) \xrightarrow{R_\alpha \gg} e^{i\mathbf{K}\cdot\mathbf{R}} + f(\theta) \frac{e^{iKR}}{R}. \quad (2.11)$$

In such framework only the relative motion degree of freedom (and often also the internal spins) are considered, since a change in the internal degrees of freedom would mean an excitation which is not inside the model space, and an *optical* central potential is used for parametrizing the interaction. This potential is commonly built as an addition of a Coulomb potential and a complex (complex meaning that has an imaginary term) nuclear potential. It results in a potential with a real part, which will give rise to the elastic scattering output channel, and an imaginary part, which removes flux from the elastic channel, i.e., it models the absorption in the elastic channel due to population of other states, coming from excitations, nucleon transfer, fusion, etc.

The Coulomb potential is usually taken as that between two uniformly charged spheres:

$$U_c(R) = \begin{cases} \frac{Z_p Z_t e^2}{R} & R \in (R_c, \infty) \\ \frac{Z_p Z_t e^2}{2R} \left(3 - \frac{R^2}{R_c^2} \right) & R \in (0, R_c] \end{cases} \quad (2.12)$$

where $e^2 = 1.4399 \text{ MeV}\cdot\text{fm}$, R_c the Coulomb radius, Z_i number of protons of target and projectile and R distance between them. The real and imaginary terms of the nuclear potential can be obtained using a microscopic description of the nucleon-nucleon interaction (called convolution potential), or using a phenomenological potential, for instance a Woods-Saxon potential. Such parametrization of the potential simplifies the, in general, non-local, ℓ and s dependent potential into a local, angular momentum independent one with the following radial shape:

$$g(R, R_x, a_x) = \frac{1}{1 + e^{\frac{R-R_x}{a_x}}} \quad (2.13)$$

where x may refer to the parameters of the real or the imaginary part of the potential, R_x the

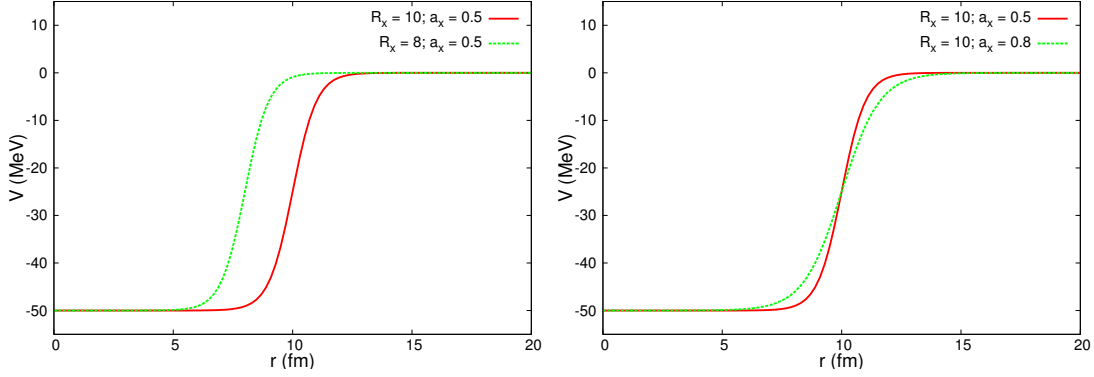


Figure 2.4: Woods-Saxon potentials for different values of radius R_x and diffuseness a_x .

radius of the well and a_x its diffuseness. In figure 2.4 is depicted the effect of modifying R_x (left side) and modifying a_x (right side). The general form of the potential will be then:

$$U_{\text{opt}}(R) = U_c(R) - V_r g(R, R_r, a_r) - iW_0 g(R, R_i, a_i) + i4a_s W_s \frac{dg}{dR}(R, R_s, a_s), \quad (2.14)$$

where V_r and W_0 are the depths of the Woods-Saxon potentials and W_s is the depth of an imaginary term that accounts for superficial absorption and has the shape of the derivative of a Woods-Saxon. Since this potential is taken to be central (i.e. it depends only on the modulus of R), it is possible to separate the Schrödinger equation into radial and angular parts. The solution of the angular part are the well-known spherical harmonics, so one has to deal only with the solution of the radial part. In this way, the three-dimensional differential equation is reduced to a set of one-dimensional equations, which are therefore simpler to solve. This is shown in more detail in the next section.

2.3.1 Partial wave expansion

The partial wave expansion permits writing the wavefunction as a sum of terms with different orbital angular momentum (the Legendre polynomials) with a radial function multiplying each of them:

$$\psi(\mathbf{R}, \mathbf{K}) = \sum_{l=0}^{\infty} C_l \frac{\chi_l(K, R)}{R} P_l(\cos \theta), \quad (2.15)$$

where we have obviated the dependence on m for simplicity. The radial functions are a solution of the Schrödinger equation for each l :

$$\left[-\frac{\hbar^2}{2\mu} \frac{d^2}{dR^2} + \frac{\hbar^2}{2\mu} \frac{l(l+1)}{R^2} + U(R) - E_0 \right] \chi_l(K, R) = 0. \quad (2.16)$$

The physical boundary conditions for determining χ_l and C_l are:

- if there is no potential $\psi \rightarrow e^{i\mathbf{K}\cdot\mathbf{R}}$,

- at sufficiently large distances the potential $U(R)$ is negligible, so the asymptotic behaviour of the wavefunction must fulfill

$$\left[-\frac{\hbar^2}{2\mu} \frac{d^2}{dR^2} + \frac{\hbar^2}{2\mu} \frac{\ell(\ell+1)}{R^2} - E_0 \right] \chi_\ell(K, R) = 0 \quad (R \rightarrow \infty). \quad (2.17)$$

A proper basis of functions for the expansion of a plain wave and a set of functions behaving as spherical waves at large radius is a basis of spherical Bessel functions $j_\ell(KR)$. A plain wave can be written as:

$$e^{i\mathbf{K}\cdot\mathbf{R}} = \sum_{\ell} i^\ell (2\ell+1) j_\ell(KR) P_\ell(\cos\theta), \quad (2.18)$$

so, if there is no potential, $C_\ell = i^\ell (2\ell+1)$ and $\chi_\ell = j_\ell(KR)$. Considering the asymptotic behavior of j_ℓ ,

$$j_\ell i^\ell \rightarrow \frac{1}{2iKR} \left[e^{iKR} - (-1)^\ell e^{-iKR} \right], \quad (2.19)$$

we see that a plain wave can be imagined as a coherent sum of incoming and outgoing spherical waves of the same intensity. In presence of a real potential, some of the flux will be redistributed from the original outgoing plain wave to different directions. This can be introduced into the equation by a phase which multiplies the outgoing spherical wave so that the coherent sum is not a plain wave anymore, but reflects the scattering in all directions:

$$\frac{\chi_\ell(K, R)}{R} \rightarrow \frac{2\ell+1}{2iKR} \left[\eta_\ell e^{iKR} - (-1)^\ell e^{-iKR} \right], \quad (2.20)$$

where η_ℓ is called the reflection coefficient, which is usually written as $\eta_\ell = e^{2i\delta_\ell}$, with δ_ℓ a real number $[0, 2\pi)$ quantifying the shift of the wave for each ℓ . In equation (2.11) we saw that the difference between the total wavefunction and the incident wave is, asymptotically, $f(\theta) \frac{e^{iKR}}{R}$, and using equations (2.18), (2.19) and (2.20) it can be calculated as:

$$f(\theta) \frac{e^{iKR}}{R} \rightarrow \frac{1}{2iKR} \sum_{\ell=0}^{\infty} (2\ell+1) (\eta_\ell - 1) e^{iKR} P_\ell(\cos\theta), \quad (2.21)$$

and using this result, the scattering amplitude is given by

$$f(\theta) = \frac{1}{2iK} \sum_{\ell=0}^{\infty} (2\ell+1) (\eta_\ell - 1) P_\ell(\cos\theta). \quad (2.22)$$

In the general case that the potential has an imaginary part, the only necessary modification is to include a positive imaginary term in $\delta_\ell = \delta_R + i\delta_I$ so that there is a negative exponential that accounts for the absorption:

$$\eta_\ell = e^{2i(\delta_R + i\delta_I)} = e^{2i\delta_R} e^{-2\delta_I}. \quad (2.23)$$

Although, for simplicity, it will not be explicitly included in the presentation of the formalisms, all the purely quantum methods included in this work (like the Coupled-channels one) use partial wave expansions for solving the equations.

2.4 Coupled channels formalism

If one is interested in the description of the excited states of the projectile or target, the model space needs to be extended so as to include these states. In the coupled-channels formalism, this is done assuming that the total wavefunction can be expanded in a basis of internal states of the projectile and/or target, as follows

$$\psi^{(+)}(\mathbf{R}, \xi) = \chi_0(\mathbf{R})\Phi_0(\xi) + \sum_{n>0}^N \chi_n(\mathbf{R})\Phi_n(\xi). \quad (2.24)$$

where the (+) clarifies the outgoing behaviour of the wave and the radial coefficients $\chi_n(\mathbf{R})$ describe the relative motion between the projectile and target when they are in the state "n", with $n=0$ denoting the ground state. The selection of the states included in the model space is formally done by truncating the summation after a given state N . The subtlety of this formalism is that the partial wave expansion is imposed not only asymptotically, but it is used for defining the wavefunction in all the space, even where the potential is not negligible. Comparing with the general asymptotic behavior of the total wavefunction, Eq. (2.4), one sees that these radial functions must verify the following asymptotic conditions:

$$\begin{aligned} \psi_0^{(+)}(\mathbf{R}, K_0) &\longrightarrow e^{i\mathbf{K}_0 \cdot \mathbf{R}} + f_{0,0}(\theta) \frac{e^{iK_0 R}}{R}, \\ \psi_0^{(+)}(\mathbf{R}, K_n) &\longrightarrow f_{n,0}(\theta) \frac{e^{iK_n R}}{R}. \end{aligned} \quad (2.25)$$

The coefficient of the outgoing wave, $f_{n,0}(\theta)$ is the scattering amplitude, and the differential cross section of each reaction channel included in the model space is given by

$$\frac{d\sigma(\theta)}{d\Omega}(0 \rightarrow n) = \frac{K_n}{K_0} |f_{n,0}(\theta)|^2. \quad (2.26)$$

Equation (2.24) adds N terms to the elastic scattering case and adds a dependence on the internal states of the nuclei in each of the terms. The internal states are obtained, in general, from the multiplication of the internal states of the projectile and the target, $\Phi_\alpha(\xi) = \Phi_p(\xi_p)\Phi_t(\xi_t)$, but in our case we will focus on the case in which only the projectile is excited,

$$H\Phi_p(\xi_p) = \varepsilon_p\Phi_p(\xi_p). \quad (2.27)$$

The procedure to follow is, therefore:

- Start with some appropriate structure model for the projectile, described by some model Hamiltonian, whose eigenfunctions and eigenvalues (energies) can be calculated.
- Then, the total Hamiltonian is defined. The Hamiltonian has to include the interactions that describe their relative motion and projectile excitation.
- Express the total model wavefunction of the system as an expansion in the internal states of the nucleus being excited, including only those states to be described explicitly. Note that, by construction, the final wavefunction is obtained as the eigenfunction of the total Hamiltonian with eigenvalue E (total energy).

Recovering the total Hamiltonian (eq. 2.2), and projecting it on each of the internal states included in the model space (this means integrating only on the internal degrees of freedom, so the dependence on the projectile-target relative coordinates will be kept) a set of coupled equations is obtained:

$$\begin{aligned}
(\Phi_n(\xi_n) | [E - \hat{T}_{\mathbf{R}} - H_n(\xi) - V(\mathbf{R}, \xi)] | \sum_{n'}^N \Phi_{n'}(\xi_{n'}) \chi_{n'}(\mathbf{R}) \rangle &= 0, \\
(\Phi_n(\xi_n) | [E - \hat{T}_{\mathbf{R}} - H_n - V(\mathbf{R}, \xi)] | \Phi_n(\xi_n) \chi_n(\mathbf{R}) \rangle &= \\
= - \sum_{n' \neq n}^N (\Phi_n(\xi_n) | [E - \hat{T}_{\mathbf{R}} - H_n(\xi) - V(\mathbf{R}, \xi)] | \Phi_{n'}(\xi_{n'}) \chi_{n'}(\mathbf{R}) \rangle & \\
[E - \hat{T}_{\mathbf{R}} - \varepsilon_n - V_{nn}(\mathbf{R})] | \chi_n(\mathbf{R}) \rangle = \sum_{n' \neq n} V_{nn'}(\mathbf{R}) | \chi_{n'}(\mathbf{R}) \rangle & \quad (2.28)
\end{aligned}$$

where $V_{nn'}$ are the so-called coupling or transition potentials. We obtain N coupled equations, one for each state n and each of the states is coupled to all the rest by a set of potentials $V_{nn'}(\mathbf{R})$. The system of equations obtained is not solvable analytically, so the resolution is tackled numerically. When the number of states included is very large, these calculations become computationally demanding. When the couplings among channels are weak, an alternative is to solve the problem perturbatively, as in the DWBA approximation described below.

2.4.1 Distorted Wave Born Approximation (DWBA)

The Distorted-Wave Born Approximation is a perturbative method for simplifying the coupled equations (2.28). It is a valid method if the coupling among the different states is weak and can be treated as a perturbation. Provided that, in a first step, the total interaction is separated into an average potential, $U(\mathbf{R})$, and a residual interaction, that encompasses the rest of the projectile-target interaction

$$V(\mathbf{R}, \xi) = U(\mathbf{R}) + \Delta(\mathbf{R}, \xi), \quad \Delta(\mathbf{R}, \xi) \ll U(\mathbf{R}). \quad (2.29)$$

Then, the distorted waves, $\tilde{\chi}_i$ and $\tilde{\chi}_f$ are introduced. They are meant to describe the projectile-target relative motion in the presence of the average potential $U(\mathbf{R})$:

$$[E - \hat{T}_{\mathbf{R}} - \varepsilon_n - U(\mathbf{R})] | \tilde{\chi}_i(\mathbf{K}_i, \mathbf{R}) \rangle = 0, \quad (2.30)$$

$$[E - \hat{T}_{\mathbf{R}} - \varepsilon_n - U(\mathbf{R})] | \tilde{\chi}_f(\mathbf{K}_f, \mathbf{R}) \rangle = 0, \quad (2.31)$$

where \mathbf{K}_i and \mathbf{K}_f are the momenta that give the direction of the incident wave and the direction of the outgoing wave, respectively. With this, the amplitude to any of the excited states, f , is obtained (see [Sat83] for the skipped steps):

$$f_{f,i}^{\text{DWBA}}(\theta) = -\frac{\mu}{2\pi\hbar^2} \int \tilde{\chi}_f^{(-)*}(\mathbf{K}_f, \mathbf{R}) \Delta_{fi}(\mathbf{R}) \tilde{\chi}_i^{(+)}(\mathbf{K}_i, \mathbf{R}) d\mathbf{R} \quad (2.32)$$

where θ is the angle formed by \mathbf{K}_i and \mathbf{K}_f . The transition potential is defined as:

$$\Delta_{fi}(\mathbf{R}) \equiv \langle \Phi_f(\xi) | V(\mathbf{R}, \xi) - U(\mathbf{R}) | \Phi_i(\xi) \rangle = \int \Phi_f(\xi)^* \Delta(\mathbf{R}, \xi) \Phi_i(\xi) d\xi. \quad (2.33)$$

In addition to the computational simplification, the DWBA offers a more transparent interpretation of the results, so it is extensively used for the interpretation of inelastic and transfer data.

2.4.2 Continuum-Discretized Coupled Channels (CDCC)

The Continuum-discretized Coupled-channels method is an extension of the Coupled-channels formalism in which not only the discrete bound excited states are included, but also states in the continuum are taken into account. Therefore, in this case the model space is the one shown in fig. 2.3 d).

We call the *continuum* of a nucleus to all the states above the separation energy, in which a nucleon or group of nucleons have enough energy to escape from the binding induced by the attraction of the rest of nucleons. We will focus in the case of the breakup of a projectile (^{11}Be) into a *core* (^{10}Be) and a *valence* particle (neutron) due to the interaction with a target (^{197}Au). Each of the three entities is considered to be inert, so the internal degrees of freedom arise from the relative motion between the valence particle and the core, characterized by the relative coordinates r, ℓ, s and j . Once the projectile is broken, all values for the relative energy between the valence particle and the core (ε) are permitted, and each of those ε correspond to a different state, so the number of states with positive energy is actually infinite.

In order to include the continuum in the coupled-channels framework, a procedure of continuum discretization has to be used. This consists in representing the continuous spectrum by a finite and discrete set of representative states. This finite representation is meant to represent the "true" continuum spectrum, at least within the range of distances which are relevant to describe the reaction mechanism. At large distances, some differences between the "true" and the representative states have to be introduced for the latter to be square-integrable.

In this framework, it is straightforward to say that, on one hand, the fewer states the more manageable the calculation, and on the other hand, the more states included, the better mapped that the continuous spectrum will be. Another important factor to be taken into account is the presence of resonances. Intuitively, a resonance is a state in the continuum which is *preferred* by the system compared to the states around it. These states are described by a wavefunction that has a considerable amplitude within the range of the potential and their half-life is relatively large, compared to the half-lives of the states in the non-resonant continuum.

The two main methods for discretizing the continuum in coupled-channels calculations are:

- Pseudo-states method: A basis of square-integrable functions is used for diagonalizing the Hamiltonian. With this method both the bound and unbound states of the system will be obtained as an expansion of the functions in the basis. Since it is necessary to truncate the basis, the obtained eigenstates and eigenvalues will be a finite approximation of the states and are usually called Pseudo-states (PS). In practice, the coefficients

for the expansion are obtained diagonalizing the Hamiltonian in a truncated basis. The negative-energy eigenvalues describe the bound states of the system, whereas those located at positive energies can be regarded as a finite and discrete representation of the continuum. By construction, the PSs do not describe correctly the continuum states asymptotically, but they are expected to be a good representation of these states at small distances.

- **Binning method:** In this method, the continuum is first truncated at a maximum excitation energy (ε_{max}) or, equivalently, a maximum linear momentum (k_{max}). The continuum between $0 < k < k_{Max}$ is divided into N subintervals called *bins*, and each of the bins will be considered as a single state. For each bin, a representative square-normalizable function is calculated as a superposition of the scattering states within the bin interval:

$$u_{\ell sj,n}(r) = \sqrt{\frac{2}{\pi N}} \int_{k_1}^{k_2} w(k) u_{k,\ell sj}(r) dk, \quad (2.34)$$

where $u_{k,\ell sj}(r)$ is the radial function for the orbital momentum ℓ of the $n+^{10}\text{Be}$ system and

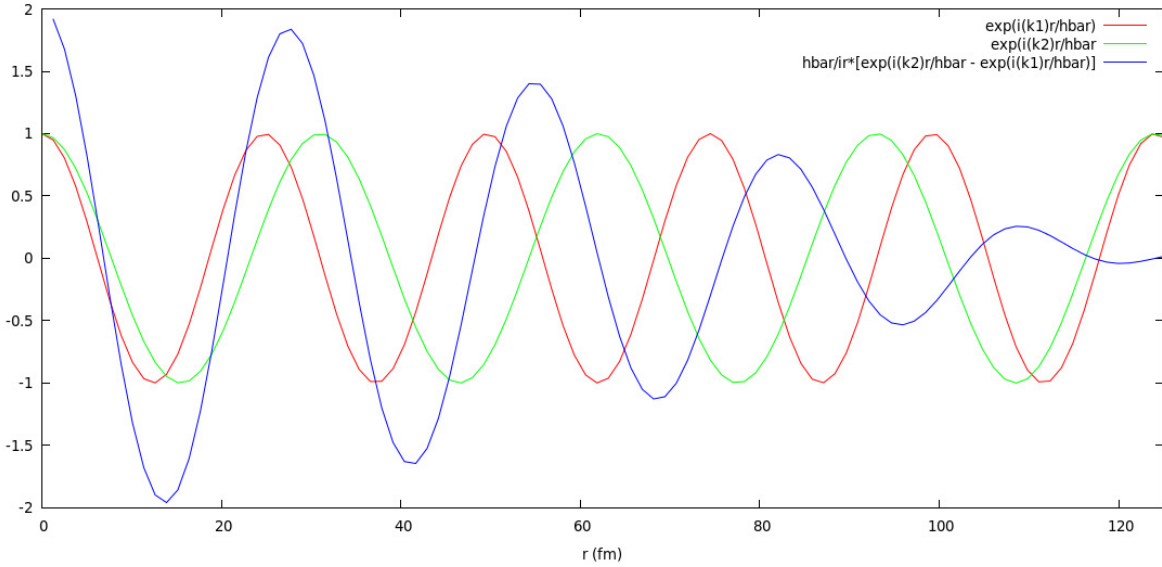


Figure 2.5: Binning method. Plane wave modelling the behaviour of the motion of the neutron with momentum k_1 (red) and k_2 (green) with respect to the ^{10}Be core and wave corresponding to the superposition of all states with moment $k_1 < k < k_2$ (blue).

$w(k)$ is a weight function that can be used to emphasize a particular region of the continuum. For example, for a bin containing a resonance, $w(k)$ can be defined in order to give a larger weight for continuum states close to the nominal energy of the resonance, so as the resulting bin will reflect better the properties of this resonance. Consequently, it has to be noted that there will be “several” continua, one for each specific quantum numbers ℓ and j . The model space will then be determined, not only by the maximum energy of the continuum included, but also by the maximum angular momentum considered. This integral is not only useful because it discretizes the continuum. It is also convenient because the destructive interference between all the $u_{k,\ell sj}(r)$, which are not square-integrable, generates a square-integrable function $u_{\ell sj,n}(r)$.

As has been mentioned along this section, the states in the continuum are defined for the $^{10}\text{Be}+n$ system. The coupling potentials, in this case, will be the matrix elements in the Φ_n basis of the *projectile-target* potential, which is the sum of the *core-target* and the *valence-target* potentials:

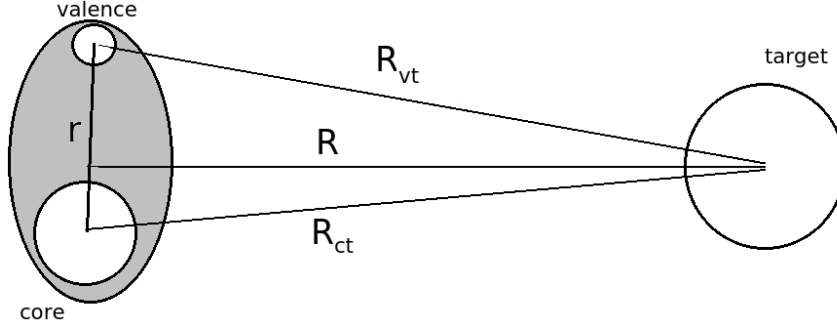


Figure 2.6: Spatial coordinates for the CDCC calculation within a three-body scattering model.

$$V_{nn'}(\mathbf{R}) = \langle \Phi_n(\mathbf{r}) | V_{ct}(\mathbf{R}_{ct}) + V_{vt}(\mathbf{R}_{vt}) | \Phi_{n'}(\mathbf{r}) \rangle \quad (2.35)$$

where \mathbf{R}_{ct} and \mathbf{R}_{vt} can be expressed in terms of (\mathbf{R}, \mathbf{r}) as shown in figure 2.6. This choice, together with the fact that the model space has to be truncated in energy and angular momentum, makes the CDCC choice specially suitable for the cases in which the relative energy and angular momentum between the neutron and the ^{10}Be core are small. Since the interaction in this case is mainly electromagnetic, we can imagine the neutron going straight ahead and the ^{10}Be being scattered away. In this picture, the lower the angle, the lower ε and ℓ will be needed for a proper description. If we aim to describe the full angular range more energies and partial waves will be needed. In any case, this approach will always offer more reliable results at forward angles.

2.4.3 Transfer to the Continuum of the target (TC)

The TC calculation is another approach to the problem within a Coupled channels formalism. In this approach, instead of describing the final states of the neutron with respect to the core, they are described with respect to the target. In general, the TC can account for both, the bound and unbound states of the n -target system that can be populated.

As was discussed in the previous subsection, when the projectile is scattered at forward angles, the momentum transferred will be small and the outgoing ^{10}Be and the neutron will have a velocity similar to that of the beam. Their energy with respect to the target will then be high. But, if one focuses on the other extreme case, in which the Be is scattered at angles close to 180° , the impact parameters is very close to 0, and it may be argued that the ^{11}Be will be almost stopped before being deflected. If breakup happens in this situation, the neutron can be *trapped* more easily by the target potential. Even if the neutron is not trapped, it is expected not to have a large relative energy with respect to the target, so the states populated can be

properly described as low energy states in the continuum of the target.

The model space that can be included is also limited when using this approach. Taking into account the discussion in this subsection and the previous one, it can be inferred that CDCC calculations will be more successful describing the scattering at forward angles and TC at backward angles. If the model space in both approaches were large enough, they would be redundant, so it is not correct to sum both contributions expecting that they complement each other. This would imply that some configurations would be counted twice.

2.4.4 CDCC including core excitation: XCDCC

The applicability of the presented CC calculations is limited to the cases in which the states can be defined using three inert bodies and the interactions among them. In a more realistic description, the role played by the collective excited states of the core can be included, and the states of the two-body nucleus will contain admixtures of excited states of the core, as we discussed in Sec. 1.3 for the ^{11}Be case. Maintaining the description in terms of a valence particle coupled to a core, the states of the system can be written as a superposition of different valence configurations, coupled to different core states.

The added value of this formalism is evidenced even before the calculation of the cross sections. For instance, in this case it allows for the more complete description of the ^{11}Be states presented in eq. (1.6) and eq. (1.7).

Focusing on the description of the scattering process, XCDCC is able to include explicitly more effects, like the dynamic core excitation during the reaction, and quantify its contribution in the reaction observables.

2.5 A semiclassical formalism. The Equivalent Photon Method

The Equivalent Photon Method [BB88], EPM from now on, is a theory for describing reactions dominated by Coulomb interaction from a semiclassical point of view. It is called semiclassical because it starts considering the classical trajectories followed by particles undergoing Rutherford scattering (in a purely quantum approach *trajectory* has no meaning) and once stated that, this model treats the internal dynamics of the projectile and target quantum mechanically.

In this approach, which is equivalent to the one proposed by Alder and Winther [Ald75], and is valid if:

1. One restricts to scattering angles dominated by the Coulomb interaction (small angles), so the classical trajectory can be approximated by a Coulomb trajectory. Moreover, for the classical trajectory approach to be meaningful, the De Broglie wavelength (λ) has to be small compared to half the collision distance ($\sim a_0$ for Coulomb dispersion). This is

condition is analogous to have a large *Sommerfeld* parameter η (see pages 41-43 of [Sat80]):

$$\eta \gg 1; \quad \eta = \frac{Z_p Z_t e^2}{\hbar v} \approx \frac{Z_p Z_t}{6.3} \left(\frac{m(u)}{E(\text{MeV})} \right)^{1/2} \quad (2.36)$$

In our case of study $\eta > 25$, so the approach is, in principle, justified.

2. If the projectile is excited, the kinetic energy lost due to the excitation is negligible, and last, that they interact interchanging virtual photons. Provided this, it can be assumed that the projectiles that are excited to small excitation energies will follow classical Coulomb trajectories, and hence, the angular distribution will be the corresponding to Rutherford scattering multiplied by a probability of populating such states.

$$\frac{d\sigma_{E\lambda}}{d\Omega} = P(\theta, E\lambda) \frac{d\sigma_{Ruth}}{d\Omega}. \quad (2.37)$$

The excitation cross section for an electric transition of polarity 2^λ is given by [Ald75]:

$$\frac{d\sigma_{E\lambda}}{d\Omega} = \left(\frac{Z_t e}{\hbar v} \right)^2 a_0^{(2-2\lambda)} \mathcal{B}(E\lambda) \frac{df_{E\lambda}(\theta, \xi)}{d\Omega} \quad (2.38)$$

with the dimensionless variable ξ called adiabaticity parameter and defined as

$$\xi = a_0 \varepsilon / \hbar v; \quad \text{with} \quad a_0 = \frac{Z_p Z_t e^2}{\mu_{pt} v^2}, \quad (2.39)$$

a_0 being half the distance of closest approach in a frontal collision, and ε the excitation energy. μ_{pt} is the reduced mass of the projectile-target system (noted like that for avoiding confusion with the projection of the order of the electric transition), and $df/d\Omega$ represents the number of equivalent photons exchanged with the target, and gives name to the formalism. This number is given by the expression:

$$\frac{df_{E\lambda}(\theta, \xi)}{d\Omega} = \frac{4\pi^2}{(2\lambda + 1)^3} \sum_{\mu} |Y_{\lambda\mu} \left(\frac{\pi}{2}, 0 \right)|^2 |I_{\lambda\mu}(\theta, \xi)|^2 \varepsilon^4 \quad (2.40)$$

with

$$\varepsilon = \frac{1}{\sin(\theta_{cm}/2)}; \quad Y_{\lambda\mu} \left(\frac{\pi}{2}, 0 \right) = \begin{cases} \sqrt{\frac{2\lambda+1}{4\pi}} \frac{\sqrt{(\lambda-\mu)(\lambda+\mu)}}{(\lambda-\mu)(\lambda+\mu)} (-1)^{(\lambda+\mu)/2} & \text{for even } \lambda + \mu \\ 0 & \text{for odd } \lambda + \mu \end{cases} \quad (2.41)$$

and $I_{\lambda\mu}$ are the Coulomb integrals defined in the second chapter of [Ald75]:

$$I_{\lambda\mu}(\theta, \xi) = \int_{-\infty}^{\infty} \frac{[\cosh(\omega) + \varepsilon + i\sqrt{\varepsilon^2 - 1} \sinh(\omega)]^\mu}{[1 + \varepsilon \cosh(\omega)]^{\lambda+\mu}} e^{i\xi(\omega + \varepsilon \sinh \omega)} d\omega. \quad (2.42)$$

In this particular case, the two excitations to be studied are the excitation to the only bound state at 320 keV, which happens through an $E1$ transition, and the breakup. The separation of the neutron from the ^{10}Be can be seen as a displacement of the center of mass with

respect to center of charge, which is the classical definition of a dipolar excitation. The dominance of the $E1$ transition in the breakup process with heavy targets is well documented. It has been observed, for instance, in the $^{11}\text{Li}+^{208}\text{Pb}$ reaction [Cub12, Fer13] at energies around the barrier and in $^{11}\text{Be}+^{208}\text{Pb}$ reaction at high energies [Fuk04], so it is expected to be dominant here, as well.

The electric transition probability, $\mathcal{B}(E\lambda; I_i \rightarrow I_f)$, is a magnitude that quantifies the likelihood of exciting a nucleus from an initial state $|I_i\rangle$ to a final state $|I_f\rangle$ through an electric transition of multipolarity λ .

$$\begin{aligned}\mathcal{B}(E\lambda; I_i \rightarrow I_f) &= \sum_{M_f \mu} |\langle I_f M_f | \mathcal{M}(E\lambda, \mu) | I_i M_i \rangle|^2 \\ &= \frac{1}{2I_i + 1} |\langle I_f || \mathcal{M}(E\lambda) || I_i \rangle|^2\end{aligned}\quad (2.43)$$

where the multipole moments are defined as the sum of the contributions of each of the k protons:

$$\mathcal{M}(E\lambda, \mu) = \sum_k e_k r_k^\lambda Y_{\lambda\mu}(\theta_k, \phi_k). \quad (2.44)$$

Considering eqs. (2.37) and (2.38), and that the Rutherford cross section can be written in the form:

$$\left(\frac{d\sigma}{d\Omega}\right)_{Ruth} = \frac{1}{4} a_0^2 \epsilon^4, \quad (2.45)$$

with the reduced mass of the system and v the relative velocity, the breakup probability is calculated as follows [Fer13]:

$$P_{bu}(\theta) = \left(\frac{Z_t e}{a_0 \hbar v}\right)^2 \frac{2\pi}{9} \int_{\epsilon_b}^{\infty} d\epsilon \frac{dB(E1, \epsilon)}{d\epsilon} (I_{1-1}^2 + I_{11}^2) \quad (2.46)$$

where $I_{1\pm 1}$ are the already defined Coulomb integrals.

The S1202 experiment

The S1202 experiment was proposed to measure the scattering of ^{11}Be on heavy targets at energies around the Coulomb barrier. It was the natural continuation of the previous experiments with ^{11}Li and ^6He beams. Due to the high resolution of the beam and the availability of TIGRESS for the charged particle detection, the experiment was performed in TRIUMF, Vancouver, Canada.

In this section I will give the details about the facility, design of the experiment, the different kind of detectors used, their disposition and the electronic modules needed for digitizing their signal into computer treatable data which gives us as much information about the experiment as possible.

As it has been described in the introduction, the experiment consisted on a ^{11}Be beam impinging on a heavy target and observing the scattered ejectiles. The experiment was performed in two occasions, the first one in 2012 using a ^{208}Pb target, and the second one in 2013 using a ^{197}Au target. Using different targets it was possible to identify the effects due to them and those effects due to the ^{11}Be and its halo configuration. In table 3.1 the different beams and targets used along this experiment are presented.

The Be beam energies (≤ 39.6 MeV) are around and below the Coulomb barrier ($V_b \simeq 40$ MeV). In nuclei with the typical compact structure this would mean that the scattering would correspond to the well known Rutherford elastic scattering. In the case of halo nuclei, as the wavefunction extends to larger radius, the probability of undergoing other processes is enhanced. This is the case of ^{11}Be . Being a one-neutron halo nucleus with a bound excited state at 320 keV, the channels of inelastic scattering and breakup are opened well below the barrier.

In this chapter the particularities of the facility where the experiment was performed and the chosen setup are explained.

3.1 Experiments with radioactive beams

Since the first experiments with radioactive beams were performed in 1985 by Tanihata and collaborators [Tan85], a new horizon of possibilities has been opened in our effort of uncovering the mysteries of nature. In the Earth no nuclear reactions are produced naturally, except in the upper layers of the atmosphere, where cosmic radiation produces some long-lived isotopes. Despite that, stable and long-lived isotopes are only a small proportion of all the nuclei that may exist, so the scientific community had to resort to inventiveness to produce the rest of them and study them. Some materials could be synthesized artificially, but were too short lived for making targets and probes out of them. The problem was solved producing a beam of such nuclei, making it possible to synthesize them and bring them to an experimental area before they decay. Nuclei with half-lives shorter than milliseconds have been analysed with such techniques. Nowadays, even nuclei beyond the driplines, which are unbound, are being synthesized, enabling the study of the limits of stability and nucleosynthesis processes (r-process, s-process and rp-process), for instance.

There are two main techniques for producing radioactive beams: The In-flight method and the ISOL method:

- **In-flight:** A heavy ion beam is accelerated to high energy and hits a thin light target. For instance, the target used for the S393 experiment [Rib15] at GSI is a 2.2 cm one made out of beryllium. The projectile is broken into a cocktail beam that flies through the target approximately with the velocity of the incoming beam. After that, the desired product is selected with a spectrometer. This is the method for producing the most exotic beams, since it is the fastest and most direct one. On the other hand, the energy resolution is worse than with the ISOL method (the energy loss of the particles flying through the target is uneven). Moreover, only high-energy beams can be produced with this method ($E_{min} \sim 50 \text{ MeV/u}$).
- **ISOL:** A high-energy light beam, generally a proton beam, hits a thick target ($\sim 20 \text{ cm}$). The nuclei in the target are broken and the products are extracted by diffusion towards an ion source. In the ion source the products are extracted and accelerated. This is the method used in TRIUMF so it will be further explained in the next section.

3.2 TRIUMF and ISAC. Facility and beam production

The experiment was performed at TRIUMF (Vancouver, Canada). The facility houses the world's largest cyclotron, able to accelerate H^- ions to energies between 475 and 520 MeV with intensities as high as $100 \mu\text{A}$. Once a hydrogen negative ion is accelerated to the desired energy, the two electrons are stripped off from it, generating a proton beam. A noteworthy variety of experiments can be undertaken with such beam. The relevant application for this study is that it has enough energy to produce nuclear reactions, and consequently to produce unstable isotopes. A broad range of products can be generated. In each case, the isotope of interest has to be selected among the different products. Then, it is accelerated to the desired energy for the study. This process of producing a radioactive beam is very delicate and that is why only a few facilities in the world are able to provide them.

The radioactive beam is produced by the ISOL method in the TRIUMF Isotope Separator and Accelerator facilities (ISAC). In ISAC-I the proton beam hits a primary target. Due to the impact of the incoming protons on this thick target ($>20 \text{ g/cm}^2$) many different reactions take place, producing :

- nearby nuclei by spallation,
- fission products and
- neutron-rich light nuclei by fragmentation.

Instead of being compact, the target is made by a set of sheets in series, made of tantalum in our case. Due to the impact of the protons and to a high current that is injected through it, the target is heated up to 2000°C . This configuration and the high temperature facilitate the diffusion of the products towards the transfer line. Coupled to the transfer line there is a tubular cavity that can act as a surface ion source. This surface ion source is used mainly for producing alkaline ion beams. In case of studying a nuclei that has an alkaline as an isobar (like ^{11}Li in our case) this ion source is nullified for reducing the contamination. In these cases a laser ion source is used instead [Bri12].

TRILIS (TRIUMF Resonant Ionization Laser Ion Source) is a Laser ion source that takes advantage of the different atomic properties of the products. The Lasers are tuned to energies corresponding to certain atomic transitions of the desired element leading to its ionization. With a convenient tuning of the set of lasers a rapid, efficient and highly selective ionization can be produced [Bri12, Ame13]. After this step, ideally, only Be isotopes will be present in the beam.

In the mass separator a dipole magnet bends the incoming cocktail beam. The different Be isotopes have different masses and rigidity, i.e., they respond differently to a determined field according to their mass over charge (A/q) ratio. By tuning the magnetic field in this dipole, a specific isotope can be selected among the produced ones. This is a key step in the beam production. The quality of the outgoing beam highly depends on the ability of obtaining a pure beam after this step.

Once selected the isotope of interest, the beam is focused in several steps while driven through the Low Energy Beam Transport (LEBT) line. After a preliminary acceleration in a Drift Tube Linac, the beam is deflected towards the ISAC-II Superconducting Linear Accelerator (SC-Linac), where it will be accelerated to the desired energy around the Coulomb barrier. For optimal acceleration in the SC-Linac, it is necessary to ionize the beam to an optimal A/q , which is done in an Electron Cyclotron Resonator ion source. Finally, some multipole magnets are used to focus the beam and some dipoles are used to deflect it and bring it to the experimental hall. The intensity of the beam in the experimental area was around 10^5 pps.

3.3 Experimental setup

In a purely experimental approach, our goal is to identify the ejectiles (either ^{10}Be or ^{11}Be) and measure the energies and angles at which they have been scattered, together with

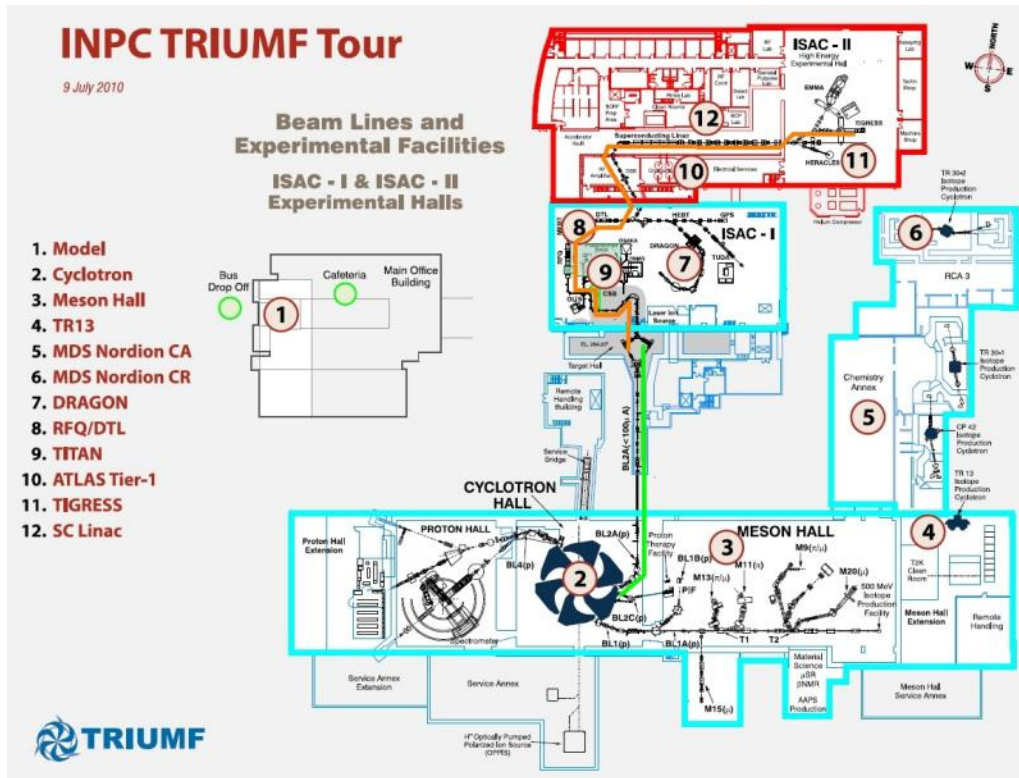


Figure 3.1: Plan of the TRIUMF facility showing the track the the beam follows to the experimental chamber at TIGRESS. The proton beam, going from the cyclotron to one of the two ISAC-I production targets is tracked in green. The radioactive beam (tracked in orange) passes through the mass separator, the LEBT and the DTL in ISAC-I. Lastly, its accelerated to the desired energy at the Superconducting Linac and is delivered to the experiment in TIGRESS.

Table 3.1: Summary of the ion beams produced for the S1202 experiment and the targets used.

2012			2013		
Isotope	Target	Energy (MeV/u)	Isotope	Target	Energy (MeV/u)
^{10}Be	^{208}Pb	3.6	^{12}C	^{197}Au	5.04
^{11}Be	^{208}Pb	3.6	^{11}Be	^{197}Au	3.6
^{11}Be	^{208}Pb	3.1	^{11}Be	^{197}Au	2.9
^{11}Be	^{208}Pb	2.9			

the γ radiation if any. A series of detectors had to be positioned in a certain geometry for doing so in the best conditions considering the experimental constraints.

First of all, the geometry had to be optimized considering the reduced space in the chamber and trying to maximize the quality of the data. The TIGRESS array limited the available space for the reaction chamber, and therefore, the number of detectors that could be fitted inside it. This was a major constraint for the detectors disposition. Their distance to the target

and the angle with respect to the incoming beam had to be thoroughly studied in order to maximize the covered angular range in θ . Some simulations and calculations were performed prior to the experiment to predict the angular distribution of the main observables and the critical angles to be covered. Figure 3.2 shows a calculation of the expected elastic cross section with a preliminary CDCC calculation and Geant4[GEA] simulations for the energy lost in different considered layouts for the detectors. The final layout of the detectors is shown in table 3.2 and in figure 3.3

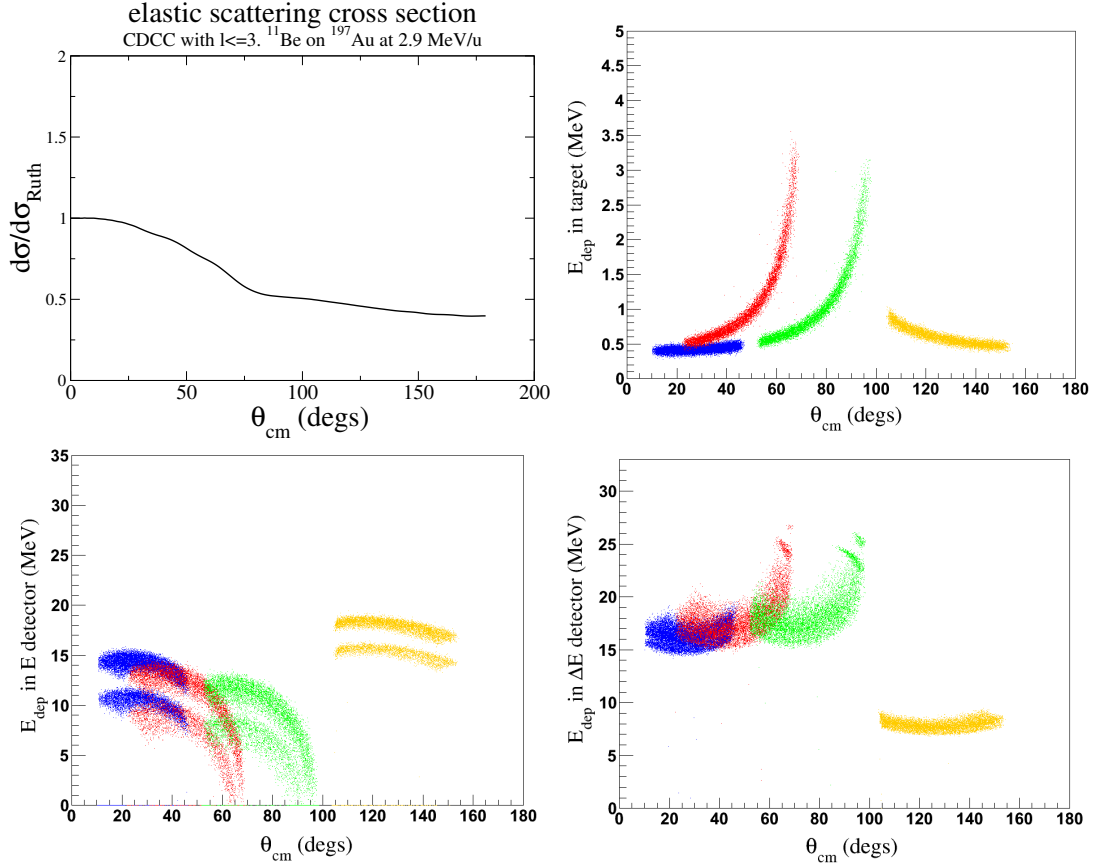


Figure 3.2: a) Preliminary CDCC calculation showing an abrupt variation of the elastic cross section around $\theta=70^\circ$. b) Simulation of the energy lost by the ^{11}Be in the target. c) Simulation of the energy lost by the ^{11}Be in the ΔE detector. d) Simulation of the energy lost by the ^{11}Be in the E detector.

Due to the axial symmetry of the reaction (there is no dependency on ϕ), in this text I will refer to the θ angle generically as angle. If another angle is referred to will be explicitly specified.

3.4 Detectors

3.4.1 Silicon detectors

Silicon detectors are the most commonly used for charged particles detection. The precise details are explained in the chapter 11 of [Kno89], but simplifying the details for easier

Table 3.2: Silicon detectors used in S1202 for charged particles detection, including their technical specifications and their configuration during the experiment.

L : Nominal distance from the center of the detector to the center of the target.

th : thickness.

DL: dead layer.

*: Serial number refers to reference number in Micron Electronics Ltd. catalog.

	Telescope	type	θ, L	Serial number*	Det. Th (μm)	front DL th. (nm)	back DL th. (nm)
ΔE	1	DSSSD	28°, 80 mm	2449-7	42	50+4%(300)	800
	2	DSSSD	45°, 60 mm	2449-10	40	50+4%(300)	800
	3	DSSSD	76°, 60 mm	2561-6	41	50+4%(300)	800
	4	SSSSD	130°, 55 mm	2752-7	20	800	800
E	1	PAD	45°, 60 mm	2712-8	500	800	800
	2	PAD	28°, 80 mm	2331-4	500	800	800
	3	PAD	76°, 60 mm	2712-11	505	800	800
	4	DSSSD	130°, 55 mm	2851-20	295	800	800

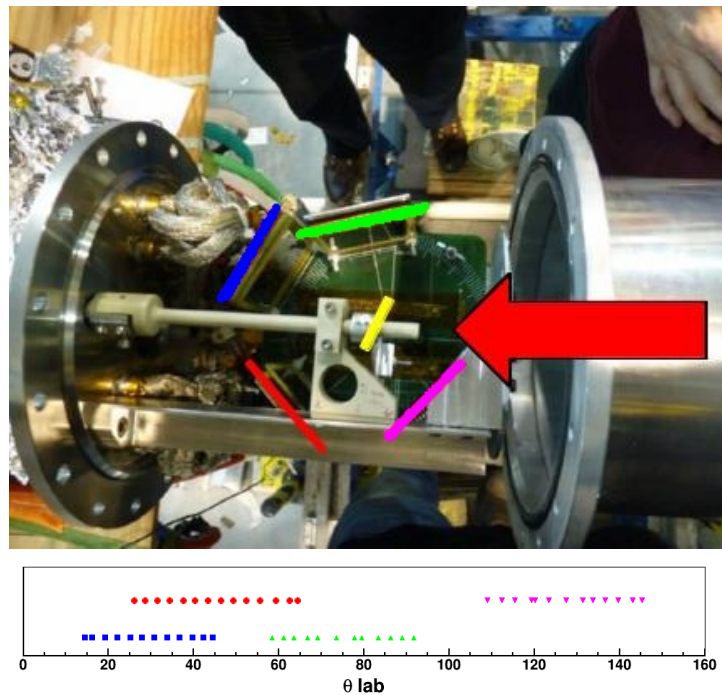


Figure 3.3: Position of the detectors in the chamber and angular range covered.

comprehension, a silicon detector consists of a silicon wafer that has different doping in different layers, forming a $p-n$ junction. In a pn -junction there is a side which has a p-type doping (p-side), which means that it has an excess of positive charge carriers (*holes*). The other side (n-side) has an excess of negative charge carriers (*electrons*). It is worth to stress that having a particular doping does not mean being charged. Before the junction both of them are neutral. However, when the junction is done, there is a diffusion process, equilibrating the density of electrons in both sides, thus creating an actually charged region around the junction called the

space charge region.

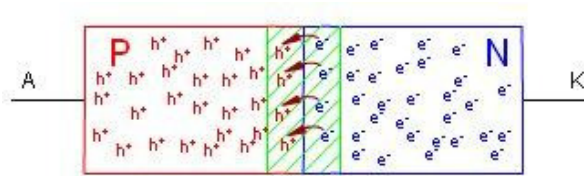


Figure 3.4: Schematic representation of a pn-junction, with the space charge region in the middle.

Silicon is a semiconductor, so when a particle goes through a silicon detector, it excites the electrons to the conduction band, producing the so-called electron-hole pairs. If this happens in the *space charge region* the electrons can be collected in one side while the holes can be collected in the other one. By reverse biasing a detector the space charge region is increased and the strength with which the electrons and holes are attracted is enhanced. It is called reverse biasing because the electrons are pulled towards the electron rich side of the junction and the holes towards the electron deficient side. This way the probability of an electron to recombine in the material of the detector is minimized. Since the energy necessary for exciting an electron to the conduction band can be considered definite, the number of electrons from the silicon collected (the integrated charge), is proportional to the energy lost by the charged particle, and produces an electrical signal that can be digitized.

There are physical constraints to the volume that the *space charge region* may cover. There is an operating voltage characteristic for the bias of each detector. Having reached this point, incrementing the voltage does not translate into an enlargement of the space charge region, and there will be some *dead layers* left out of it. They are called *dead* because particles lose energy in them but no electric signal is produced. In contrast, the space charge region is called sensitive volume.

The dead layers are, typically, thin layers in both surfaces of each detector. In addition to the region where the silicon is not able to produce a signal there are other contributors to the dead layers: the ohmic contacts. The material used for the electrical connection is typically aluminum, and is used for both, biasing the detector and carrying the generated signal. The aluminum layer (or aluminum strip, depending on the detector) is a physical obstacle in the path of the charged particles. When the charged particles travel through the aluminum used for the connections of the strips, or the silicon out of the sensitive volume, some information is lost. Despite that, this energy loss can be estimated in average to be accounted for, as will be explained in next chapter.

All the silicon detectors used in this experiment are bought to the firm Micro Electronics Ltd., and are referenced in table 3.2, giving precise information on their thickness and the thickness of their dead layers.

3.4.1.1 Double-Sided Silicon Strip Detectors (DSSSDs)

Both electrons and holes carry the same energy information, and both produce a current which, integrated in time, is proportional to the energy left in the sensitive volume of the detector. This fact is used in Double Sided Silicon Strip Detector (DSSSD) for angle determination. One of the sides, usually the front p-doped one, is divided into vertical strips, and the back side (n-doped) into horizontal strips. When a particle hits the detector, a signal is collected in one of the vertical strips and in one of the horizontal strips, giving information of the hit position in the X and Y axis of the detector.

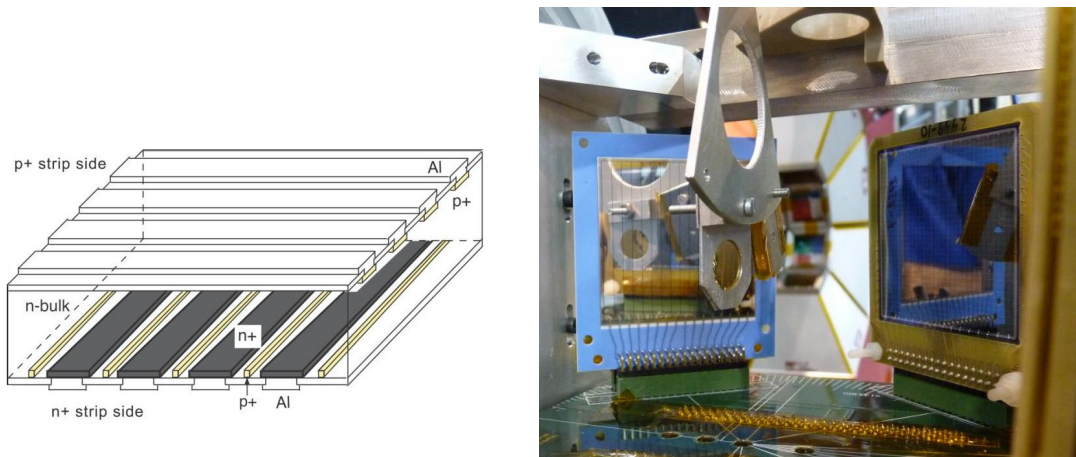


Figure 3.5: Schematic representation of a DSSSD detector on the left. On the right side, picture of a SSSSD (with blue frame) and a DSSSD (yellow frame).

The detectors used for this experiment (see figure 3.5) were 16×16 DSSSDs (256 pixels) and each strip has a width of 3 mm. Placing the detectors around 6 cm away from the target the uncertainty in the angle is below 3° . The great advantage of DSSSDs like these is that $16 \times 2 = 32$ channels of electronics allow for 256 micro-detectors.

3.4.1.2 SSSSD

In a Single Sided Silicon Strip Detector (SSSSD) only one side has the electrode divided in strips, so only provides information of the position in one axis. They are often chosen because SSSSDs can be manufactured thinner compared to DSSSDs. They can also be a preferential choice if the number of electronic channels available is reduced.

3.4.1.3 PAD

A PAD detector is a simple and relatively thick silicon detector with a single connection for biasing and reading the signal that is produced when the particles lose kinetic energy in it. Due to their simple construction, they are more robust but not position sensitive, and can be used to ensure that the particles are stopped in them (as E detectors).

3.4.2 Telescope configuration

The telescope configuration is a particular disposition of the detectors used for particle identification. A single silicon detector is able to provide information on the energy left by a particle in its active detecting volume, but no information on the nature of the particle. The telescope configuration (referred to as telescope or ΔE -E detector) is a combination of two or more silicon detectors in series. Charged particles go through the first detector, losing some of its energy, and are stopped in the second one, losing the remaining energy in it. The detectors have to be chosen conveniently so that the particles are not stopped in the front detector but lose enough energy for proper particle identification. This identification is done using two-dimensional plots with the ΔE energy loss in the Y axis and the energy lost in the back detector, or the total Energy (the sum of the two contributions) in the X axis. In table 3.2 the detectors used in our experiment and their configuration are stated.

Telescopes 1, 2 and 3 consisted of a 40 μm DSSSD backed with a PAD detector. Telescope 4 was formed of a 20 μm Single Sided Silicon Strip Detector (SSSSD) and a DSSSD behind it. This ΔE detector was chosen thinner in this case due to kinematics. Particles that go in the detection of telescope 4 have been backscattered and, hence, have lost more energy. Since they have less remaining velocity they leave more energy per length unit. Precisely, the energy deposition per length unit is proportional to $Z^2 \frac{\ln v^2}{v^2}$, as it can be seen in the non-relativistic Bethe formula 3.1.

$$-\frac{dE}{dx} = \frac{4\pi n Z^2}{m_e v^2} \left(\frac{e^2}{4\pi\epsilon_0} \right)^2 \left[\ln \left(\frac{2m_e v^2}{I} \right) \right] \quad (3.1)$$

In this case the ions that have to be separated are ^{10}Be and ^{11}Be , which have the same Z. Resolution has to be good enough for identifying the different ejectiles, even in the most unfavourable case that they have the same velocity. In that case they would deposit the same energy in the ΔE detector (same Z, same v), but as the total energy is a function of the mass, $E_{^{10}\text{Be}} \simeq 10/11 E_{^{11}\text{Be}}$ and the separation will arise from the energy deposited in the back detector. The Full Width at Half Maximum (FWHM) of the peaks has to be well below the separation energy $S_n = 504$ keV, which is achievable with the available Silicon detectors, and also below the energy difference of the isotopes $\text{FWHM} < 1/11 E_{^{11}\text{Be}}$.

3.4.3 Plastic Detector

Plastic detectors are a particular category of scintillator detectors. Scintillator materials produce light when charged particles or electromagnetic radiation lose energy in them. This light is collected in a Photo-Multiplier Tube (PMT) and converted into an electric signal. The PMT has a photodiode as a first stage, which emits electrons by photoelectric effect. Then there are a series of dinodes which multiply the number of electrons emitted in each step. A more detailed description can be found in chapter 8 of [Kno89].

A plastic detector was placed in the beam direction to monitor its intensity. The intensity of its signal is evaluated constantly to detect any fluctuation of the beam in intensity or direction. Moreover, checking the monitored intensity with and without a 2 mm collimator the size of the beamspot and the accuracy of its positioning could be estimated.

3.4.4 Germanium detectors

Germanium detectors are semiconductor detectors with the same operating principles as silicon detectors. Despite that, there are some differences that make them more suitable for a different purpose: γ spectroscopy. The main differences are two (chapter 12 of [Kno89]):

- The energy necessary for exciting an electron to the conduction band is smaller. $E_{Ge} = 0.67$ eV, $E_{Si} = 1.12$ eV.
- Germanium has larger Z . $Z_{Ge} = 32$, $Z_{Si} = 14$.

The first feature implies that the electrons can be excited to the conduction band very easily at room temperature, so they have to be cooled down for operation. That is a technological challenge which is nowadays solved by automatically refilled liquid nitrogen containers. Nevertheless, this is an expensive procedure and germanium is more expensive, as well, so silicon detectors are used for charged particle spectroscopy.

The second difference has important consequences, since the probability of interaction of the light with matter is a growing function of Z for all the relevant processes (Compton scattering, photoelectric effect and $e^+ - e^-$ pair production). Furthermore, under proper cryogenic conditions, the energy resolution of the germanium detectors for γ radiation is unequalled.

These considerations make it a common choice, when one wants to perform high-resolution gamma spectroscopy, to use germanium detectors. Since interaction of light with matter is discrete, in contrast with interaction of charged particles with matter that is continuous, the interaction of light with the dead layer is rare and is not something that has to be taken into account for the energy calibration in this case.

3.5 Printed circuit board

A Printed circuit board (PCB) was designed to accomplish a double function: Having a stable and permanent detector configuration, and providing a circuitry that allowed for a comfortable cabling of the detectors.

The basis of the PCB was made of glass fiber and epoxy, in which the circuits were printed. The PCB had four layers in which different circuits were printed and after ensembling had a total thickness of 1 mm. Two PCBs were plugged together with two 120-pin connectors. On the top one, five 34-pin connectors (one for each DSSSD and one for the SSSSD) were welded in the position where the detectors had to be placed. The PAD detectors backing some DSSSDs were attached to them using plastic screws, while plastic washers were used for keeping a distance between them, avoiding a contact that could damage the silicon or produce undesired electrical connections. A plane of the PCB with the position of the detectors and the connectors drawn on it can be seen in figure 3.6.

This technical solution minimized the uncertainty in the position of the detectors. The algorithm for optimizing the angle and solid angle assigned to each pixel will be explained in the next chapter, but it is remarkable that the variations with respect to the design values are

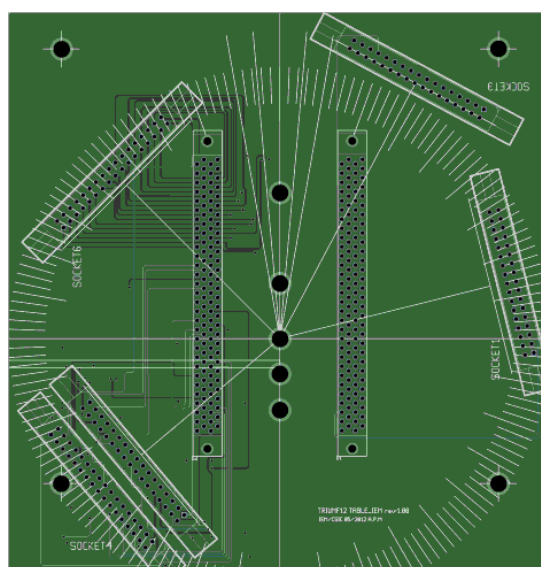


Figure 3.6: Plane of the Printed Circuit Board with the position of the detectors and the connecting pins drawn on it.

within tenths of millimeters and millimeters.

Mounted on the bottom PCB there were twelve 20-pin connectors to which the cables to the preamplifiers were plugged. There was a dedicated room between this PCB and the bottom of the chamber for the cables to be passed towards the feedthroughs.

3.6 Target

The two chosen targets for the S1202 experiment were ^{208}Pb and ^{197}Au . ^{208}Pb was the first option since it is a doubly magic nucleus, with no low lying excited states. This was a desirable feature for minimizing the nuclear effects of the target in the dynamics of the reaction. The thickness of the target was a compromise between resolution and statistics. The thicker the target, the more ^{208}Pb nuclei in the way of the beam and more probable will be the interaction, enhancing the statistics. On the other hand, the beam loses energy as it travels through the target. The thicker the target, the larger difference between the energy at the front side and the back side. Since the reaction can happen at any point of the target, the energy at which it happens is more spread in this case, reducing the resolution. The thickness of the target for the part of the experiment performed in 2012, taking these factors into account, was 1.45 mg/cm^2 .

For the 2013 run the target selected was ^{197}Au . The beamtime was considerably shorter, so for enhancing the statistics a thicker target was selected. The thickness of the ^{197}Au target was 1.9 mg/cm^2 .

The sheet of the target material was mounted on an aluminum target holder. The aluminum piece has a 1 cm circular hole, which is big enough for placing the sheet in position and remain the aluminum away of the beam direction.

In turn, the target holder was mounted on a target wheel, which is shown in figure 3.7. The wheel could be rotated from outside of the chamber for placing different elements in the target position on convenience. It was designed to operate in three positions, which were chosen to be: target position, collimator position and blank. In the target position the ^{197}Au target (^{208}Pb in 2012) was mounted. The blank position is kept without any object interfering the beam for performing the beam optimization without scattering on any device. A 2 mm diameter collimator was mounted in the wheel for fine alignment of the beam. Checking the transmission to the Plastic detector without and with the collimator a very precise positioning of the beamspot was performed. Similarly, when there were suspicions of a misalignment of the beam it was checked with the collimator. During normal operation and with proper alignment, the intensity with collimator was 80% of the intensity without it. Considering a two-dimensional, axially symmetric gaussian beamspot, this corresponds to a r.m.s = 1.4 mm of the beam in the target position, which ensures that the beam hits the target material and not the target holder or the target wheel.

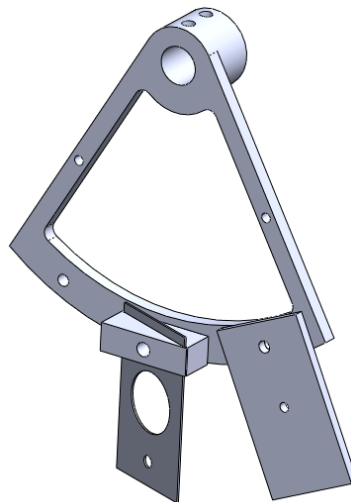


Figure 3.7: Drawing of the target wheel with the target and the collimator mounted on it. There is a third position of the wheel which was left blank for performing beam optimization operations without scattering on any object.

The energy loss in the target has to be considered for the calculations as well. The energy selected for the calculations is not the energy of the beam, but the energy of the beam after having traveled through half of the target. This is chosen arbitrarily, but is considered the more sensible choice. The energy loss was calculated using SRIM [Zie84]

The decision of the target and the detectors position was taken simultaneously because they influence each other. The position of the target is selected for minimizing the shade in the detectors. The normal to the detector forms a 15° angle with respect to the beam direction. The shade phenomena may be due to two main reasons: touching the target holder after scattering or traveling a long path along the target itself. In figure 3.8 these effects are graphically explained.

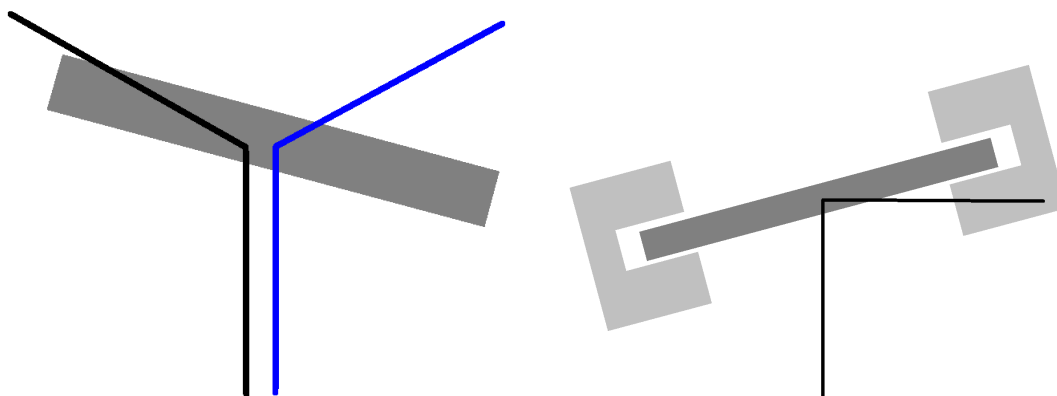


Figure 3.8: Illustrations showing the shade phenomena. On the left side a good event is shown in blue. An event traveling a long path along the target and, thus, losing a lot of energy in it, is shown in black. On the right side an example of frame scattering after interaction with a nucleus of the target is shown.

3.7 The chamber design

The reaction chamber was explicitly designed for this experiment. The geometrical constraints from both the outer and the inner side resulted in the development of a very specific design able to accomplish all the requirements, which is shown in figure 3.9.

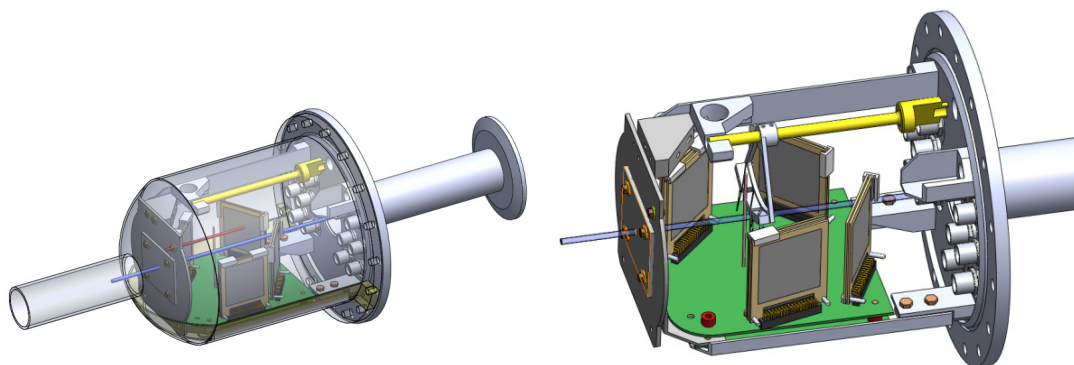


Figure 3.9: Drawing of the reaction chamber closed with the experimental setup mounted inside.

The major outer constraints were the configuration of the TIGRESS detectors and the available extra space for placing the preamplifiers and opening the chamber with the railed structure mounted in the ISAC-II experimental hall. In order to be able to place 4 telescopes we had already waived out the possibility of using all the available clovers, so only half of the chamber had to be spherical. For simplicity, a bullet shape was chosen, in which the cylindric extension enhanced the available volume inside the chamber and the circular plain end flange supposed no major challenge for drilling and setting up the feedthroughs. The flange was united through a bellow to a railed structure housing the beam dump. Opening the chamber meant moving the whole structure so it was only done when it was inevitable. The preamplifiers were placed on a fixed table which was not united to the rest of the structure and then

reduced the maneuverability when opening the chamber.

The inner design had to accomplish more specific requirements:

- Keep the PCB board and the detectors on it in position.
- Book space for cabling the PCB to the flange
- Provide a structure for mounting the target wheel.
- Book space for moving the target wheel without hitting any detector .

3.8 TIGRESS

TIGRESS [Bal07] is a High Purity Germanium Detector Array. It is made out of 16 clovers, each of them consisting on 4 High-Purity Germanium crystals. The clovers are distributed covering an important part of the solid angle around the reaction chamber and at representative angles. Four of the clovers are at $\theta_{lab} = 45^\circ$, four at 135° and the remaining eight are arranged in a ring at 90° . Each of the crystals in a clover is divided into eight segments for more accurate gamma tracking.



Figure 3.10: TIGRESS array closed around the reaction chamber. In this shot the eight clovers forming a ring at 90° can be seen. In particular, it is the BGO crystals surrounding each of the clovers that are visible.

For our experiment the TIGRESS clovers at 45° could not be used. Our reaction chamber was too big for the complete ball to be closed. The chamber was bullet shaped, with a hemisphere fitting with 12 Tigriss clovers and a cylindric extension in the beam direction towards a flange where the feedthroughs were drilled for cabling the detectors inside.

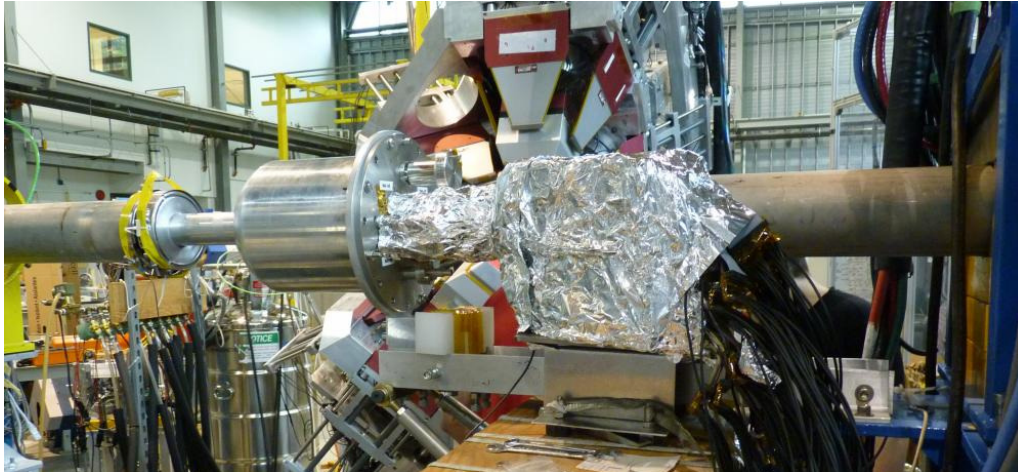


Figure 3.11: Reaction chamber, specially designed for this experiment, surrounded by the opened TIGRESS array. Preamplifiers wrapped in aluminum foil and close to the chamber to minimize the noise. The incoming beam line is on the left and the beam line to the beam dump is on the right.

3.9 Electronic chain

A complex electronic chain is necessary for performing a Nuclear Physics experiment. It is necessary to translate the intensity of the electrons and holes pulled out from the detectors to a signal interpretable by computers. This is made in several steps using different modules:

- **Preamplifier:** The first module for amplification of the electric signal produced in the detectors. They are placed as close to the reaction chamber as possible to minimize the noise to signal ratio. It is fundamental that they are able to collect all the charge produced by the incident particles in the detector. The chosen preamplifiers were MPR-64, with 64 independent channels for reading 64 strips distributed in four 16-pin connectors. Typically, each of these connectors can receive in parallel the signal of all the strips in one side of a DSSSD. The module allows for selecting the dynamic range between two values, 25 and 100 MeV. Given a dynamic range of operation, which is the range of energies of the detected particles, the preamplifiers have a fixed gain.
- **Amplifier:** Second and last amplification stage, where the desired gain can be selected. The amplitude of any signal after this stage has to be in the range of 0-2 V for being properly digitized. The modules used in this experiment (STM-16+) are able to deal with 16 input signals simultaneously. It has 33 output signals. 16 correspond to the electric signal after amplification, 16 correspond to the time signal providing information about the time at which the input signal was received and a trigger signal. The trigger is a fast pulse which is emitted if any of the 16 input channels has an input signal above a preset threshold. It is called trigger because it is used to start the digitizing system and the acquisition after some synchronization treatment.
- **Analog to Digital Converter (ADC):** This module converts the analog energy signal into a digital one. It is done dividing the maximum amplitude that the input signal may have (2 V) into 4096 (actually 2^n , with $n=12$ in our case) and allocate each of them to a channel.

The number of the output channel is a discretization proportional to the maximum amplitude of the input one. This signal can be stored and processed by computers for the analysis of the data. The ADC needs the mentioned trigger to be ready for reading and digitizing the energy signal. The trigger will be described in detail in the next subsection.

- Constant Fraction Discriminator (CFD): This module is conceived for correcting the time assigned to an event. If the time stamp is created when the signal surpasses a threshold, two simultaneous events with different amplitude will have a different time signature. This module duplicates, delays and inverts a signal, and then sums it to the original one. The resulting signal surpasses the offset value at the same moment independently on the amplitude, providing a good reference for the time stamp, as shown in figure 3.12.

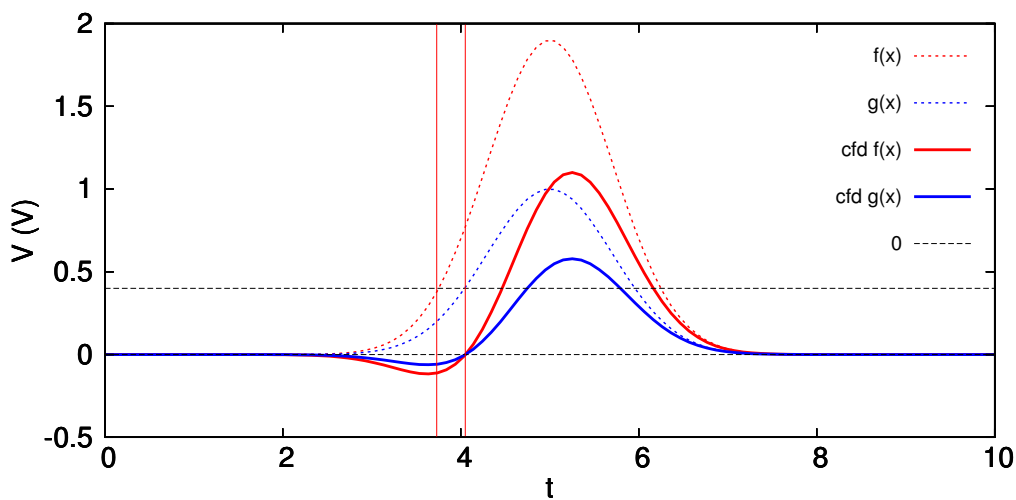


Figure 3.12: Two simultaneous signals before (dashed) and after the Constant Fraction Discriminator. After the CFD they surpass the offset simultaneously independently on their amplitude, providing a good time stamp.

- Fan In Fan Out (FIFO): This module is able to sum input signals (like an OR gate) and replicate output signals.
- Three fold Logic: Module that can operate as an OR gate or an AND gate at convenience.
- Dual timer (also known as Gate and Delay): This module is able to delay the input signal and convert a single peak signal into a step signal, generating the gate which is used for triggering the ADCs.
- Pulser: The pulser is a module that generates electric pulses similar to the signal produced by an ion interacting with a silicon detector. It is not a module in the electronic chain, but is an auxiliary electronic module that is very useful when performing experiments. The main adjustable parameters are the polarity (positive, negative, or bipolar), the raising and decaying time, the total amplitude and the frequency. Each of the 4 connectors of the MPR-64 preamplifier has an auxiliary input for the pulser signal. If a pulser is connected, the generated signal is replicated and is observed in the 16 output channels.

Most of the electronic modules were provided by the TIGRESS group. The digital electronics and acquisition system are permanent and are common for all the experiments per-

formed with TIGRESS. The two main advantages of this are an important saving of time during the setup and the possibility of changing all the parameters of the electronics by remote control. The disadvantage is that some exceptional problems would be solved more easily with hands-on analog devices.

The permanent devices that we used were all of the modules conforming the electronic chain of the Germanium detectors and all of the modules for the electronic chain of the silicon detectors after the preamplifiers. In addition to that, the collaboration had to provide the preamplifiers for the Silicon detectors, the reaction chamber and everything that had to go inside of it. Basically, the silicon detectors themselves, the connectors for taking their signals out of the chamber and the structure for positioning the detectors in the right configuration.

3.9.1 Trigger and data acquisition system

The trigger is the signal that activates the digitizing and the acquisition system. In this case the trigger was set as an OR gate between all the Silicon detectors. That means that if any of the amplifiers had an input signal above a preset threshold, the acquisition system was activated. It also means that this is a necessary condition for the acquisition of data. The TIGRESS detectors were not in the trigger. They were only read when one of the silicon detectors was fired. If a gamma ray was detected in TIGRESS and nothing in the Silicon detectors, this event was not stored.

The trigger is set like a Heaviside step function, with its value set to 0 until some event is detected. When an event is detected the function is set to 1 for a certain time t_g , and then set back to 0. A usual time gate is $t_g \sim 3ms$, which is big enough for the full signals to be read and for possible simultaneous events to be stored as coincident. The ADC reads all the energy signals while the trigger is set to 1 and when it is reset to 0 it stops reading and begins the digitizing process. While the module is digitizing it is not able to read new inputs, so it sends a *VETO* signal which closes the input channel. This is the origin of the acquisition dead time and the intensity has to be kept low enough so that the dead time does not go above the 3%. This is rarely a problem with RIBs but when working with stable beams is a parameter worth checking during the experiment.

This chapter deals with the path followed for obtaining the relevant observables from the data. It is divided in two main blocks. In the first one the different techniques used in the different steps to transform the raw data into precise data with physical meaning will be explained. The topics treated in this first block will be: the accurate positioning of the detectors, the energy calibration of the silicon detectors, the efficiency calibration of the TIGRESS detectors, Doppler correction of the gamma spectra, the methods for measuring the apparent inhomogeneities in the thickness of some detectors and the criteria used to determine which events are valid. The second block will be devoted to present the data analysis procedure, focusing mainly on the particle identification, the extraction of the cross sections and the error calculation.

4.1 Data preparation

In most Nuclear Physics experiments, the amount of data generated is extremely large. It is important to store them properly so that all the relevant underlying physics can be analysed and as few as possible are missed. In this case, data are stored event by event. The information directly obtained for each detected event is:

- Telescope or telescopes that have stored data of the event.
- Vertical (or front) strips of the ΔE detector that have been hit¹.
- Amplitude of the signal due to the charge collected in each front strip of the ΔE detector.
- Horizontal (or back) strips of the ΔE detector that have been hit².
- Amplitude of the signal due to the charge collected in each back strip of the ΔE detector.
- Amplitude of the signal due to the charge collected in the E detector.
- Amplitude of the signal due to the charge collected in in each Germanium crystal.
- Amplitude of the signal due to the charge collected in in each BGO crystal.

¹In the case of telescope 4, also vertical strip of the E detector.

²In the case of telescope 4, back strip of the E detector, instead.

From that information, our goal is to extract the information on the outgoing channels after the beam-target interaction. This information will mainly be:

- Direction in which the ion is emitted. The direction coordinates (θ, ϕ) were defined in the second chapter (see figure 2.2).
- Solid angle covered by each pixel.
- Energy deposited in the ΔE detector.
- Energy deposited in the E detector.
- Direction of the γ radiation emitted in coincidence, if any.
- Energy of the γ radiation emitted in coincidence, if any.

4.1.1 Energy calibration of the Si detectors

For the Silicon detectors, some calibration runs were performed at the beginning and the end of the experiment, what allowed us for checking the stability of the amplification along the beam time. A double-sided alpha source was placed in the target position so that all the telescopes were irradiated at the same time. This way, saving time compared to the cases where individual calibration runs have to be performed for each detector. The source was a triple-alpha source, which is made of three different alpha radiation emitters, ^{239}Pu , ^{241}Am and ^{244}Cm . None of the three alpha particles emitted by the source are able to go through 40 μm of silicon, so it was necessary to perform two calibration runs each time, one for the ΔE and one the E detectors. As the ΔE of telescope 4 is too thin for stopping the alphas emitted by this source (see ranges in table 4.1) a ^{148}Gd source was used for its calibration.

Table 4.1: Energy of the alpha radiation emitted by a triple alpha source and a ^{148}Gd source and range of the alpha ions in a silicon crystal. All these alpha emitters have other alpha-transitions with less intensity at slightly lower energies (labeled here as b and c). Our energy resolution was enough for the most intense peak to be separated from the others except in the case of the lowest energy alpha (see figure 4.1). In that case, the nominal energy used for the calibration before considering the energy loss in the dead layer (E_{cal}) is the weighted average between the two contributions to the peak.

	Triple alpha			^{148}Gd
	^{239}Pu	^{241}Am	^{244}Cm	
E_a (keV)	5156.6	5485.6	5804.8	3182.79
R_{α_i} (μm)	25.5	27.9	30.3	13.0
I (%)	73.3	85.2	76.4	100
E_b (keV)	5144.3	5442.90	5762.7	
I (%)	15.1	12.8	23.6	
E_c (keV)	5105.5	5388	5664	
I (%)	11.5	1.4	0.022	
E_{cal} (keV)	5154.5	5485.6	5804.8	3182.79

The problem with a calibration using only a triple alpha source is that the energies of the ions emitted are below 6 MeV. In most of the events stored during the experiment, the energy

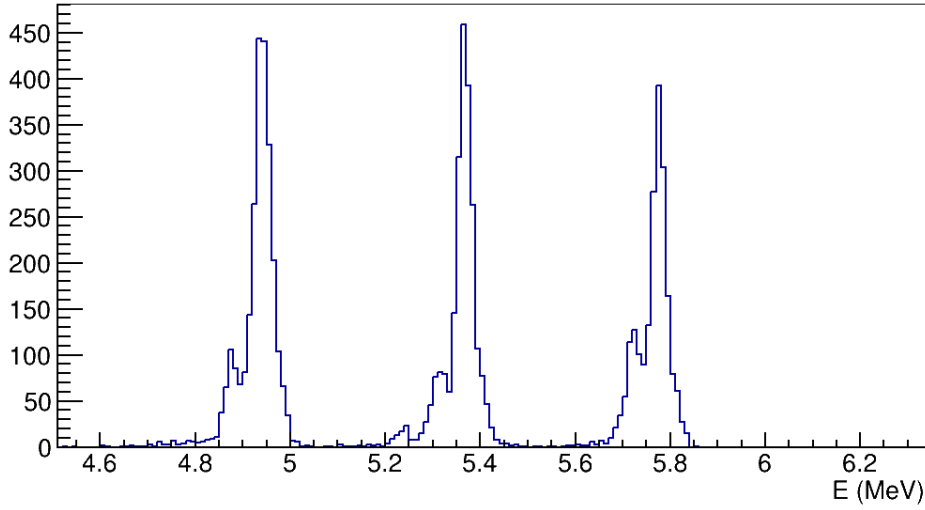


Figure 4.1: Spectrum of the 3-alpha source on a pixel (DSSSD 3, vertical strip 3, horizontal strip 7). The position of the peaks is shifted to the lower energies because the energy loss in the dead layers. The energy resolution is enough for separating the different peaks of each alpha emitter, with exception of the least intense peak of ^{244}Cm , which has very low intensity, and the second peak in ^{239}Pu , which is only 12 keV away from the mean one. The FWHM of the alpha peaks is 32 ± 1 keV in the DSSSD.

deposition in the ΔE and the E is lower than 25 MeV. This would make it necessary to extrapolate for calibrating our data, which is undesirable. For solving that problem, the energy lost in the detectors during the stable beam runs was also considered for doing the calibration. The energy deposition of the ^{12}C is < 34 MeV for the ΔE and < 32 MeV for the E . With this, the range in which the calibration is reliable was enhanced.

The calibration was done calculating the energy deposition per length unit (dE/dx) for the ^{12}C in silicon with SRIM [Zie84]. As the particle travels through the silicon it losses energy continuously due to the interaction with the electrons in the material. The energy lost per length unit depends on the energy of the ion (actually on the velocity, as presented in the Bethe formula (3.1) $dE/dx = dE/dx(v)$), so the energy deposited in the detector has to be calculated considering this variation. This is done numerically, dividing the detector thickness X_t into 1000 divisions and recalculating the dE/dx after each of them.

$$x_i = \frac{X_t}{N}; \quad E_{i+1} = E_i - x_i \frac{dE}{dx}(E_i); \quad E_{det} = E_0 - E_N \quad (4.1)$$

The calibrations were done pixel by pixel, so for each pixel the energy deposited in the ΔE and the E was calculated. The main parameters taken into account for this calculation are:

- Energy lost by the beam in the target before the interaction (which is considered to happen in the center of the target).
- Energy lost in the interaction, taking into account the direction in which the particle is detected.

- Energy lost in the target after the interaction. The thickness that the beam has to go through after the interaction depends on the scattering angle and the target disposition (which is tilted 15° with respect to the beam direction). This is taken into account.
- The energy lost in the front dead layer of the ΔE detector. The angle between the particle trajectory and the normal to the detector (θ_{det}) is also considered. The path that the particle has to go through depends on this angle in the form shown in eq. (4.2). This is taken into account for the energy lost in the dead layers and for the energy lost in the ΔE .

$$X = \frac{X_0}{\cos(\theta_{det})} \quad (4.2)$$

- The energy lost in the sensible volume of the ΔE detector.
- The energy lost in the back dead layer of the ΔE detector.
- The energy lost in the dead layer of the E detector.
- The remaining energy. In none of our cases of study the energy is enough for *punching through* the E detector, so the energy that remains after the ΔE and the dead layers is the energy deposited in the E detector.

Despite the energy lost in the dead layer does not produce an electrical signal, it is something that can be accounted for using the information of the thickness and composition of the dead layer provided by the manufacturer. Known that, and the energy of the incoming particle, the energy loss can be estimated.

Once the energy lost in the active detection volume is estimated, a correspondence between it and the peak position in the raw spectra is determined. The peaks are located and then fitted to a Gaussian. For giving an equitative weight to the low and high energy regions of the spectra, only the lowest energy peak of the triple-alpha source and the peak from the ^{12}C were used for the calibration. The other two peaks coming from the source were used for validating the calibration for each pixel. A set of programs were written in C++, using some ROOT libraries [Bru07], for performing all these actions on all the pixels of the telescope simultaneously. The incidence angle on each pixel was taken into account for estimating the energy deposited in the ΔE and the E detectors considering the path followed by the particles, through the sensible volumes and the dead layers.

The runs used for the calibration were those taken at the beginning of the experiment because they had more statistics. The calibration runs taken at the end were used to cross check the calibration, proving that the response of the electronics and of the detectors to the radiation were stable along all the experiment.

As has been mentioned, the SSSSD in telescope 4 needed the use of a ^{148}Gd source for calibration, because it emits alpha radiation at 3.182 MeV that can be stopped in $20 \mu\text{m}$ of silicon. Nevertheless, this would only provide one peak for the calibration, and a calibration using one peak is too imprecise for our purpose. In some pixels, this was not the case because the alpha with lowest energy from the triple-alpha source (5.156 MeV) could be stopped in the ΔE . The reason was that this detector is very close to the target, so the particles going close to the detector frame will have a large θ_{det} , and the path that the particles had to go through

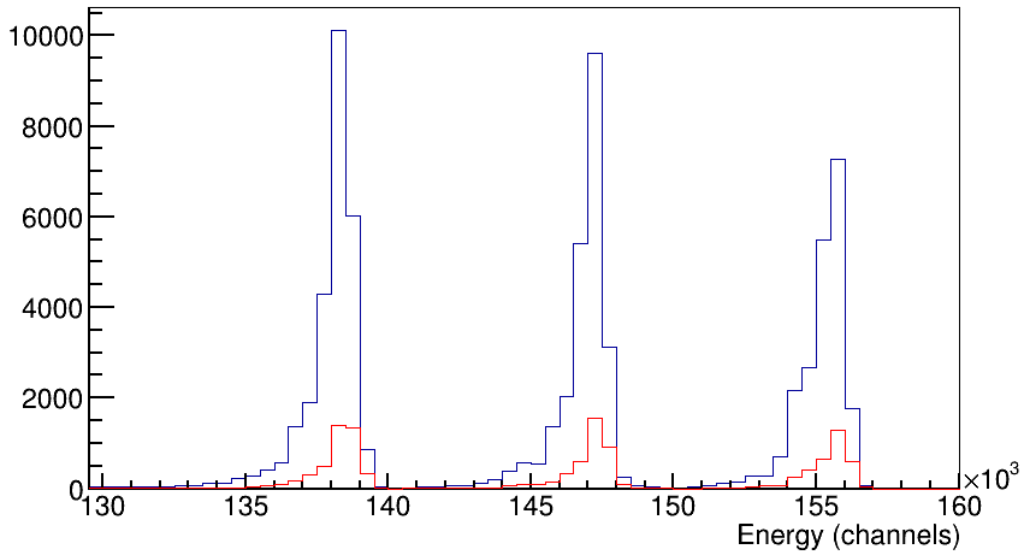


Figure 4.2: Calibration runs taken at the beginning (blue) and the ending (red) of the experiment. The same position of the peaks in both runs proves that the response of the detectors is stable along the the experiment.

was large enough for these alpha particles to be stopped. This should be reflected in the hit pattern of the DSSSD backing the telescope 4, but the observed hit pattern was uneven, indicating probable inhomogeneities in the thickness of the SSSSD. This motivated the thickness measurement that will be explained in the following section.

The calibration of the remaining strips was performed with the help of the pulser. The pulser signal is the same for all the strips connected to the connector in the MPR-64, so it will be the same for all the strips in the SSSSD. If the pulser is observed in different channels of the ADC for the different strips is because of the slightly different gain of each electronic chain. This is what actually defines the calibration. The fix amplitude of the generated pulse can be calibrated like the energy of an incoming particle with a fix energy. In the strips in which the 5.156 MeV alpha is stopped, the detector is calibrated using it and the gadolinium, and the equivalent energy of the signal of the pulser is determined. That energy is used in the rest of the strips, together with the gadolinium source, for calibrating them.

As an indication of the energy resolution of the SSSSD4, table 4.2 shows the Full Width at Half Maximum (FWHM) of the observed peaks.

Table 4.2: FWHM of the peaks measured with the SSSSD in telescope 4.

Peak	^{148}Gd (3182.8 keV)	^{239}Pu (5156.6 keV)	Pulser (4.00 GeV)
FWHM (keV)	50.6	52.3	8.81

4.1.2 Thickness determination

Observing the hit pattern of the back detector of telescope 4 it was deduced that the thickness of the ΔE may not be even. The calibration files showed that the penetration of the alphas through SSSSD4 was not regular and did not correspond to particles going through a homogeneous volume.

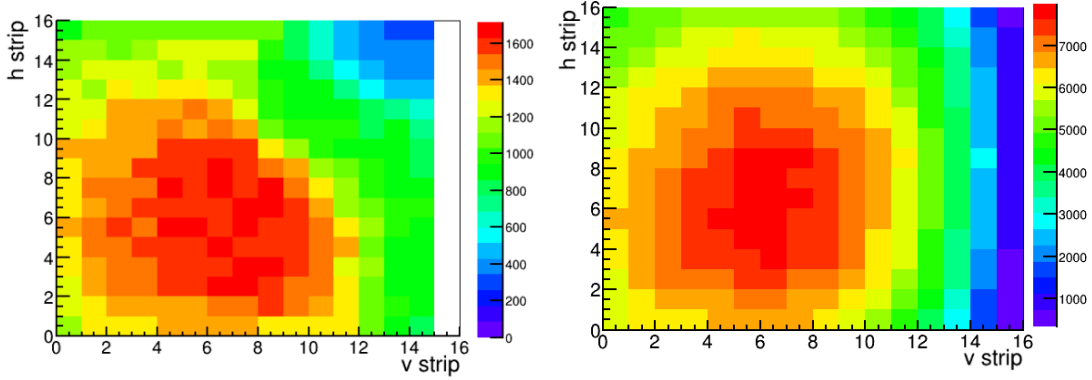


Figure 4.3: On the left, a hit pattern of the alphas going through SSSSD4 and hitting DSSSD4 is shown. On the right, an even hit pattern is shown for comparison, corresponding to the hit pattern of alphas on DSSSD3. The pattern on SSSSD4 shows a reduction in the expected number of counts towards the top right corner of the detector, which was caused by an increase in the thickness of the detector in that area.

A simple experiment was performed at our laboratory for determining the thickness of this detector. It was based on the fact that the thickness that we want to determine is slightly smaller than the range in Silicon of the alphas emitted by a typical triple-alpha source. In this conditions the three different alphas emitted by the source should go through it, but if the detector is tilted, particles have to go through a longer path and may be stopped. Using different tiltings and taking advantage of the different ranges of the three particles (see table 4.1) a mapping of the detector can be performed. Moreover, a DSSSD is placed behind the SSSSD in telescope configuration for two reasons: to assure that particles actually go through and to have more accurate information of the thickness along each strip. In figure 4.4 a simplified outline of the setup is shown.

With this method, only an upper and lower limit to the thickness of each pixel can be given. If the ion goes through the SSSSD and is detected in the DSSSD behind it, it means that the path the ion has gone through in the SSSSD is shorter than the range of the particle in silicon. This case would give an upper limit to the detector thickness.

$$\Delta X < R_{\alpha_i} \cos \theta_d \quad (4.3)$$

where R_{α_i} is the expected range of the particle in silicon, presented in table 4.1, θ_d is the incidence angle of the alpha radiation, calculated considering the tilting of the detector in each case and the position of the studied pixel in the detector. If the particle does not go through the SSSSD, it means that the path in that detector is longer than the range of alphas in silicon and a lower constraint to the thickness can be set.

$$\Delta X > R_{\alpha_i} \cos \theta_d \quad (4.4)$$

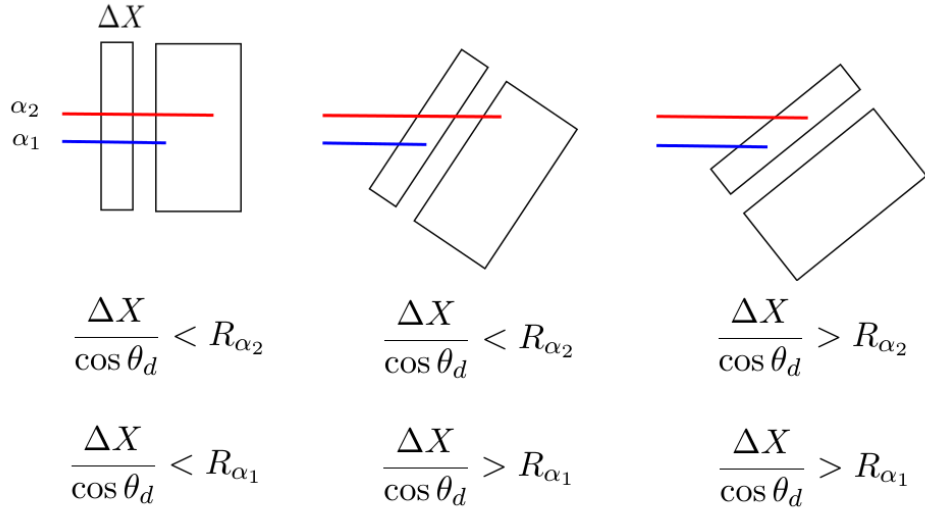


Figure 4.4: Outline of the setup for determining the thickness of the SSSSD4. The range of the different alpha particles emitted, R_{α} , compared with the path followed by the particles depending on the incidence angles can provide upper and lower limits to the thickness of each pixel.

The source was mounted in a fix position at 8 cm from the SSSSD. The telescope with the SSSSD and the DSSSD was mounted on a structure that allowed for its rotation using a stick that emerged out of the chamber. The chosen inclination for the telescope were: 67.5° , 90° (perpendicular to the source-detector direction), 97.5° , 105° , 112.5° , 120° and 127.5° . θ_d is calculated strip by strip taking into account the setup for each case. Among all the data from the three alphas and all the inclinations, the most restrictive constraints are chosen for each pixel.

The thickness obtained ranged from 19 to $25.5 \mu\text{m}$, which is a significant 25% variation. In previous work, this uneven distributions were documented but not quantified. Here, in Appendix B an upper and lower limit for the thickness of SSSD4 pixel by pixel is provided.

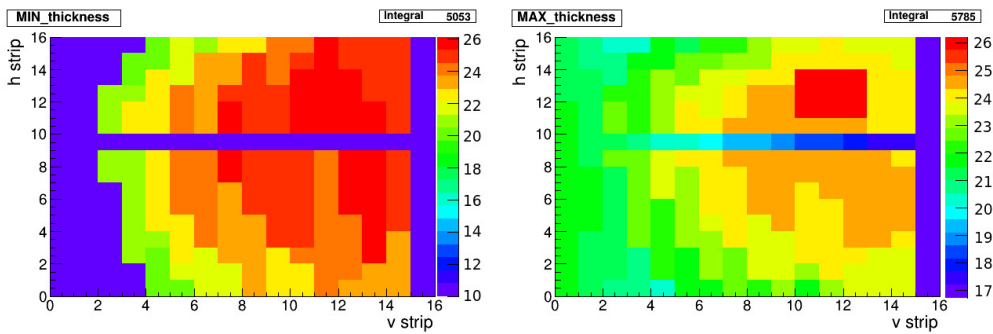


Figure 4.5: Maximum and minimum constraint measured for the thickness of the SSSSD4. There is a horizontal dead strip in the DSSSD but no abrupt change is expected in that area. It is observed, as expected from the hitmap obtained in the calibration runs of the experiment, an irregular thickness increasing towards the top-right corner of the detector.

4.1.3 Position optimization

The position of each pixel can be calculated knowing the dimensions of the detectors (length and width of the strips, gap between strips...) and their disposition around the target. In the previous chapter it was explained that the setup has a fixed geometry as the detectors are attached to the PCB board. However, the accuracy in the positioning of each pixel, taking into account only the design values, is limited. That uncertainty can be minimized with some data analysis.

Reaction cross sections are often represented with respect to Rutherford scattering cross section, which, recalling eq. 2.45) can be written in the form:

$$\frac{d\sigma_{Ruth}}{d\Omega} = \left(\frac{Z_{targ} Z_{beam} e^2}{4E_{cm}} \right)^2 \frac{1}{\sin^4\left(\frac{\theta_{cm}}{2}\right)}$$

Thus, for a particle undergoing Rutherford scattering, the expected number of counts (N_c) in a detector covering a solid angle $\Delta\Omega$, placed at a certain scattering angle θ_{cm} , for an incoming beam intensity I_b taken during a time t is:

$$N_c = I_b \cdot t \cdot \rho_s \cdot \frac{d\sigma_{Ruth}}{d\Omega} \Delta\Omega = I_b \cdot t \cdot \rho_s \cdot \left(\frac{Z_{targ} Z_{beam} e^2}{4E_{cm}} \right)^2 \frac{\Delta\Omega}{\sin^4\left(\frac{\theta_{cm}}{2}\right)} = k_1 \frac{\Delta\Omega}{\sin^4\left(\frac{\theta_{cm}}{2}\right)} \quad (4.5)$$

where ρ_s is the superficial density of the target. For a given beam and a given target, k_1 is constant and, in this case, it will be the same for all the detectors in each of the studied reactions (^{11}Be at 2.9 MeV/u, ^{11}Be at 3.6 MeV/u and ^{12}C at 5.0 MeV/u). Fixing that, the angular distribution depends only on the solid angle and the angle of each pixel.

The dependency on the angle goes like $1/\sin^4(\theta/2)$, so in the region where $\theta \sim 0$ the sensitivity to this parameter is paramount. A non-precise correspondence between the pixel and its angle would mean a large error in all our observables. Hence, an important effort has been devoted to obtain the most precise assignation to the pixels position.

It is also necessary to introduce a change in the system of reference for being rigorous, since not only the angle, but also the solid angle in the laboratory frame is slightly different to the solid angle in the center of mass frame (see figure 4.6 for a graphical explanation). The solid angle obtained directly based in geometrical considerations (dimensions and position of the pixel in the laboratory) corresponds to the laboratory frame one. The same way that there is a shift between laboratory and CM θ angle, the size of the rings corresponding to a particular θ may (and does) change, and is something quantified and taken into account.

$$\frac{d\sigma_{cm}}{d\sigma_{lab}} = \frac{(1 - x^2 \sin^2(\theta_{LAB}))^{1/2}}{(x \cos(\theta_{LAB}) + (1 - x^2 \sin^2(\theta_{LAB}))^{1/2})^2}, \quad (4.6)$$

where x is the ratio between projectile and target masses.

With all these considerations implemented, the optimization was performed using the data form the scattering of ^{12}C on ^{197}Au at 5.04(1) MeV/u (the Coulomb barrier for this reaction is $V_b \sim 59.3 \xrightarrow{lab} 63$ MeV). This is a well bound and compact nucleus, so below the barrier

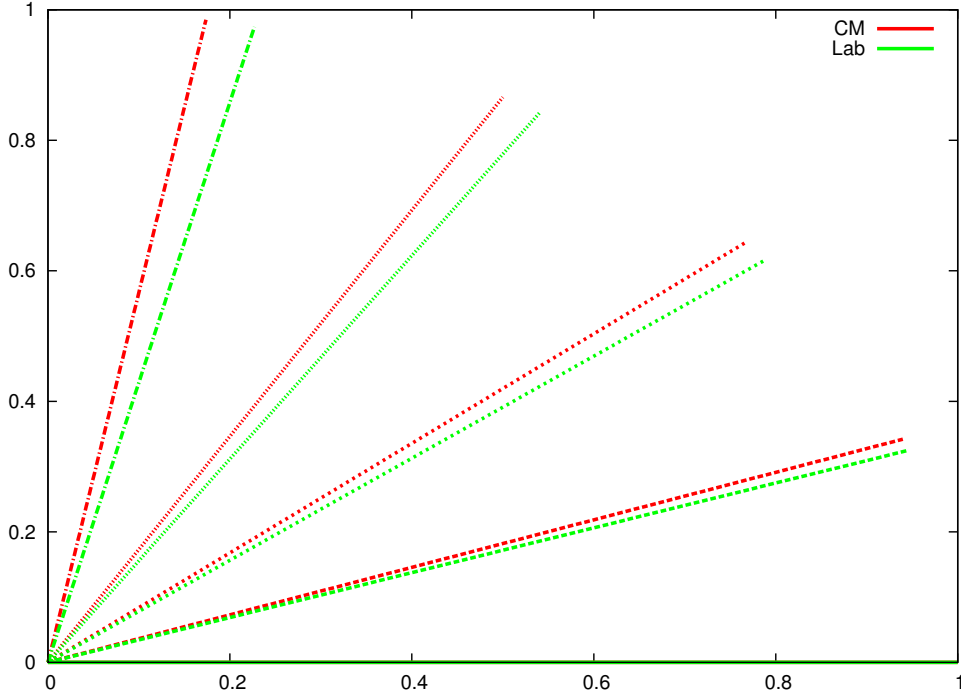


Figure 4.6: Angles in the Center of Mass (CM) and the Laboratory (LAB) systems. The red lines correspond to 20, 40, 60 and 80° in the CM reference frame and the green lines are the corresponding angles in the LAB frame. The area between two consecutive green lines is smaller than between two consecutive red lines, which evidences how the solid angle changes in the different representations.

the scattering is expected to follow a Rutherford distribution (some comments on this will be made later in this chapter). In addition to that, since it is a beam of a stable and easily produced nucleus, it has a considerably larger yield in the production target, so we had enough statistics for a proper position optimization. This optimization will be performed using equation (4.5) and the number of counts in each pixel of the detector.

The detector is considered a single piece which can be translated in the x , y and z axis and rotated around the x and y axis. The horizontal position of the beamspot and the constant k_1 from equation 4.5 are also included as variable parameters. The optimization consisted on finding the configuration of these parameters that minimized (using the method of least squares) the difference between the number of counts calculated from them and the number of counts measured during the experiment. The following procedure was performed telescope by telescope:

1. Restrict the interval of values for each parameter ($X_d, Y_d, Z_d, \alpha_x, \alpha_y, X_t, k_1$). Initially all the geometrical parameters were set to 0 and k_1 was set to 1. All the geometrical parameters set to 0 correspond to the exact design position for the ΔE detector. In all the cases the translations were lower than 7mm and the rotations lower than 5°.
2. Calculate the angle (θ_{cm}) and the solid angle ($\Delta\Omega$) of each pixel as a function of its position and orientation relative to the beam direction and the beamspot position.

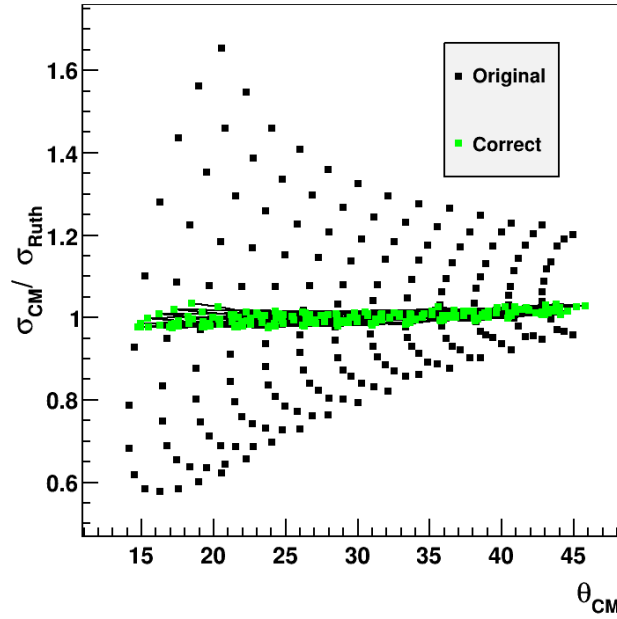


Figure 4.7: Elastic cross section per pixel with respect to Rutherford cross section of ^{12}C on ^{197}Au at 5.04 MeV/u measured in telescope 1. The black points correspond to the cross section by pixel before the optimization of the position, and the green points to the cross section after optimization.

3. Calculate the expected count rate pixel by pixel (using eq. 4.5) and the total number of counts for all the detector $\hat{N}_t^{(0)} = \sum \hat{N}_i^{(0)}$.
4. Dividing the measured number of counts in all the detector into the calculated one in the previous step, a first estimation for k_1 is obtained:

$$k_1 = \frac{N_t \frac{d\sigma_{cm}}{d\sigma_{lab}}}{\hat{N}_t^{(0)}} \quad (4.7)$$

5. Calculate the expected count rate for each pixel, considering the obtained value for k_1 : $\hat{N}_i = k_1 \hat{N}_i^{(0)}$.
6. Perform a least square minimization using Minuit, including explicitly the fixed and free parameters:

$$L = \sum_{\text{pix}} \frac{(N_i \frac{d\sigma_{cm}}{d\sigma_{lab}} - \hat{N}_i)^2}{N_i} \quad (4.8)$$

7. Control that the values of the parameters are not in the limit of the restricted interval.
8. Repeat the procedure departing from 4, changing, if desired, the free parameters until a satisfactory minimum is obtained.

Since the number of parameters is high, the optimization often depends on the initial conditions and on the first parameters to be optimized. For assuring that the obtained min-

ima were stable, the optimization was performed several times, varying the free parameters and the order in which they were freed, until reliable values were obtained following different paths.

Once the position of the telescope 1 had been optimized (fig. 4.7), the whole procedure, except for step 4, was repeated for telescopes 2 and 3. As has been exposed at the beginning of this section, the parameter k_1 only depended on the target and beam conditions, so this was considered a fix parameter for the position optimization of telescopes 2 and 3.

Since there are some angles which are covered by more than one telescope, and the physics do not depend on the telescope, observing that different telescopes measured the same cross sections (for all the observables) in the overlapping interval was a cross check that the positioning was correct and no ad-hoc normalization parameter was needed.

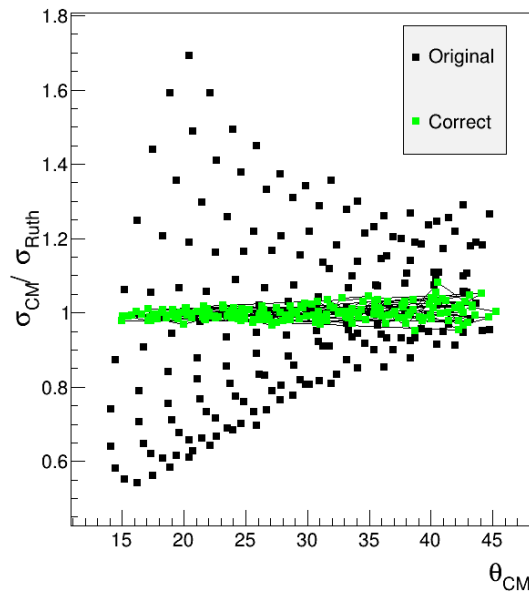


Figure 4.8: Total cross section (elastic + inelastic + breakup) per pixel with respect to Rutherford cross section of ^{11}Be on ^{197}Au at 3.6 MeV/u measured in telescope 1. The black points correspond to the cross section by pixel before any optimization of the position (even before the ^{12}C one), and the green points to the cross section after optimization.

For studying the ^{11}Be beams a second iteration of optimization was performed (fig. 4.8). Although the reaction chamber was not opened and the detectors should be in the same disposition, it was considered appropriate to account for the possible change of the beam position and focusing. For this optimization, we departed from the position obtained after the ^{12}C optimization. Since other reaction channels are opened, namely inelastic scattering and breakup, it may seem not very accurate to compare the data with a Rutherford scattering pattern. In any case, at forward angles, the sum of the three contributions (the two mentioned plus the elastic scattering one) can be compared to the Rutherford cross section with minimal error.

The angle in formula 4.5 is the angle of the projectile in the center of mass frame. In the cases in which the projectile undergoes breakup there is a difference between the center of mass of the projectile after the fragmentation (center of mass of the $^{10}\text{Be}+n$ system) and the detected fragment (only the ^{10}Be). Although in an ideal case, like the one shown in figure 4.9, this is not a major effect, when going to larger θ angles, around 90° , this effect is maximized and it is added to the fact that the sum of the three cross sections is not necessarily equal to Rutherford. For this reason this correction is only performed considered up to the first 8 strips in telescope 3.

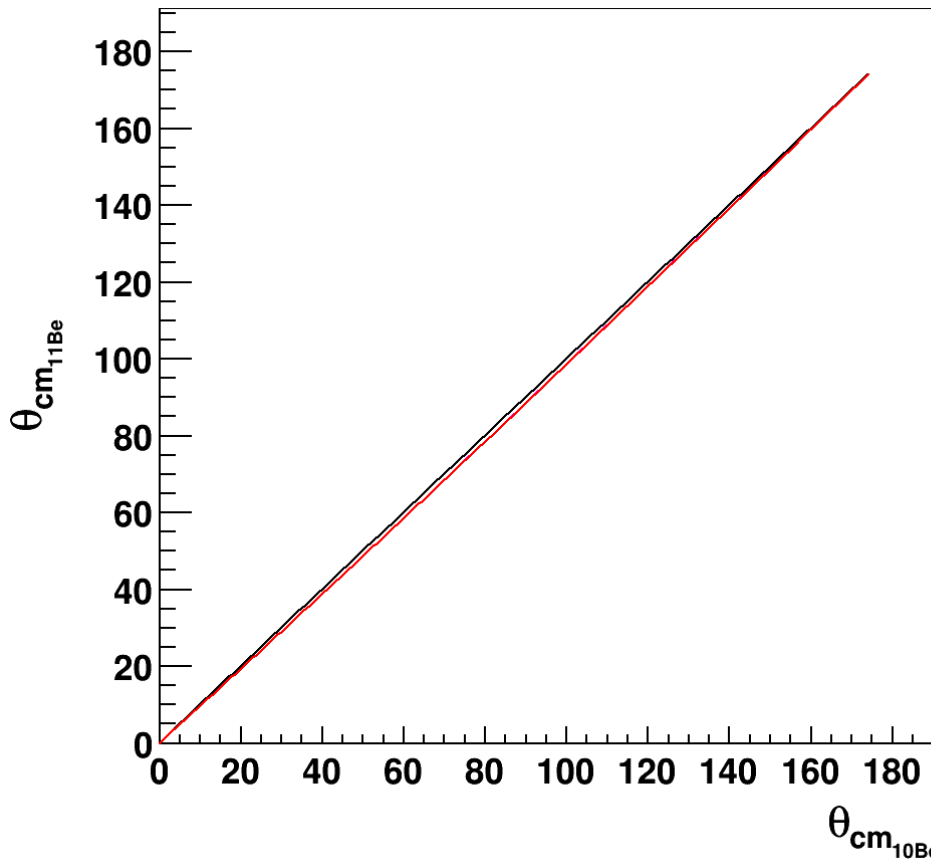


Figure 4.9: Relation between the angle at which the ^{10}Be is detected and the angle of the center of mass of the ^{11}Be (red), considering that the breakup happens at the distance of closest approach and the trajectories of the projectile and the ejectile are hyperbolic (Coulomb trajectories). A one to one relation is depicted in black for comparison.

It can be noticed that in this section no reference is made to telescope 4. There are several reasons for this. The main one is that the sensitivity of the Rutherford cross section to the polar angle is extremely low at angles close to 180° . Another fact to be considered is the different configuration of this telescope. In the other telescopes we are only sensible to the position of the ΔE detector, because the E detector is not segmented and everything detected in the ΔE will be detected in the E as well. In those cases the E detector does not introduce any efficiency factor, but the treatment of telescope 4 is more delicate in this sense. The back detector in *tel4* is a fragmented strip detector, so some ions detected in the ΔE will hit the gaps between the

strips of the E detector, reducing the efficiency of the telescope.

For this reason, in the case of telescope 4 we are more sensitive, in terms of efficiency, to the position of the E detector.

The last factor to be taken into account in the determination of the position of telescope 4 is that the energy we are measuring is $E_{lab} = 60$ MeV ($E_{cm} = 56.6$ MeV), which is close to the Coulomb barrier for the $^{12}\text{C}-^{197}\text{Au}$ system ($V_b \sim 59.3 \xrightarrow{lab} 63$ MeV). The reason for choosing this energy was making sure that the stable beam went through the ΔE of all 4 telescopes, leaving a significant energy in both ΔE and E for helping with the calibration. The drawback is that, in this case, it is inadequate to consider that the elastic cross section at backward angles follows a Rutherford distribution. This is illustrated in figure 4.10, where the angular distribution for ^{12}C on a ^{208}Pb target, extracted from [San01], is shown at different energies close to the Coulomb barrier, which for that case is $V_b \sim 60.8 \xrightarrow{lab} 64.3$ MeV.

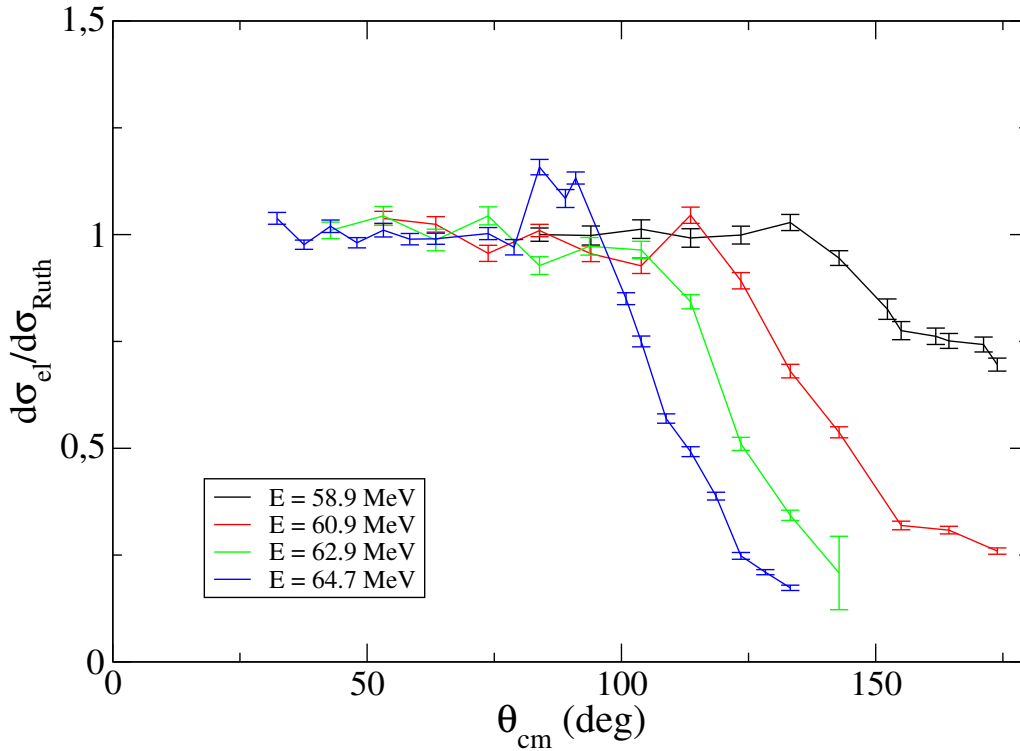


Figure 4.10: $^{12}\text{C}-^{208}\text{Pb}$ angular distribution around the Coulomb barrier from [San01]. It is observed that for large scattering angles, the angular distribution differs significantly from Rutherford. It can be inferred that in the range of telescope 4 ($110^\circ < \theta < 150^\circ$) it is not suitable to normalize to a Rutherford distribution.

In figure 4.11 the angular distribution obtained for the ^{12}C on the ^{197}Au target is shown before and after optimization for the telescopes 1, 2 and 3. In telescope 4 the only parameter that has been optimized is the distance, for reproducing a reasonable behaviour of the angular distribution.

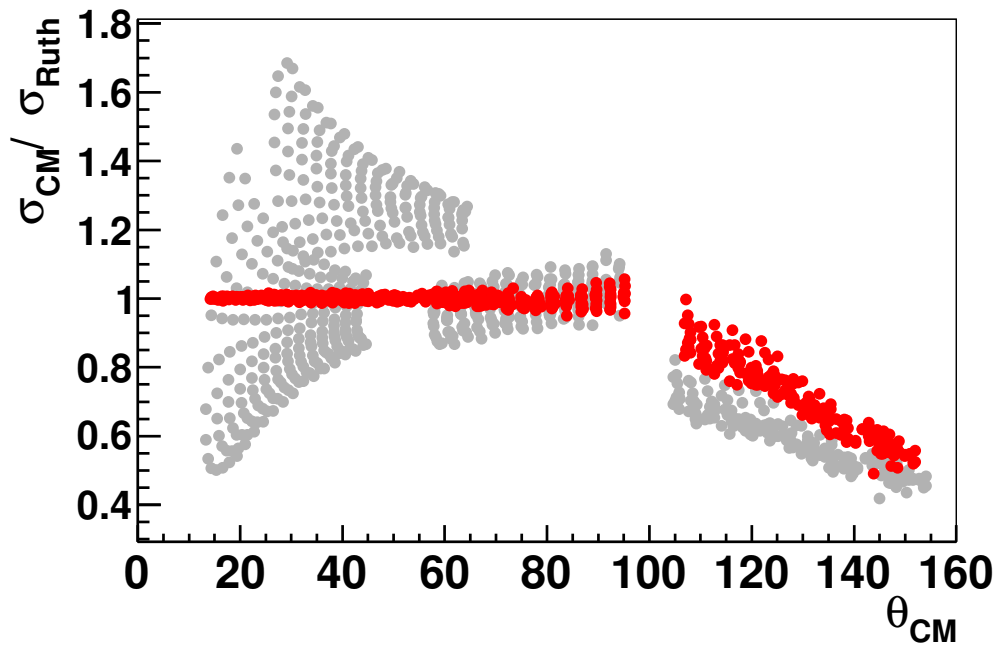


Figure 4.11: $^{12}\text{C}-^{197}\text{Au}$ angular distribution around the Coulomb barrier after optimization of the position of telescopes 1, 2 and 3.

4.1.4 Efficiency calibration of TIGRESS

The energy calibration of the germanium detectors was provided by the TIGRESS group and was checked during the experiment, proving it to be excellent, so no actions were performed on it. Considering that, only an efficiency calibration had to be performed. There are some articles (for instance, [Bal07]) in which the efficiency of the array is published. However, the size, thickness and composition of the reaction chamber and the detectors that the gamma rays may find in their way to the germanium crystals may affect the efficiency, so it is worth to recalculate it for each particular case.

For the correct study of the inelastic scattering it is essential to understand the particular set up of each case. In this case, the main features to take into account are:

- Every gamma detector has a factor of the efficiency dependent on its probability of interaction with light (intrinsic efficiency) and another one dependent on its configuration around the reaction spot (geometric efficiency). Any variation in the configuration may be relevant for the efficiency of the gamma detection, ranging from the position of a clover, to the position of a Silicon detector in the way of the gamma ray to the crystal. For minimizing the uncertainties of all these factors, measurements of gamma sources with known activity were taken with the same configuration, leaving the Silicon detectors, the target wheel and, of course, the TIGRESS clovers in the same position they were during the experiment.

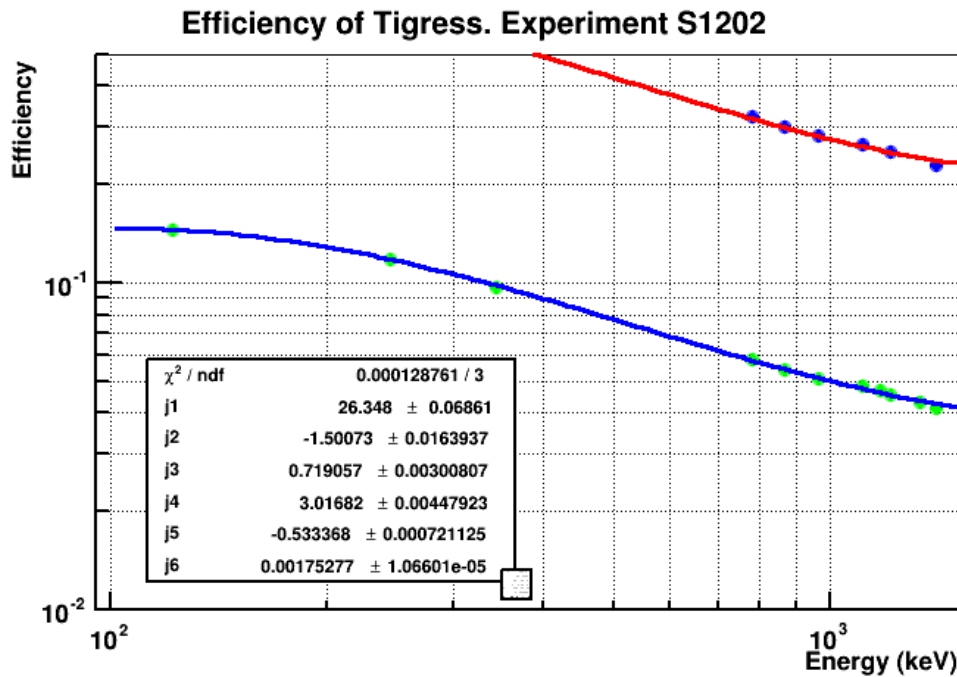


Figure 4.12: Fit of the relative efficiency calculated with a ^{152}Eu source to a Jackel function (red line) and fit of the total efficiency of the 12 clovers of TIGRESS used in the experiment to a Jackel function (blue line), using a ^{152}Eu source and a ^{152}Eu source with a well-known activity.

- Our charged particles detectors did not have enough resolution to resolve the inelastic from the elastic scattering. Breakup events can be separated from what could be called quasi-elastic, where actually elastic and inelastic contributions are added. This factor, jointly with the limited efficiency, has to be considered for the measurement of the cross sections. Three different cases will leave an event inside the quasi-elastic area of the two-dimensional plot:
 - An elastic event.
 - An inelastic event in which the corresponding gamma was also detected.
 - An inelastic event in which the corresponding gamma was not detected due to limited gamma detection efficiency. This case is experimentally indistinguishable from the first one. The only thing that can be done is evaluate the probability of such events to occur and correct it statistically in the analysis.
- Trigger is set on particle detectors only. This means that the observation of a γ -ray without any particle in coincidence is not possible.

For the efficiency calibration two different sources were used, a ^{60}Co one and a ^{152}Eu one. The ^{60}Co had a very well known activity, providing a very accurate absolute efficiency calibration at the two energies of its gamma lines. The ^{152}Eu has an extense variety of gamma lines. Comparing their branching ratios and the detected intensity, the dependence of the efficiency with the energy can be extracted, but the activity of this source is not known with the same precision than the cobalt one. Using both sources the absolute efficiency in all the range

of interest could be determined.

In this range, it is known that the efficiency of germaniums detectors follows the Jäckel function [Jä87]. In figure 4.12 (in blue) the fit to the Jäckel function and the obtained fit parameters can be seen. The efficiency at 320 keV, which is the critical one for the determination of the cross sections, is $\varepsilon = 0.121(5)$.

4.1.5 Doppler correction and γ gating

The proceeding for identifying the inelastic scattering events was to gate on the 320 keV gamma corresponding to the deexcitation after populating the $j^\pi = 1/2^-$ bound state in the ^{11}Be . Since the deexcitation gamma is emitted by a particle moving at around $\beta = v/c = 0.08$, it is necessary to Doppler correct the spectra for gating properly. To do this correction, the energy, the θ and the ϕ of both the gamma and the ^{11}Be have to be measured.

The formula for the Doppler correction is:

$$E_{Dop} = E_{det}(1 - \beta \cos(\alpha_{rel}))\gamma \quad (4.9)$$

where E_{Dop} is the Doppler corrected energy (the actual energy with which the γ -ray is emitted in the frame of the charged particle, and E_{det} the energy detected for the γ -ray; α_{rel} is the angle between the momentum of the charged particle and the momentum of the gamma ray that it is emitting,

$$\cos(\alpha_{rel}) = \sin(\theta_{part}) \sin(\theta_\gamma) \cos(\phi_{part} - \phi_\gamma) + \cos(\theta_{part}) \cos(\theta_\gamma); \quad (4.10)$$

β is the relative velocity of the emitting particle and γ is the corresponding Lorentz factor, the special relativity magnitudes for calculating Lorentz boosts:

$$\beta = \frac{v}{c}; \quad \gamma = \frac{1}{\sqrt{1 - \beta^2}} \quad (4.11)$$

The FWHM of the 320 keV peak (fig. 4.13 and fig. 4.14), summing the Doppler corrected spectra from all the clovers, was 7 keV. The gate for considering an event in the inelastic channel was made taking the events with:

$$E_{det} > 282\text{keV}; \quad 300\text{keV} < E_{Dop} < 340\text{keV}. \quad (4.12)$$

A lower limit is set in order to avoid coincidence with the gamma coming from the Coulomb excitation of ^{197}Au . The background is estimated from the number of counts at the two edges of the gate and is considered linear.

The peak corresponding to the in-flight deexcitation of the ^{11}Be is the only one that improves its FWHM when performing the Doppler correction. In figure 4.15 the non-corrected gamma spectrum is shown with the gamma lines identified. No lines were identified above 2125 keV. It is remarkable that no evidence of the 3368 keV gamma line from a possible ^{10}Be deexcitation has been found.

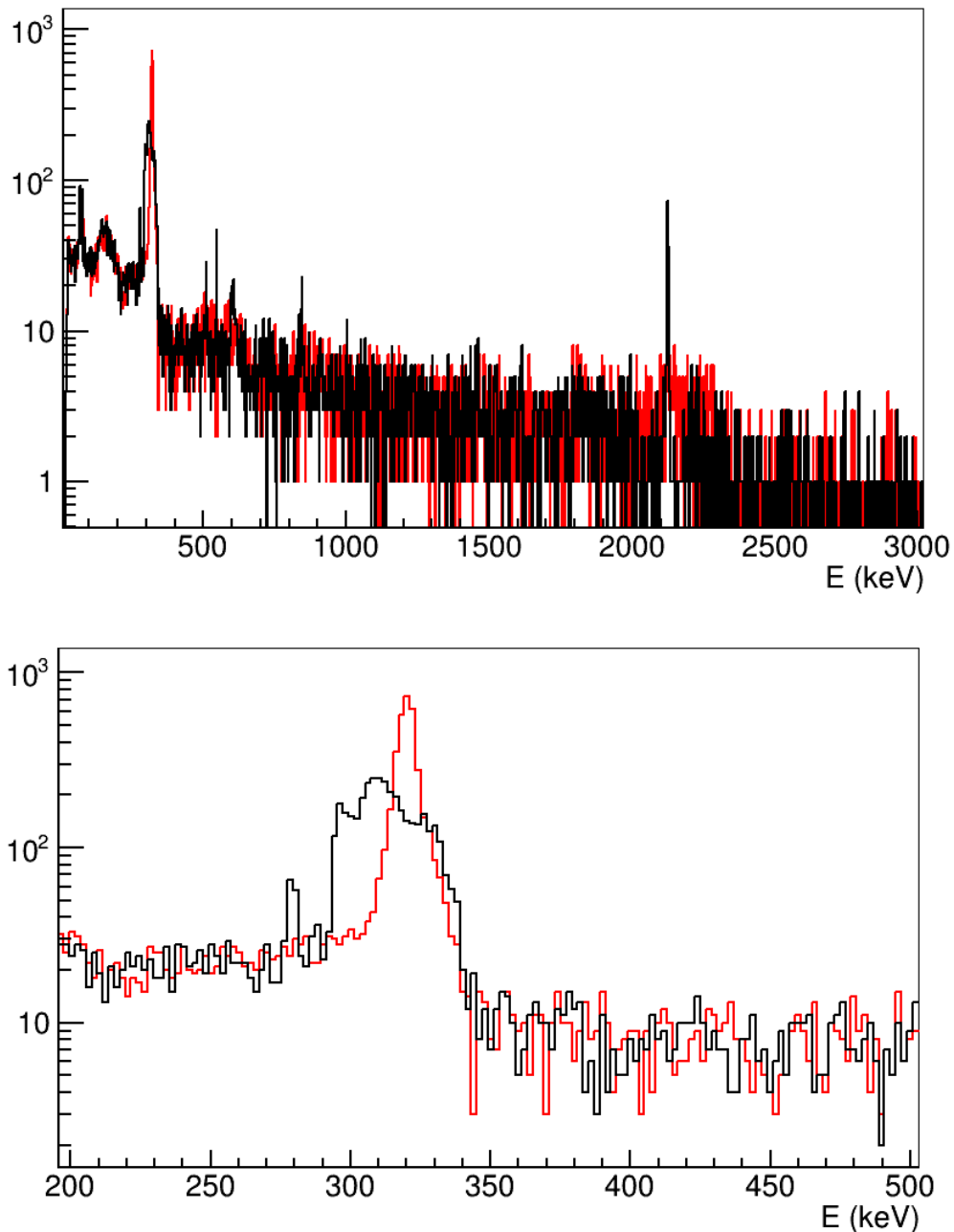


Figure 4.13: Gamma spectra before (black) and after (red) Doppler correction. Gamma spectra zoom around the 320 keV peak corresponding to the deexcitation energy from the excited bound state in ^{11}Be . It is observed that the correction produces a net shifting to the right of the peak centroid. This is caused because we use the TIGRESS clovers at 90° and 135° and not the one at 45° , and most of the detected charged particles go at small scattering angles. With this experimental conditions, most of the detected coincidences will correspond to $\alpha_{rel} > 90^\circ$ and, as can be seen in eq. (4.9), the detected energy will be shifted to low energies with respect to the emission one.

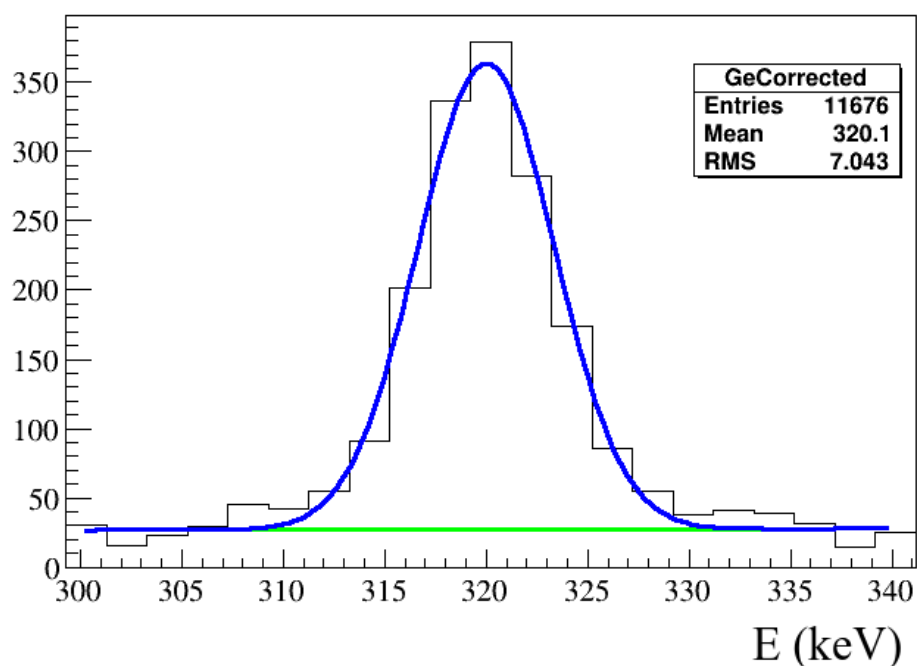


Figure 4.14: Gamma gate for considering an event in the inelastic channel. It is centered in 320 keV (after Doppler correction). The linear estimation of the background is also shown in green under a gaussian fit for the peak. The FWHM is 7 keV.

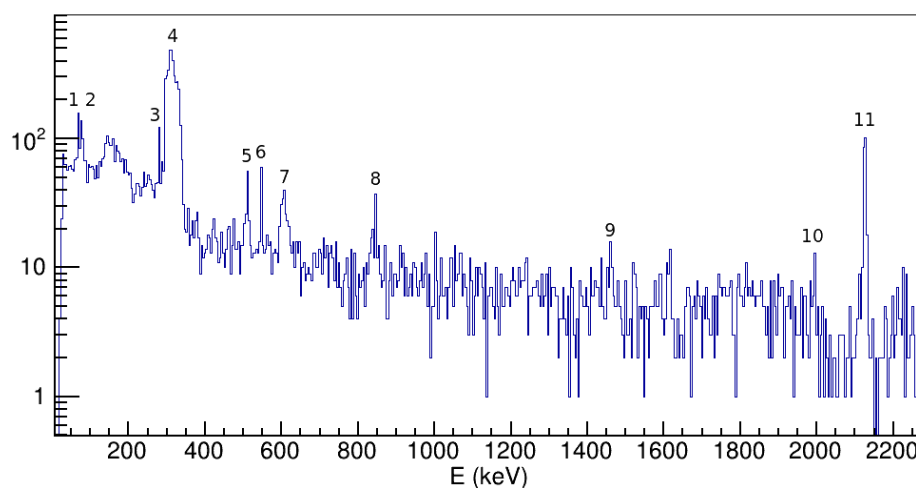


Figure 4.15: Gamma spectra with identified gamma lines.

4.1.6 Data selection

The last step before analysing the data is sorting it, in order to assure that the events that we are including are physical events produced in the reaction that we want to study. There are two kind of detected events that we want to rule out of the analysis:

Table 4.3: Lines identified in the gamma spectrum.

#	E (keV)	isotope
1	68.75	⁷³ Ge
2	77.3	¹⁹⁷ Au
3	279.01	¹⁹⁷ Au
4	320.	¹¹ Be
5	511	-
6	547.5	¹⁹⁷ Au
7	597.79	⁷³ Ge
8	843.76	²⁷ Al
9	1460.8	⁴⁰ K
10	1992.7	⁷³ Ge
11	2124.47	¹¹ Be $\xrightarrow{\beta}$ ¹¹ B

- Events digitized by the ADC that do not correspond to any actual detection. They are often referred to as *noise*, and their origin is manifold. Independently of their origin, they consist on an electric pulse generated at some stage of the electronic chain that gets to the ADC and is then digitized. Assuming that they are caused by random fluctuations, these fluctuations are more likely to have low amplitudes, which will be digitized as low energy events.
- Physical events stored at the wrong energy. Similarly to the first case, if a fluctuation is overlapped with a real signal, the energy associated to the event will differ from the energy deposited in the detector. For a given type of detector and a given measurement, the noisier the detector, the broader the peaks in the spectra.
- Physical events coming from undesired processes. The main sources of these events are beam contamination and scattering. This scattering can happen, mainly, in the target frame, in the upstream collimator and in the detector frame. The contamination of the beam depends to a large extent on the RIB production method and the isotope that wants to be studied. In our case, TRILIS and an atypical mass over charge ratio of 5.5 (the beam is ¹¹Be²⁺) were used for reducing the beam contamination to unnoticeable levels.

The procedure to rule these three types of events out is to impose some conditions to the data and, in our case, these conditions are mainly imposed on the DSSSDs energy signals. The *p* and *n* sides of the DSSSD provide two independent read outs of the same event, so the energy value has to be same for the two of them, within an interval. A signal from the *p* side that has no coincident signal from the *n* side can be considered noise and dismissed. If the signals coming from the *p* and *n* side have a substantial energy difference it is impossible to discern which value is the correct one and which one has been shifted. In the case they are approximately equal, a criterium has to be established for the energy assignation.

In figure 4.16 the energy difference between the *p* and *n* sides is represented. It is observed that most of the detected events have a *p* – *n* energy difference within ± 25 keV, which is an indication of proper calibration of both sides. The average FWHM of this difference is 44 ± 4 keV. Different criteria for ruling out events were tested ($E_{diff} > 40$ keV, 100 keV, 200 keV,

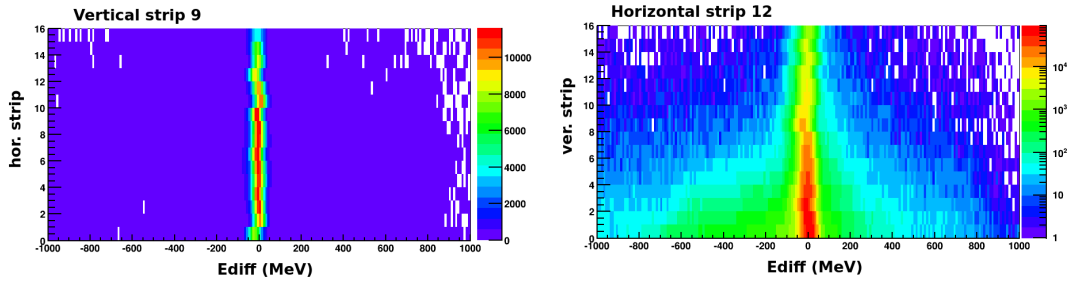


Figure 4.16: Energy difference between front and back side of the DSSED in telescope 1. On the left, energy difference between a vertical strip (9) and all the horizontal strips. On the right, energy difference between a horizontal strip (12) and all the vertical strips. Horizontal strips cover a larger range of θ angles, so a variation in the cross section is observed along the strip (a logarithmic scale is chosen for that reason).

400 keV, 500 keV and 1900 keV) for assuring that the choice did not influence the physics. Since the resolution with no restriction was already enough for separating the ^{11}Be and ^{10}Be fragments in most cases, a not very restrictive constraint was set. It has to be considered that along the experiment, the gain of one strip may have little variations that the energy difference center can be shifted out from 0. In such case, a very restrictive constraint may reduce excessively the number of accepted events. Setting an upper limit in $E_{diff} < 200$ keV (considerably larger than the FWHM), the total number of counts stored by each pixel was not affected by the criteria and the error introduced was minimized.

For the events that were considered *good* events, the energy is taken from the p -side, because it was observed that, systematically, the FWHM of the peaks in the n -side were broader. It was considered that taking an average of the two values for the energy would have meant an unnecessary reduction in the resolution, so the energy in the n -side was only used for checking the energy difference and assuring that the event had a physical origin.

The effect of some physical events being stored at the wrong energy can be observed in figure 4.17, where the events in the two cuts are cleaned if events with multiplicity one are imposed. Multiplicity one means that if more than one vertical strip or more than one horizontal strip have been hit, the event is dismissed. This condition is only imposed for understanding the spectrum, rejecting the possibility of an unexpected reaction channel, after that, events with multiplicity more than one are included in the analysis.

The strips adjacent to the frames are also removed of the analysis because they often have border effects. Since detectors are perpendicular to the direction of the scattered particles and the detectors are very close to the target, the incident angle of the particles changes considerably along the detector depending on the pixel. This, added to the distance between the ΔE and the E (~ 6 mm) means that some particles hitting the border strips do not touch the back detector and are lost, faking a loss in intensity which has no meaning from a physical point of view.

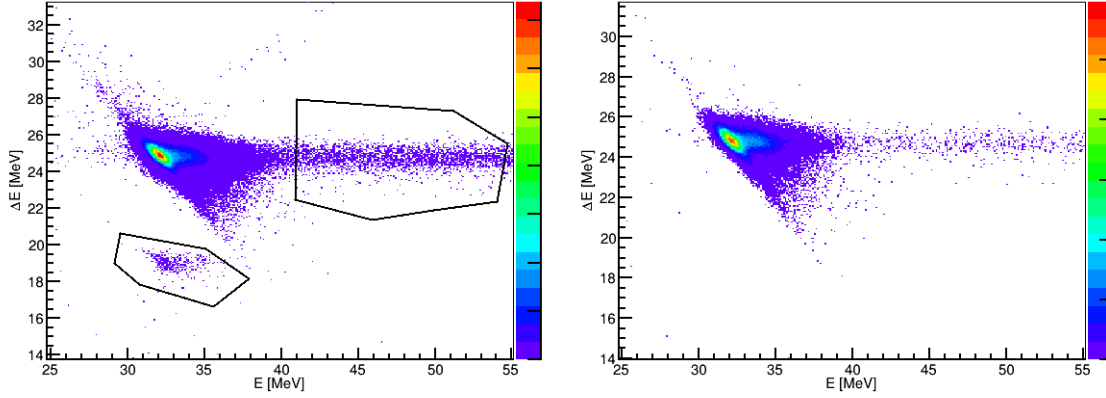


Figure 4.17: $\Delta E - E$ plot without any multiplicity restriction (left) and restricting to events with multiplicity one (right). It is observed that there is a spot at $E_b \sim 33$ MeV $\Delta E \sim 19$ MeV that disappears if multiplicity one is imposed. The fact that we observe the same behaviour for ^{11}Be and ^{12}C beams and that it gets cleaned imposing multiplicity one indicates that it is not a reaction channel but an experimental limitation, causing that some physical events are stored at the wrong energy. This also reduced the tail of events towards high energy in the E -detector, caused by superposition of events in the E -detector that cannot be distinguished since it is not fragmented.

4.1.7 Examples of spectra

In this section some examples of spectra are shown in order to evidence the statistics and the quality of the data. First, in figure 4.18, the two-dimensional plot for ^{12}C is shown. No remarkable feature is observed, except for the spot already commented in the previous section, caused by experimental limitations.

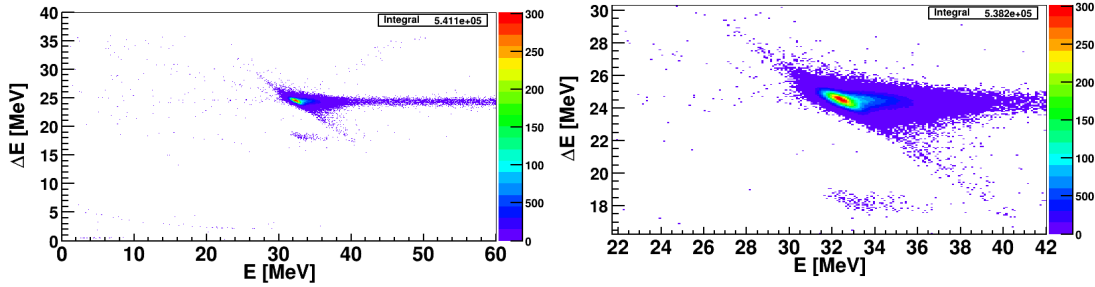


Figure 4.18: $\Delta E - E$ plots for ^{12}C on ^{197}Au . Energy left in the ΔE detector in the y axis, versus energy left in the E detector in the x axis.

Figures 4.19 and 4.21 show in a $\Delta E - E$ plot the scattering of ^{11}Be on a ^{197}Au target at the two measured energies for the same pixel (at $\theta = 18^\circ$). The separation between the ^{11}Be and the ^{10}Be fragment is evidenced. The next section is focused in the analysis of these data.

In figures 4.22 and 4.26 some $\Delta E - E$ plots are shown for a central pixel of each of the 4 telescopes at energies below the Coulomb barrier. Reminding the polar angle at which the center of the telescope is, $\theta_{lab,t1} = 28^\circ$, $\theta_{lab,t2} = 45^\circ$, $\theta_{lab,t3} = 76^\circ$, $\theta_{lab,t4} = 130^\circ$. It is observed how the energy distribution of the ^{10}Be fragments evolves. This observation will be commented in

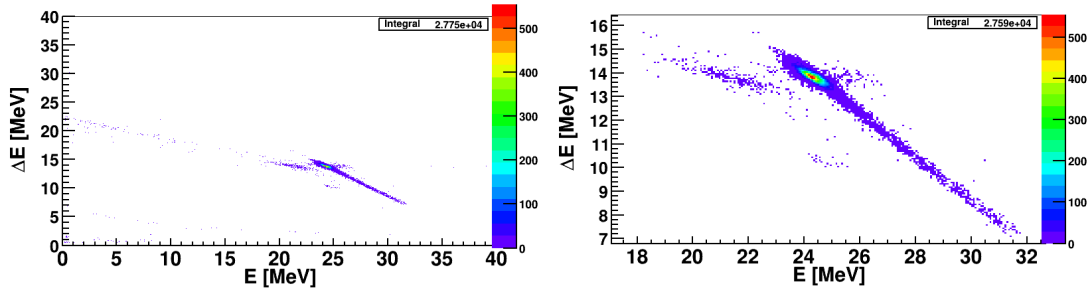


Figure 4.19: $\Delta E - E$ plots for ^{11}Be on ^{197}Au around the Coulomb barrier. Energy left in the ΔE detector in the y axis, versus energy left in the E detector in the x axis. Breakup and quasielastic are well separated. These are all the events stored along the experiment in a single pixel at $\theta = 18^\circ$ at $E_{lab} = 3.6$ MeV/u.

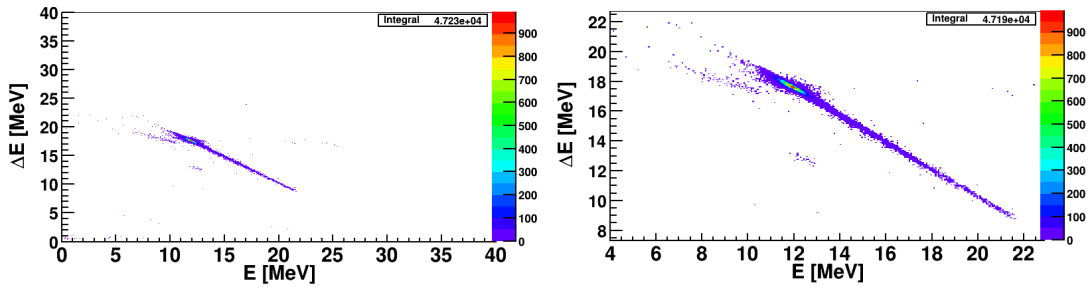


Figure 4.20: $\Delta E - E$ plots for ^{12}C on ^{197}Au . Energy left in the ΔE detector in the Y axis, versus energy left in the E detector in the X axis.

Figure 4.21: $\Delta E - E$ plots for ^{11}Be on ^{197}Au below the Coulomb barrier. Energy left in the ΔE detector in the y axis, versus energy left in the E detector in the x axis. It is observed that breakup and quasielastic are well separated. These are all the events stored along the experiment in a single pixel at $\theta = 18^\circ$ at $E_{lab} = 2.9$ MeV/u.

the discussion chapter. In figure 4.23 a $\Delta E - E_{back}$ and a $\Delta E - E_{tot}$ plot corresponding to the same events are presented together, evidencing that the fragment identification is more easily performed if the E_{back} is represented in the X axis.

4.2 Data analysis

In this section the treatment of the data for the analysis and the obtained results will be exposed. The main goal from the experimental point of view is the identification of the output channels and their energy and angular distribution. The way of doing so is considering the number of ^{11}Be and ^{10}Be ions detected in each pixel, and the gamma radiation detected in coincidence. This way, the population of the elastic, inelastic and breakup channels obtained in the same conditions can be measured, which provides very valuable information on the different cross sections.

4.2.1 Identification of breakup channel

The identification of the different reaction channels is probably the most critical step in the analysis, and the assignation of an event to a channel is not always criteria independent.

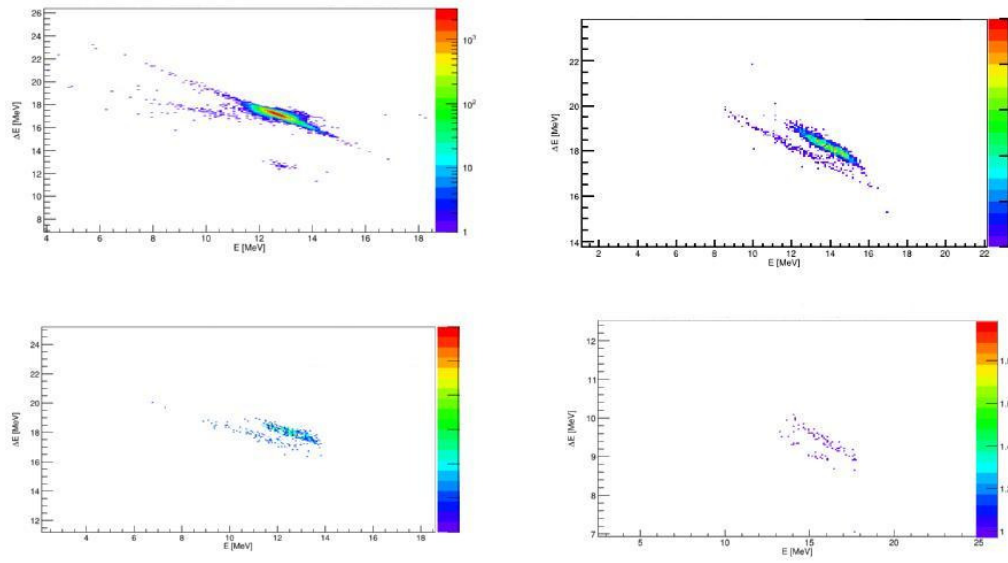


Figure 4.22: $\Delta E - E$ plots for central pixels in all telescopes, corresponding to $\theta_{lab,t1} = 28^\circ$, $\theta_{lab,t2} = 45^\circ$, $\theta_{lab,t3} = 76^\circ$, $\theta_{lab,t4} = 130^\circ$. Breakup and quasielastic are well separated in all four telescopes. It is observed how the energy distribution of the ^{10}Be fragments evolves.

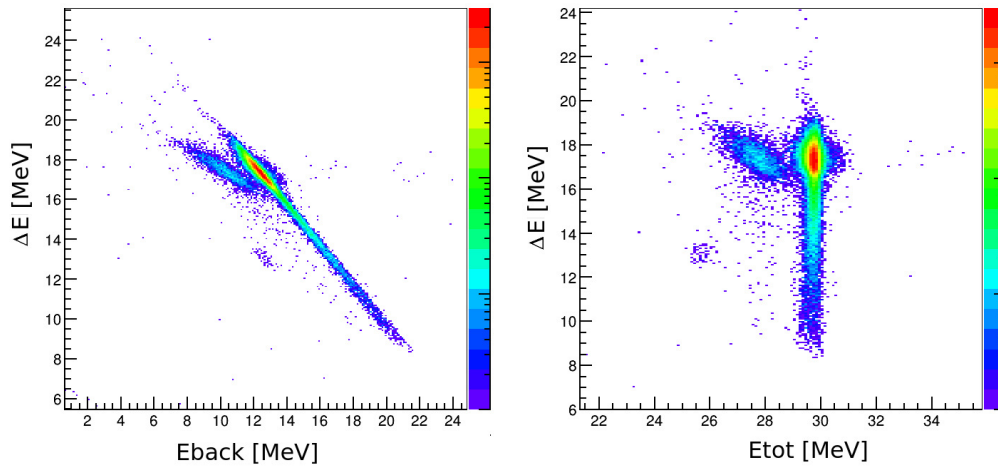


Figure 4.23: $\Delta E - E_{back}$ versus $\Delta E - E_{tot}$ plot. It can be noticed that the limits of the spots are more clearly defined if E_{back} is used in the X axis, reason why this representation is chosen for the analysis. It is observed that there is a tail towards low energies in the ΔE detector that corresponds to a channeling effect. The channeling effect corresponds to ions finding a dislocation in the Silicon wafer of the ΔE that makes them travel without losing any energy. This energy is recovered in the E detector, so the total energy of the event is correct and is seen as a vertical line in the $\Delta E - E_{tot}$ plot.

The first step is identifying the ^{10}Be and the ^{11}Be fragments. Although they are very close in mass, it was possible to separate them, thanks to the high energy resolution of the beam and the detectors.

This energy resolution, however, is not enough for separating the fragments in the elastic and the inelastic channels. The struggling of the particles going through the target and the ΔE detector broadens the peak, and the 320 keV lost in the excitation of the ^{11}Be do not suffice for separating the inelastic contribution from the elastic one. This motivates the definition of the quasielastic channel, which agglutinates elastic and inelastic scattering of ^{11}Be fragments together, in contrast to the breakup channel that is observed in the separated yield of ^{10}Be fragments.

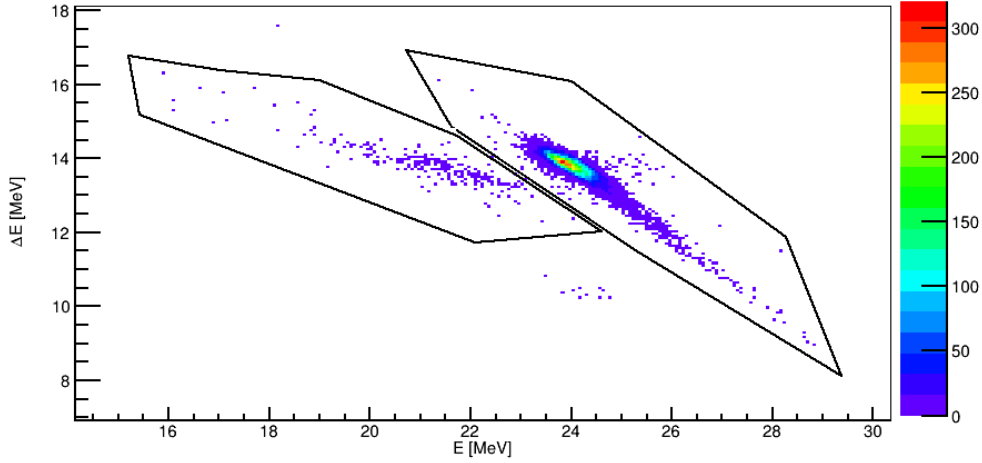


Figure 4.24: Two dimensional plot with the ^{10}Be and ^{11}Be fragments identified.

In the $\Delta E - E$ plots there are two main spots identifiable. Observing figure 4.24, the spot with more statistics, and (most often) at a higher total energy ($\Delta E + E$) corresponds to the quasielastic scattering of the ^{11}Be , while the spot at *lower* energy will correspond to the breakup channel. This offers pixel by pixel information on the reaction channels. The most direct information that can be extracted is:

- Quantity of ^{10}Be detected at one pixel, calculated integrating the number the counts inside the breakup cut.
- Quantity of ^{11}Be calculated integrating the number the counts inside the quasielastic cut.
- The breakup probability, calculated as the ratio between ^{10}Be and ^{11}Be fragments.

$$P_{bu} = \frac{N_{bu}}{N_{bu} + N_{qe}} \quad (4.13)$$

The advantage of working with probabilities is minimizing the effect of some experimental errors. Any particularity in the collection, amplification, calibration or selection of the events will affect evenly to all the events in the same pixel. If, for example, the particles detected in one pixel suffer from a lot of struggling in the target because they are in a shaded area of a detector, the count rate in that pixel will be reduced and the same will happen with the cross section directly obtained from it. On the other hand, this reduction will be observed both in elastic and breakup events, so the ratio will not be affected and it can be used for giving more accurate information on the reaction process.

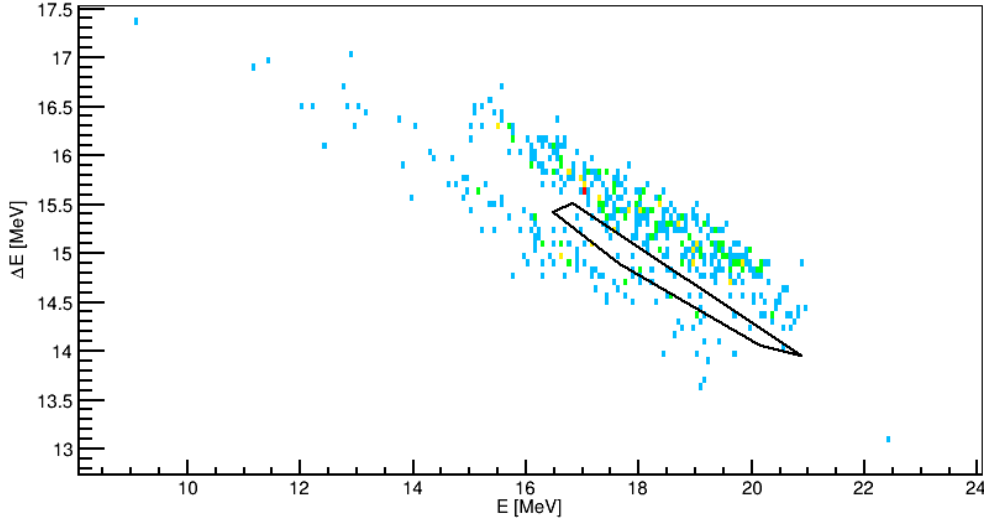


Figure 4.25: Intersection area between ^{11}Be and ^{10}Be fragments, where the events cannot be clearly identified as any of them. This is included in the error calculation as a systematic error source. The value of this systematic error is estimated performing several selections of the data with different criteria, and calculating the standard deviation of the sets calculated with each criterium. See the text for more details.

Although the fragments can be separated, there is an intersection area in which the events cannot be clearly identified as ^{11}Be or ^{10}Be . An example of that situation is shown in figure 4.25. The election of a criterium for the cuts, and the shape of the cuts for a given criterium, are the most *subjective* processes in all the experimental procedure, so it is important to control it somehow. In this work, this is done considering it as a source of systematic error. The methodology chosen for quantifying this systematic error is:

- Perform different cuts, using different criteria. For example,
 - two set of cuts were performed considering what I considered the *most sensible* criterium. The cuts were performed in different weeks, in order to be as independent as possible in their selection.
 - A set of cuts was performed trying to count as much breakup as possible, which would impose an upper limit to the breakup probability.
 - A set of cuts was performed trying to count as much quasielastic as possible, which would impose a lower limit to the breakup probability.
- The value of the probability was calculated as the weighted average between the probabilities of the different cases,

$$P = \frac{\sum \frac{P_i}{\sigma_i^2}}{\sum \frac{1}{\sigma_i^2}}. \quad (4.14)$$

- The systematic error σ_s was calculated as the standard deviation of the obtained probability for each pixel.

$$\sigma_p = \sqrt{\sum_i \frac{(P - P_i)^2}{\sigma_i}}, \quad (4.15)$$

where σ_i is the error obtained from the error propagation in the number of counts for the set i

$$\begin{aligned}\sigma_i &= \sqrt{\left(\frac{dP}{dN_{bu}}\sigma(N_{bu})\right)^2 + \left(\frac{dP}{dN_{qel}}\sigma(N_{qel})\right)^2} \\ &= \sqrt{\left(\left(\frac{1}{N_{qel} + N_{bu}} - \frac{N_{bu}}{(N_{qel} + N_{bu})^2}\right)\sqrt{N_{bu}}\right)^2 + \left(\frac{-N_{bu}\sqrt{N_{qel}}}{(N_{qel} + N_{bu})^2}\right)^2}. \quad (4.16)\end{aligned}$$

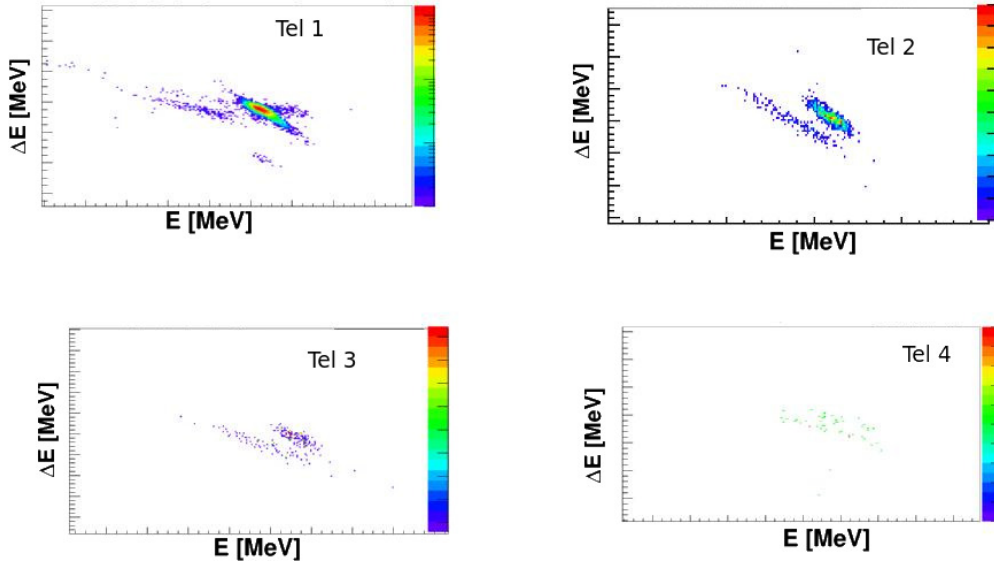


Figure 4.26: $\Delta E - E$ plots for central pixels in all telescopes, corresponding to $\theta_{lab,t1} = 28^\circ$, $\theta_{lab,t2} = 45^\circ$, $\theta_{lab,t3} = 76^\circ$, $\theta_{lab,t4} = 130^\circ$. Breakup and quasielastic are well separated in all four telescopes. It is observed how the energy distribution of the ^{10}Be fragments evolves, what envisages that the transfer to the target gains relevance at large scattering angles.

It has been said that the spot at a higher total energy ($\Delta E + E$) corresponds to the elastic scattering of the ^{11}Be , while the spot at lower energy will correspond to the breakup channel. This is strictly true if the particle undergoes direct breakup. In that case the ^{10}Be fragment will have the same velocity that the ^{11}Be had. The energy deposition per length unit depends on the velocity and the Z , so the energy left in the ΔE for ^{10}Be and ^{11}Be will be the same. The difference in this case will only sit on the different mass of the fragments. For the same velocity, the lower mass, the lower energy. The total energy, and hence, the energy deposited in the E detector will be lower for the ^{10}Be than for the ^{11}Be , and we will be able to separate them.

In the case that the neutron is transferred to the ^{197}Au , the energy difference between the original unbound state $n+^{197}\text{Au}$ and the final bound state ^{198}Au will be invested in accelerating the ^{10}Be ejectile. The velocity (and hence the energy) of the ejectile will be increased. It may happen that some ^{10}Be fragments have more energy than the original ^{11}Be . Even in this case, the different velocity will be translated into a lower energy deposition in the ΔE detec-

tor, allowing for fragment identification even in this case thanks to our good energy resolution.

An indication of the dominance of the different processes can be noticed in figure 4.26, where the position of the breakup spot with respect to the elastic one changes for the different angles. For larger angles, the neutron transfer picture gains importance. This is noticed in the lower energy loss in the ΔE detector, cause by the postacceleration of the ^{10}Be after the transfer.

4.2.1.1 Angular binning

At forward angles, the statistics and the clear separation make it possible to perform the cuts pixel by pixel. However, it is evident, from the observation of figure 4.26, that the statistics in a single pixel in telescope 4 are not enough for identifying the fragments. At larger angles, the low count rate, make it necessary to sum the events from different pixels. Since the reaction process only depends on the polar angle, it was considered reasonable to sum the statistics from pixels at a similar θ , generating angular bins of 3° . The bin size was chosen to be similar to the angular distance between pixel, as a compromise for the obtained data to be consistent, and not losing information on the angular distribution.

Representing together the data from different pixels helps, not only to identify the ^{10}Be and ^{11}Be fragments, but also to reduce considerably the number of cuts that have to be performed manually, using common cuts for the pixels at the same angle, and to minimize the statistical fluctuations, summing up enough events for minimizing the statistical error.

When using the same cut for different pixels within the same angular bin some precautions have to be taken. In principle, all the particles hitting pixels in the same bin should have the same energy, i.e., should leave a similar ΔE - E signature. Nevertheless, some difference may arise due to the different path they have to go through in the detector. In addition to the polar angle with respect to the beam direction, the incidence angle on the detector has to be considered. If we imagine two particles at the same energy and same θ , hitting a central and a border pixel respectively, the one hitting the central pixel will have a trajectory perpendicular to the detector, traveling a shorter path in the ΔE and leaving less energy in it. Although the energy deposition in a detector is not linear, a first order correction of this type,

$$E_b = E_b + \Delta E \left(1 - \frac{1}{\cos \alpha}\right), \quad (4.17)$$

$$\Delta E = \frac{\Delta E}{\cos \alpha}, \quad (4.18)$$

where the subindex b is added for clarifying that E_b refers to the the energy lost in the back detector, can reduce this effect and help in bringing the centroids of different pixels together. In addition to this one, an *ad hoc* correction is introduced for selecting the cuts. It consisted on finding the centroid in the X and Y axis (ΔE and E_{back}) of the elastic peak in each pixel and in the angular bin, and add the difference to the E_{back} :

$$\Delta X = E_{bin} - E_{pix}; \quad \Delta Y = \Delta E_{bin} - \Delta E_{pix}; \quad \hat{E}_{pix} = E_{pix} + \Delta X + \Delta Y. \quad (4.19)$$

The improvement with this correction was found trying among different combinations and it

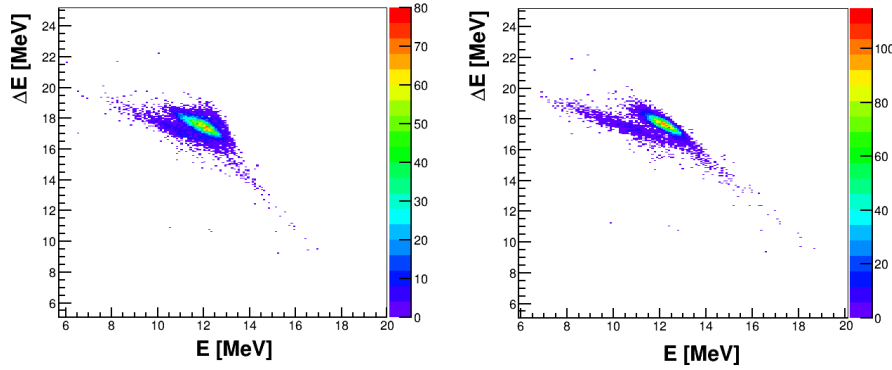


Figure 4.27: $\Delta E - E$ plots with and without introducing corrections for the angular bin between 66° and 69° . The first correction takes into account the angle of incidence on the detector and the second is an adhoc correction for positioning the centroid of the elastic peak of each pixel within an angular bin at the same position than the centroid of the whole bin.

resulted to be the one that made it easier to select the cuts. In figure 4.27 the statistics summed for an angular bin with and without the two corrections are shown.

4.2.1.2 Angular distribution of breakup probability

The resulting angular distribution of the breakup probability, summing the information of the pixels into angular bins of 3° , is shown in figure 4.28. It is observed that, even below the barrier, the probability of breaking the ^{11}Be into a ^{10}Be fragment and a neutron is considerable.

4.2.2 Identification of the inelastic channel

The inelastic channel cannot be separated from the elastic channel using charged-particle spectroscopy alone. The HPGe detector array TIGRESS is used for detecting the gamma radiation emitted after the deexcitation of ^{11}Be in coincidence with the fragments. The use of the gamma detectors make it indispensable to correct for the efficiency of the array. This fact, together with the low probability of excitation, and the subsequent low count rate, entails an increase in the uncertainty with respect to the breakup calculation.

In this case, the inelastic scattering probability is defined as:

$$P_{inel} = \frac{N_{in}}{\varepsilon_\gamma N_{Be}} \quad (4.20)$$

where N_{in} is the number of events in coincidence with the TIGRESS detector gated on the 320 keV line, ε_γ is the efficiency of TIGRESS at the energy of the gamma, 320 keV, and N_{Be} are the number of counts of the Be fragments of any kind. No distinction between elastic and inelastic is made for introducing as few sources of error as possible. Likewise, the statistics per pixel are not considered for this observable. At large angles of telescope 3, the number of coincidences of particles with a 320 keV gamma per pixel is of the order of 5, and in telescope 4 there are many pixels with no coincidence at all. For minimizing the error, the probability is calculated

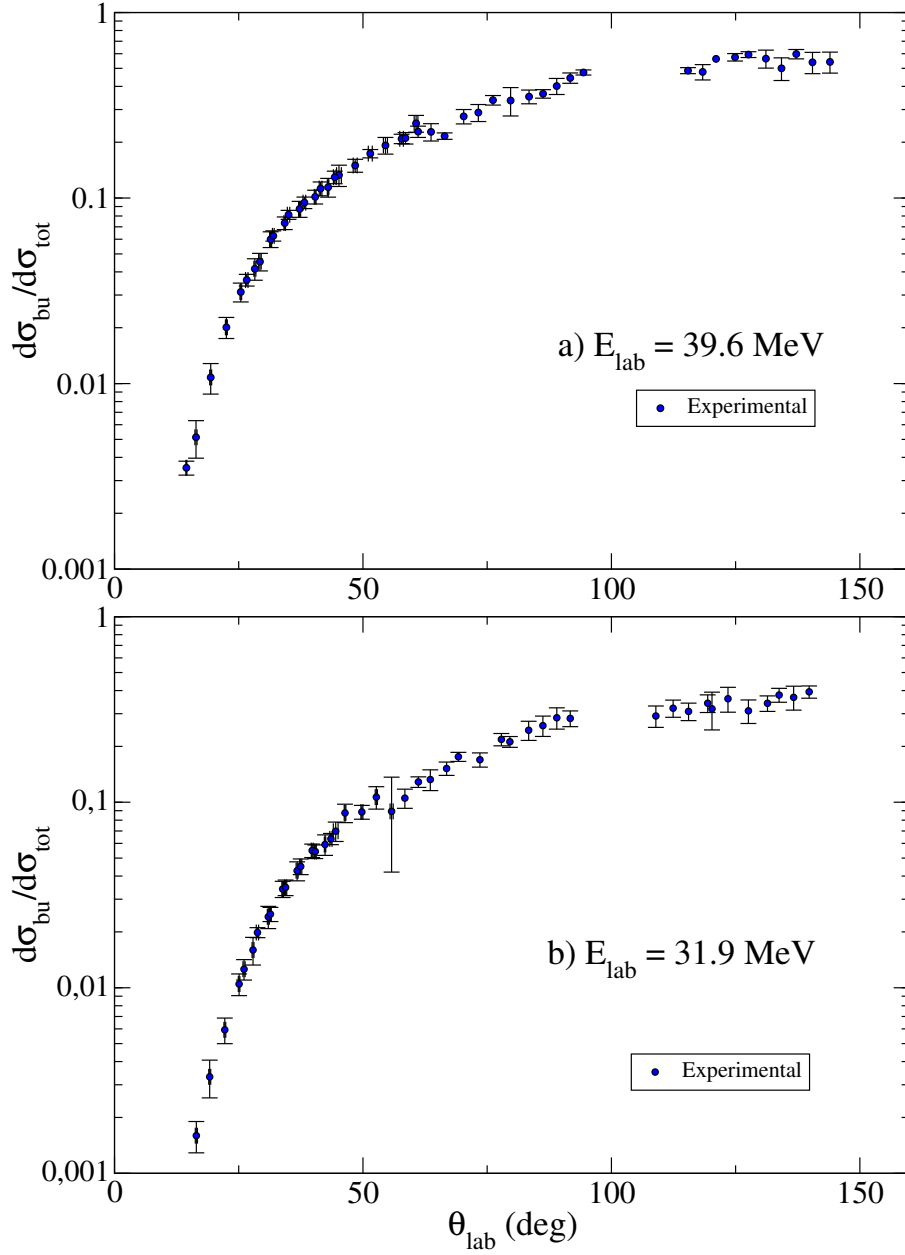


Figure 4.28: Angular distribution of the breakup probability data.

summing all the statistics in the angular bin. An example of the coincidences per pixel and per bin is shown in figure 4.29.

In this case, the error calculation is directly obtained as

$$\begin{aligned}
 \sigma_{inel} &= \sqrt{\left(\frac{dP}{dN_{in}}\sigma(N_{in})\right)^2 + \left(\frac{dP}{dN_{Be}}\sigma(N_{Be})\right)^2 + \left(\frac{dP}{\varepsilon}\sigma(\varepsilon)\right)^2} \\
 &= \sqrt{\left(\frac{\sqrt{N_{in}}}{\varepsilon_{\gamma}N_{Be}}\right)^2 + \left(\frac{-N_{in}\sqrt{N_{Be}}}{(\varepsilon_{\gamma}N_{Be})^2}\right)^2 + \left(\frac{-N_{in}\sqrt{\varepsilon_{\gamma}}}{(\varepsilon_{\gamma}N_{Be})^2}\right)^2}.
 \end{aligned} \tag{4.21}$$

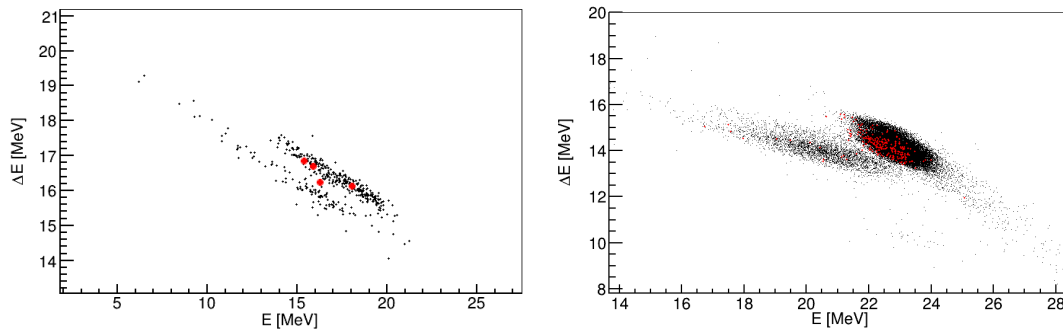


Figure 4.29: $\Delta E - E$ plots in coincidence with 320 keV gamma (red points) represented on $\Delta E - E$ plots with no gating. On the left the case with a single pixel, where the poor number of counts is evidenced. On the right the number of counts summed for all the angular bin.

This is actually an upper limit to the error, because N_{in} and N_{Be} are not independent, but the contribution of N_{Be} to the error is marginal and the effect of the covariance is not expected to be noticeable.

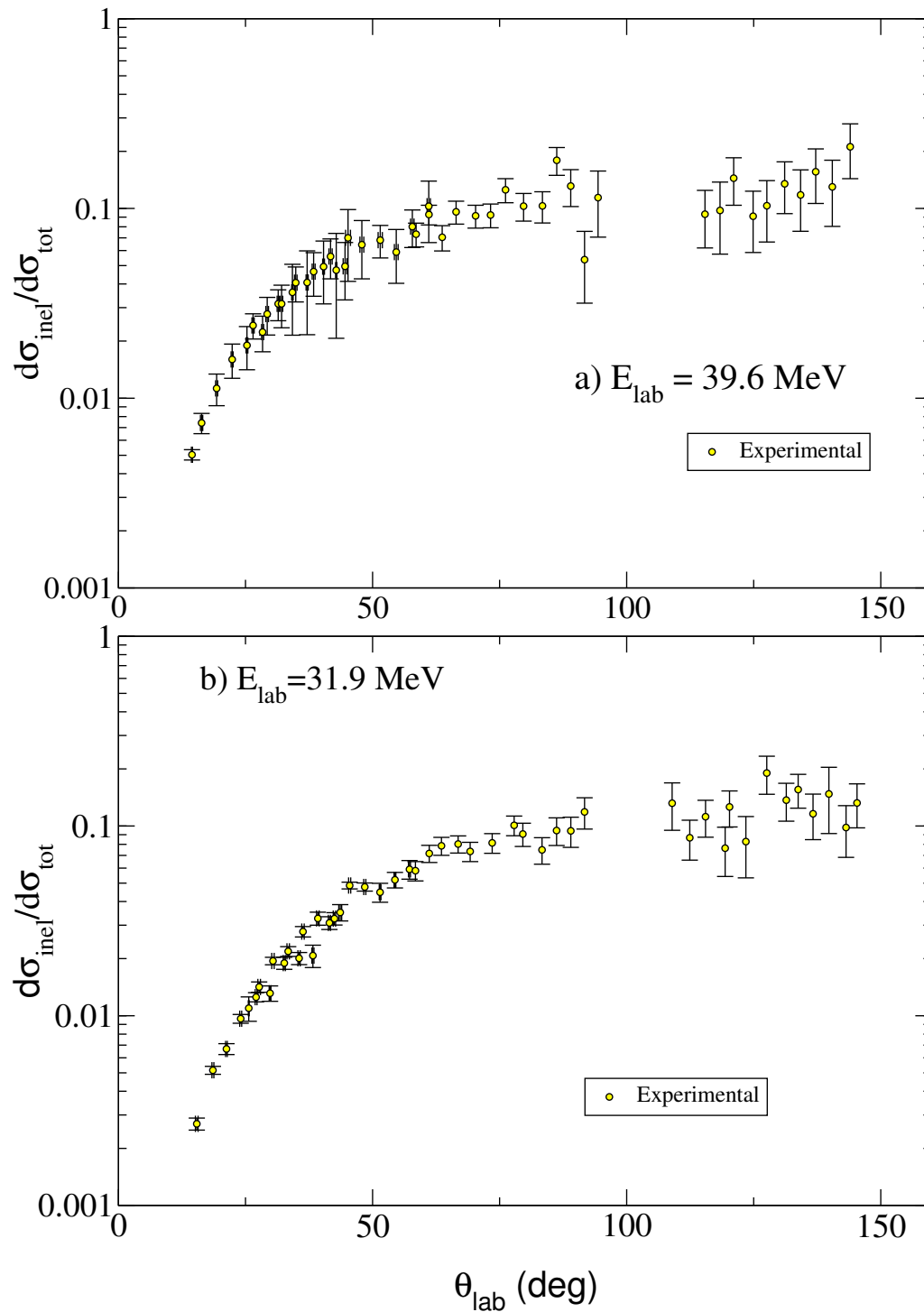


Figure 4.30: Angular distribution of the inelastic scattering probability.

4.2.3 Identification of the elastic channel

The elastic scattering probability is calculated subtracting the inelastic from the quasielastic

$$\begin{aligned}
 P_{el} &= \frac{N_{qel} - \frac{N_{in}}{\varepsilon_\gamma}}{N_{Be}} \\
 &= \left(\frac{N_{qel}}{N_{Be}} \right) - \left(\frac{N_{in}}{\varepsilon_\gamma N_{Be}} \right) \\
 &= (1 - P_{bu}) - (P_{in})
 \end{aligned} \tag{4.22}$$

This development is trivial, because if we are only considering these three channels, the sum of the probability of populating them has to be 1, but is useful for the error calculation. Knowing that our greater source of error is the inelastic scattering,

$$\sigma_{el} = \sqrt{(\sigma_{bu})^2 + (\sigma_{in})^2} \simeq \sigma_{in} \tag{4.23}$$

In figure 4.31 the elastic scattering probability is shown at energies around and below the Coulomb barrier.

4.2.4 Calculation of absolute cross sections

For the calculation of absolute cross sections the total number of counts per pixel, divided by the solid angle, is compared to the Rutherford cross section at forward angles,

$$\frac{N_t/\Delta\Omega}{d\sigma_{Ruth}/d\Omega(\theta_{pix})} = K. \tag{4.24}$$

This value will be different for each beam, since it depends on the beam time and intensity, but it is the same for all the telescopes. The value was calculated pixel by pixel and averaged for all the pixels in the first telescope. Once obtained for the total measured cross section, and giving values of

$$K_{E=39.6MeV} = (5.9 \pm 0.2) \times 10^{-3}, \quad K_{E=31.9MeV} = (5.7 \pm 0.2) \times 10^{-3}; \tag{4.25}$$

the value of K were used for converting the number of counts in a certain reaction channel to absolute cross section:

$$\frac{d\sigma_{ch}}{d\Omega}(\theta) = K \frac{N_{ch}}{\Delta\Omega} \tag{4.26}$$

It is straightforward to notice that the solid angle covered by each pixel has to be determined with high accuracy for the absolute cross section to be correctly determined. This means that in this case, the absolute cross section for telescope 4 cannot be properly calculated and will not be presented. The absolute inelastic scattering and breakup cross sections are shown in figures 4.32 and 4.33, respectively.

In addition to the angular distribution of the breakup cross section, an observable that can be compared with the calculations is the energy distribution of the fragments. In this case, in which we measure inclusive breakup, we have access to the experimental energy distribu-

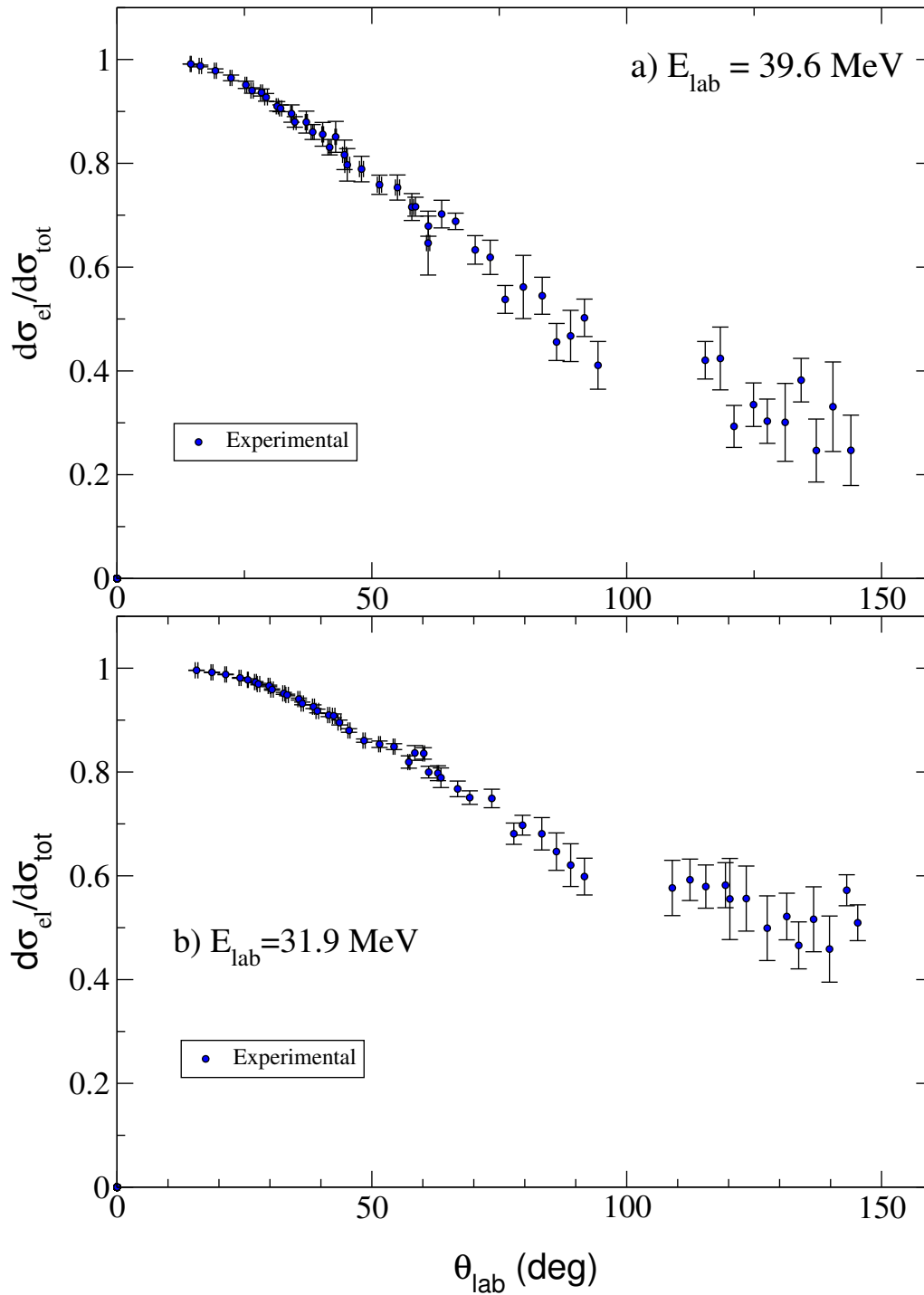


Figure 4.31: Angular distribution of the elastic scattering probability.

tion of the ^{10}Be fragment. One can consider the double differential cross section, depending explicitly on the angle and the energy of the core fragment:

$$\frac{d^2\sigma}{d\Omega_c dE_c} = \int \frac{d^3\sigma}{d\Omega_c dE_c d\Omega_n} d\Omega_n \quad (4.27)$$

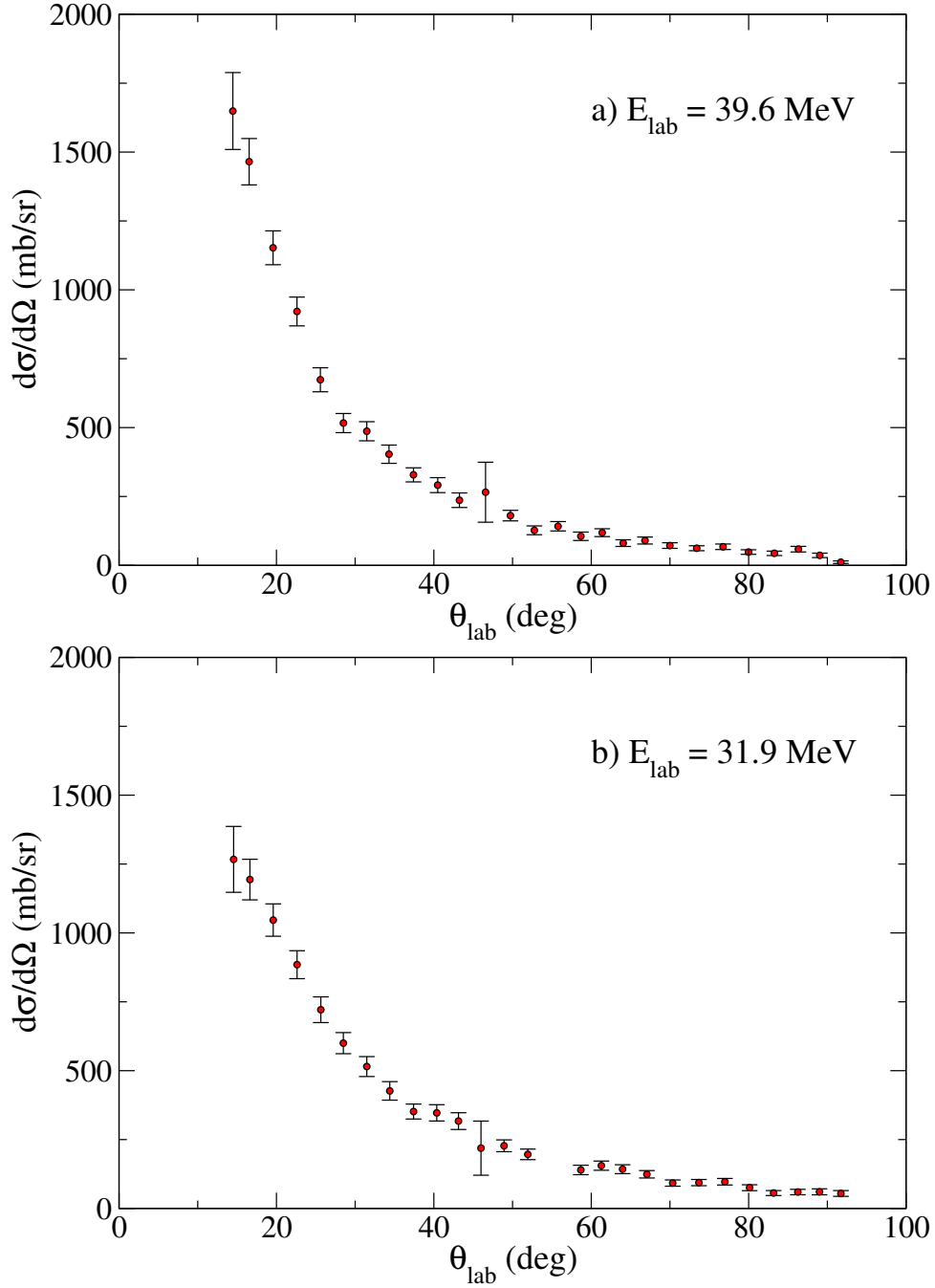


Figure 4.32: Experimental angular distribution of the inelastic scattering cross section.

From such double differential cross section, the energy distribution of the fragments detected within an angular range (θ_1, θ_2) can be calculated as

$$\left. \frac{d\sigma}{dE}(E) \right|_{\theta_1 < \theta_2} = \int_{\theta_1}^{\theta_2} \frac{d^2\sigma}{d\Omega dE} d\Omega = \int_{\theta_1}^{\theta_2} \frac{d^2\sigma}{d\theta dE} 2\pi \sin(\theta) d\theta. \quad (4.28)$$

Experimentally, the double-differential cross section has to be obtained in a pixel by pixel basis. The procedure is:

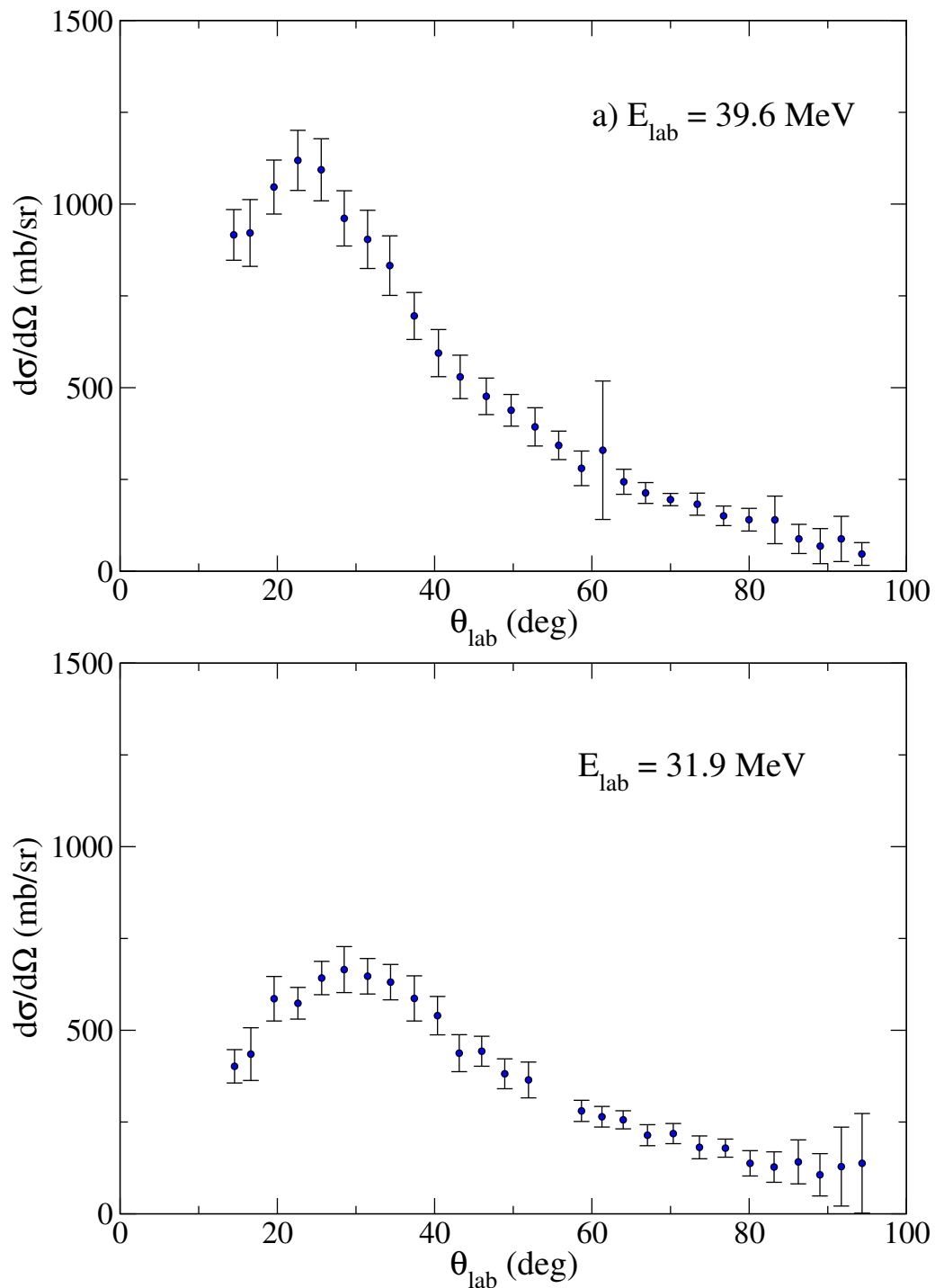


Figure 4.33: Experimental angular distribution of the inelastic scattering cross section.

1. Selecting the cut corresponding to the ^{10}Be fragments in the 2-dimensional plot for each pixel i .
2. Represent the selected events in a histogram with respect to their total energy.

3. If it is assumed that the total cross section is equal to the Rutherford cross section, the breakup cross section at a certain energy can be calculated as:

$$\frac{d^2\hat{\sigma}_i}{d\Omega dE}(E, \theta_i) = \frac{N_{bu,i}(E)}{\Delta\Omega} K \frac{1}{\Delta E_{bin}}. \quad (4.29)$$

where

- $N_{bu,i}(E)$ is the number of counts of ^{10}Be in the bin at energy E ,
- ΔE_{bin} is the width of the energy bin in the generated ^{10}Be -histogram

$$\frac{d\sigma_{\text{Ruth}}}{d\Omega}(\theta_i) = \frac{d\sigma_{\text{Ruth}}}{d\Omega}(\theta_{cm,i}) \frac{d\sigma_{lab}}{d\sigma_{cm}}(\theta_{lab,i}). \quad (4.30)$$

The experimental energy distribution is then obtained as the numerical integral in θ , which is the summation of each contribution multiplied by the effective angular width of the pixel $\Delta\theta$

$$\left. \frac{d\sigma}{dE}(E) \right|_{\theta_1 < \theta < \theta_2} = \sum_i^{N_{pix}} \frac{d^2\hat{\sigma}_i}{d\Omega dE}(E, \theta_{lab}) 2\pi \sin(\theta_{lab}) \Delta\theta. \quad (4.31)$$

N_{pix} is the number of pixels in the angular range we are integrating ($\theta_1 < \theta < \theta_2$) and $\Delta\theta$ is the *bin size* in θ . If we are integrating the cross section in intervals of 3° , it can be considered that the $\Delta\theta$ covered by each pixel is:

$$\Delta\theta = 3^\circ \frac{\pi}{180^\circ} / N_{pix}. \quad (4.32)$$

The energy distribution of the breakup cross section for the fragments detected between 24° and 27° is presented in figure 4.34. It is compared to simple kinematical calculations in which only the scattering angle and the Q-value of the reaction are considered. The brown vertical line corresponds to 10/11 the energy of a ^{11}Be inelastically scattered, being excited to a state at $E_x = 0.504$ MeV which corresponds to the neutron separation energy. The orange dashed line corresponds to the transfer of one neutron to a state 1 MeV above the separation energy of the ^{198}Au . When integrating between 60° and 100° the vertical line are substituted by boxes because a broader angular distribution corresponds to a broader energy distribution.

In principle, at forward angles one expects that the distribution should correspond to a direct breakup, thus, being closer to the brown line. This is not what we observed and the angular distribution of the elastic cross section was also compared with kinematical calculations. They are shown in figure 4.35 and show a good agreement with the expected values (vertical lines). The study of the energy distribution and its comparison with the CDCC and XCDCC calculations is still on-going, so these results have to be evaluated with caution.

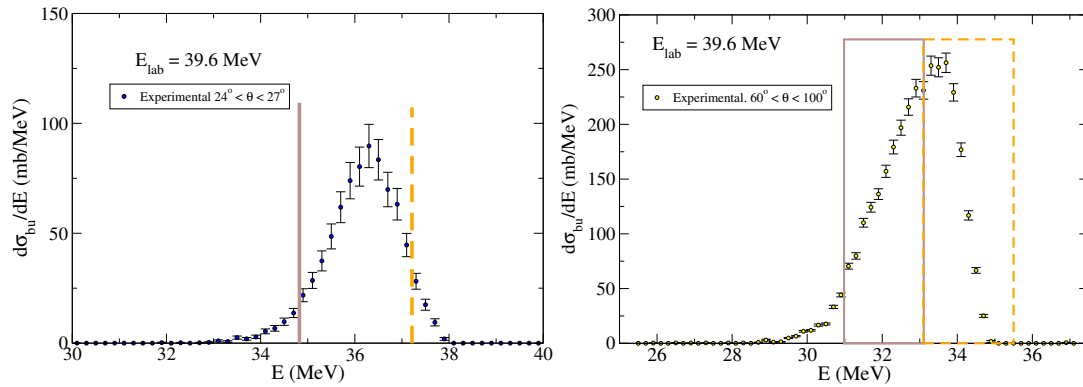


Figure 4.34: Energy distribution of the ^{10}Be fragments detected between 24° and 27° (on the left) and between 60° and 100° (on the right). The straight brown line corresponds to the energy at which a ^{10}Be fragment would be scattered considering only a Q -value of 0.504 MeV for exciting the projectile. The dashed orange line corresponds to the case in which a neutron is transferred to the ^{197}Au target, populating a state 1 MeV above the threshold.

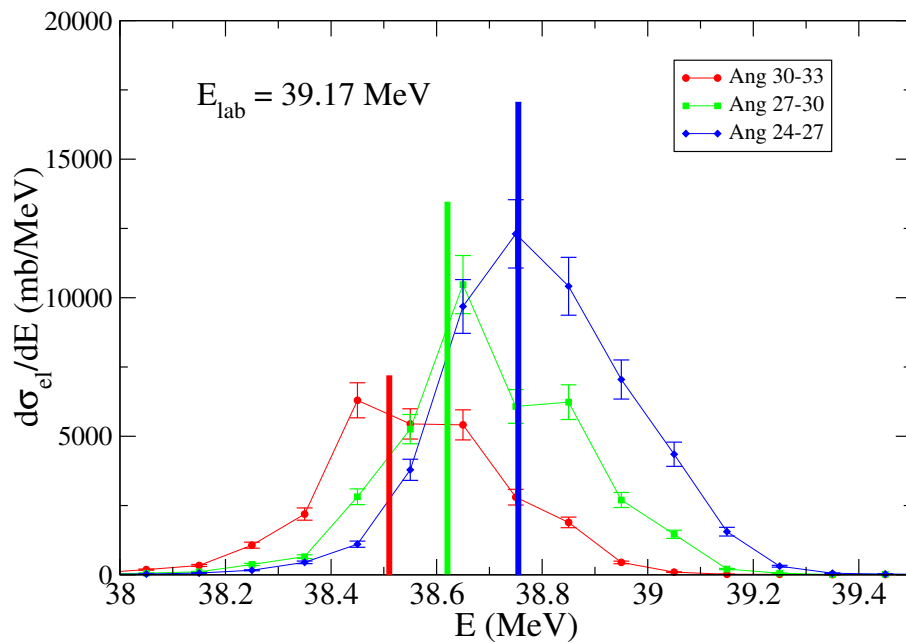


Figure 4.35: Energy distribution of the elastically scattered ^{11}Be fragments telescopes in different ranges at forward angles compared to the expected energy from a kinematical calculation.

Analysis of the results and discussion

This chapter is dedicated to the presentation of the measured cross sections and their comparison with different formalisms.

Although the ultimate aim of an experimentalist is to provide valuable data with original content on relevant aspects of physics, having novel data available is always a deep attracting potential acting on a surrounding physicist and his/her inherent curiosity for understanding the nature. For this reason, although it was not within the first scope of this work, some calculations were performed by myself, which, compared to the data, allowed for a deeper understanding of the underlying processes.

The calculations performed by myself are optical model, CDCC and TC calculations. All of them were performed using the code `fresco` [Tho88]. In addition to those three, other calculations are compared to the data, namely EPM (performed by J.A. Lay) and XCDCC calculations (performed by A.M. Moro). They have been involved in this work thanks to a long-standing very fruitful experimental/theoretical collaboration between my group at IEM-CSIC and the Nuclear Physics group in the Universidad de Sevilla.

It is important to emphasize, before going into detail, that the only fits to our data were those performed for the $^{11}\text{Be}+^{197}\text{Au}$ elastic scattering within the optical model framework. This phenomenological potential provided a first phenomenological insight of the present data and, in addition, it was used as incoming channel optical potential in the TC calculations. In the rest of the formalisms (CDCC, XCDCC, and EPM), the required potentials were adopted from previous works, so the prediction power of the models for this reaction will be evidenced.

The measurements will be presented and compared to different formalisms. This way, the discussion of the results will be focused, in each case, in the information that can be extracted from the model it is compared with. This comparison will be made beginning with a simple optical model, and going through more sophisticated approaches sequentially, thus obtaining interesting features of the reaction and the ^{11}Be structure in all of them.

The global properties of the $^{11}\text{Be}+^{197}\text{Au}$ interaction are evidenced within an optical model formalism, and strong large range couplings show up through the radius and diffuse-

ness of the nuclear potentials that reproduce the scattering data. The first order Equivalent Photon Method, allows for quantifying the contribution of the dipolar Coulomb excitation to the population of the bound excited state and of the continuum. The 3-body CDCC formalism gives information based on a simple two-body model of the ^{11}Be nucleus. The partial success of this formalism in the description of the observables gives valuable information on the dynamics of the reaction and the halo structure and, in addition, the limitations of this description for the case of ^{11}Be are a prove that evidence the need of including the core structure for a proper description of the reaction process. This is done using a particle-rotor structure model for the ^{11}Be projectile (coupling the valence neutron to a rotor core, modeled including a deformation in the ^{10}Be nucleus). This particle-rotor model is used within the XCDCC reaction framework, an extended version of the CDCC method which takes into account core excitation effects in the structure of the projectile, as well as in the core-target interaction. These XCDCC calculations yield an improved description of the data, with respect to the standard CDCC method. The reaction will also be studied from a transfer approach, where the final states of the system will be defined as bound and unbound states of ^{198}Au . This approach has been very useful for understanding the ^6He and the ^{11}Li scattering data on heavy targets at energies around the barrier, especially the differential cross section at large scattering angles.

5.1 Analysis within the optical model

The optical model formalism provides a description of the reaction in terms of an effective potential, which only depends on the projectile-target distance. The coupling to the internal degrees of freedom are described effectively by a potential with a real and imaginary part, where the latter accounts for the flux subtracted from the elastic scattering. The parameters of the potential are fitted, then, to reproduce the elastic scattering data, and the values of the parameters of the model evidence some global properties of the reaction, such as the strength of the couplings, their range and their character (more or less diffractive or absorptive).

In this case, the real and imaginary potentials are modeled using a Woods-Saxon parametrization. The parameters to be fitted, for each of the potentials, are the radius of the interaction (R_x), the diffuseness (a_x) and the depth of the well. Recalling equation (2.13) and adapting (2.14) to our particular case:

$$U_{\text{opt}}(R) = U_c(R) - V_r f(R, r_r, a_r) - iW_0 f(R, r_i, a_i), \quad (5.1)$$

where the Woods-Saxon form factor is

$$f(R, R_x, a_x) = \frac{1}{1 + e^{\frac{R - R_x}{a_x}}}$$

As has been mentioned, and can be inferred from eq. (5.1), the fit to the data was performed within an optical model considering a Woods-Saxon form factor for the real and the imaginary part. No spin-orbit or surface terms were included. The fit was performed using the code `sfresco`, which is a subroutine of `fresco` that provides Chi-squared searches of po-

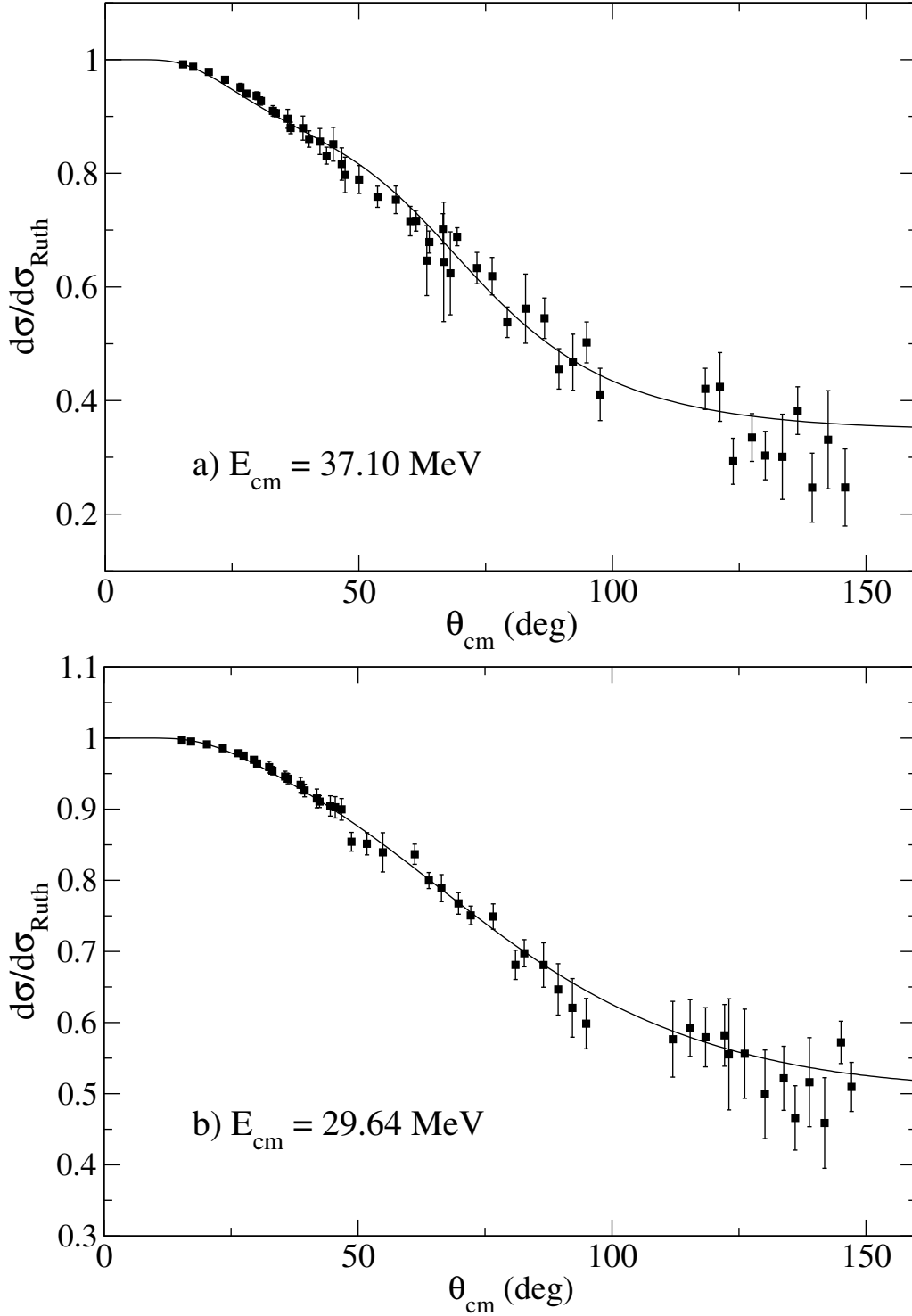


Figure 5.1: Elastic scattering cross section. Experimental data and fit within an optical model including a Woods-saxon potential for the real and the imaginary parts. The measurements were performed at two beam energies: 3.6 MeV/u (39.6 MeV) and 2.9 MeV/u (31.9 MeV). For all the calculations the reaction is supposed to happen in the center of the target, and the energies at which the reaction takes place are $E_{\text{lab}} = 39.17$ MeV ($E_{\text{cm}} = 37.09$ MeV) and $E_{\text{lab}} = 31.30$ MeV ($E_{\text{cm}} = 29.64$ MeV), which are around and below the Coulomb barrier ($V_b \sim 40$ MeV), respectively.

tential and coupling parameters. The initial values for the parameters was taken from [Kol07], where J.J. Kolata and collaborators studied the scattering of ^{10}Be on ^{208}Pb at energies around the Coulomb barrier. Two parameters were varied and 4 parameters were fixed for each minimization step. We usually started varying W and a_i , then V and a_r , then r_r and r_i , and then W and a_i again, until stable values were obtained. After the four mentioned minimization steps the results were consistent. Three fits were performed, one to the low energy data, one to the high energy data, and one to both of them. The initial values for the parameters, and the values obtained for the different fits are presented in table 5.1.

Table 5.1: Optical model parameters for $^{11}\text{Be}+^{197}\text{Au}$ at energies around the Coulomb barrier. We present a set of values fitted to each of the measured energies, and another fitted to both of them simultaneously. The first line corresponds to the original parameters obtained by Kolata et al [Kol07] from the optical model analysis of the $^{10}\text{Be}+^{208}\text{Pb}$ data.

	V (MeV)	r_V (fm)	a_V (fm)	W (MeV)	r_W (fm)	a_W (fm)	χ^2
Kolata [Kol07]	113.	1.06	0.63	169	1.196	0.30	
$E_{cm} = 37.10$ MeV	13.95	1.19	3.05	0.21	1.2	8.68	1.3
$E_{cm} = 29.64$ MeV	9.24	1.19	3.77	0.179	1.2	8.73	1.0
both E	13.33	1.19	3.21	0.188	1.2	8.39	1.8

The first experimental evidence of the low binding energy of a nucleus in a scattering experiment on heavy nuclei at energies around the Coulomb barrier is its strong reduction in the elastic channel with respect to the Rutherford cross section. In addition to the strong reduction, the scattering with halo nuclei adds a new signature in the angular distribution of the elastic channel: the absence of a maximum in the $d\sigma/d\sigma_{Ruth}$ in the region where the nuclear and Coulomb potentials interfere. This maximum is not observable due to a long range absorption. For fitting this data, a large diffuseness of the imaginary potential is necessary, which will be translated into a significant absorption even at forward scattering angles. This absorption will dominate over the interference and vanish the diffraction pattern.

The absorption in the elastic channel below the Coulomb barrier offers clear evidence of the halo structure of ^{11}Be . Below the barrier, in ordinary nuclei, the projectile does not penetrate into the target and the nuclear potential has no influence. In figure 5.2, the values of the elastic cross section for different values of the real and imaginary diffuseness for illustration. It is shown that at $E_{cm} = 29.64$ MeV ($V_b \sim 40$ MeV), the diffuseness is a critical parameter for understanding the influence of the real and imaginary part of the nuclear potential. In figure 5.2b, the calculations with low diffuseness in the imaginary part (green line), show the same behaviour that the calculation with no imaginary potential (blue line). An extremely large value for the imaginary diffuseness is necessary for explaining the observed absorption at 20° (black line). In figure 5.2a, the fitted parameters are compared to the calculation with no imaginary potential and the values for the diffuseness of the real part is reduced. It is observed that the typical values for the diffuseness in ordinary nuclei ($a_r \approx 0.7$ fm, see [Kol07] for the ^{10}Be case, for instance) would correspond, at this energy, to a pure Rutherford cross section (blue line). A small diffuseness corresponds to nuclei in which the density falls sharply, and a large diffuseness corresponds to densities being diluted softly, so it is precisely large val-

ues for the diffuseness like the one we obtained that can be imagined macroscopically as a *halo*.

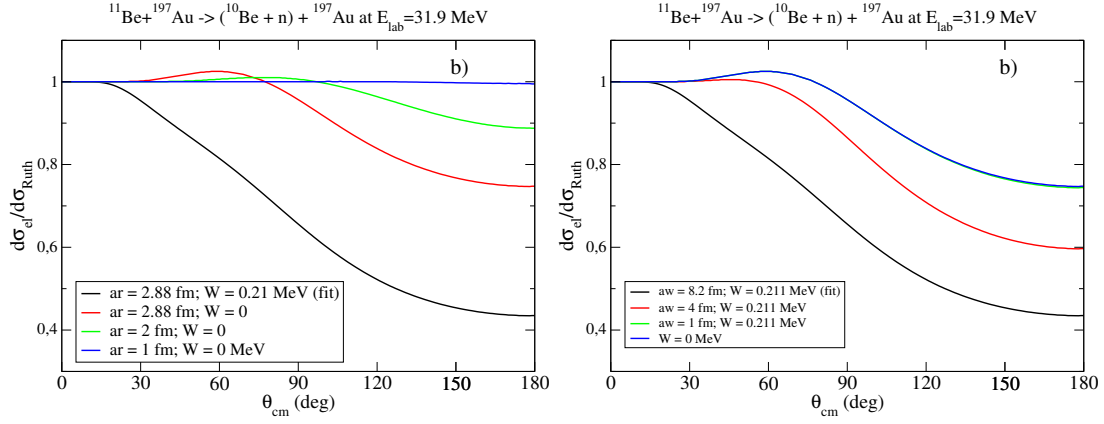


Figure 5.2: Optical model calculations at $E_{cm} = 29.64$ MeV, varying the diffuseness of the real (a) and imaginary part (b) of the nuclear potential. The black line shows is, in both cases, the calculation fitted to the data. In a) the imaginary potential is set to zero and the elastic scattering cross section obtained with different values for the real diffuseness is shown. Values of $a_r = 1$ fm, close to the typical values of nuclei with no halo, show a Rutherford cross section, as expected for these nuclei below the barrier. In b) the real potential is calculated with the parameters of the fit and only the diffuseness of the imaginary part is modified. the calculations with low diffuseness (green line) show the same behavior that the calculation with no imaginary potential (blue line).

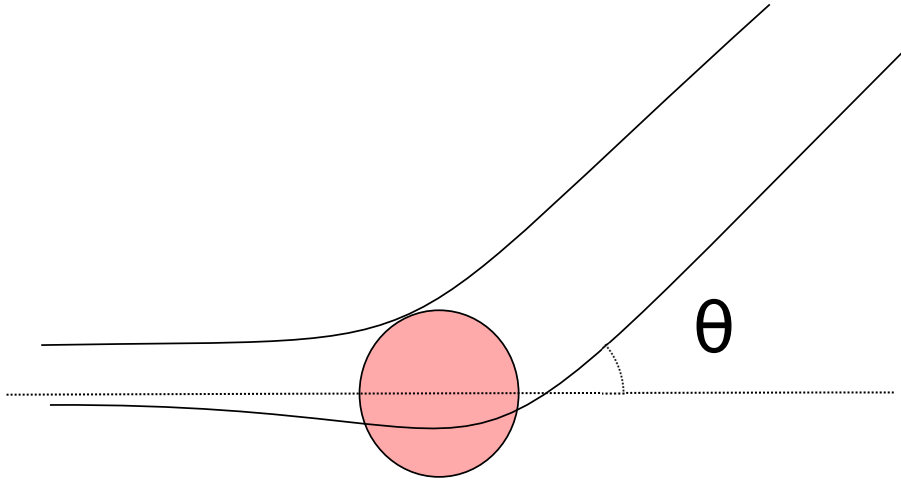


Figure 5.3: Example of short and long trajectories scattered at a certain angle θ . The interference of the different trajectories causes a Fraunhofer diffraction pattern.

If we imagine the interaction as a function of the impact parameter, the projectiles scattered at forward angles will have distant trajectories, only affected by the Coulomb potential. The projectiles scattered at backward angles will have a distance of closest approach inside the range of the nuclear potential and will be, then, affected by it. Between these two extreme cases, there will be some angle, named *grazing angle*, at which the projectile has a trajectory tangent to the target (the projectile grazes the target nucleus), and nuclear effects begin to influence the trajectory. If the nuclei involved in the scattering are ordinary nuclei, around this angle there is an enhancement of the elastic scattering cross section, caused by the constructive

interference among the possible trajectories (qualitatively depicted in figure 5.3). The amplitude of this interference for different values of the depth of the real potential is shown in figure 5.4. It is observed that with no imaginary potential, this interference also leads to a reduction of the elastic scattering at large angles. If the potential is increased sufficiently, another maximum appears (at $\sim 90^\circ$ with $V = 28$ MeV), evidencing that these structures correspond to an emerging interference pattern. In the case of halo nucleus the absorption begins at very forward angles, disguising the effects of this interference, and evidencing the need of including a long-range imaginary potential for parametrizing the observed absorption.

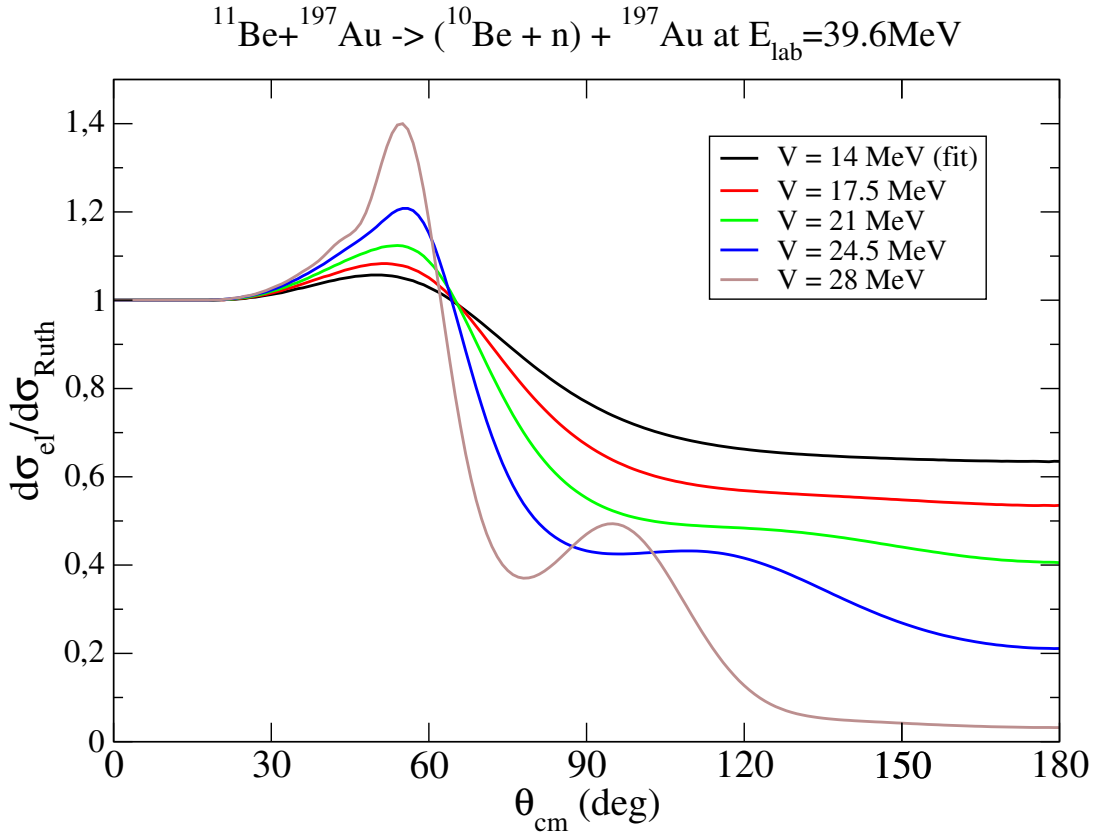


Figure 5.4: Elastic scattering cross section calculated considering only the real part of the potential and different depths V . It can be observed that without an imaginary potential, the nuclear and the Coulomb potential produce a maximum around a certain angle and an interference pattern that is amplified as the depth of the nuclear potential increases.

Another useful information that can be extracted from the OM analysis is the so-called radius of sensitivity. It is well known that the elastic scattering cross section is mostly determined by the value of the optical potential at a certain distance (the radius or distance of sensitivity). This means that it is possible to reproduce the elastic scattering using different potential parameters, provided that they give similar values at this sensitivity radius. In order to obtain this value in the present case, we have performed a series of fits of the elastic data at 39.6 MeV, fixing the value of the difuseness of the imaginary part at a value close to the optimal value ($a_i = 8.7$ fm), and varying the rest of the parameters to minimize the χ^2 with the data. The results are shown in Fig. 5.5 for the imaginary part of the optical potential. It is

clearly seen, that these best-fit potentials cross at a distance of about $r \approx 35-40$ fm. This large value is to be compared with the sum of the radii of the projectile and target, i.e.

$$R_{int} = R_{11Be}^{halo} + R_{197Au} = 7.31 fm + 6.97 fm = 14.28 fm, \quad (5.2)$$

where, for the ^{197}Au we have taken the typical parametrization $R = 1.2 fm \times A^{1/3}$ and for the ^{11}Be we have taken the radius of the valence neutron, to which we expect to be sensitive, calculated from the rms: $R_{11Be} = 7.31 \pm 0.26 fm$ [Tan88]. Even taking this large radius, as shown in figure 5.5, we find the sensitivity radius at much larger distance, at around $r_{sen} \sim 35-40$ fm. Such value justifies the extremely large diffuseness obtained in the fit ($a_i = 8.7 fm$, see figure 5.6) compared, for instance to the one obtained by Kolata for $^{10}\text{Be}+^{208}\text{Pb}$, $a_i = 0.3 fm$ [Kol07]. It is also a clear indication of the importance of the long range couplings in this reaction, that will be studied more in detail within the CDCC formalism.

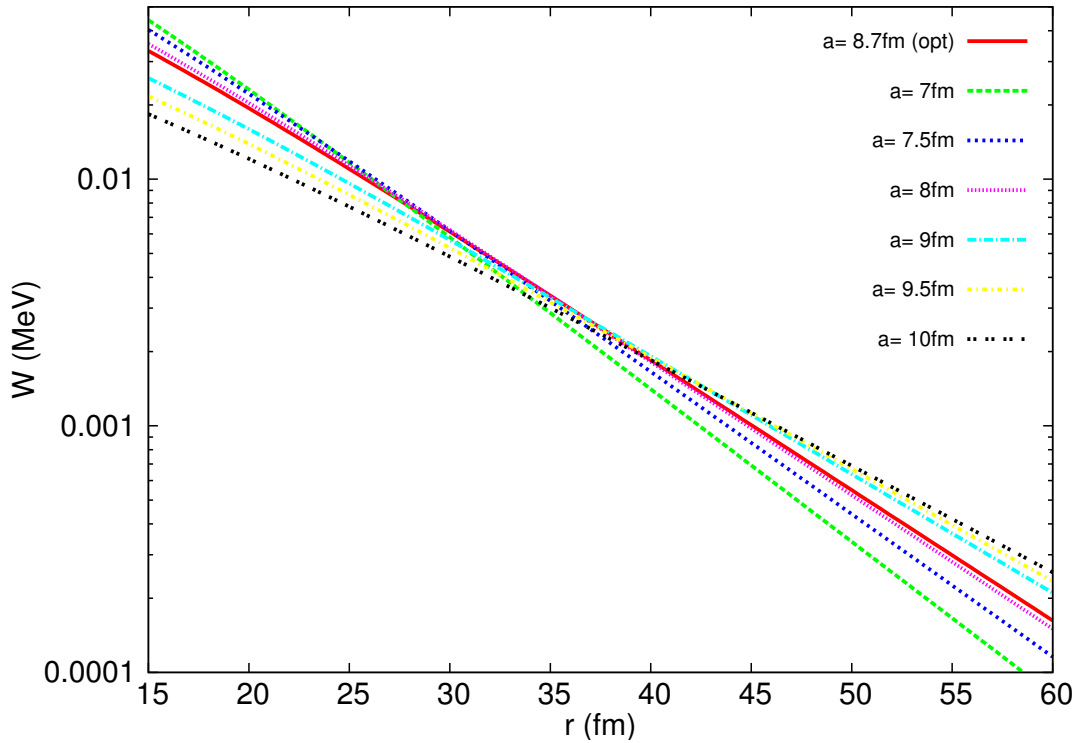


Figure 5.5: Study of the sensitivity radius for the imaginary potential. The study is performed fixing the value for the radius parameter ($r_i = 1.2 fm$) and fitting the imaginary depth for different diffuseness values. We represent the imaginary potential in logarithmic for appreciating better little variations.

The main conclusions that can be extracted from the present optical model analysis are:

- The halo structure of the ^{11}Be is evidenced in the large diffuseness of the potentials necessary to account for the absorption at both energies. It is specially remarkable at energies below the Coulomb barrier, where the typical values of diffuseness ($a \sim 0.65 fm$) translate into no effect of the elastic channel.

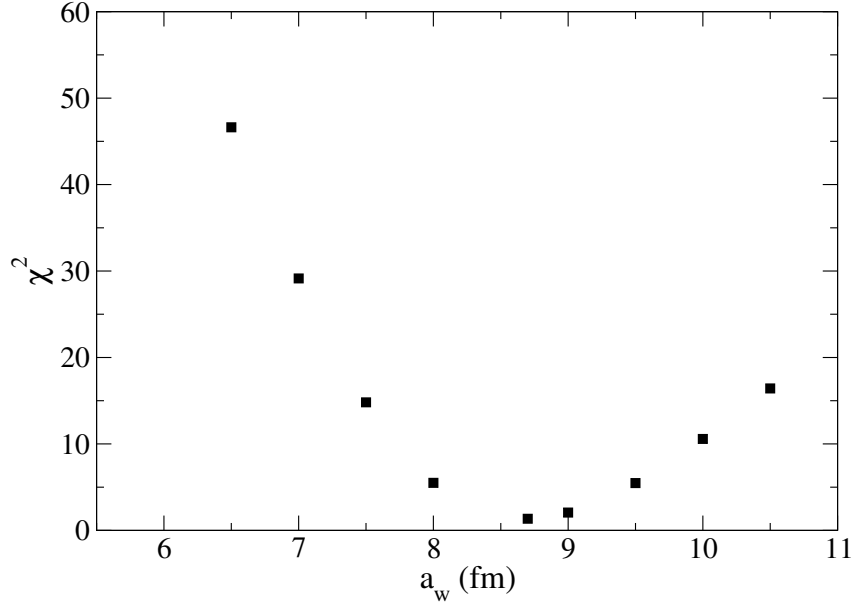


Figure 5.6: Optimization of the imaginary diffuseness a_i . The obtained χ^2 for the different fits shows that the minimum is obtained for abnormally large values for this parameter.

- The couplings to the channels in the continuum are strong, which is evidenced in the absorption in the elastic channel. The deviation from the Rutherford scattering at very forward angles is a first indication of the importance of long range couplings.
- The sensitivity radius is at 35-40 fm, which is a considerably larger value than the sum of the ^{11}Be and ^{197}Au radii. This value is a more solid indication of the importance that long range couplings have in the reaction.
- For obtaining information on the structure, the inelastic scattering and the breakup cross section have to be used. Such an analysis requires a more sophisticated model.

5.2 Analysis within the EPM

Recalling the explanation of the formalism in chapter 2, the Equivalent Photon Method [Ald75, BB88] studies the excitations of the projectile semiclassically. This semiclassical approach considers that the excitation does not influence the trajectory of the projectile, so the excited and not excited ions will follow classical Coulomb trajectories. In such formalisms the excitation is treated perturbatively and, in the EPM model in particular, the excitation is treated to first order. Provided this, the differential cross section of exciting the projectile can be obtained as the probability that a particle detected at a certain angle has been excited in the scattering process. As equation (2.37) stated:

$$\frac{d\sigma_{E\lambda}}{d\Omega} = P(\theta, E\lambda) \frac{d\sigma_{Ruth}}{d\Omega}.$$

In our case, this method is used for calculating the probability of undergoing breakup and excitation to the excited bound state of the ^{11}Be through an dipole Coulomb excitation ($E1$). In previous reactions of halo nuclei on heavy targets at different energies [Fer13, Cub12, Fuk04], it was concluded that the $E1$ transition was the dominant contribution to the breakup. The EPM approach offers a transparent interpretation of the significance of this particular process in our studied reaction. The excitation of the projectile, as mentioned in the introduction, also happens mainly through an $E1$ transition ($1/2^+ \rightarrow 1/2^-$) and has the strongest $\mathcal{B}(E1)$ measured between bound states: $\mathcal{B}(E1; 1/2^+ \rightarrow 1/2^-) = 0.116 \pm 12 e^2 fm^2$.

Considering the excitation as a first order perturbation means considering that excitation happens in one single step. The main reasons for considering that this approach is suitable are two:

- The absence of other excited bound states. If there were other excited states strongly coupled to the ground state or among them, it could be possible that the excitation to this $j^\pi = 1/2^-$ state happened in several steps, populating other states first, specially if these states were at excitation energies $E_x < 320$ keV. This second order processes can still happen populating in the first step a state in the continuum, but they are unlikely.
- There is documented evidence that the breakup of ^{11}Li impinging on ^{208}Pb at energies around the Coulomb barrier can be considered a first order $E1$ transition at forward angles. Considering that in this case there is also a strong coupling and a low excitation energy to the states in the continuum, it can be expected that the dynamics of the excitation process in this case is similar.

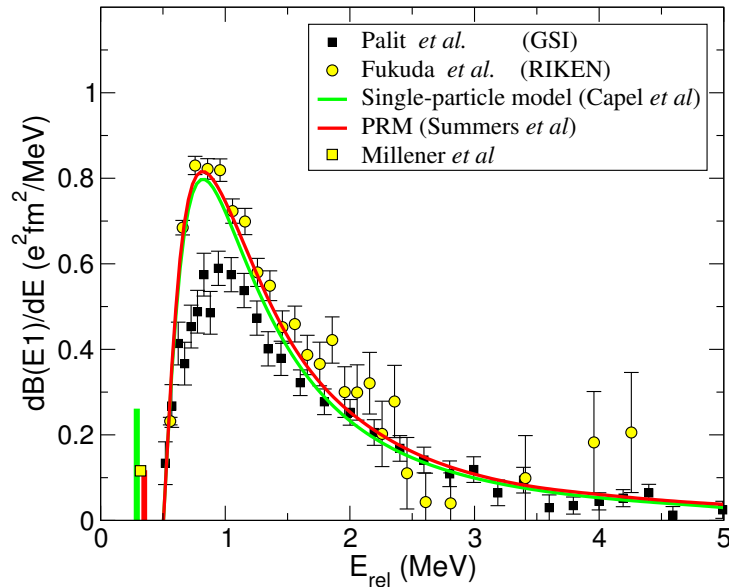


Figure 5.7: $\mathcal{B}(E1)$ distribution of the ^{11}Be obtained in different experiments and within different models. It is observed that the $\mathcal{B}(E1)$ obtained using the Particle-rotor model (PRM) is in good agreement with the experimental $\mathcal{B}(E1)$ to the bound state measured by Millener [Mil83] and the experimental $\mathcal{B}(E1)$ to the continuum measured by Fukuda [Fuk04].

Table 5.2: Parameters for the $^{10}\text{Be}+n$ potential within a particle-rotor model. These parameters were extracted from table 1 in [Sum07]. Among the sets of parameters presented in that table, the third one was chosen because it was the most successful in reproducing the experimental $\mathcal{B}(E1; 1/2^+ \rightarrow 1/2^-)$.

V_{even} (MeV)	V_{odd} (MeV)	V_{so} (MeV)	r (fm)	a (fm)	β_2	$\mathcal{B}(E1)$ ($e^2\text{fm}^2$)
55.04	48.10	5.0	2.483	0.65	0.67	0.116

The ingredients needed for the calculating the breakup and the excitation probability are the excitation energy and the dipolar electric transition probability, $\mathcal{B}(E1)$, of each process. The transition probability to the excited bound state, taken from half-life measurements [Mil83], is $\mathcal{B}(E1; 1/2^+ \rightarrow 1/2^-) = 0.116 e^2\text{fm}^2$. The $\mathcal{B}(E1)$ used for the breakup calculation is calculated using a particle-rotor model, which will be briefly explained in the section referred to the XCDCC calculation, using the parameters presented in table 5.2. The $\mathcal{B}(E1)$ calculated with this PRM model turns out to be very similar to that extracted in [Fuk04] from a Coulomb dissociation experiment of ^{11}Be on ^{208}Pb at 70 MeV/u, as can be seen in Fig. 5.7. Also included in this figure is the $\mathcal{B}(E1)$ distribution obtained in a similar experiment performed at GSI by Palit et al [Pal03]. It is seen that the latter is significantly smaller and, therefore, the present analysis can help to assess these two distributions.

Experimentally, this probability can be measured considering the gamma rays detected in coincidence with the ^{11}Be at different scattering angles θ , correcting by the TIGRESS efficiency, and dividing by the total number of fragments detected at that angle. This actually means that, in this stage, the same assumption than when optimizing the detectors position is made, i.e., it is considered that the total number of counts, corresponding to the sum of the elastic, inelastic and breakup channels, follows a Rutherford scattering cross section. The experimental and calculated probabilities of exciting the projectile are compared in figure 5.8, showing the angular distribution at both measured energies. It is observed that, at forward angles, the calculation reproduces the data within the error bars. The conclusion that can be extracted is that the excitation to the bound state in ^{11}Be can be understood as a first order process in this angular range, which is up to $\sim 50^\circ$ at energies around the barrier, and up to $\sim 70^\circ$ at energies below the barrier. At larger angles the calculation overestimates the probability. Although with this calculation it is not possible to disentangle the origin of this disagreement, some qualitative interpretation can be done, based on the limitations of this approach. Firstly, large scattering angles correspond to trajectories with small impact parameter. In those trajectories, it is more doubtful that the interaction is dominated by the Coulomb interaction and that nuclear potential has no influence in the trajectory, which are premises of the Alder and Winther semiclassical formalism. Furthermore, in this first order calculation the closeness of the continuum is not taken into account in any way. The larger the scattering angle, the deeper in the target that the projectile will penetrate and the more probable it is a second order process, that could redistribute some of the feeding to other reaction channels (graphically depicted in figure 5.9).

Figure 5.10 shows the experimental breakup probability compared to the breakup probability obtained with an EPM calculation. Compared to our data, the breakup probability is clearly underestimated by the calculation in all the angular range for the case at energies below

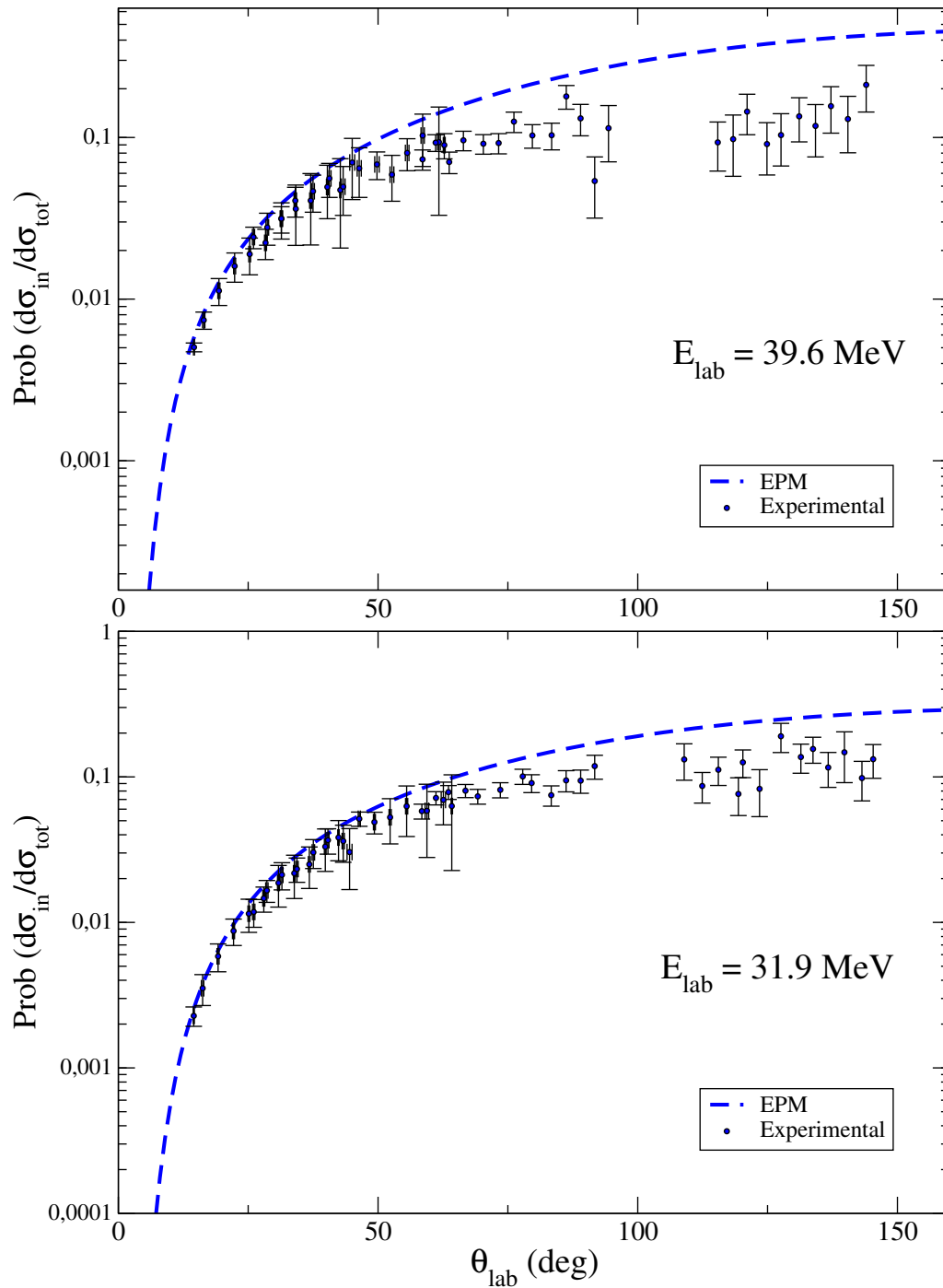


Figure 5.8: Experimental inelastic scattering probability data compared with a first order EPM calculation. For the calculation the experimental accepted value $\mathcal{B}(E1; 1/2^+ \rightarrow 1/2^-) = 0.116 e^2 \text{ fm}^2$ was used. See the text for details.

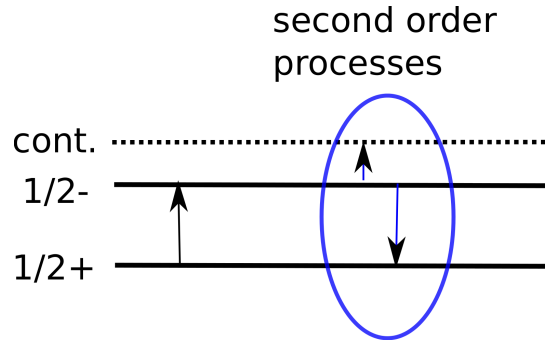


Figure 5.9: Graphical representation of possible second order processes which can be important at large scattering angles and are not considered in these calculations.

the barrier and at forward angles (where this approach was expected to be more justified) for the case around the Coulomb barrier. This is an indication of one of the two possibilities:

- The $\mathcal{B}(E1)$ to the continuum used for the calculations is not correct.
- The assumption that the direct Coulomb breakup dominates is not correct.

In the case of ^{11}Li , the same kind of underestimation was observed if the calculations were performed with the $\mathcal{B}(E1)$ obtained from high energy experiments at RIKEN [Nak06]. The $\mathcal{B}(E1)$ obtained with the experiment at energies around the Coulomb barrier [Fer13, Cub12], obtained from a three-body model which reproduced the breakup probability data when used in a four-body CDCC calculation, was considerably larger than that reported from a Coulomb dissociation experiment at intermediate energies. Moreover, to produce this large $\mathcal{B}(E1)$ close to the threshold, the dipole resonance predicted by this three-body model had to be placed near the breakup threshold ($E_x = 0.69$ MeV). Since the 2-body structure of ^{11}Be is more simple than the 3-body one of ^{11}Li , this work can motivate a reopening of that discussion. Nevertheless, I prefer to postpone this discussion to the conclusions chapter, where the results will already have been discussed within all the formalisms included in this text.

The main conclusions on the reaction that can be extracted within the Equivalent Photon Method are:

- The inelastic scattering at forward angles is a first order process, where Coulomb excitation clearly dominates.
- In the rest of the angular range the calculation overestimates the data, since in this case nuclear effects and higher order processes, which are not included in the EPM, are more probable.
- The breakup cannot be explained within the formalism, either because the nuclear breakup is also important or because the breakup is not a first order process.

5.3 Analysis within a CDCC formalism

The Continuum-Discretized Coupled-Channels formalism [Aus87] offers a full quantum description of the $^{11}\text{Be}+^{197}\text{Au}$ reaction, starting from a two-body structure model for the halo-nucleus. In the performed CDCC calculations, the ^{11}Be is described as an inert ^{10}Be core and

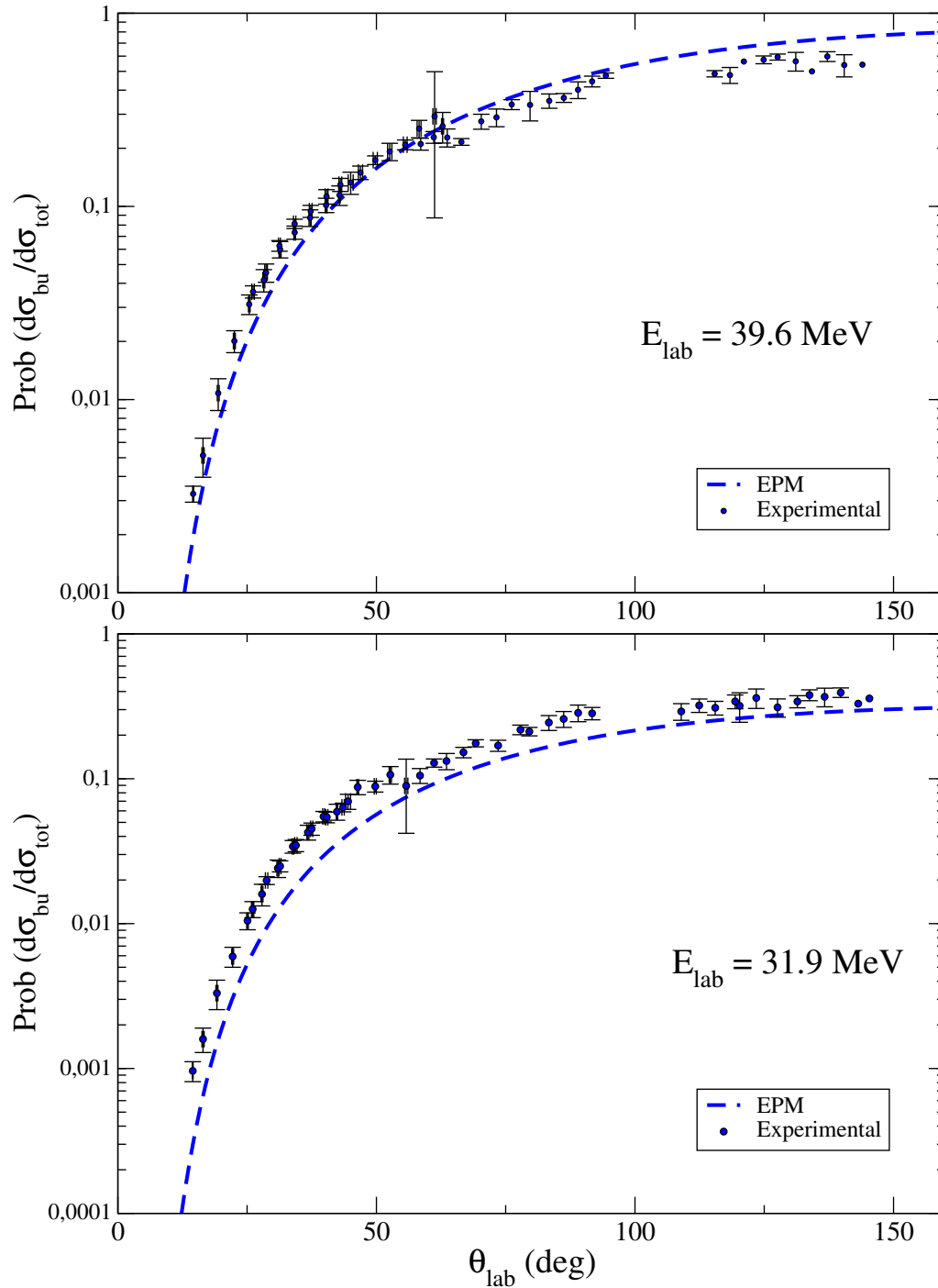


Figure 5.10: Experimental breakup probability data compared with a first order EPM calculation. The $\mathcal{B}(E1)$ used for the calculation is the one obtained with the parameters presented in table 5.2.

a valence neutron, interacting between them via a central plus spin-orbit potentials, as introduced in section 2.4.2. The states in the continuum are constructed following the binning method. Each of these states is defined by the orbital angular momentum (ℓ) and the total angular momentum ($j = \ell \pm 1/2$) of the neutron with respect to the core, and by the minimum and maximum relative linear momentum k included in the bin (talking about relative linear momentum is analogous to talk about the excitation energy (ε) in the internal Hamiltonian of the ^{11}Be . For the comparison with the experimental data, the breakup cross section will be obtained as the summation of the cross section to all the included channels in the continuum.

The internal states of the ^{11}Be included in the calculation were the two bound states (ground state with $S_n = 0.502$ MeV, $s = 1/2, \ell = 0, j = 1/2$ and excited bound state at $S_n = 182$ keV, $s = 1/2, \ell = 1, j = 1/2$) and the states in the continuum of the $^{10}\text{Be}+n$ up to $\ell_{max} = 10$ and $\varepsilon_{max} = 10$ MeV.

Once the states included in the model space are defined, the only ingredients necessary for a CDCC calculation are the interaction potentials. Three potentials have to be introduced into the calculation in this 3-body model: A $^{10}\text{Be}-n$ potential, a $^{10}\text{Be}-^{197}\text{Au}$ potential and a $n-^{197}\text{Au}$ potential. The parameters of the potentials used are given in table 5.3 and discussed below.

Table 5.3: Parameters of the potentials used in the CDCC calculation. See the text for details.

	$n + ^{197}\text{Au}$		$^{10}\text{Be} + ^{197}\text{Au}$	
	V	46.56	V (MeV)	113
	r_V	1.237	r_v (fm)	1.063
	a_V	0.652	a_v (fm)	0.63
	W	0.21	W (MeV)	169
	r_W	1.237	r_w (fm)	1.196
	a_W	0.652	a_w (fm)	0.30
	r_c	0.0		
	W_d	3.95		
	r_{Wd}	1.257		
	a_{wd}	0.508		
$^{10}\text{Be} + n$				
$V_{\ell \text{ even}}$ (MeV)	62.52			
$V_{\ell \text{ odd}}$ (MeV)	39.74			
r_0 (fm)	2.585			
a (fm)	0.6			

^{10}Be -neutron potential

The potential for the $^{10}\text{Be}-n$ system is used in the CDCC method for calculate the bound and unbound states of the projectile. The potential used in our calculations was extracted from the work of P. Capel and collaborators [Cap04a], where they adjusted a potential able to reproduce the three major low-lying states in ^{11}Be , the two bound states plus a $j^\pi = 5/2^+$ resonance at 1.278 ± 18 MeV above the separation energy. Different potentials were chosen for ℓ even and for ℓ odd in order to model the parity inversion explained in chapter one. With the used parameters, the energies of the three states are well reproduced. The only feature not well reproduced is the width of the resonance, which is overestimated by the calculation by a 60%

compared to the accepted experimental value: $\Gamma_{exp} = 100 \pm 20$ keV, $\Gamma_{th} = 160$ keV. They use this potential for performing a time-dependent analysis of the $^{11}\text{Be} + ^{12}\text{C}$ reaction measured at RIKEN at 67 MeV/u [Fuk04]. In this reaction on a light target, the nuclear effects are dominant and two low-energy resonances in the $^{10}\text{Be} + n$ continuum were clearly measured. The calculation showed a good agreement with the breakup differential cross section up to relative energies of around 2.5 MeV (just below the second resonance, not included in the model).

The $d\mathcal{B}(E1)/dE$ calculated with this model is shown in Fig. 5.7 (green line). It is found to describe very well the "experimental" $d\mathcal{B}(E1)/dE$ distribution extracted from the Coulomb dissociation data by Fukuda et al [Fuk04]. On the other hand, the $\mathcal{B}(E1)$ for the bound excited state is overestimated by a factor of more than 2,

$$\mathcal{B}(E1; 1/2^+ \rightarrow 1/2^-)_{exp} = 0.116 \text{ e}^2\text{fm}^2; \quad \mathcal{B}(E1; 1/2^+ \rightarrow 1/2^-)_{th} = 0.26 \text{ e}^2\text{fm}^2.$$

¹⁹⁷Au-n potential

For this potential we used the global parametrization of *Koning-Delaroche* [Kon03] evaluated at the energy per nucleon of the present experiment, namely, $E_n = 2.9$ MeV and 3.6 MeV for the two energies of the experiment. The subindex d in some parameters in table 5.3 stands for the imaginary surface (i.e. Woods-Saxon derivative) term. The spin-orbit term is ignored in this case.

¹⁰Be-¹⁹⁷Au potential

There are no experimental data for ^{10}Be scattering on a ^{197}Au target, so no direct information of the interacting potential is available for this system. Since this is a necessary input for our calculation, it has to be estimated somehow. The most similar experiment with available data and published information on the potentials was performed by J.J. Kolata and collaborators [Kol07], so the potential is extracted from that article. In that work, a systematic study of the scattering of ^{10}Be on a ^{208}Pb target at energies around the Coulomb barrier was performed, covering the energy range from $E_{cm} = 38.4$ MeV ($E_{lab} = 4.02$ MeV/u) to $E_{cm} = 43.9$ MeV ($E_{lab} = 4.60$ MeV/u). Some tests were performed, increasing and reducing the depth of the real and imaginary potentials by a 20%, showing that our sensitivity to the nuclear part of the potential is minimal, and that the Coulomb interaction will dominate, even at backward scattering angles.

Results and interpretation

Breakup results will be the first to be commented, since they are the strong point of the CDCC calculation in this case. For consistency, although the `fresco` output are the cross sections, in this section we will continue presenting the data in terms of probabilities. The probabilities are presented in the laboratory frame, so the procedure followed was:

1. Changing the frame of the obtained elastic and inelastic scattering differential cross section from CM to Lab.
2. For each continuum bin, transforming the angular differential cross section from the CM to the LAB frame. In this transformation, the Q-value was estimated from the nominal

energy of the bin. The differential cross section to all the bins was added for obtaining the breakup differential cross section.

3. Summing the differential cross sections of the three processes for obtaining a total differential cross section.

$$\frac{d\sigma_{el}}{d\Omega}(\theta) + \frac{d\sigma_{inel}}{d\Omega}(\theta) + \frac{d\sigma_{bu}}{d\Omega}(\theta) = \frac{d\sigma_{tot}}{d\Omega}(\theta). \quad (5.3)$$

4. Calculating the probabilities as the ratio of each channel to the total. For instance,

$$P_{bu}(\theta) = \frac{d\sigma_{bu}(\theta)}{d\sigma_{tot}(\theta)}. \quad (5.4)$$

In figure 5.11, it is observed that this CDCC calculation succeeds in explaining the breakup data at energies below the Coulomb barrier in all the angular range if the ℓ_{max} included in the calculation is large enough. The large number of partial waves necessary for convergence of the calculation ($\ell_{max} = 10$) is a clear indication of the size of the model space that can be populated in this reaction. The calculations above the barrier do not succeed in matching the data at angles above 75° .

The data that cannot be explained by this calculation correspond to the high-energy case among the two we are treating and large scattering angles, which, in turn, is the case in which the projectile penetrates most into the target. In this case, other processes, such as non-elastic breakup or neutron transfer, are more likely to occur, but those channels cannot be described within the CDCC framework. A transfer approach, which will be presented afterwards, is expected to be more suitable for this case.

Focusing on the strong points, these are calculations at all orders performed using potentials from other reactions at other energies. The $d\mathcal{B}(E1)/dE$ to the continuum obtained is compatible with the one obtained from the Coulomb dissociation experiment by Fukuda et al. [Fuk04]. Unlike in the case of ^{11}Li , it is not necessary to increase the $d\mathcal{B}(E1)/dE$ at low relative energies to explain our data. The two body structure of the ^{11}Be is more easily manageable from a theoretical point of view, and the model space that can be included in the calculations is larger, compared to the 4-body calculations performed for the $^{11}\text{Li}+^{208}\text{Pb}$ reaction. It is an open issue under study, but considering the analogies of the reactions, it is possible that if the model space could be enlarged for the calculations of $^{11}\text{Li}+^{208}\text{Pb}$ at low energies the coupling among states would result in a higher breakup cross section, like it happened in our case.

As has been mentioned, the $\mathcal{B}(E1)$ for the transition to the bound excited state obtained with this model, is clearly overestimated. This is mainly a consequence of the fact that we are considering a single-particle model of ^{11}Be , with an inert ^{10}Be core. We have not been able to reproduce both $\mathcal{B}(E1)$, to the continuum and to the bound state, within this frozen-core description. For this reason, the overestimation observed in figure 5.12 is somehow expected.

An interesting work performed by K. Rusek [Rus09a, Rus09b] tried to reduce the radius of the ^{11}Be system in the 2-body structure model until the $\mathcal{B}(E1; g.s. \rightarrow 1/2^-)$ to the bound state agreed with the experimental data. The result was a parallel reduction of the $\mathcal{B}(E1)$ to the

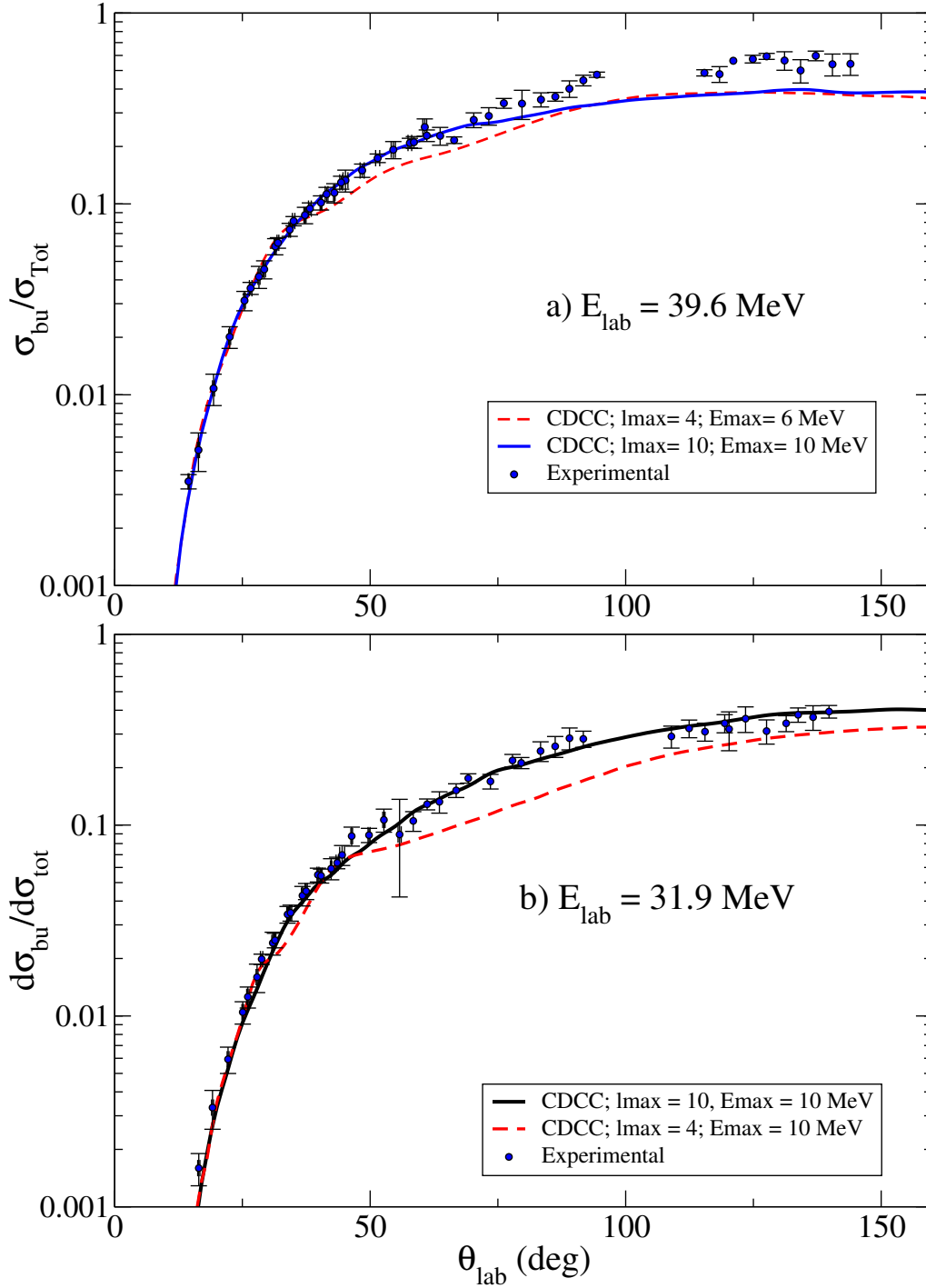


Figure 5.11: Experimental breakup probability data at energies around (a) and below (b) the barrier compared with CDCC calculations with valence-core partial waves up to $\ell_{\text{max}} = 4$ and relative energy up to $E_{\text{max}} = 10 \text{ MeV}$. The red dashed line shows a CDCC calculation including a smaller model space, with valence-core partial waves up to $\ell_{\text{max}} = 4$. See the text for details.

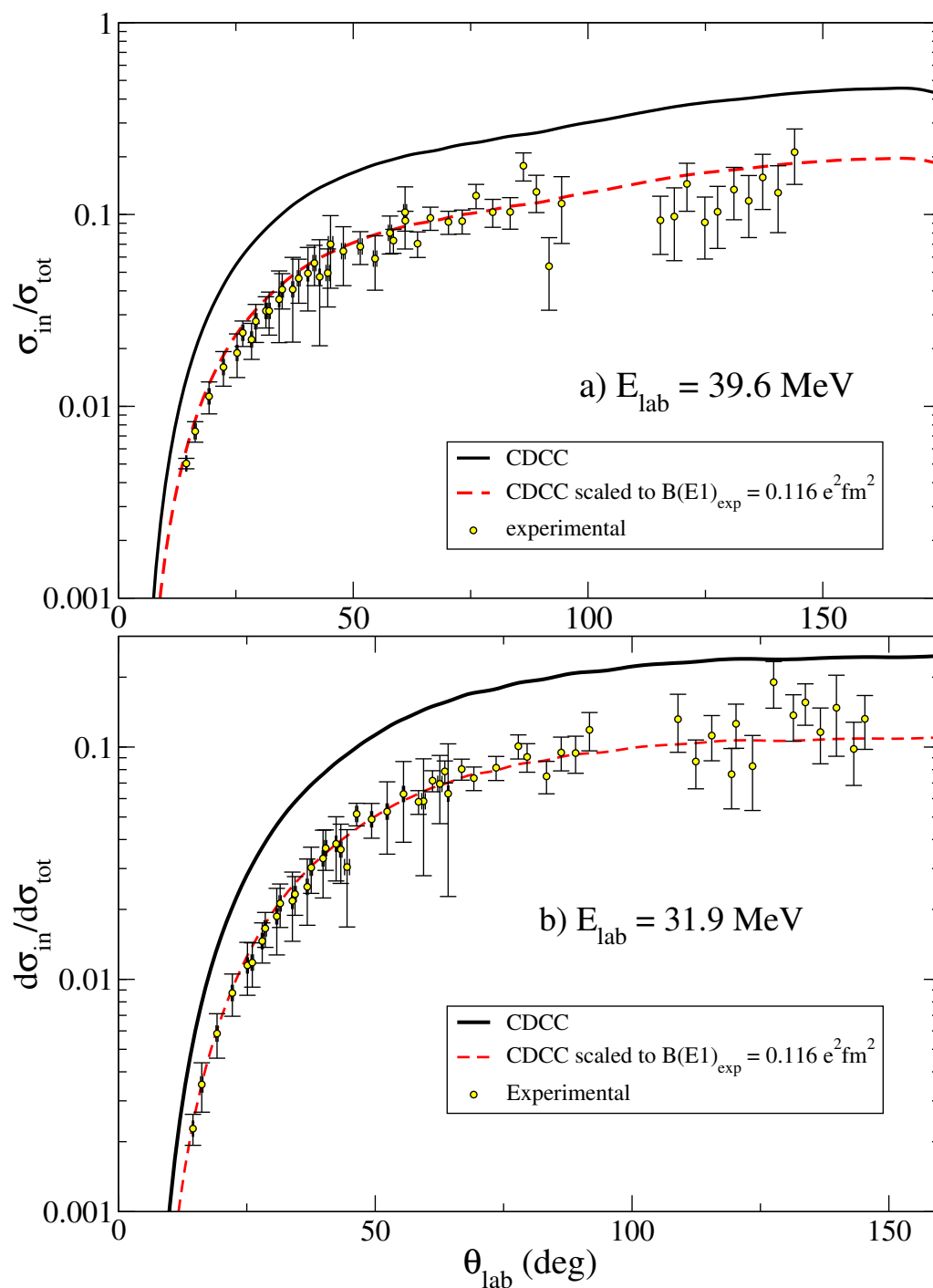


Figure 5.12: Experimental inelastic scattering probability data compared with CDCC calculations at energies around (a) and below the barrier. See the text for details.

continuum that underestimates the $\mathcal{B}(E1)$ distribution of Fukuda et al., translating the problem from one observable to the other one. In our case, we kept the structure model and scaled *manually* the inelastic scattering cross section obtained with the CDCC to the experimental $\mathcal{B}(E1)$:

$$C = \frac{\mathcal{B}(E1)_{exp}}{\mathcal{B}(E1)_{cap}} = 0.446; \quad \hat{P}_{inel}(\theta) = CP_{inel}(\theta). \quad (5.5)$$

The scaled probability values match the experimental data at both energies.

The elastic scattering cross section is presented in figure 5.13. It is the last channel to be treated in this section because it was thought that the previous study of the breakup and inelastic channel would help in the comprehension of these results. The first thing that is clearly evidenced is that the calculation underestimates the data. Nevertheless, if one considers that the total cross section, at least at forward angles, is expected to be similar to Rutherford cross section, that the breakup is well explained, and the inelastic overestimated, it is not that surprising that the elastic cross section is underestimated. Actually, the dashed line corresponds to adding the overestimation in the inelastic channel to the elastic cross section. Taking C from eq. (5.5),

$$\hat{P}_{el}(\theta) = P_{el}(\theta) + (1 - C)P_{inel}(\theta). \quad (5.6)$$

The success of this correction in explaining the data offers an interesting interpretation of the results. The strong coupling between the two bound states translates into a redistribution of the cross section between them without influencing the breakup channel. Another proof in this sense is shown in figure 5.14, in which we compare the experimental and calculated quasielastic cross sections, defined as the sum of the elastic and inelastic cross sections (see chapter 4). There the concept of *quasielastic* introduced in The ideas previously discussed for the inelastic and the elastic channels are reinforced in this figure, where no correction is needed for explaining the sum of both contributions.

Details of the calculation

The case of the reaction of a halo nucleus on a heavy target at energies around the Coulomb barrier is particularly delicate to tackle from a numerical point of view. The strong Coulomb interaction of the target is felt by the projectile at very large distances, so the partial wave expansion of the incident plane wave has to include an unusually large amount of terms. Classically, this can be understood as the need of including trajectories with large impact parameters. In this case, the expansion was made up to $J = 1200$.

Likewise, states of the ^{11}Be with large j can be populated, so many states have to be included in the model space. In particular, depending on the *binning* used, the number of states oscillated between 120 and 260.

In order to ensure that the calculated observables are meaningful, one has to verify that the calculation is converged with respect to the size of the model space. This means that the results should be stable with respect to:

- i) increasing the maximum excitation energy,
- ii) decreasing the bin size and

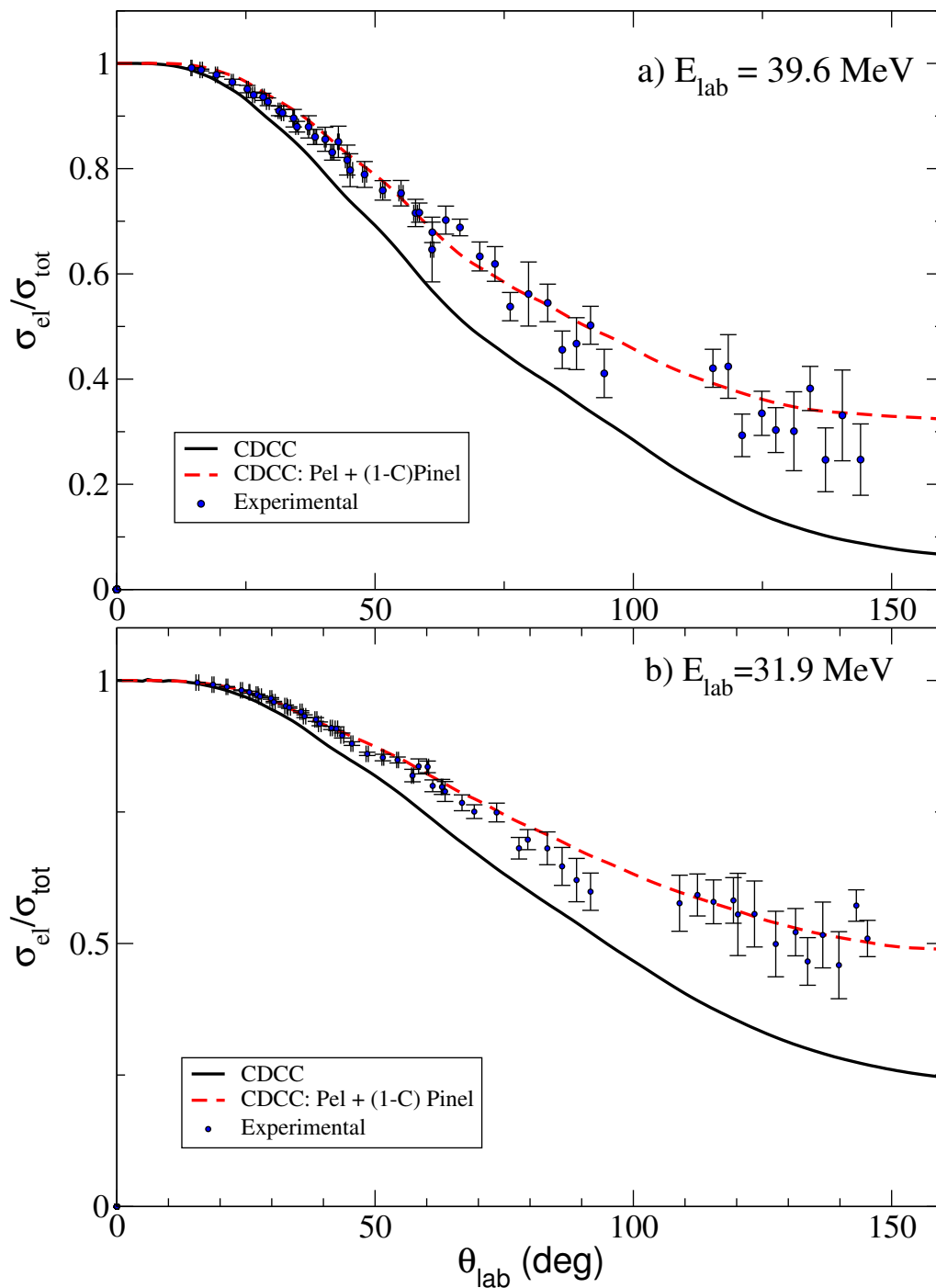


Figure 5.13: Experimental elastic scattering probability data compared with CDCC calculations at energies around (a) and below the barrier. See the text for details.

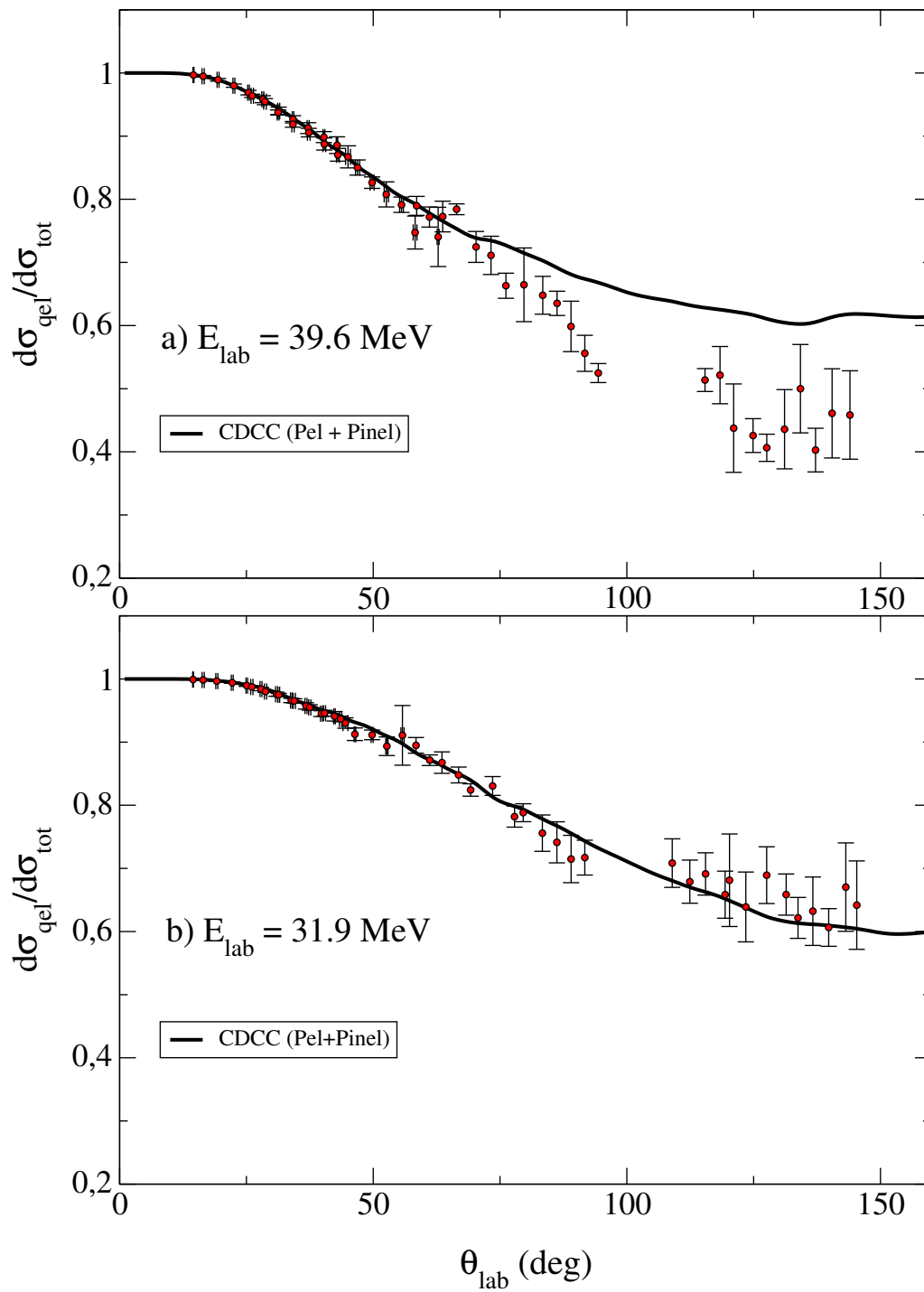


Figure 5.14: Experimental quasielastic scattering probability data compared with CDCC calculations at energies around (a) and below the barrier. It is called quasielastic the sum of elastic and inelastic channels. See the text for details.

iii) increasing the number of angular momenta for the valence-core relative motion.

In practice, the procedure of getting stable and converged results is not absent of numerical difficulties, particularly in reactions involving heavy targets at energies around the Coulomb barrier, as it is in our case. Some of these difficulties are:

- When decreasing the bin size, the number of bins increases, and so does the number of coupled equations. This makes the calculation not only more lengthy, but also more unstable from the numerical point of view.
- Furthermore, decreasing the bin size will soften the destructive interference, making the bins of longer range. This, in turn, gives rise to long-range coupling potentials, which are more difficult to handle numerically.
- Practical implementations of the coupled-channels calculate N independent solutions of the coupled-equations (this is done, for example, integrating N times with different initial conditions). Then, the physical solutions are constructed by equating a linear combination of the computed solutions to the physical boundary conditions (i.e., an incident wave in the elastic channels, and outgoing waves in all channels). This results in a system of ordinary algebraic equations. If numerical inaccuracies occur during the integration, the linear dependence among the solutions is lost, and the solution of this system of equations become ill-conditioned (see Ref.[Tol86]). This occurs, for example, if integration needs to be done inside the classically forbidden region. This happens for larger values of the total angular momentum because the large centrifugal barrier tends to move the classical turning point to very large distances. It also occurs at energies around and below the barrier, because the Coulomb barrier itself will also give rise to distant turning points. Moreover, the heavier the colliding nuclei, the bigger the Coulomb barrier will be, thus enhancing this effect.

All these situations take place in our reaction, so it was necessary to make use of a stabilization procedure, similar to that proposed in Refs. [Bay82a, Bay82b]. The stabilization algorithm was recently implemented into the `fresco` code by the group of Sevilla. This improvement allowed for the inclusion of waves up to $\ell = 10$ in the continuum and energies for the neutron with respect to the target of up to 10 MeV. Formerly, the code was not able to deal with more than six partial waves in the continuum and up to relative energies of around 5-6 MeV.

The conclusions that can be highlighted from the study of the reaction using a CDCC method and two-inert-body model for the ^{11}Be are:

- It is necessary to include a very large model space (up to $\ell = 10$ and $E = 10$ MeV) and include a large amount of terms of the partial wave expansion (up to $J = 1200$) for obtaining convergence in the calculations.
- The calculation at all orders is necessary even at forward scattering angles for explaining the breakup cross section.
- The calculation reproduces the breakup data below the barrier in all the angular range. Above the barrier, for large scattering angles, the calculation underestimates the data.

- The population of the inelastic channel is overestimated as a consequence of the $\mathcal{B}(E1; 1/2^+ \rightarrow 1/2^-)$ of the model overestimating the experimental one.
- A two-inert-body model is not able to explain all the observables simultaneously. It is able to explain the breakup and the quasielastic, which is the sum of the elastic and the inelastic channels.

5.4 Analysis within the TC formalism

The transfer to the continuum (TC) can be understood as a formalism analog to the CDCC in which the states are defined with respect to the target. At least for non-resonant breakup, there is no physical difference between the unbound states *of the target* and the unbound states *of the projectile*, so these two descriptions would be analogous if the model space of both representations were large enough¹. However, there are some reasons that make the different approaches more suitable for different situations.

First, the computational constraints do not allow for all the continuum to be included in the model space. The states will be truncated with respect to n - ^{10}Be energy in the case of CDCC and with respect to the n - ^{197}Au energy in the case of TC. Moreover, during the reaction, both bound and unbound states of the target can be populated. The bound states of the $n+^{197}\text{Au}$ system are also included in the TC calculation so, in general, a transfer approach is more suitable for the cases in which the neutron penetrates more into the target potential and may end in a state with lower relative energy with respect to the target than with respect to the core.

Another situation that is represented by TC and not by CDCC is the inelastic breakup. We call inelastic breakup to those channels in which the projectile is broken up, but the unobserved particle (the neutron in our case) scatters non-elastically with the target. This comprises, for example, target excitation or neutron absorption (incomplete fusion). These processes are out of the model space in CDCC, although they are effectively included as part of the absorption of the fragment-target potential. TC does not include those state explicitly either, because it also considers the valence particle, the core and the target to be inert. However, as long as the basis used to describe the fragment-target states is complete (for example, the bound and unbound solutions in some mean-field potential) one may argue that the sum over these states should provide results close to those obtained if the sum were done over the true physical states. In this sense, it is expected that the TC approach accounts approximately for the total breakup (i.e. elastic and non-elastic breakup). This has been formally justified by Austern and Vincent [AV87].

Doorway states

In the calculations of transfer to heavy targets, the description of the bound states of the target+valence ($^{197}\text{Au}+n = ^{198}\text{Au}$) system are often complicated. There are excited states due to vibrational modes, rotational modes, and shell model configurations involving several protons and neutrons and spin-orbit splittings. Not only, but particularly at large excitation

¹assuming that the breakup process is not dominated by two-body resonances of the projectile or target, in which case, the representation containing this resonance would be in principle more appropriate

energy their density is high and their spins, parities and spectroscopic factors are often difficult to assign.

Instead of including all the physical states, a set of states called *doorway states* can be used for modeling them. Starting from a mean field (e.g. a Hartree-Fock) calculation, the single-particle spectra for the valence particle (either a neutron or a proton) is obtained. Hartree-Fock calculations provide the single-particle energies and the wavefunctions of the proton and the neutron states. If the states are filled up to the Fermi level taking into account the Pauli exclusion principle, the occupation number and the bound excited single-particle levels are obtained.

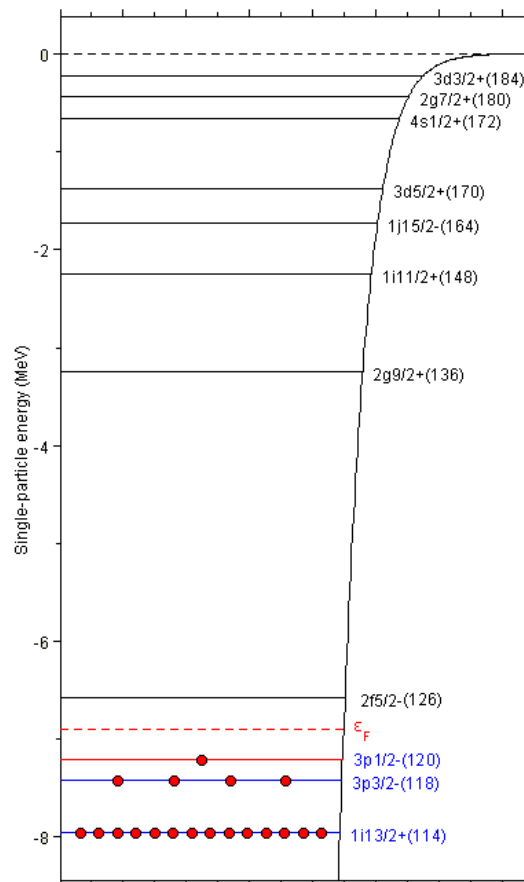


Figure 5.15: Neutron single-particle states of ^{198}Au obtained with a mean-field calculation.

In our case, we will only focus on the neutron single-particle states, considering that the protons do not play any role. These neutron single-particle states, shown in figure 5.15 are not the physical states of the system, but the latter can be understood as the result of the fragmentation of these single-particle levels due to their coupling with the residual interactions not considered in the mean-field approach. The single-particle strength associated to each mean-field orbital will be then distributed among several physical states, according to some spectroscopic factors. The main advantage of using these states instead of the physical ones is that we are using a complete basis, which avoids running the risk of leaving states out of the

description of the $^{197}\text{Au}+n$ system. Ignoring the spreading in energy of the fragmented levels, one may expect that the sum of the cross sections over the doorway states is similar to the sum over the physical states.

$^{11}\text{Be}+^{197}\text{Au}$ potential

For this calculation, in addition to all the potentials used for the CDCC calculation ($^{10}\text{Be}-n$, $^{10}\text{Be}-^{197}\text{Au}$, $n-^{197}\text{Au}$), it is necessary to include the optical potential for the $^{11}\text{Be}+^{197}\text{Au}$ system in the incident channel. We took the potential extracted in section 5.1 from the fit of the present elastic data.

$^{10}\text{Be}+n$ potential

In this case the ^{11}Be system is also described using the model proposed by P. Capel et al. [Cap04a], since the $\mathcal{B}(E1)$ given by this model, as was seen in the previous section, reproduces the experimental values from a dissociation experiment [Fuk04], using a spectroscopic factor of $S = 1$.

Results and interpretation

In this section only the breakup cross section will be discussed, where it may be suitable to remind to the reader that we are using an inclusive approach to the so-called *breakup*, so we are generically referring to all the situations in which the detected fragment is a ^{10}Be . The elastic cross section will be discussed because it is obtained directly with the already discussed OM calculation, and the inelastic scattering channel is not included in the calculation.

The TC calculation shows convergence problems similar to those found in the CDCC calculations. A stabilization procedure similar to the one used in the CDCC case might help to improve the stability of the calculations. However, the stabilization procedure has not yet been implemented in *fresco* for transfer calculations. For this reason, the ℓ_{max} and the E_{max} in this calculation are considerably smaller than in the CDCC case, and so is the number of states included in the model space. In spite of the convergence problems, it is observed that the calculation is able to explain the breakup cross section at energies close to the Coulomb barrier and large scattering angles, where the CDCC approach was not successful.

The main conclusions that can be extracted from the transfer calculation are:

- Although it was not possible to perform a converged TC calculation, the obtained transfer cross section succeeded in explaining the data around the Coulomb barrier at large scattering angles.
- It can be interpreted that, around the Coulomb barrier, and for trajectories with small impact parameter, the neutron populates states of low relative energy and orbital angular momentum with respect to the ^{197}Au .

5.5 Analysis within an XCDCC formalism

As explained in more detail below, one of the limitations of the CDCC calculations presented in the previous section is the fact that this model ignores the effect of the excitation of

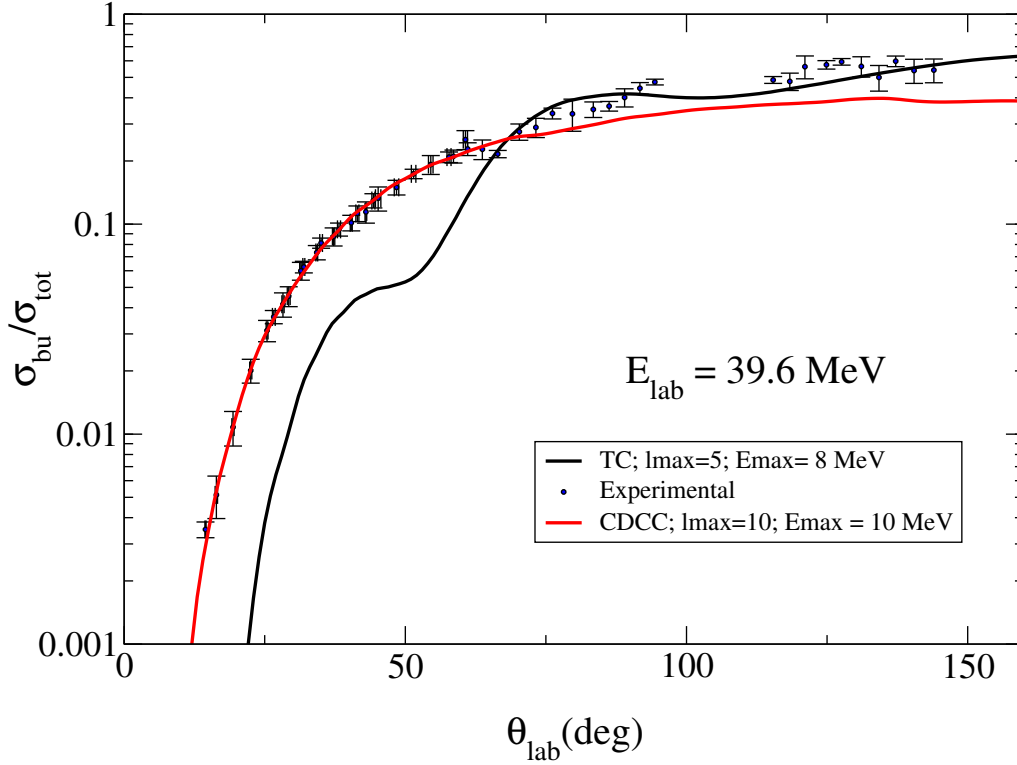


Figure 5.16: Experimental breakup probability data compared with TC calculations at energies around the Coulomb barrier. It is observed, as expected from the results of the CDCC calculation, that the data at high energies and large scattering angles, which is the case in which the neutron of the halo penetrates most into the target, are well described by this approach. See the text for details.

the ^{10}Be . A pure single-particle description of the ^{11}Be as $^{10}\text{Be}+n$ has been proved to be very useful, and succeeds in explaining our experimental data to a large extent. However, there are experimental and theoretical evidences which emphasize the importance of these core-excited components in the states of ^{11}Be . Recently, the CDCC method has been extended to accommodate these effects in the formalism [Sum06, dDALA14]. The XCDCC formalism is a step forward in the CDCC approach in which, in addition to the neutron-core degree of freedom, also some internal (typically collective) degrees of freedom of the core are included. As a matter of fact, these developments have been partially motivated the present data, since we are providing simultaneous data on the three main reaction channels and none of the formalisms presented so far is able to explain all of them satisfactorily.

In this case, the reaction is particularly sensitive to the description of the loosely bound ^{11}Be nucleus, so a more accurate representation of this nucleus is introduced in this step. As was presented in the introduction, there are several works [For99, Sch12, Win01, Zwi79] that prove a non-negligible contribution of the neutron in a d orbit, which has to be coupled to a 2^+ excited state of the ^{10}Be core, in the ground state wavefunction of ^{11}Be . Likewise, in [Sch12] a mixing was also observed in the bound excited state wavefunction, where contributions of the neutron in configurations other than $p_{1/2}$ proved to be relevant. Taking into account these observations, one can consider a more sophisticated description of the projectile, without abandoning the two-body description of ^{11}Be as $^{10}\text{Be}+n$, but adding an extra degree of freedom to

Table 5.4: Parameters for the $^{10}\text{Be}+n$ potential within a particle-rotor model. These parameters were extracted from table 1 in [Sum07]. Among the sets of parameters presented in that table, the third one was chosen because it was the most successful in matching the $\mathcal{B}(E1; 1/2^+ \rightarrow 1/2^-)$.

V_{even} (MeV)	V_{odd} (MeV)	V_{so} (MeV)	r (fm)	a (fm)	β_2	$\mathcal{B}(E1)$
55.04	48.10	5.0	2.483	0.65	0.67	0.116

the core, which allows it to populate the excited 2^+ state.

In this case, this was done considering a particle-rotor model. The main feature of this model is a deformed ^{10}Be core, which is allowed to rotate, and which attracts the neutron with a potential that depends not only on the distance, but also on the position of the neutron with respect to the deformation axis, as schematically shown in figure 5.17.

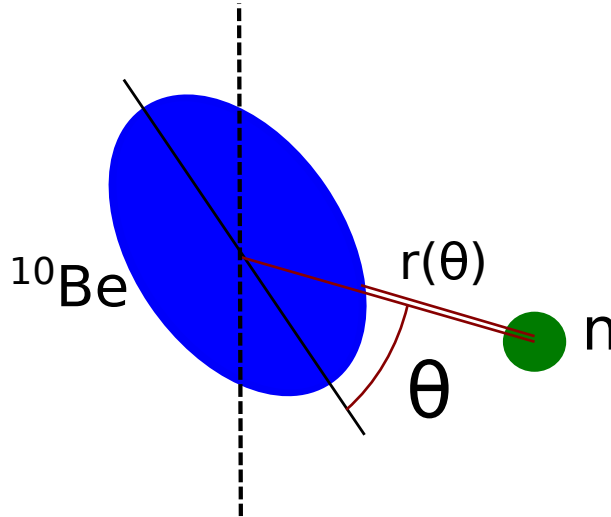


Figure 5.17: Scheme of the coordinates in the particle-rotor model.

The ^{10}Be nucleus has a quadrupolar deformation corresponding to a prolate nucleus, with a surface that can be parametrized as

$$R(\theta, \phi) = R_c(1 + \beta_2 Y_{20}(\theta, \phi)), \quad (5.7)$$

where R_c is the average radius and β_2 the deformation parameter corresponding to a quadrupolar deformation. The only internal degree of freedom of ^{10}Be that will be considered is a rotation. The other degree of freedom will arise from the orientation of the neutron with respect to the deformation axis, that defines the distance from the ^{10}Be surface to the neutron. With that parametrization,

$$V = V(r(\theta)) = V(r_n - R_c[1 + \beta_2 Y_{l0}(\theta, 0)]) \quad (5.8)$$

The parameters in table 5.4, where used for the potentials in the internal Hamiltonian of ^{11}Be . The solutions to this Hamiltonian were calculated in a basis of pseudo-states. In particular, a basis of transformed harmonic oscillator (THO) functions was used, which basically

consists on a finite number of THO functions (which are constructed transforming the asymptotic behaviour of the HO functions from gaussian to exponential) is then used to diagonalize the ^{11}Be Hamiltonian. The resulting eigenvalues and eigenfunctions are then used as a discrete representation of the actual spectrum of the system and of the corresponding wavefunctions [Lay12b].

The obtained wavefunctions for the two bound states of ^{11}Be , using the particle-rotor model with the parameters in table 5.4 (extracted from table 1 in [Sum07]) and using a THO basis which includes an orbital angular momentum for the ^{10}Be -n up to $\ell = 3$ and the $j^\pi = 0^+, 2^+$ states of the ^{10}Be core, are:

$$\begin{aligned} |^{11}\text{Be}(\text{g.s.})\rangle_{1/2^+} &= \alpha |^{10}\text{Be}(0^+) \otimes \nu(s1/2)\rangle_{1/2^+} \\ &+ \beta |^{10}\text{Be}(2^+) \otimes \nu(d5/2)\rangle_{1/2^+} \\ &+ \gamma |^{10}\text{Be}(2^+) \otimes \nu(d3/2)\rangle_{1/2^+} \end{aligned} \quad (5.9)$$

with spectroscopic factors $\alpha^2 \sim 0.879$, $\beta^2 \sim 0.094$, $\gamma^2 \sim 0.027$ and

$$\begin{aligned} |^{11}\text{Be}^*\rangle_{1/2^-} &= a |^{10}\text{Be}(0^+) \otimes \nu(p1/2)\rangle_{1/2^-} \\ &+ b |^{10}\text{Be}(2^+) \otimes \nu(f5/2)\rangle_{1/2^-} \\ &+ c |^{10}\text{Be}(2^+) \otimes \nu(p3/2)\rangle_{1/2^-} \end{aligned} \quad (5.10)$$

with spectroscopic factors $a^2 \sim 0.672$, $b^2 \sim 0.322$ and $c^2 \sim 0.007$ and using the same structure model used in [Sum07] and originally proposed by F. Nunes [Nun96].

Now that we have a model for the ^{11}Be , the coupled equations of the complete Hamiltonian have to be solved for obtaining the cross sections. R. de Diego [dDALA14] published a work in which the extension of the CDCC formalism to include core excitations, using a pseudo-state basis, is presented. Due to the admixture of configurations present in each state, the solution of the equation system becomes more computationally demanding, which complicates the convergence of the calculation, as will be explained later.

In figure 5.18 the breakup probability obtained with the XCDCC is compared to the data. The calculation seems to explain the data even at large scattering angles at 39.6 MeV, where the CDCC failed. Since this calculation is in progress, these results have to be taken with caution, but an improvement can be observed, which could be caused by the more realistic description of the projectile, or to a sensitivity to the ^{10}Be - ^{197}Au potential, since this interaction is more precisely described within this formalism.

The problems of convergence mentioned before can be noticed in figure 5.18, where there is a change in the trend between 30° and 70° . For this reason, the study of the convergence of these calculations is still in progress.

The success of the calculation is clear if the whole picture is considered. The elastic and inelastic channels are shown in figures 5.19 and 5.20, respectively. The success of the calculation in all the angular range for those channels (with no normalization or scaling) together

with the encouraging results in the breakup cross section help us to understand more deeply

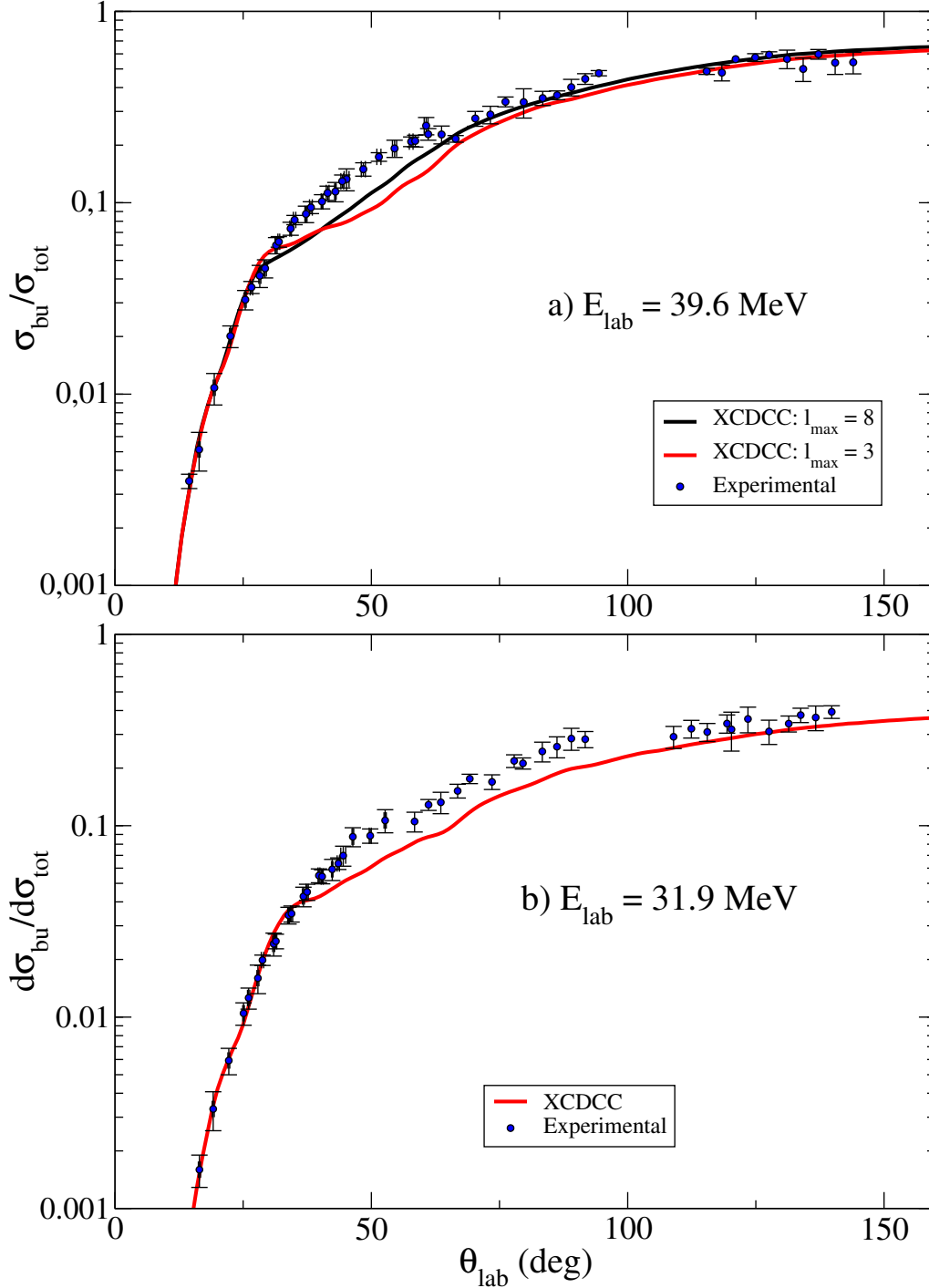


Figure 5.18: Experimental breakup probability data at energies around and below the Coulomb barrier compared to preliminary XCDCC calculation. At both energies, the calculation explains the data at small and large scattering angles. At intermediate angles some convergence problems cause an irregularity in the cross section. It is expected that as we improve our capability to deal with the computational limitations, the description of the breakup does not differ from the one obtained with CDCC calculation.

the structure of the ^{11}Be and the role it plays in the reaction.

The improvement obtained with the XCDCC calculation can also be noticed when comparing the measured and calculated absolute cross sections, as seen in figure 5.21. The convergence problems of the XCDCC calculation around the grazing angle are noticeable for the breakup cross sections, but the improvement in the inelastic scattering cross section evidences that the description of the reaction process is more accurate.

A realistic structure model of the ^{11}Be nucleus including excited components of the core is necessary for describing simultaneously the main reaction channels (elastic, inelastic and breakup). The XCDCC also allows for a process not included in the previous formalisms, which is the dynamic core excitation. To evaluate the importance of these dynamic core excitations, we have performed also calculations omitting them, that is, using a central $^{10}\text{Be}+^{197}\text{Au}$ interaction, as in the standard CDCC calculations. The results so obtained are almost identical to those obtained in the full XCDCC calculations, thus indicating that these dynamic core excitation effects are negligible and that the improvement obtained with the XCDCC calculation is a consequence of modifying the structure of the ^{11}Be states themselves.

Those results support the results obtained in a study performed for the CDCC calculations. In order to be sure that the $^{10}\text{Be}-^{208}\text{Pb}$ potential by Kolata could be used for modelling the $^{10}\text{Be}-^{197}\text{Au}$ interaction, calculations were performed introducing variations of the 20% in the depth of the real and imaginary potentials. These variations had no influence in the reaction. That result evidenced low sensitivity to the core-target nuclear interaction. It seemed improbable that, if the nuclear potential does not play a significant role, that a dynamic excitation of the core in the reaction explained the improvement of the results. As has been said, the result of the test performed for the XCDCC calculation reinforces this conclusion.

The main conclusions from the study of the reaction within the XCDCC formalism are:

- Extended CDCC calculations, based on a particle-core model of ^{11}Be with a deformed ^{10}Be core, have been performed for the $^{11}\text{Be}+^{197}\text{Au}$ reaction. The comparison of the calculated elastic, inelastic and breakup angular distributions with the measured data shows very encouraging results.
- It has not been possible to obtain fully converged results, since the states of the ^{10}Be -n system that could be included in the CDCC calculation have not been included yet in the XCDCC one. It has been observed that states with large energy and orbital angular momentum of the neutron with respect to the ^{10}Be are important.
- The calculation succeeds in explaining simultaneously population of the elastic, inelastic and breakup channels in the reaction at forward and backward scattering angles. In the region of intermediate angles, the calculations seem to be improved as a larger model space for the ^{10}Be -n system (both in E and ℓ) is considered.
- Comparing the results of these calculations with a calculation in which the core is not allowed to be excited during the process no major difference was observed. It can be inferred, then, that the improvement of the XCDCC calculation with respect to the CDCC is due to a more complex structure model (mixing of different core states in the states

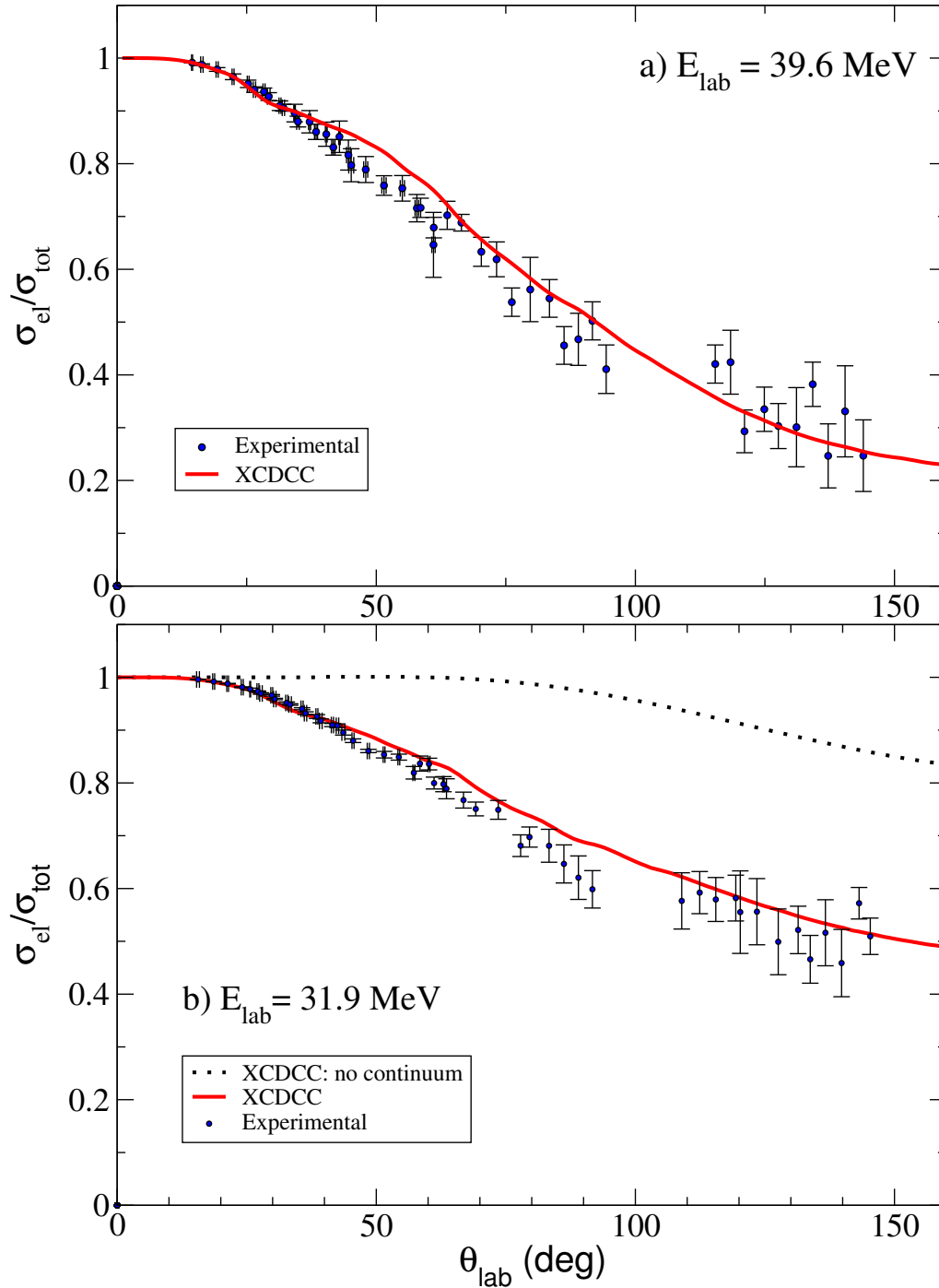


Figure 5.19: Experimental elastic scattering cross section at energies around and below the Coulomb barrier compared to XCDCC calculation. Below the barrier (b) the calculation explains the data with no need of ad-hoc scaling or parametrization.

of ^{11}Be) more than to an important role of the dynamic core excitation in the reaction process.

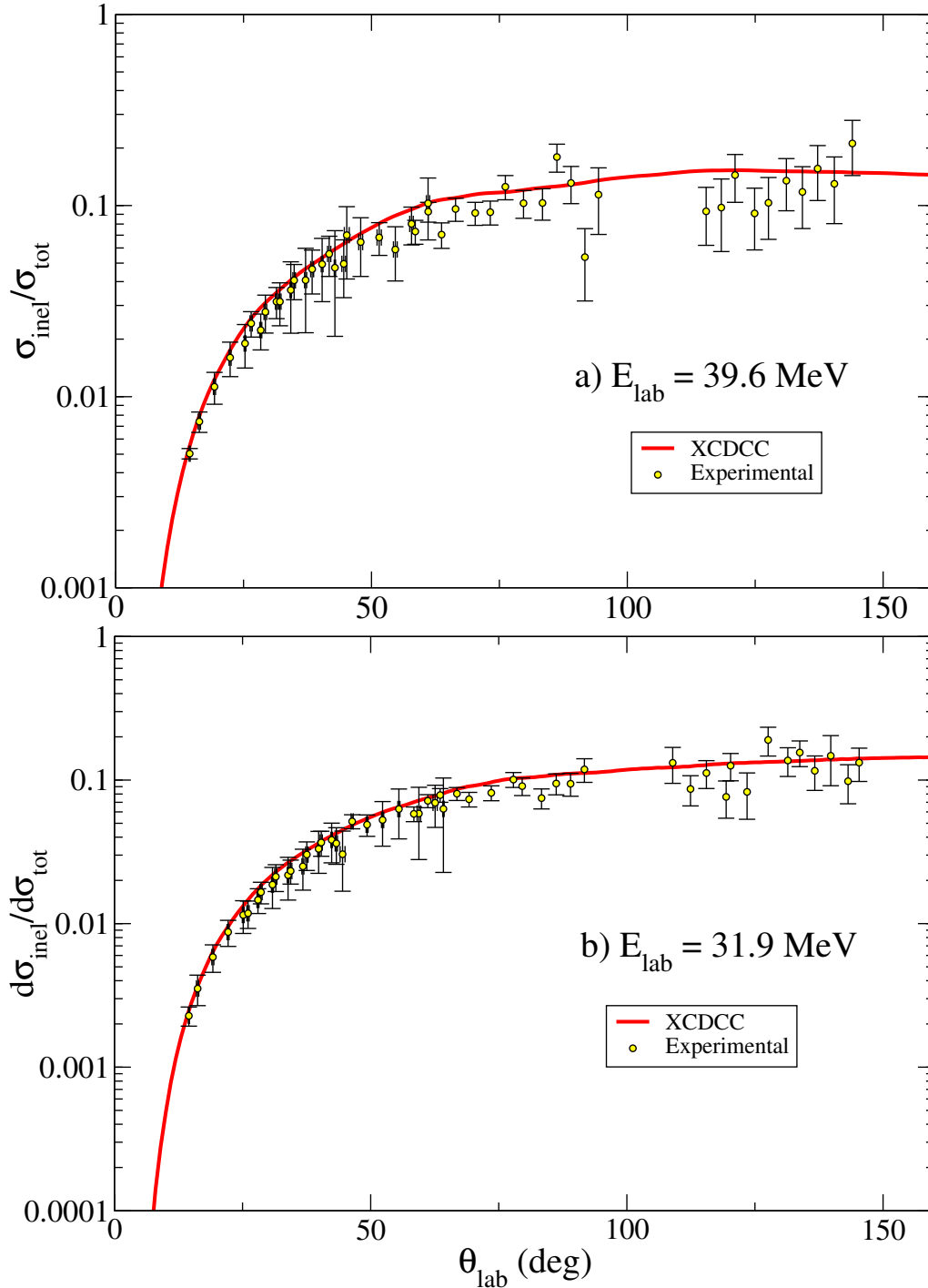


Figure 5.20: Experimental inelastic scattering probability data at energies around and below the Coulomb barrier compared to XCDCC calculation. The calculation XCDCC calculation explains the data with no need of ad-hoc scaling or parametrization, like in the case of the CDCC.

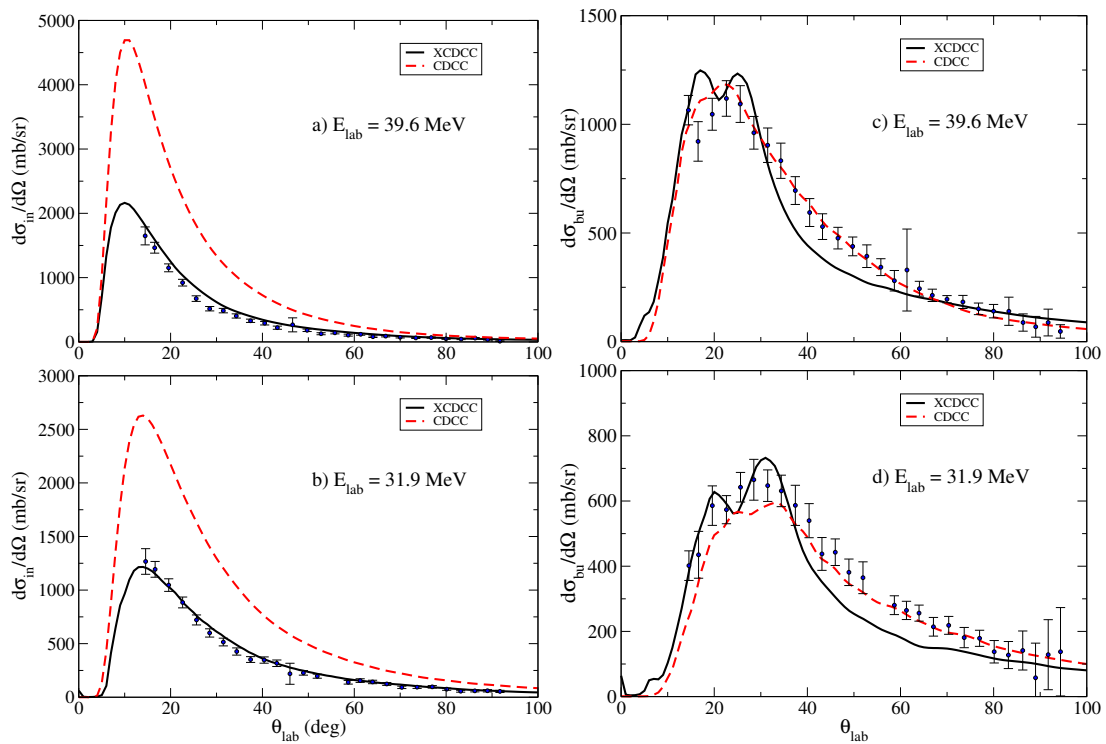


Figure 5.21: Experimental inelastic scattering and breakup cross sections, compared to CDCC and XCDCC calculations. The convergence problems of the XCDCC calculation around the grazing angle are noticeable for the breakup cross sections, but the improvement in the inelastic scattering cross section evidences that the description of the reaction process is more accurate.

Summary and conclusions

In this work, we have performed a comprehensive analysis of the $^{11}\text{Be}+^{197}\text{Au}$ reaction measured in 2013 at TRIUMF (Vancouver, Canada), within an international collaboration led by the IEM-CSIC and the Universities of Huelva and Seville (Spain). The measured data consist of elastic, inelastic (populating the only bound state of ^{11}Be) and inclusive breakup (^{10}Be fragments) angular distributions. These data have been compared with a variety of theoretical models, from which relevant information on the structure of ^{11}Be and on the reaction dynamics has been extracted. The main conclusions are:

- For the first time, the reaction of ^{11}Be on ^{197}Au at energies around the Coulomb barrier has been measured. The elastic, inelastic and breakup channels have been studied at beam energies of $E_{lab} = 31.9$ MeV and $E_{lab} = 39.6$ MeV, which are below and around the Coulomb barrier ($V_b \sim 40$ MeV), respectively. The energy at which the reaction takes place is estimated assuming that the reaction happens in the center of the target and subtracting the energy lost by ^{11}Be in ^{197}Au per unit length. The resulting reaction energies, that will be used for the calculations, are $E_{lab} = 39.17$ MeV ($E_{cm} = 37.10$ MeV) and $E_{lab} = 31.30$ MeV ($E_{cm} = 29.64$ MeV), respectively.
- The high energy resolution of the beam, together with the optimized experimental setup, using $40\ \mu\text{m}$ thick DSSSD detectors backed by 0.5 mm PAD detectors in telescope configuration, allowed for high-granularity and high-resolution charged-particle spectroscopy. This enabled us to identify fragments with a mass difference of around $1/11$.
- The geometrical position of the detectors and the target was studied for optimizing the angular range covered and minimizing the shades on the detectors. The detectors were mounted on a PCB board that was designed to accomplish a double function, namely having a stable and permanent detector configuration, and providing a circuitry that allowed for a comfortable cabling of the detectors.
- The energy calibration of the silicon detectors was performed with a triple-alpha source and the ^{12}C ions elastically scattered on the ^{197}Au target at 5.04 MeV/u. The energy loss in the target, in the scattering process and in the dead layers are incorporated in the energy evaluation. The resolution of the particle detectors was of 32 ± 1 keV.
- The position of the detectors is optimized using the number of counts per pixel from the scattering of ^{12}C on ^{197}Au at 5.04 MeV/u. This improves the assignment of the polar

angle and solid angle to each pixel. A second optimization position is performed for the ^{11}Be beams at forward angles, assuming that the sum of the measured cross sections correspond to a Rutherford distribution.

- The ΔE detector of the Tel4 is a $20\ \mu\text{m}$ thick SSSSD, which was found to have an uneven thickness. A procedure for measuring its thickness was designed. The thickness was measured, observing that the inhomogeneities were of the order of 25%.
- The signal from the silicon detectors was included in the acquisition trigger. The data was selected imposing an energy difference between the signal from the front and back side of the DSSSDs, $E_{diff} < 200\ \text{keV}$. The strips next to borders were ruled out of the analysis.
- The ^{11}Be and ^{10}Be fragments detected after the scattering of ^{11}Be on the ^{197}Au target at both energies can be separated in two dimensional ΔE - E plots built for angular bins of 3° . It was chosen to represent E_{back} instead of E_{tot} in the x axis because the separation of the fragments was better in this display. Two regions were well distinguished: one with the ^{11}Be fragments, which corresponds to the *quasielastic* scattering, and sums together the elastic and inelastic scattering contributions. The region of the ^{10}Be fragments corresponds to the inclusive breakup, since the neutron is not detected.
- The use of a HPGe detector array, called TIGRESS, allowed for high resolution gamma spectroscopy in coincidence, so the elastic, inelastic and breakup channels could be measured simultaneously. We used 8 clovers in a ring at $\theta_{lab} = 90^\circ$ and 4 clovers in another ring at $\theta_{lab} = 135^\circ$, and each of the clovers is formed by 4 Ge crystals. That granularity allowed for a precise determination of the direction of the gamma rays. In addition to the calibrated gamma spectra, the Doppler corrected spectra was obtained, considering energies of the particle and the gamma and their relative angle. The only γ -peak width that improved with the Doppler correction was the 320 keV gamma from the in-flight deexcitation of the ^{11}Be . The good energy resolution in the gamma spectra made it possible to separate the 320 keV gamma-ray from the excitation of ^{11}Be and the 297 keV gamma-ray coming from the Coulomb excitation of the ^{197}Au target.
- The efficiency of the TIGRESS array was determined for our configuration, with the setup of Si detectors placed inside the reaction chamber in position and with the BGO crystals for Compton suppression. A ^{152}Eu source is used for the relative efficiency calibration of the spectra and a ^{60}Co source is used for the absolute calibration. With the 12 clovers of TIGRESS that we use, the measured efficiency for gamma rays at 320 keV is $\varepsilon (E=320\ \text{keV}) = 0.121(5)$. The inelastic channel was identified performing particle-gamma coincidences, gating on the 320 keV gamma ray and correcting for the efficiency.
- The differential cross sections were studied an given first as *probabilities*. The inelastic scattering probability, for instance, is defined as the fraction of fragments that have been inelastically scattered relative to all the fragments detected in a pixel. Working with probabilities, minimized the source of experimental errors, because any problem (noise, electronics, shade), will affect to all the observables in one pixel in the same way.
- The differential cross sections are then calculated using the number of counts, the solid angle and a constant of proportionality for converting from N_{counts}/sr to millibarns (mb).

- The first evidence of a halo structure is a strong reduction of the elastic cross section with respect to the usual behaviour for ordinary nuclei, even at energies well below the Coulomb barrier. The reduction is noticeable at very forward angles, which evidences the effect of the halo. In the optical model analysis, this effect manifests itself as an anomalously large value of the diffuseness for the imaginary potential, $a_i = 8.6$ fm, which is needed to reproduce the data. The sensitivity radius is found at around $r_{sens} = 35-40$ fm. Compared to the sum of the radii of ^{11}Be and ^{197}Au ($R \approx 14.3$ fm), it suggests the importance of long range couplings and the dominance of the Coulomb potential in the reaction dynamics.
- A first order calculation using the Equivalent Photon Method is able to explain the inelastic scattering data at forward angles, but clearly underestimates the breakup cross section in all the angular range. This differs significantly from the case of the $^{11}\text{Li}+^{208}\text{Pb}$ reaction, where the first order calculation was able to describe the forward-angle breakup probability.
- The elastic, inelastic and breakup data have been compared with continuum-discretized coupled-channels (CDCC) calculations. These calculations are based on a three-body reaction model, consisting on a two-body projectile ($^{10}\text{Be}+n$) and an inert target (^{197}Au). Coupling to the bound excited state as well as to the breakup channels, due to both the Coulomb and nuclear interactions, are included to all orders. The ^{11}Be bound and continuum states are generated with a phenomenological Woods-Saxon potential [Cap04a], with parameters determined to give the separation energy of the bound states and the position of the low-lying $5/2^+$ resonance at $E_x = 1.78$ MeV (above g.s.). Moreover, this model was found to reproduce the $\mathcal{B}(E1)$ to the continuum states extracted from the Coulomb dissociation experiment performed at RIKEN by Fukuda et al [Fuk04].

Continuum states were truncated in the orbital angular momentum (ℓ) and excitation energy, and discretized using the standard *binning* method. Convergence of the calculated observables required a remarkably large model space ($\ell_{max} = 10$, and $E_{max} = 10$ MeV). The converged calculation reproduces reasonably well the quasielastic cross sections, but not the elastic and inelastic cross sections separately. In particular, it overestimates the inelastic probability by a factor of ~ 2 , which is attributed to the overestimation of the $\mathcal{B}(E1; 1/2^+ \rightarrow 1/2^-)$ value of the assumed ^{11}Be model. On the other hand, the breakup probability is rather well reproduced by this model.

- This experimental work motivated also new theoretical developments, materialized in two tangible improvements in the field of reaction theory:
 - Firstly, an stabilization algorithm for the highly demanding CDCC calculations, which needed the inclusion of a large model space in the $^{10}\text{Be}+n$ continuum (partial waves up to $\ell_{max} = 10$ and energies up to $E_{max} = 10$ MeV).
 - Secondly, an extension of the CDCC method, in order to allow the inclusion of core-excited components in the description of the ^{11}Be states.
- Transfer calculations to bound and unbound states of the target were performed to quantify the contribution of the neutron transfer to bound and unbound states of the ^{197}Au target at the energy around the Coulomb barrier. This calculation evidenced that this process is dominant, precisely, in the case where the CDCC failed, which is for angles larger than $\theta = 75^\circ$.

- Extended CDCC calculations (XCDCC) have been also performed and compared to the data. The XCDCC method is an extension of the conventional CDCC formalism, which takes into account core excitation effects in the structure of the projectile (allowing for core-excited admixtures in the states of ^{11}Be) as well as in the reaction dynamics (accounting for possible excitation and deexcitation of the ^{10}Be core during the collision). The preliminary XCDCC calculations presented here, reproduce the three studied observables rather well, except for some underestimation of the breakup probability at intermediate angles. This improvement over the standard CDCC method was found to be mostly due to the more realistic description of the states of ^{11}Be . Dynamical effects, due to core (de)excitations during the collision, were found to be relatively small in this reaction, in agreement with the results found for $^{11}\text{Be} + ^{208}\text{Pb}$ at higher energies [dDALA14].

Taken as a whole, this work presents an approach to the complete process of designing a nuclear physics experiment, performing it, analysing the data and explaining the results within different theories. It is also evidenced how the study of nuclear reactions allows to learn not only about the reaction process (we learned the importance of large range couplings and high order effects in this reaction, for example), but also about the properties of the reacting species (for instance, understanding the effects of including the deformed ^{10}Be core in the description of the ^{11}Be for explaining the results). In addition to developing the skills and acquiring the knowledge for performing efficiently a large variety of tasks, this work provided me a global comprehension of all of them as necessary pieces, contributing in different ways, but all of them indispensable for completing the complex puzzle of scientific progress to which one expects to contribute.

Appendices

Cross sections and probabilities

In this appendix the experimental cross sections and probabilities of the elastic scattering, inelastic scattering and breakup channels are presented.

Table A.1: Elastic scattering cross section with respect to Rutherford of the $^{11}\text{Be} + ^{197}\text{Au}$ reaction at $E_{\text{lab}} = 39.6$ MeV.

Angle (θ)	$d\sigma/d\sigma_{\text{Ruth}}$	Ang. error	Cross sec. error
14.5	0.9915	0.1	0.0001
16.3	0.9876	0.2	0.0017
19.3	0.9784	0.2	0.0035
22.4	0.9646	0.2	0.0054
25.3	0.9512	0.2	0.0070
26.5	0.9402	0.2	0.0053
28.3	0.9365	0.2	0.0069
29.2	0.9272	0.3	0.0073
31.4	0.9098	0.2	0.0091
32.1	0.9060	0.2	0.0065
34.2	0.8959	0.1	0.0167
34.9	0.8797	0.2	0.0101
37.1	0.8794	0.2	0.0212
38.4	0.8603	0.3	0.0144
40.4	0.8558	0.2	0.0229
41.7	0.8310	0.3	0.0149
42.9	0.8510	0.1	0.0297
44.6	0.8163	0.4	0.0284
45.2	0.7971	0.5	0.0312
48.0	0.7889	0.4	0.0246
51.5	0.7587	0.4	0.0185
55.0	0.7533	0.4	0.0243
57.8	0.7158	0.3	0.0259
58.6	0.7164	0.5	0.0182

Angle (θ)	$d\sigma/d\sigma_{\text{Ruth}}$	Ang. error	Cross sec. error
61.0	0.6463	0.3	0.0616
61.1	0.6789	0.5	0.0194
63.7	0.7022	0.5	0.0266
66.4	0.6882	0.5	0.0158
70.3	0.6331	0.5	0.0275
73.2	0.6188	0.5	0.0330
76.2	0.5377	0.5	0.0269
79.7	0.5617	0.5	0.0609
83.4	0.5448	0.5	0.0356
86.2	0.4557	0.5	0.0356
89.0	0.4674	0.5	0.0493
91.7	0.5023	0.5	0.0360
94.4	0.4107	0.5	0.0460
115.4	0.4205	0.5	0.0362
118.4	0.4239	0.5	0.0605
121.1	0.2930	0.5	0.0405
124.9	0.3348	0.5	0.0420
127.6	0.3031	0.5	0.0426
131.1	0.3009	0.5	0.0750
134.2	0.3822	0.5	0.0420
137.2	0.2466	0.5	0.0607
140.5	0.3310	0.5	0.0863
144.0	0.2469	0.5	0.0678

Table A.2: Elastic scattering cross section with respect to Rutherford of the $^{11}\text{Be} + ^{197}\text{Au}$ reaction at $E_{\text{lab}} = 31.9$ MeV.

Angle (θ)	$d\sigma/d\sigma_{\text{Ruth}}$	Ang. error	Cross sec. error
15.6	0.9960	0.3	0.0003
18.6	0.9920	0.2	0.0004
21.3	0.9880	0.2	0.0006
24.1	0.9814	0.2	0.0008
25.7	0.9776	0.1	0.0020
27.2	0.9734	0.2	0.0009
27.7	0.9695	0.2	0.0014
29.8	0.9659	0.2	0.0015
30.4	0.9589	0.2	0.0014
32.7	0.9516	0.2	0.0019
33.4	0.9484	0.3	0.0014
35.7	0.9405	0.2	0.0019
36.4	0.9320	0.2	0.0026
38.5	0.9258	0.2	0.0036
39.3	0.9176	0.3	0.0037
41.5	0.9096	0.2	0.0030
42.5	0.9083	0.2	0.0035
43.6	0.8954	0.3	0.0047
45.5	0.8801	0.2	0.0035
48.5	0.8606	0.2	0.0032
51.5	0.8535	0.2	0.0062
54.4	0.8489	0.2	0.0056
57.3	0.8192	0.2	0.0118
58.4	0.8367	0.5	0.0142
60.2	0.8358	0.2	0.0111

Angle (θ)	$d\sigma/d\sigma_{\text{Ruth}}$	Ang. error	Cross sec. error
61.1	0.7997	0.5	0.0112
63.0	0.7976	0.1	0.0143
63.5	0.7889	0.5	0.0190
66.8	0.7676	0.5	0.0151
69.2	0.7507	0.5	0.0131
73.5	0.7491	0.5	0.0178
77.9	0.6811	0.5	0.0205
79.6	0.6975	0.5	0.0191
83.3	0.6809	0.5	0.0312
86.2	0.6466	0.5	0.0361
89.0	0.6206	0.5	0.0412
91.7	0.5985	0.5	0.0354
108.9	0.5766	0.5	0.0533
112.4	0.5923	0.5	0.0399
115.5	0.5793	0.5	0.0416
119.4	0.5820	0.5	0.0434
120.2	0.5553	0.5	0.0782
123.5	0.5562	0.5	0.0627
127.6	0.4991	0.5	0.0623
131.4	0.5216	0.5	0.0450
133.7	0.4659	0.5	0.0452
136.7	0.5162	0.5	0.0626
139.8	0.4588	0.5	0.0637
143.2	0.5722	0.5	0.0298
145.3	0.5095	0.5	0.0345

Table A.3: Inelastic scattering probability of the $^{11}\text{Be} + ^{197}\text{Au}$ reaction at $E_{\text{lab}} = 39.6 \text{ MeV}$.

Angle (θ)	Prob	Ang. error (θ)	Prob.
15.3	0.0050	0.5	0.0000
17.3	0.0074	1.0	0.0043
20.4	0.0113	0.3	0.0026
23.6	0.0160	0.4	0.0044
26.6	0.0190	0.5	0.0051
27.3	0.0196	0.1	0.0022
29.9	0.0223	0.3	0.0043
30.2	0.0241	0.5	0.0050
33.1	0.0314	0.5	0.0115
33.2	0.0264	0.6	0.0066
36.0	0.0361	0.6	0.0135
36.1	0.0367	0.6	0.0111
39.0	0.0407	0.4	0.0161
39.7	0.0419	0.6	0.0091
42.4	0.0494	0.7	0.0287
43.0	0.0524	0.9	0.0190
45.0	0.0473	0.5	0.0286
45.9	0.0437	0.5	0.0118
47.4	0.0700	0.5	0.0287
49.2	0.0547	0.7	0.0105
52.8	0.0644	1.1	0.0206
55.9	0.0574	0.8	0.0186
59.0	0.0762	1.0	0.0206
61.3	0.0732	0.5	0.0105

Angle (θ)	Prob	Ang. error (θ)	Prob.
62.1	0.0898	1.2	0.0210
63.9	0.0929	0.5	0.0110
66.6	0.0704	0.5	0.0107
69.4	0.0960	0.5	0.0132
72.8	0.0914	0.5	0.0126
75.7	0.0923	0.5	0.0132
78.2	0.1253	0.5	0.0182
82.3	0.1029	0.5	0.0171
86.6	0.1031	0.5	0.0193
89.4	0.1794	0.5	0.0300
92.2	0.1313	0.5	0.0290
94.9	0.0537	0.5	0.0220
97.6	0.1141	0.5	0.0434
118.3	0.0932	0.5	0.0313
121.2	0.0976	0.5	0.0401
123.8	0.1444	0.5	0.0405
127.5	0.0910	0.5	0.0324
130.1	0.1034	0.5	0.0368
133.5	0.1350	0.5	0.0411
136.5	0.1178	0.5	0.0420
139.4	0.1562	0.5	0.0499
142.5	0.1300	0.5	0.0496
145.9	0.2114	0.5	0.0678

Table A.4: Inelastic scattering probability of the $^{11}\text{Be} + ^{197}\text{Au}$ reaction at $E_{\text{lab}} = 31.9 \text{ MeV}$.

Angle (θ)	Prob	Ang. error (θ)	Prob.	Angle (θ)	Prob	Ang. error (θ)	Prob.
15.4	0.0027	0.3	0.0002	61.1	0.0717	0.5	0.0074
18.6	0.0052	0.2	0.0003	63.5	0.0786	0.5	0.0086
21.2	0.0067	0.2	0.0004	66.8	0.0804	0.5	0.0083
24.0	0.0096	0.2	0.0005	69.2	0.0735	0.5	0.0086
25.6	0.0110	0.1	0.0016	73.5	0.0815	0.5	0.0097
27.1	0.0125	0.2	0.0007	77.9	0.1008	0.5	0.0120
27.7	0.0142	0.3	0.0009	79.6	0.0907	0.5	0.0127
29.8	0.0131	0.2	0.0012	83.3	0.0749	0.5	0.0120
30.4	0.0194	0.2	0.0009	86.2	0.0947	0.5	0.0157
32.6	0.0190	0.2	0.0014	89.0	0.0942	0.5	0.0171
33.4	0.0218	0.2	0.0013	91.7	0.1186	0.5	0.0223
35.5	0.0201	0.2	0.0015	108.9	0.1318	0.5	0.0369
36.3	0.0278	0.2	0.0017	112.4	0.0867	0.5	0.0206
38.3	0.0207	0.2	0.0028	115.5	0.1120	0.5	0.0247
39.2	0.0326	0.3	0.0026	119.4	0.0764	0.5	0.0222
41.5	0.0309	0.2	0.0024	120.2	0.1260	0.5	0.0271
42.5	0.0325	0.2	0.0024	123.5	0.0828	0.5	0.0294
43.6	0.0351	0.3	0.0035	127.6	0.1902	0.5	0.0431
45.5	0.0486	0.2	0.0020	131.4	0.1370	0.5	0.0310
48.5	0.0477	0.2	0.0024	133.7	0.1557	0.5	0.0315
51.5	0.0448	0.2	0.0051	136.7	0.1160	0.5	0.0313
54.4	0.0521	0.2	0.0049	139.8	0.1476	0.5	0.0563
57.3	0.0591	0.2	0.0067	143.2	0.0982	0.5	0.0298
58.4	0.0581	0.5	0.0068	145.3	0.1323	0.5	0.0345

Table A.5: Breakup probability for $^{11}\text{Be} + ^{197}\text{Au}$ at $E_{\text{lab}} = 39.6 \text{ MeV}$.

Angle (θ)	Prob	Ang. error (θ)	Prob.
14.5	0.0035	0.1	0.0003
16.4	0.0051	0.2	0.0012
19.4	0.0108	0.2	0.0020
22.5	0.0201	0.2	0.0026
25.4	0.0312	0.2	0.0036
26.6	0.0362	0.2	0.0026
28.2	0.0416	0.2	0.0055
29.3	0.0454	0.3	0.0049
31.4	0.0599	0.2	0.0059
32.0	0.0626	0.2	0.0040
34.3	0.0733	0.2	0.0057
35.0	0.0813	0.2	0.0046
37.3	0.0873	0.2	0.0086
38.2	0.0945	0.3	0.0067
40.4	0.1015	0.2	0.0087
41.5	0.1125	0.3	0.0096
43.0	0.1144	0.2	0.0132
44.3	0.1296	0.3	0.0101
45.2	0.1329	0.5	0.0175
48.4	0.1498	0.4	0.0120
51.5	0.1736	0.4	0.0090
54.5	0.1923	0.4	0.0198
57.8	0.2087	0.4	0.0121
58.6	0.2104	0.5	0.0149

Angle (θ)	Prob	Ang. error (θ)	Prob.
60.7	0.2526	0.4	0.0261
61.1	0.2281	0.5	0.0159
63.7	0.2273	0.5	0.0243
66.4	0.2158	0.5	0.0086
70.3	0.2755	0.5	0.0245
73.2	0.2888	0.5	0.0303
76.2	0.3369	0.5	0.0198
79.7	0.3355	0.5	0.0584
83.4	0.3520	0.5	0.0299
86.2	0.3648	0.5	0.0192
89.0	0.4014	0.5	0.0399
91.7	0.4440	0.5	0.0285
94.4	0.4752	0.5	0.0150
115.4	0.4863	0.5	0.0182
118.4	0.4785	0.5	0.0453
121.1	0.5625	0.5	0.0420
124.9	0.5742	0.5	0.0267
127.6	0.5936	0.5	0.0215
131.1	0.5642	0.5	0.0627
134.2	0.5000	0.5	0.0700
137.2	0.5973	0.5	0.0345
140.5	0.5391	0.5	0.0707
144.0	0.5417	0.5	0.0700

Table A.6: Breakup probability for $^{11}\text{Be}+^{197}\text{Au}$ at $E_{lab} = 31.9$ MeV.

Angle (θ)	Prob	Ang. error (θ)	Prob.
14.5	0.0010	0.1	0.0002
16.5	0.0016	0.2	0.0003
19.2	0.0033	0.2	0.0008
22.2	0.0059	0.2	0.0009
25.1	0.0105	0.2	0.0014
26.1	0.0126	0.2	0.0016
27.9	0.0160	0.2	0.0027
28.8	0.0198	0.2	0.0012
30.9	0.0241	0.2	0.0033
31.4	0.0249	0.2	0.0022
33.8	0.0341	0.2	0.0034
34.4	0.0347	0.2	0.0034
36.7	0.0427	0.2	0.0050
37.5	0.0451	0.2	0.0044
39.8	0.0549	0.2	0.0046
40.4	0.0543	0.2	0.0046
42.4	0.0592	0.1	0.0075
43.6	0.0635	0.2	0.0044
44.5	0.0698	0.5	0.0083
46.4	0.0876	0.2	0.0100
49.8	0.0886	0.2	0.0076
52.7	0.1065	0.2	0.0148
58.4	0.1052	0.5	0.0124

Angle (θ)	Prob	Ang. error (θ)	Prob.
61.1	0.1286	0.5	0.0084
63.5	0.1325	0.5	0.0170
66.8	0.1521	0.5	0.0126
69.2	0.1758	0.5	0.0099
73.5	0.1695	0.5	0.0149
77.9	0.2181	0.5	0.0167
79.6	0.2118	0.5	0.0142
83.3	0.2442	0.5	0.0288
86.2	0.2587	0.5	0.0325
89.0	0.2852	0.5	0.0375
91.7	0.2829	0.5	0.0276
108.9	0.2916	0.5	0.0384
112.4	0.3210	0.5	0.0341
115.5	0.3087	0.5	0.0335
119.4	0.3416	0.5	0.0373
120.2	0.3187	0.5	0.0733
123.5	0.3611	0.5	0.0553
127.6	0.3107	0.5	0.0450
131.4	0.3415	0.5	0.0326
133.7	0.3784	0.5	0.0324
136.7	0.3678	0.5	0.0542
139.8	0.3936	0.5	0.0298

Table A.7: Inelastic scattering cross section of the $^{11}\text{Be}+^{197}\text{Au}$ reaction at $E_{lab} = 39.6$ MeV.

Angle (θ)	$d\sigma/d\Omega$ (mb/sr)	error (mb/sr)
14.5	1649	140
16.5	1465	84
19.6	1152	61
22.6	921	52
25.6	674	44
28.5	516	35
31.5	487	35
34.3	403	33
37.4	329	26
40.5	291	27
43.2	236	27
46.6	265	109
49.7	181	19
52.8	127	16

Angle (θ)	$d\sigma/d\Omega$ (mb/sr)	error (mb/sr)
55.8	142	17
58.7	106	15
61.4	119	14
64.1	81	12
66.8	90	13
70.0	72	10
73.4	62	9
76.7	67	10
80.0	48	8
83.3	44	8
86.3	59	10
89.0	36	8
91.7	12	5

Table A.8: Inelastic scattering cross section of the $^{11}\text{Be}+^{197}\text{Au}$ reaction at $E_{lab} = 31.9$ MeV.

Angle (θ)	$d\sigma/d\Omega$ (mb/sr)	error (mb/sr)	Angle (θ)	$d\sigma/d\Omega$ (mb/sr)	error (mb/sr)
14.6	1267	120	51.9	196	19
16.6	1194	74	58.7	140	17
19.6	1047	59	61.3	155	17
22.6	885	51	64.0	143	16
25.6	721	47	67.1	124	13
28.5	600	38	70.3	92	11
31.5	515	36	73.7	94	11
34.4	427	34	77.0	97	12
37.4	352	27	80.1	75	11
40.4	347	29	83.2	56	9
43.1	317	30	86.2	60	10
46.0	219	98	89.0	60	11
48.9	228	21	91.7	54	10

Table A.9: Breakup cross section for the $^{11}\text{Be}+^{197}\text{Au}$ reaction at $E_{lab} = 39.6$ MeV.

Angle (θ)	$d\sigma/d\Omega$ (mb/sr)	error (mb/sr)	Angle (θ)	$d\sigma/d\Omega$ (mb/sr)	error (mb/sr)
14.5	916	69	55.8	343	39
16.5	921	91	58.7	280	47
19.6	1046	73	61.4	330	189
22.6	1119	82	64.1	244	34
25.6	1093	85	66.8	213	28
28.5	961	75	70.0	195	17
31.5	904	79	73.4	183	30
34.3	832	81	76.7	151	27
37.4	695	64	80.0	140	31
40.5	594	64	83.3	140	65
43.2	529	59	86.3	88	40
46.6	476	50	89.0	68	48
49.7	438	43	91.7	88	62
52.8	393	52	94.3	47	31

Table A.10: breakup cross section of the $^{11}\text{Be}+^{197}\text{Au}$ reaction at $E_{lab} = 31.9$ MeV.

Angle (θ)	$d\sigma/d\Omega$ (mb/sr)	error (mb/sr)
14.6	402	45
16.6	435	72
19.6	586	61
22.6	573	43
25.6	642	45
28.5	665	63
31.5	647	48
34.4	631	48
37.4	587	62
40.4	540	52
43.1	438	50
46.0	443	41
48.9	381	41
51.9	365	49

Angle (θ)	$d\sigma/d\Omega$ (mb/sr)	error (mb/sr)
58.7	280	29
61.3	264	28
64.0	256	25
67.1	214	29
70.3	219	27
73.7	181	31
77.0	179	25
80.1	138	34
83.2	127	42
86.2	141	60
89.0	58	106
91.7	129	107
94.4	138	136



Thickness of SSSSD4

In this appendix a map of the thickness of the Single Sided Silicon Strip Detector used in telescope 4 is presented. The thickness was obtained by the procedure explained in chapter 4. Although the detector is only segmented on one side, using a Double Sided Silicon Strip Detector as an E detector in telescope configuration, the thickness is known pixel by pixel.

Table B.1: Minimum thickness of the SSSSD used in telescope 4 in μm . The thickness of the area coincident with the horizontal strip 6 could not be determined because that strip of the DSSSD was dead. In some pixels the procedure did not allow for obtain a lower limit to the thickness.

	Vertical Strip															
	0	1	2	3	4	5	6	7	8	9	10	11	12	13	14	15
0	-	-	-	-	-	-	-	-	-	-	-	-	-	-	-	-
1	-	-	-	20.3	20.0	21.6	23.2	22.9	24.7	24.4	25.1	25.6	25.3	25.0	24.7	-
2	-	-	-	20.4	22.1	21.8	23.4	23.1	24.8	24.5	26.0	25.7	25.4	25.1	24.8	-
3	-	-	20.8	20.5	22.2	23.8	23.5	25.2	24.9	24.6	26.1	25.8	25.5	25.2	24.9	-
4	-	-	20.9	22.6	22.3	23.9	23.6	25.3	25.0	24.7	25.4	25.9	25.6	25.3	25.0	-
5	-	-	21.0	22.7	22.4	24.0	23.7	25.4	25.1	24.8	25.5	26.0	25.7	25.4	25.1	-
6	-	-	-	-	-	-	-	-	-	-	-	-	-	-	-	-
7	-	-	21.1	20.8	22.5	24.1	23.8	25.6	25.2	24.9	24.5	24.2	25.8	25.5	25.2	-
8	-	-	21.2	20.8	22.5	24.2	23.8	25.6	25.3	24.9	24.6	24.2	25.8	25.5	25.2	-
9	-	-	-	20.9	22.6	24.2	23.8	23.5	25.3	24.9	24.6	24.2	25.9	25.5	25.2	-
10	-	-	-	20.9	22.6	24.2	23.8	23.5	25.3	24.9	24.6	24.2	25.9	25.5	25.2	-
11	-	-	-	20.8	22.5	22.2	23.8	23.5	23.2	24.9	24.6	24.2	23.9	25.5	25.2	-
12	-	-	-	20.8	20.5	22.2	23.8	23.5	23.2	24.9	24.5	24.2	23.9	25.5	23.6	-
13	-	-	-	20.8	20.4	22.1	21.8	23.3	23.1	22.8	24.5	24.1	23.8	25.4	23.5	-
14	-	-	-	-	20.4	22.0	21.7	21.4	23.0	22.7	22.4	24.1	23.7	23.4	23.1	-
15	-	-	-	-	-	-	-	-	-	-	-	-	-	-	-	-

Table B.2: Maximum thickness of the SSSSD used in telescope 4. The thickness of the area coincident with the horizontal strip 6 could not be determined because that strip of the DSSSD was dead.

		Vertical Strip															
		0	1	2	3	4	5	6	7	8	9	10	11	12	13	14	15
Horizontal strip	0	-	-	-	-	-	-	-	-	-	-	-	-	-	-	-	-
	1	-	20.9	20.6	21.9	21.7	22.7	22.5	23.3	23.2	24.1	24.1	24.0	24.0	23.9	23.8	-
	2	-	21.0	20.7	22.0	23.0	22.9	23.6	23.5	24.0	24.2	26.1	26.0	25.8	24.0	23.9	-
	3	-	21.1	22.4	22.2	23.2	23.8	23.7	24.2	24.3	24.3	26.2	26.1	25.9	24.1	24.0	-
	4	-	21.2	22.5	22.3	23.3	23.9	23.8	24.3	24.4	24.4	26.2	26.2	26.0	24.2	24.1	-
	5	-	21.3	22.6	22.3	23.3	24.0	23.9	24.4	24.5	24.5	24.5	24.4	24.4	24.3	24.2	-
	6	-	-	-	-	-	-	-	-	-	-	-	-	-	-	-	-
	7	-	21.4	22.7	22.5	23.5	24.1	24.0	24.5	24.4	24.6	24.6	24.5	24.5	24.4	24.3	-
	8	-	21.5	21.2	22.5	23.5	23.3	24.0	23.9	24.4	24.3	24.6	24.6	24.5	24.4	24.3	-
	9	-	21.5	21.2	22.5	23.5	23.3	24.1	23.9	24.4	24.3	24.2	24.6	24.5	24.4	24.3	-
	10	-	21.5	21.2	22.5	22.2	23.3	24.1	23.9	24.4	24.3	24.2	24.1	24.5	24.4	24.3	-
	11	-	21.5	21.2	22.5	22.2	23.3	23.8	23.9	23.7	24.3	24.2	24.1	24.5	24.4	24.3	-
	12	-	21.4	21.1	22.5	22.2	23.3	23.0	23.9	23.7	23.5	24.2	24.0	24.5	24.4	24.3	-
	13	-	21.4	21.1	20.8	22.1	21.9	23.0	22.8	23.6	23.5	24.1	24.0	23.8	23.7	23.5	-
	14	-	21.3	21.0	20.7	22.1	21.8	22.9	22.7	23.6	23.4	23.2	23.9	23.8	23.6	23.5	-
	15	-	-	-	-	-	-	-	-	-	-	-	-	-	-	-	-



C.1 Introduction

This work is part of a series of experiments performed by an international collaboration led by the nuclear physics groups at the IEM-CSIC (Madrid) and the Universities of Seville and Huelva. The global aim of these experiments is the understanding of the dynamics of the collisions of weakly-bound light nuclei on heavy targets at Coulomb barrier energies. Previous to the present work, this collaboration had measured the reactions ${}^6\text{He}+{}^{208}\text{Pb}$ (at Louvain-la-Neuve), ${}^{11}\text{Be}+{}^{120}\text{Sn}$ (CERN-ISOLDE) and ${}^{11}\text{Li}+{}^{208}\text{Pb}$ (TRIUMF).

Along the same lines, in this thesis we have studied the reaction of ${}^{11}\text{Be}$ on a gold (${}^{197}\text{Au}$) target at two incident energies, 32 MeV and 39 MeV, which are below and around the Coulomb barrier (V_b *sim* 40 MeV), respectively. These experimental data, together with a proper interpretation using different theoretical calculations, contributes to the understanding how the halo structure, observed in some nuclei close to the neutron and proton driplines, influences the dynamics of the reaction around and below the Coulomb barrier, where nuclear effects should be of minor relevance. The data analysed as part of this PhD work were acquired in the S1202 experiment performed at TRIUMF in July of 2012 and June of 2013, which will be thoroughly described along the text.

The ${}^{11}\text{Be}$ nucleus is a one-neutron-halo nucleus composed of 4 protons and 7 neutrons. Halo nuclei are weakly bound systems, close to the neutron or proton driplines, in which one or two nucleons have a large probability of being at large distances of the center of the nucleus, well beyond the range of the nuclear potential. The major source of information of these nuclei are nuclear reactions. Being unstable systems (for example ${}^{11}\text{Be}$ decays in 13.76(7) s by beta emission to ${}^{11}\text{B}$), these reactions require a mechanism to produce these unstable nuclei and to accelerate them, using them as projectiles that bombard a stable target nucleus.

A reaction on a heavy target was chosen for this study. Heavy targets have a large amount of protons, translating into a strong electrostatic field felt by the projectile. In a very simplistic representation, and due to the loosely bound neutron in the ${}^{11}\text{Be}$ projectile, the reaction ${}^{11}\text{Be}+{}^{197}\text{Au}$ can be imagined as the neutron in the halo not feeling the field while the core is pushed away, being easily broken apart. This process is known as Coulomb breakup and

previous works in other energy regimes or for similar reactions [Sá08, Esc07, Fer13, Cub12, Nak97, Aum00, Fuk04, Pal03] concluded that it has a major contribution in reactions with halo nuclei. The importance of this particular process in this case will be reported here.

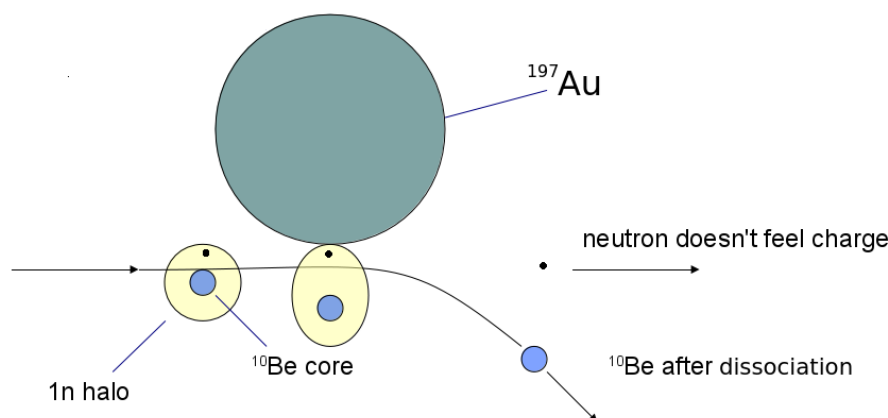


Figure C.1: *Simplistic representation of the breakup process that the ^{11}Be on the heavy target may undergo.*

Since the ^{11}Be nucleus is unstable, this experiment requires a facility capable of producing radioactive beams. The high quality of the ^{11}Be beam produced at TRIUMF (Vancouver, Canada) and the possibility of using the HPGe array TIGRESS for detecting the gamma radiation produced in the reaction were the reasons for choosing that facility.

The ^{11}Be nucleus

In general, a halo nucleus is a system composed of a compact core, formed by most of its nucleons, and a diffuse halo formed by one or two weakly bound nucleons. In principle both, proton and neutron, can form a halo. However, in the case of protons, the Coulomb barrier tends to confine the nucleons inside the nucleus, thus hindering the development of a halo structure. Such structures are observed close to the driplines, where there is an excess of either protons or neutrons that still can be bound to the nucleus but with very low binding energy. As a consequence, if they are in orbits of low ℓ , these nucleons can be found at large distances of the center of the nucleus. Saying it with quantum mechanics correctness, the wavefunction of these particles has a long tail, i.e. their density is not negligible up to abnormally large radii, compared to other nuclei with the same mass.

Berillium is the fourth element in the periodic table, what means that it has 4 protons. The particular case of ^{11}Be has, as its name indicates, 11 nucleons, the 4 protons plus 7 neutrons. The only stable isotope of berillium is ^9Be which has an structure that may be thought of as two alpha particles bound together by a neutron. That neutron plays a role comparable to the one that the electron does in a covalent bond. Adding another neutron ^{10}Be is obtained, which has the same structure, but with two neutrons making this kind of covalent binding. The ^{10}Be nucleus ($j^\pi = 0^+$) decays through β^- to ^{10}B ($j^\pi = 3^+$) with a half-life of $t_{1/2} = 1.6 \times 10^6$ years, so it may be said to be such an stable one. The addition of an extra neutron brings a completely different structure to the stage. The half-life of ^{11}Be ($j^\pi = 1/2^+$), decaying through

β^- to ^{11}B ($j^\pi = 3/2^-$), is $t_{1/2} = 13.76(7)$ s (10^{12} times lower) [Kel12], so the experimental requirements to study this nucleus will be more challenging.

Within a simple single-particle picture, the ground state of ^{11}Be is formed by adding a neutron to the s orbit in the sd -shell ($J^\pi = 1/2^+$) due to an inversion between the $s_{1/2}$ and the $1p_{1/2}$ levels. For $N = 7$, as protons are removed from ^{15}O , the gap typically found at $N=8$ (between the $1p$ and sd major shells) becomes smaller. Instead, as the $p_{1/2}$ orbit goes higher in energy, the gap appears at $N=6$, giving the so-called ‘‘closed shell’’ structure to ^{10}Be . The energy needed for exciting the ^{10}Be to the first excited state, at 3368 keV, compared to the energy to the first excited states in ^{12}Be (2101 keV) reinforces the statement that the shell is closed at $N = 6$. The closed shell of the ^{10}Be nucleus, the s -orbit of the last neutron and the low binding energy, all together contribute to make the ^{11}Be nucleus a weakly bound one-neutron halo system with a ^{10}Be core. Using a pure single-particle approach, the wavefunction of the ground state of ^{11}Be can be written as

$$|^{11}\text{Be}(\text{g.s.})\rangle_{1/2^+} = |^{10}\text{Be}(0^+)\rangle \otimes \nu(s_{1/2})\rangle_{1/2^+}. \quad (\text{C.1})$$

The neutron separation energy is $S_n=501.6$ keV. Despite being low, it is high enough for the inverted p -orbit to be below the threshold, so there is one bound excited state ($J^\pi = 1/2^-$), which lies at $E_x = 320.04(10)$ keV above the ground state ($S_n = 181.6$ keV),

$$|^{11}\text{Be}^*\rangle_{1/2^-} = |^{10}\text{Be}(0^+)\rangle \otimes \nu(p_{1/2})\rangle_{1/2^-}. \quad (\text{C.2})$$

It is possible to populate this state through an $E1$ transition from the ground state, and it is remarkable that, with a strength of $\mathcal{B}(E1) = 0.116 \pm 0.012 e^2 fm^2$ [Mil83], it is the strongest $\mathcal{B}(E1)$ measured between bound states.

The pure simple-particle approach leading to equations C.1 and eq. C.2 is useful, but is a functional simplification of an underlying more complicated system. Experimental and theoretical studies have evidenced that the low-lying states of ^{11}Be contain significant admixtures of core excited components. Maintaining the description in terms of a ^{10}Be core and a valence neutron, but considering these excited components, the ^{11}Be ground-state can be written in the form

$$\begin{aligned} |^{11}\text{Be}(\text{g.s.})\rangle_{1/2^+} = & \alpha |^{10}\text{Be}(0^+)\rangle \otimes \nu(s_{1/2})\rangle_{1/2^+} \\ & + \beta |^{10}\text{Be}(2^+)\rangle \otimes \nu(d_{5/2})\rangle_{1/2^+} \\ & + \gamma |^{10}\text{Be}(2^+)\rangle \otimes \nu(d_{3/2})\rangle_{1/2^+} \\ & + \dots \end{aligned} \quad (\text{C.3})$$

with weights $\alpha^2 \sim 0.86$, $\beta^2 \sim 0.12$ and $\gamma^2 \sim 0.02$ extracted from [Lay12b] (using the model in [Nun96], and consistent with the experimental results [Zwi79, For99, Win01, Sch12]). Likewise,

the only bound excited state is better described in the following form:

$$\begin{aligned}
 |^{11}\text{Be}^*\rangle_{1/2^-} = & a |^{10}\text{Be}(0^+) \otimes \nu(p1/2)\rangle_{1/2^-} \\
 & + b |^{10}\text{Be}(2^+) \otimes \nu(f5/2)\rangle_{1/2^-} \\
 & + c |^{10}\text{Be}(2^+) \otimes \nu(p3/2)\rangle_{1/2^-} \\
 & + \dots
 \end{aligned} \tag{C.4}$$

with weights $a^2 \sim 0.79$, $b^2 \sim 0.21$ and $c^2 \sim 0.004$ extracted from [Lay12a], and compatible with the experimental values measured by Schmitt [Sch12]. In [Nun96], the extra configurations resulting from the coupling of excited states of the core with the valence particle, have been interpreted within the particle-rotor model, assuming a permanent deformation of the ^{10}Be nucleus ($\beta = 0.67$). Independently of the model, in these extra configurations the neutron is in a d -orbit, so they are not halo configurations (halos are mainly observed in s and p orbits).

Above the neutron separation energy, many other states have been identified in ^{11}Be (see [Kel12] for a recent review). Among them, we note here the two narrow resonances observed in the experiment of Fukuda et al. [Fuk04], one at 1.78 MeV ($J^\pi = 5/2^+$) and one at 3.41 MeV ($J^\pi = 3/2^+$).

Several reactions of ^{11}Be on different targets and at different energies have been already studied. The experiments more similar to ours are listed below:

- $^{208}\text{Pb}(^{11}\text{Be}, ^{10}\text{Be}+n)^{208}\text{Pb}$: Exclusive breakup measurements, in which the outgoing neutron and ^{10}Be are measured in coincidence, have been performed at RIKEN at energies ~ 70 MeV/u [Nak97, Fuk04] and at GSI at energies ~ 520 MeV/u [Pal03]. They have provided information on the direct Coulomb breakup probability, which in loosely bound nuclei on heavy targets is dominated by an $E1$ transition. Although the extracted $\mathcal{B}(E1)$ distributions differ quantitatively among the different experiments, they all predict a large $\mathcal{B}(E1)$ strength near the breakup threshold, as expected for a halo nucleus. These experiments also derived a spectroscopic factor of the $\nu 2s_{1/2} \otimes ^{10}\text{Be}(0^+)$ single-particle configuration in the ^{11}Be ground state, associated with the dipole-strength: $S = 0.61 \pm 0.05$ [Pal03] and $S = 0.72 \pm 0.04$ [Fuk04].
- $^{12}\text{C}(^{11}\text{Be}, ^{10}\text{Be}+n)^{12}\text{C}$: The breakup measurements on light targets (ej. ^{12}C), in which nuclear effects are dominant, allowed the identification of low-lying resonances and their spin-parity assignment. In [Fuk04] the states at $E_x = 1.78$ MeV and $E_x = 3.41$ MeV are observed.
- $^{64}\text{Zn}(^{11}\text{Be}, ^{11}\text{Be})^{64}\text{Zn}$ [Pie13] and $^{120}\text{Sn}(^{11}\text{Be}, ^{11}\text{Be})^{120}\text{Sn}$ [Aco11]: These experiments at CERN-ISOLDE showed the differences of the reactions using several Be isotopes ($^9,^{10},^{11}\text{Be}$) on medium-mass targets at energies around the Coulomb barrier. For ^{11}Be , a large absorption in the elastic channel was observed at all the measured angles ($10^\circ < \theta_{cm} < 120^\circ$). This absorption also produces the disappearance of the characteristic interference pattern at the grazing angle, where the projectile reaches the radius at which the Coulomb and nuclear potentials are of the same order. In the experiment with the Zn target, the resolution at forward angles was enough for separating the breakup fragments for which they estimated an integrated cross section of $\sigma = 1100 \pm 150$ mb.

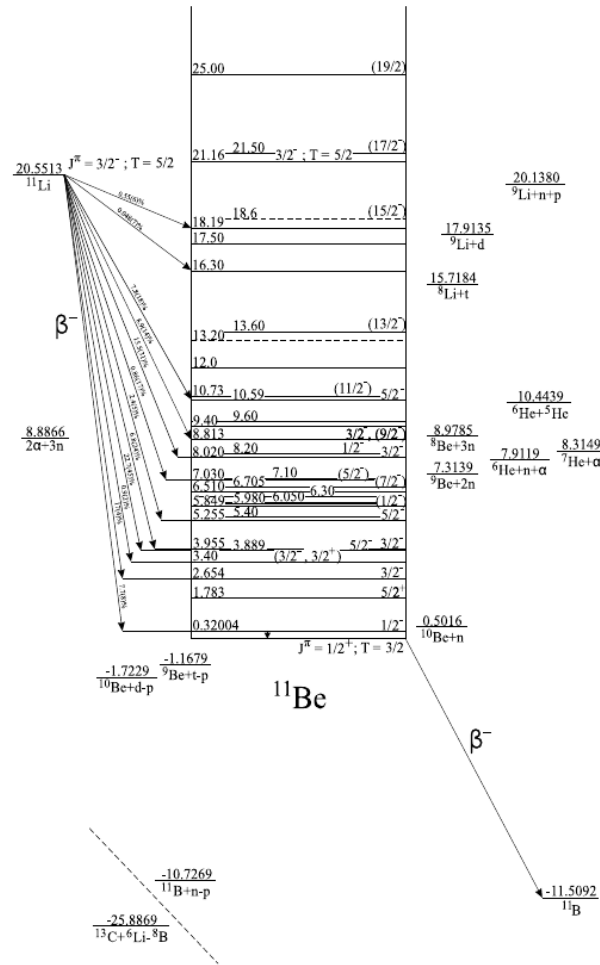


Figure C.2: ^{11}Be level scheme obtained from β -decay and reaction studies [Kel12].

The experiment analysed in this work was performed a beam energies close to the Coulomb barrier. The Coulomb barrier can be defined as the maximum positive value of the real potential, obtained adding the electrostatic potential and the bare part of the nuclear potential. It arises naturally due to the long range of the electromagnetic interaction compared to the short range of the nuclear force. As the distance between the colliding nuclei increases, the nuclear potential tends to zero within few fermi (10^{-15} m), where the repulsive Coulomb potential still has non-negligible values, becoming the dominant force. This creates a (positive) maximum in the potential at a certain radius. Classically, if the energy of the reaction is below this threshold, the projectile cannot penetrate in the potential and the interaction would be purely electromagnetic. Within this picture, a reasonable estimate of the value of the Coulomb barrier is given by

$$V_b = \frac{1}{4\pi\epsilon_0} \frac{Z_p Z_t e^2}{R_b} \quad (\text{C.5})$$

with R_b is an estimate of the distance at which the top of the barrier occurs, and is given by $R_b = 1.44 \times (A_t^{1/3} + A_p^{1/3})$ fm, where A is the mass number.

As mentioned above, similar experiments have been performed by the same collaboration for other halo nuclei, namely ${}^6\text{He}$ [Esc07, Sá08] and ${}^{11}\text{Li}$ [Cub12, Fer13]. The knowledge acquired in those works is the cornerstone of this one, and their common features and differences can help in understanding the dynamics of reactions with halo nuclei, and the particularities of the case with a ${}^{11}\text{Be}$ nucleus.

C.2 Objectives

The motivation to undertake this study is manifold. Mainly, there was a research line of study of halo nuclei in the Experimental Nuclear Physics group at IEM-CSIC and our collaborators, which had performed studies on ${}^{11}\text{Li}$ and ${}^6\text{He}$. Furthermore, no previous data were available for reactions of ${}^{11}\text{Be}$ on heavy targets. The most similar measurement of this kind, namely, the ${}^{11}\text{Be} + {}^{120}\text{Sn}$ reaction measured by the same collaboration at ISOLDE [Aco11] faced several problems which prevented a clear separation of the breakup events from the elastic and inelastic ones. Moreover, in the present experiment, in addition to obtaining a clear separation of the breakup events, we aimed at separating the elastic and inelastic contributions with the help of gamma coincidences.

The final goal of this work, as mentioned earlier, is to contribute to understanding how the halo structure influences the reaction dynamics. Such purpose can be tackled in many ways, so an explanation of the scope of this particular work may help the reader to have an idea of the content of this thesis.

The experimental data provided here are the energy and detection angles of the Be ejectiles after scattering on the ${}^{197}\text{Au}$ target, identifying and extracting the elastic, inelastic and breakup processes. With that, the angular and energy distribution for these three channels will be obtained and compared with calculations.

This work focuses on the simultaneous study of all the channels. Using Silicon and Germanium detectors with high granularity, high resolution charged-particle and gamma spectra could be obtained. The extracted angular distributions provided new experimental data which motivated some theoretical calculations.

The energy of the ${}^{11}\text{Be}$ beam used in this work is 20 times lower than the previous studies of the ${}^{11}\text{Be} + {}^{208}\text{Pb}$ reaction [Fuk04, Nak97, Pal03, Aum00], so the interaction mechanism is completely different. In the high energy regime, the interaction time is considerably shorter than the characteristic time of the electromagnetic interaction (the dominant one), so the interaction can be treated perturbatively. In that framework, first-order calculations are a good approach to the problem. This approximation is also referred to as *sudden*, since beyond this *step*, there is no re-arrangement of the system during the reaction.

The interaction time can be approximated by the time that takes to the incoming particles to cross the distance of closest approach $2 \times a_0$. In our case, this means $t_i \sim 1.21 \times 10^{-21}$ s and

$t_i \sim 0.87 \times 10^{-21}$ s, at 2.9 and 3.6 MeV/u, respectively (the distance of closest approach is $a_0 = 14.3$ fm for the low energy case and $a_0 = 11.5$ fm for the other one). These times are of the same order than the characteristic time of the electromagnetic processes, so including high-order processes becomes essential for a correct description of the data. This gives information on how the systems minimizes its energy through the reaction dynamics.

C.3 Direct reaction theory

The goal of scattering theory is to develop models that, containing relevant information of the colliding nuclei and the dynamics of the process, are able to generate outputs comparable to the measured observables. In this experiment, the measured observables are the angular and energy distribution of the elastic scattering cross section, the inelastic scattering cross section and the breakup cross section. Considering the low energy of the reaction, and the interacting nuclei, five different models were used:

- Optical model:

The optical model is the simplest quantum scattering formalism between composite systems, in which only the elastic scattering is considered explicitly. This means that the internal degrees of freedom of the projectile and target are not considered explicitly and the interaction between them is described by an effective potential depending only on their relative coordinate. The interaction potential is generally built as the sum of the Coulomb potential and a complex (complex meaning that has an imaginary term) nuclear potential. It results in a potential with a real and an imaginary part, where the latter will model the population of other states, removing flux from the elastic channel.

- Equivalent Photon Method (semiclassical calculation).

The Equivalent Photon Method, is a theory for describing reactions dominated by Coulomb interaction from a semiclassical point of view. It treats the relative motion of the projectile and target in terms of classical trajectories, whereas the internal motion of the projectile is treated quantum mechanically.

- Continuum Discretized Coupled-Channels Calculations (CDCC).

The Continuum-discretized Coupled-channels method is an extension of the Coupled-channels formalism in which, in addition to the bound states, continuum states are also taken into account. We call the *continuum* of a nucleus to all the states above the separation energy, in which a nucleon or group of nucleons have enough energy to escape from the binding induced by the attraction of the rest of nucleons. We will focus in the case of the breakup of a projectile (^{11}Be) into a *core* (^{10}Be) and a *valence* particle (neutron) due to the interaction with a target (^{197}Au). Each of the three entities is considered to be inert, so the internal degrees of freedom arise from the relative coordinates of the valence particle with respect to the core (\mathbf{r}, ℓ, s, j). Once the projectile is broken, all values for the relative energy between the valence and the core (ε) allowed by energy conservation can be populated, and each of those ε correspond to a different state, so the number of states with positive energy is actually infinite.

These states are grouped in a finite number of states, either using the binning method,

either using the pseudo-states method, and resulting in a finite number of discrete and square-normalizable states that can be included in the coupled equations system.

- Continuum Discretized Coupled-Channels Calculations including core excitations (XCDCC).

The XCDCC formalism [Sum06, dDALA14] is a CDCC approach, which takes into account possible excitations of one (or both) of the fragments of the projectile. These excitations affect the structure of the projectile (giving rise to core-excited admixtures in the states of the projectile) as well as the reaction dynamics, by allowing excitations and deexcitations of this fragment during the collision.

- Neutron-transfer to the bound and unbound states of the target [Mor06].

This calculation is another approach to calculate breakup. In this approach, instead of describing the states of the neutron with respect to the core, they are described with respect to the target. In general, the TC can account for both, the bound and unbound states of the n+target system that can be populated.

C.4 Experiment and setup

The experiment was performed at TRIUMF (Vancouver, Canada). The facility houses the world's largest cyclotron, able to accelerate H^- ions to energies between 475 and 520 MeV with intensities as high as $100 \mu A$. Once a hydrogen negative ion is accelerated to the desired energy, the two electrons are stripped off from it, generating a proton beam. In ISAC-I the proton beam hits a primary target and produces the radioactive beam using the ISOL method. This method consists of a high-energy beam of light ions, generally a proton beam, that hits a thick target (~ 20 cm). The nuclei in the target are broken and the products are extracted by diffusion towards an ion source. In the ion source the products are selected, extracted and accelerated. The intensity of the ^{11}Be beam, once separated and post-accelerated, was around 10^5 pps in our setup.

Table C.1: Summary of the ion beams produced for the S1202 experiment and the targets used.

2012			2013		
Isotope	Target	Energy (MeV/u)	Isotope	Target	Energy (MeV/u)
^{10}Be	^{208}Pb	3.6	^{12}C	^{197}Au	5.04
^{11}Be	^{208}Pb	3.6	^{11}Be	^{197}Au	3.6
^{11}Be	^{208}Pb	3.1	^{11}Be	^{197}Au	2.9
^{11}Be	^{208}Pb	2.9			

The beam was steered to the reaction chamber, where the ^{197}Au target and the detectors were placed in the position specified in table C.2. The detectors were mounted on a Printed Circuit Board (PCB). The PCB was designed to accomplish a double function, namely having

Table C.2: Silicon detectors used in S1202 for charged particles detection, including their technical specifications and their configuration during the experiment.

L : Nominal distance from the center of the detector to the center of the target.

th : thickness.

DL: dead layer.

θ : Angle between the beam direction and the direction to the center of the detector.

*: Serial number refers to reference number given by the production firm, Micron Electronics Ltd.

	Telescope	type	θ, L	Serial number*	Det. th. (μm)	front DL th. (nm)	back DL th. (nm)
ΔE	1	DSSSD	28°, 80 mm	2449-7	42	50+4%(300)	800
	2	DSSSD	45°, 60 mm	2449-10	40	50+4%(300)	800
	3	DSSSD	76°, 60 mm	2561-6	41	50+4%(300)	800
	4	SSSSD	130°, 55 mm	2752-7	20	800	800
E	1	PAD	45°, 60 mm	2712-8	500	800	800
	2	PAD	28°, 80 mm	2331-4	500	800	800
	3	PAD	76°, 60 mm	2712-11	505	800	800
	4	DSSSD	130°, 55 mm	2851-20	295	800	800

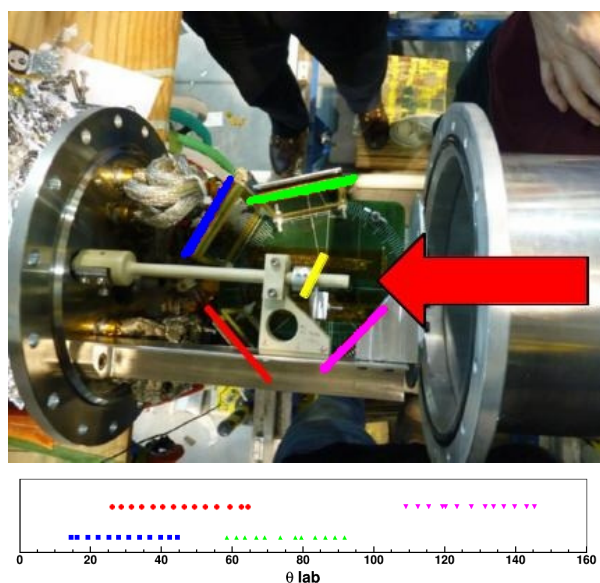


Figure C.3: Position of the detectors in the chamber and angular range covered.

a stable and permanent detector configuration, and providing a circuitry that allowed for a comfortable cabling of the detectors.

The reaction chamber was explicitly designed for this experiment. The geometrical constraints from both the outer and the inner side resulted in the development of a very specific design able to accomplish all the requirements, which basically were:

- Keep the PCB board and the detectors on it in position.
- Leave enough space for cabling the PCB to the flange.

- Provide a structure for mounting the target wheel.
- Leave enough space for moving the target wheel without touching any detector.
- Allow the TIGRESS clovers, around the chamber, to be as close as possible to the target.

The detectors inside the chamber were silicon detectors in telescope configuration, which allowed for particle identification. Basically they consist of two detectors in series. In the first detector, the ions leave only a part of their energy, and in the second they leave the rest. The identification of the ions hitting the detector can be made taking into account that energy deposited by an ion per unit length depends on its Z and its velocity. The first detector (ΔE) had a thickness of $40\ \mu\text{m}$ in all the telescopes except in telescope 4, the one at largest scattering angles, which was a $20\ \mu\text{m}$ one.

Segmented detectors were used in all the telescopes in order to have precise information on the direction in which the fragments were scattered. Using 16×16 Double Sided Silicon Strip Detectors, the angle subtended by a pixel was 3° .

The reaction chamber was surrounded by the TIGRESS detectors. TIGRESS [Bal07] is a High Purity Germanium Detector Array. It is made out of 16 clovers, each of them consisting on 4 High-Purity Germanium crystals. The clovers are distributed covering an important part of the solid angle around the reaction chamber. Four of the clovers are at $\theta_{lab} = 45^\circ$, four at 135° and the remaining eight are arranged in a ring at 90° . Each of the crystals in a clover is divided into eight segments for more accurate gamma tracking. In figure C.4 the reaction chamber with the ring at 90° is shown.

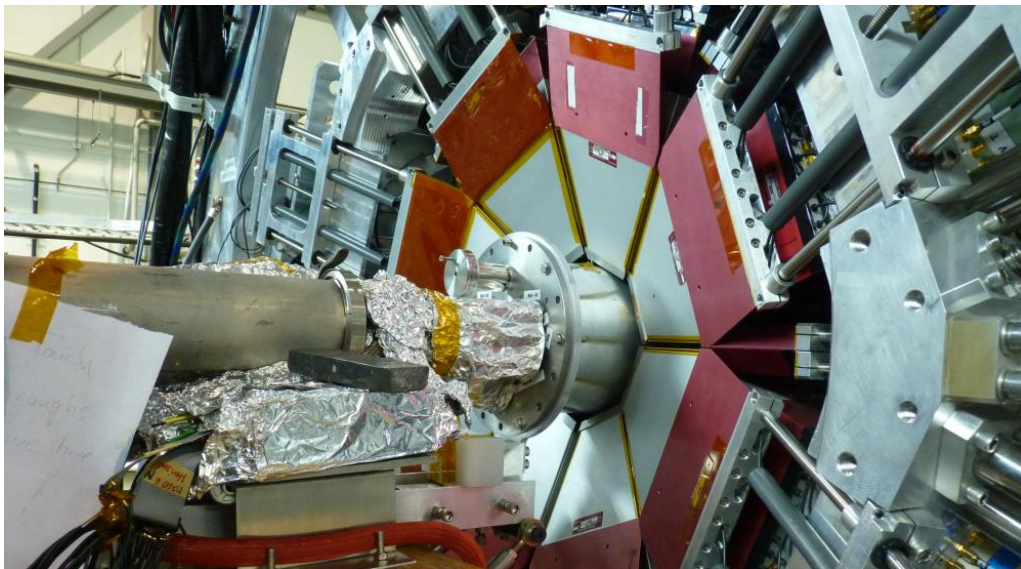


Figure C.4: TIGRESS array closed around the reaction chamber. In this shot the eight clovers forming a ring at 90° can be seen. In particular, it is the BGO crystals surrounding each of the clovers that are visible.

For our experiment the TIGRESS clovers at 45° could not be used. Our reaction chamber was too big for the complete ball to be closed. The chamber was bullet shaped, with a hemisphere fitting with 12 Tigriss clovers and a cylindric extension in the beam direction towards

a flange where the feedthroughs were drilled for cabling the detectors inside.

C.4.1 Calibrations

The three main calibrations performed where:

- Energy calibration of the silicon detectors.
- Optimization of the silicon detector position.
- Efficiency calibration of TIGRESS.

The energy calibration of the silicon detectors was performed using a triple-alpha source and the ^{12}C elastically scattered on the ^{197}Au target. For the SSSSD in telescope 4, it is performed with a ^{152}Gd source and the lowest energy of the triple-alpha source in the cases in which it was stopped. In the rest of the cases it was performed with the Gd source and the signal from a pulser.

The position optimization of the detectors was performed integrating the number of counts per pixel for the ^{12}C scattering, and comparing it with the number of counts obtained with the Rutherford differential cross section, improving the results as shown in figure C.5.

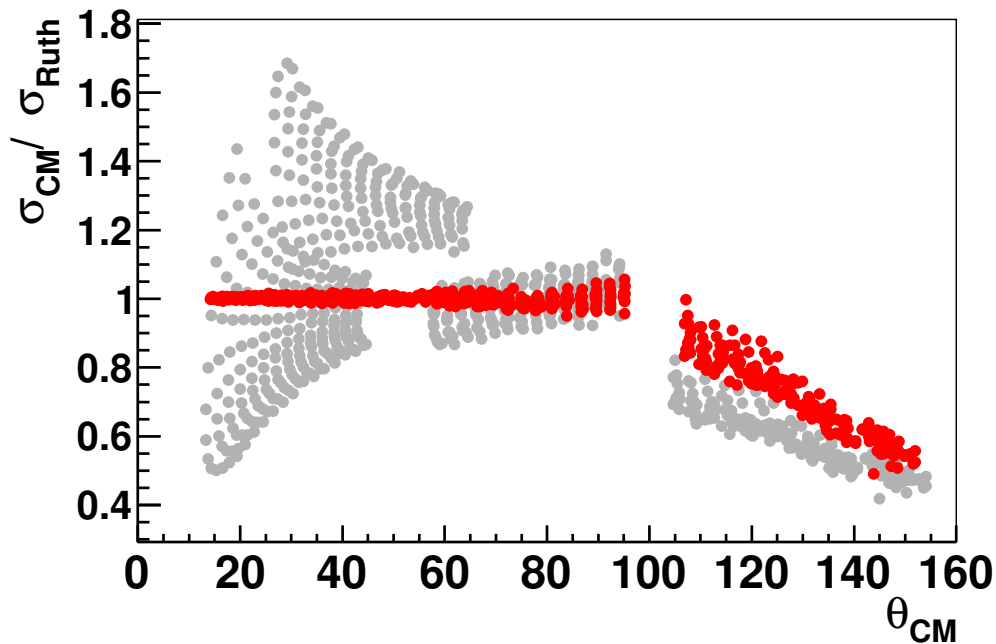


Figure C.5: ^{12}C - ^{197}Au angular distribution around the Coulomb barrier after optimization of the position of telescopes 1, 2 and 3.

The efficiency calibration of the TIGRESS detectors was performed using two gamma sources, a ^{60}Co one and a ^{152}Eu one. The ^{60}Co had a precisely known activity, providing a very accurate absolute efficiency calibration at the two energies of its gamma lines. The ^{152}Eu

has an extensive variety of gamma lines. Comparing their branching ratios and the detected intensity, the dependence of the efficiency with the energy can be extracted, but the activity of this source is not known with the same precision than the cobalt one. Using both sources the absolute efficiency of the TIGRESS in all the energy range of interest could be determined. The efficiency for gammas at 320 keV, which we are interested for identifying the inelastic process, is 0.121(5).

In addition to the calibrations, some conditions were imposed for the data to be included in the analysis. The main one was $p - n$ coincidences in the DSSSD, with an energy difference between them of $E_{diff} < 200$ keV. The FWHM of the peaks in the triple-alpha spectrum was 32 ± 1 keV. It can be noticed that the cut chosen for the E_{diff} is clearly larger than the FWHM. This value was chosen because, in some isolated cases, the energy difference $p-n$ was significant, and it was decided to perform a cut that improved the spectra, but did not introduce an additional error for counting in some pixels more proportion of events than in others.

C.5 Results

In the resulting $\Delta E - E$ plots there are two main regions can be identified. Observing figure C.6, the region with more statistics, and (most often) at a higher total energy ($\Delta E + E$) corresponds to the quasielastic scattering of ^{11}Be , while the region at *lower* energy will correspond to the breakup channel. This offers pixel by pixel information on the reaction channels. The most direct information that can be extracted is:

- Quantity of ^{10}Be fragments detected in one pixel, calculated integrating the number the counts inside the breakup cut.
- Quantity of ^{11}Be fragments detected in one pixel, calculated integrating the number the counts inside the quasielastic cut.
- The breakup probability, calculated as the ratio between ^{10}Be and ^{11}Be fragments.

$$P_{bu} = \frac{N_{bu}}{N_{bu} + N_{qe}} \quad (\text{C.6})$$

The advantage of working with probabilities is minimizing the effect of some experimental errors. Any particularity in the collection, amplification, calibration or selection of the events will affect evenly to all the events in the same pixel. If, for example, the particles detected in one pixel suffer from a lot of struggling in the target because they are in a shaded area of a detector, the count rate in that pixel will be reduced and the same will happen with the cross section directly obtained from it. On the other hand, this reduction will be observed both in elastic and breakup events, so the ratio will not be affected and it can be used for giving more accurate information on the reaction process. For the same reason, the statistics of the pixels at similar polar angle is summed up, presenting the obtained probabilities in angular bins of 3° .

The inelastic channel cannot be separated from the elastic channel using charged-particle spectroscopy alone. The HPGe detector array TIGRESS is used for detecting the gamma radiation emitted after the deexcitation of ^{11}Be in coincidence with the fragments. The use of the

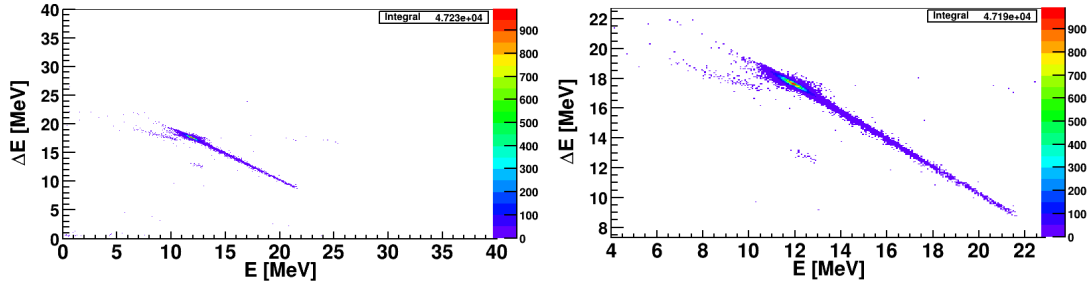


Figure C.6: Two dimensional $\Delta E - E$ plots for ^{11}Be on ^{197}Au below the Coulomb barrier. Energy deposited in the ΔE detector in the Y axis, versus energy deposited in the E detector in the X axis. It is observed that breakup and quasielastic are well separated. These are all the events collected during the experiment in a single pixel for at $E_{lab} = 2.9 \text{ MeV/u}$.

gamma detectors make it indispensable to correct for the efficiency of the array. This fact, together with the low probability of excitation, and the subsequent low count rate, entails an increase in the uncertainty with respect to the breakup calculation.

In this case, the inelastic scattering probability is defined as:

$$P_{inel} = \frac{N_{in}}{\varepsilon_{\gamma} N_{Be}} \quad (\text{C.7})$$

where N_{in} is the number of events in coincidence with the gamma of interest, at 320 keV, in TIGRESS, ε_{γ} is the efficiency of TIGRESS at this energy, and N_{Be} is the number of counts of the Be fragments of any kind. The events after gating on the gamma are shown in figure C.7. For minimizing The elastic scattering probability is calculated subtracting the inelastic from the quasielastic.

$$\begin{aligned} P_{el} &= \frac{N_{qel} - \frac{N_{in}}{\varepsilon_{\gamma}}}{N_{Be}} \\ &= \left(\frac{N_{qel}}{N_{Be}} \right) - \left(\frac{N_{in}}{\varepsilon_{\gamma} N_{Be}} \right) \\ &= (1 - P_{bu}) - (P_{in}). \end{aligned} \quad (\text{C.8})$$

C.5.1 Discussion

The obtained results are compared to calculations performed using several formalisms. The different formalisms focus on different aspects of the reaction, so it is worth to explain the results within the scope of each calculation.

The first evidence of the halo structure in ^{11}Be is an unusual behaviour of the elastic scattering, with a disappearance of the Coulomb-nuclear interference peak, and a departure of the Rutherford cross section at relatively small angles. This is explicitly evidenced within the Optical Model (fit in figure C.8) in the need of a extremely large value in the diffuseness of the imaginary potential $a_i = 8.6 \text{ fm}$. The sensitivity radius is found at around $r_{sens} = 35\text{-}40 \text{ fm}$, which, compared the the sum of the radii of ^{11}Be and ^{197}Au ($R = 14.3 \text{ fm}$), evidenced the im-

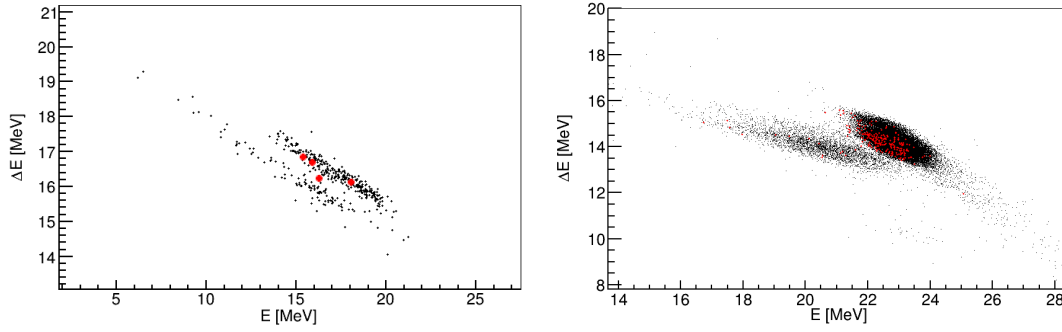


Figure C.7: Two-dimensional $\Delta E - E$ plots in coincidence with 320 keV gamma (red points) represented on $\Delta E - E$ plots with no gating. On the left the case with a single pixel, where the low number of counts is evidenced. On the right the number of counts summed for all the angular bin of 3° .

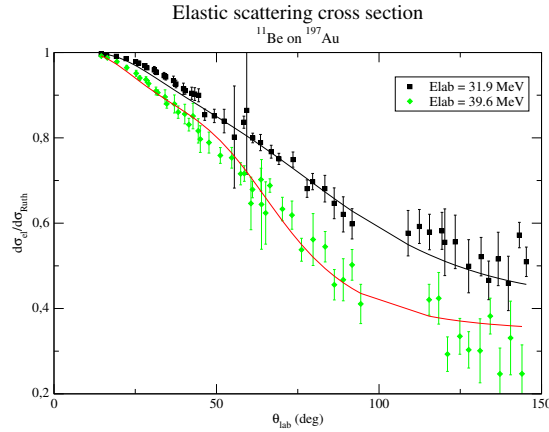


Figure C.8: Elastic scattering relative to Rutherford cross section. Experimental data and fit within an optical model including a Woods-Saxon potential for the real and the imaginary part. The measurements were performed at two beam energies: 3.6 MeV/u (39.6 MeV) and 2.9 MeV/u (31.9 MeV). For all the calculations the reaction is supposed to happen in the center of the target, and the energies at which the reaction takes place are $E_{lab} = 39.17$ MeV ($E_{cm} = 37.09$ MeV) and $E_{lab} = 31.30$ MeV ($E_{cm} = 29.64$ MeV), which are around and below the Coulomb barrier ($V_b \sim 40$ MeV), respectively.

portance of long range couplings and the dominance of the Coulomb repulsion in the reaction dynamics.

A first order calculation using the Equivalent Photon Method is able to explain the inelastic scattering data at forward angles (up to $\sim 50^\circ$), but clearly underestimates the breakup cross section at forward angles, where it is expected to be a good approach (see figure C.9). This differs significantly from the case of the $^{11}\text{Li}+^{208}\text{Pb}$ reaction, where the breakup probability at small angles could be well reproduced with a first order calculation.

CDCC calculations were performed, including states in the continuum of the $^{10}\text{Be}-n$ system up to $E_{max} = 10$ MeV and $\ell_{max} = 10$. These calculations reproduce the breakup data (see figure C.10), without introducing any modification in the $\mathcal{B}(E1)$, only including a large model space and solving the coupled equations at all orders. This results show an unexpected relevance of high-order effects at forward angles. Although the adiabaticity parameter is of the

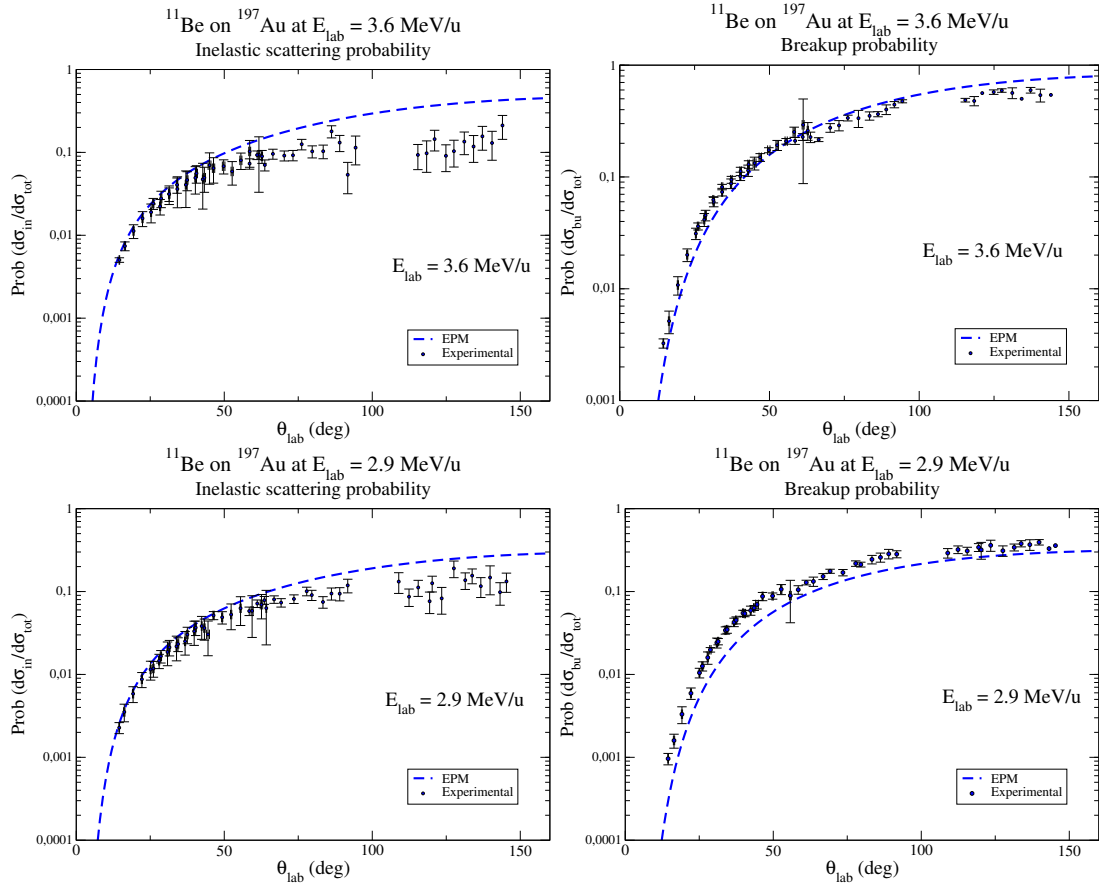


Figure C.9: Left: Experimental inelastic scattering probability data compared with a first order EPM calculation. For the calculation the experimental accepted value $B(E1; 1/2^+ \rightarrow 1/2^-) = 0.116 e^2 fm^2$ [Mil83] was used. The calculations show a good agreement with data at forward scattering angles for both energies. Right: experimental breakup probability data compared with a first order EPM calculation. The $B(E1)$ used for the calculation is the one obtained with the particle rotor model using the parameters in table 5.4 (presented in the text and extracted from [Sum07]), which explains previous experimental data at higher energies. This approach is expected to be correct where the Coulomb interaction is dominant, i.e., at forward angles. However, we have found that the calculation underestimates the results, evidencing the influence of multistep couplings (beyond first order), or the importance of higher multipoles.

order of one, which should imply that the probability of interacting in more than one step is not negligible, forward scattering corresponds to distant trajectories, where usually the couplings are not very strong, reason why it was expected that the breakup in this angular range could be explained within a first-order calculation.

The converged CDCC calculation is able to match the experimental breakup cross section but

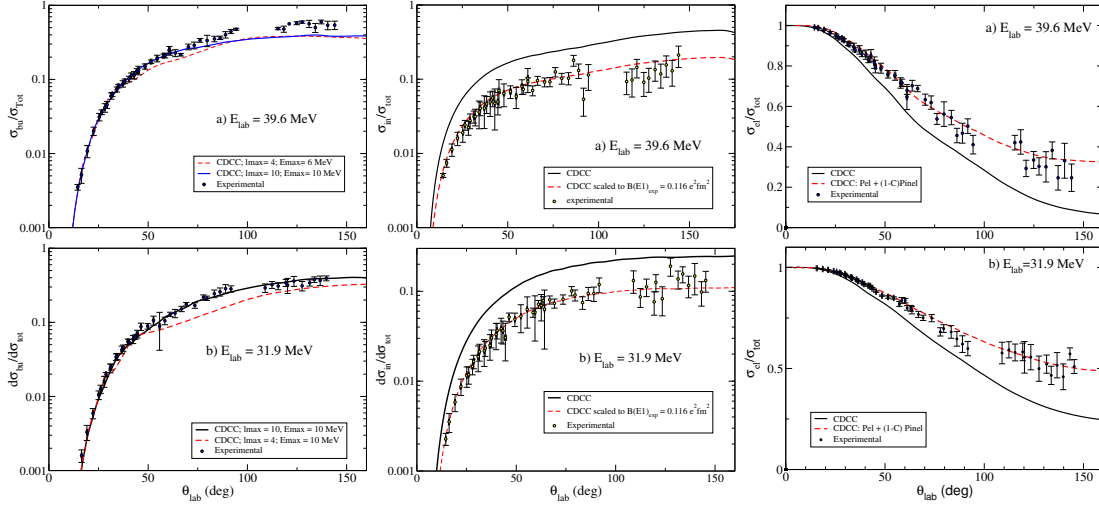


Figure C.10: Left: experimental breakup probability data compared with CDCC calculations at energies around and below the barrier. It is observed that the calculation explains the data below the barrier. Around the barrier, underestimates the data at angles larger than 80° . Large angles and high energy correspond to the cases in which the neutron of the halo penetrates most into the target and is more likely that we populate $^{197}\text{Au}+n$ states, which are difficult to describe within the CDCC approach. Center: the inelastic scattering probability is shown for both energies. The calculation overestimates the data, but scaling from the $B(E1)$ that we have in the single-particle model we use, to the experimental $B(E1)$, there is an agreement between the calculation and the data. Right: the elastic scattering probability is shown. For the data to be explained, it is necessary to add the same amount the cross section extracted previously from the inelastic channel.

fails in the precise assignment to the elastic and inelastic channels (see figure C.10). Also in the cases where the valence neutron penetrates more in the target potential underestimates the breakup cross section.

The XCDCC calculations (shown in figure C.11) showed a clear improvement over the other formalisms, being able to describe the data in all the reaction channels with a single calculation. The improvement is attributed to the fact that a particle-rotor model is used to describe the $^{10}\text{Be}-n$ system (thus taking into account the deformation of the ^{10}Be and including a more realistic wavefunction of the ^{11}Be states), rather than to a dynamic excitation of the core during the interaction. The subtle influence of the complete wavefunction of the ^{11}Be in the reaction dynamics is evidenced in a low energy scattering experiment on a heavy target.

Transfer calculations to bound and unbound states of the target were performed to quantify the contribution of the neutron transfer to bound and unbound states of the ^{197}Au target at the energy around the Coulomb barrier. This calculation evidenced that this process is dominant, precisely, in the case where the CDCC failed, which is for angles larger than $\theta = 75^\circ$ (see figure C.12).

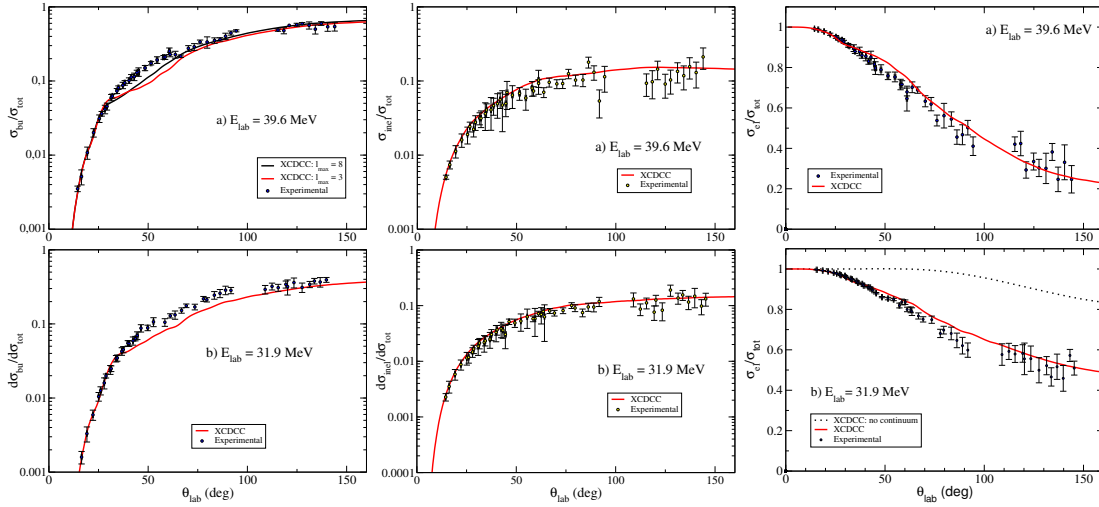


Figure C.11: Left: experimental breakup probability data at energies around and below the Coulomb barrier compared to preliminary XCDCC calculations. At both energies, the calculation explains the data at small and large scattering angles. At intermediate angles some convergence problems cause an irregularity in the cross section. It is expected that as we improve our capability to deal with the computational limitations, the description of the breakup will not differ from the one obtained with CDCC calculation. Center: the inelastic scattering probability which explains the data with no need of scaling or correction. Right: the elastic scattering is also well explained by the calculation except at intermediate angles, where the convergence problems are more evident.

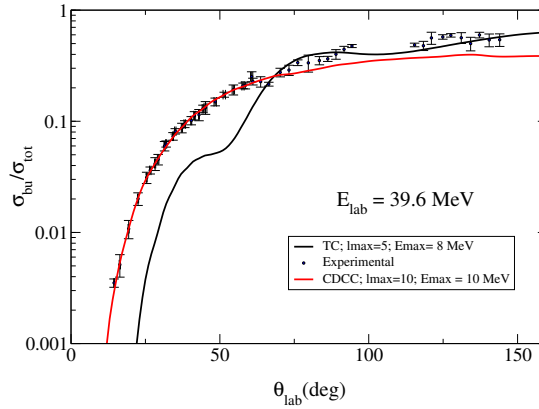


Figure C.12: Experimental breakup probability data compared with TC calculations at energies around the Coulomb barrier. It is observed, that the data at high energies and large scattering angles, conditions in which the neutron of the halo penetrates most into the target, are well described by this approach.

C.6 Conclusions

In this work, we have performed a comprehensive analysis of the $^{11}\text{Be}+^{197}\text{Au}$ reaction measured in 2013 at TRIUMF (Vancouver, Canada), within an international collaboration led by the IEM-CSIC and the Universities of Huelva and Seville (Spain). The measured data consist of elastic, inelastic (populating the only bound state of ^{11}Be) and inclusive breakup (^{10}Be fragments) angular distributions. These data have been compared with a variety of the-

oretical models, from which relevant information on the structure of ^{11}Be and on the reaction dynamics has been extracted. The main conclusions are:

- The setup, specifically designed for the experiment, together with the use of the High-purity Ge detector array TIGRESS, were suitable for obtaining the desired data, identifying the main reaction channels along a large angular range, from $13^\circ < \theta < 150^\circ$.
- TRIUMF and ISAC-II have delivered a continuous ^{11}Be beam with high energy resolution, low contamination and high yield.
- There are clear evidences of the important role played by long range couplings. Experimental observations in this direction are the strong absorption in the elastic channel, even at forward angles, and the large number of partial waves in the CDCC calculations that are needed for reproducing the data. For reproducing the angular distribution at energies close to the barrier a TC approach has resulted more successful than a CDCC approach, showing that the neutron populates unbound states of the ^{198}Au .
- The specific structure of ^{11}Be , with a deformed ^{10}Be core that can rotate, plays a role in the reaction process, as can be inferred from the fact that an XCDCC calculation is necessary to explain all the measured observables, in contrast to the 3-body CDCC calculation using a 2-inert-bodies model for describing the ^{11}Be projectile.
- The scope for the near future is analysing the data of the $^{11}\text{Be}+^{208}\text{Pb}$ reaction, measured at TRIUMF in 2012, and continue working on the convergence of the XCDCC and TC calculations.

The work presented here has succeeded in its initial goals: to study the elastic, inelastic and breakup cross sections of ^{11}Be , a one-neutron halo nucleus, in a strong electric field created by a heavy target at energies around and below the Coulomb barrier. Valuable and original experimental data has been provided and has contributed to a better understanding of the reactions at low energies involving halo nuclei and heavy targets.



D.1 Introducción

Este trabajo es parte de una serie de experimentos llevados a cabo por una colaboración internacional liderada por los grupos de física nuclear del IEM-CSIC y de las Universidades de Sevilla y Huelva. El objetivo de estos experimentos es la comprensión de la dinámica de las colisiones de núcleos ligeros débilmente ligados con blancos pesados a energías cercanas a la barrera de Coulomb. Previamente al trabajo presente, esta colaboración ha medido las reacciones ${}^6\text{He}+{}^{208}\text{Pb}$ (en Louvain-la-Neuve), ${}^{11}\text{Be}+{}^{120}\text{Sn}$ (CERN-ISOLDE) y ${}^{11}\text{Li}+{}^{208}\text{Pb}$ (TRIUMF).

Continuando en la misma línea, en esta tesis estudiamos la reacción del núcleo ${}^{11}\text{Be}$ con un blanco de oro (${}^{197}\text{Au}$) a dos energías incidentes, 31.9 y 39.6 MeV, que están por debajo y alrededor de la barrera de Coulomb ($V_b \sim 40$ MeV), respectivamente. Estos datos experimentales, junto con una interpretación adecuada utilizando diferentes cálculos teóricos, contribuye a la comprensión de cómo la estructura de halo, observada en algunos núcleos cercanos a las líneas de goteo de protones y neutrones, influye en la dinámica de la reacción de alrededor y por debajo de la barrera de Coulomb, donde los efectos nucleares deben ser poco relevantes. Los datos analizados como parte de este trabajo doctoral se adquirieron en el experimento S1202 realizado en TRIUMF, que se describirá a fondo a lo largo del texto.

El núcleo ${}^{11}\text{Be}$ es un núcleo con halo de un neutrón. Los núcleos con halo son sistemas débilmente ligados, cerca de la línea de goteo de protones o de neutrones, en los que uno o dos nucleones tienen una probabilidad alta de encontrarse a grandes distancias del *core* del núcleo, más allá del rango del potencial nuclear. La principal fuente de información de estos núcleos son reacciones nucleares en las que estos núcleos se hacen colisionar con núcleos blanco estables. Dado que son sistemas inestables (por ejemplo el ${}^{11}\text{Be}$ decae en 13.76 (7) s por emisión beta a ${}^{11}\text{B}$), estas reacciones requieren un mecanismo para producir estos núcleos inestables y acelerarlos, usándolos como proyectiles que bombardean un blanco compuesto por núcleos estables.

Para este estudio, se eligió una reacción con un núcleo blanco pesado. Los núcleos pesados tienen una gran cantidad de protones, que se traduce en una fuerte repulsión electrostática

sentida por el proyectil. En una representación muy simplista, las reacción $^{11}\text{Be}+^{197}\text{Au}$ puede ser imaginada como el neutrón del halo no sintiendo el campo mientras que el núcleo es repelido por el blanco, produciéndose fácilmente la ruptura (*breakup*) del proyectil. En particular, este proceso se conoce como disociación dipolar coulombiana, y anteriores trabajos en otros regímenes de energía o para reacciones similares [Sá08, Esc07, Fer13, Cub12, Nak97, Aum00, Fuk04, Pal03] concluyeron que tiene una importante contribución en reacciones con núcleos con halo. La importancia de este proceso en este caso concreto y las demás contribuciones a las secciones eficaces serán objeto de este estudio.

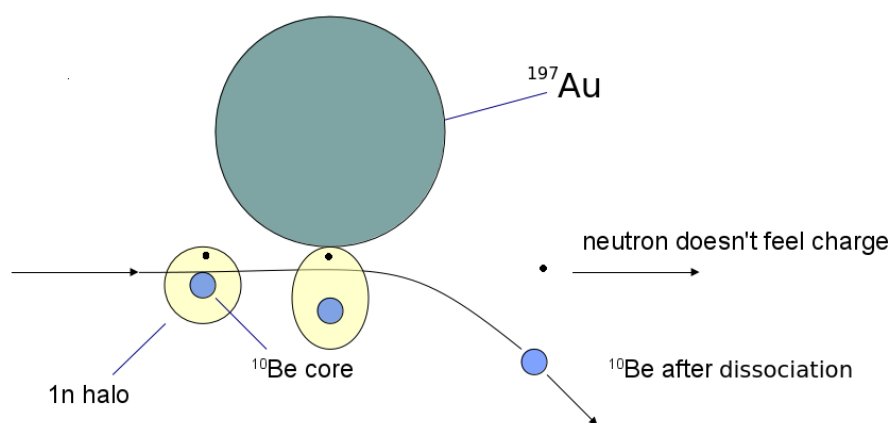


Figure D.1: Representación simplificada del proceso de ruptura que el ^{11}Be puede sufrir al dispersarse con un blanco pesado.

La realización de este experimento requiere una instalación capaz de producir haces radioactivos. La alta calidad del haz de ^{11}Be producido en TRIUMF (Vancouver, Canadá) y la posibilidad de utilizar el conjunto de detectores de alta pureza TIGRESS para la detección de la radiación gamma producida en la reacción, fueron las razones para elegir esa instalación.

El núcleo ^{11}Be

En general, un núcleo halo es un sistema compuesto de un *core* compacto, formado por la mayoría de sus nucleones, y un halo difuso formado por uno o dos nucleones débilmente ligados. En principio, tanto protones como neutrones pueden formar un halo. Sin embargo, en el caso de los protones, la barrera de Coulomb tiende a confinar los nucleones dentro del alcance del potencial, lo que dificulta la formación de una estructura de halo. Tales estructuras se observan cerca de las líneas de goteo, donde hay un exceso de protones o de neutrones que todavía pueden estar unidos al núcleo pero con energía de ligadura muy baja. A consecuencia de esto, estos nucleones se pueden encontrar a grandes distancias del centro del núcleo. Por decirlo con corrección cuántica, la función de onda de estas partículas tiene una larga cola, es decir, su densidad se extiende hasta radios anormalmente grandes, en comparación con otros núcleos de la misma masa.

El berilio es el cuarto elemento en la tabla periódica, lo que a su vez significa que tiene 4 protones. El caso particular de ^{11}Be tiene, como su nombre lo indica, 11 nucleones, los 4

protones y 7 neutrones. El único isótopo estable de berilio es ${}^9\text{Be}$, que tiene una estructura que puede ser imaginada como dos partículas alfa unidas por un neutrón. Ese neutrones juega un papel comparable al que el electrón hace en un enlace covalente. Añadiendo otro neutron se obtiene ${}^{10}\text{Be}$, que tiene la misma estructura, pero con dos neutrones llevando a cabo esta especie de función covalente. El núcleo ${}^{10}\text{Be}$ ($j^\pi = 0^+$) decae a través de β^- a ${}^{10}\text{B}$ ($j^\pi = 3^+$) con una vida media de $t_{1/2} = 1,6 \times 10^6$ años, por lo que puede considerarse estable en términos de reacciones nucleares. La adición de un neutrón extra al ${}^{10}\text{Be}$ supone la aparición en escena de una estructura completamente diferente. La vida media del ${}^{11}\text{Be}$ ($j^\pi = 1/2^+$), que decae por emisión β^- a ${}^{11}\text{B}$ ($j^\pi = 3/2^-$), es $t_{1/2} = 13,76$ (7) s (10^{12} veces menor) [Kel12], por lo que los requisitos experimentales el estudio de este núcleo serán más exigentes.

Describiendo el ${}^{11}\text{Be}$ a partir solamente a partir de los estados monoparticulares del neutrón en el campo medio del ${}^{10}\text{Be}$, su estado fundamental se encuentra con el neutrón en una órbita s de la capa sd ($j^\pi = 1/2^+$) debido a una inversión entre las órbitas $s_{1/2}$ y $1p_{1/2}$. Para $N = 7$, a medida que se quitan protones del núcleo ${}^{15}\text{O}$, el *gap* que típicamente se encuentra a $N = 8$ (entre las capas $1p$ y sd) se hace más pequeño. En su lugar, al subir la posición en energía de la órbita $p_{1/2}$, el *gap* aparece en $N = 6$, dando lugar a la llamada estructura de capa cerrada al ${}^{10}\text{Be}$. La energía necesaria para acceder al primer estado excitado de ${}^{10}\text{Be}$ (3368 keV), comparada con la energía de los primeros estados excitados del ${}^{12}\text{Be}$ (2101 keV), refuerza la hipótesis de que la capa se cierra para $N = 6$. La capa cerrada del núcleo ${}^{10}\text{Be}$, junto con la órbita s y la pequeña energía ligadura del último neutrón, son factores que contribuyen a que el ${}^{11}\text{Be}$ sea un núcleo halo, con un halo formado por un neutrón débilmente ligado a un *core* de ${}^{10}\text{Be}$. Esquemáticamente, la función de onda del estado fundamental del ${}^{11}\text{Be}$ puede escribirse como

$$|{}^{11}\text{Be}(\text{g.s.})\rangle_{1/2^+} = |{}^{10}\text{Be}(0^+)\rangle \otimes \nu(s_{1/2})\rangle_{1/2^+}. \quad (\text{D.1})$$

La energía de separación del último neutrón es $S_n = 501.6$ keV. A pesar de ser baja, es suficientemente alta como para que órbita p quede por debajo de la energía umbral de separación, por lo que el ${}^{11}\text{Be}$ presenta un estado excitado ligado ($J^\pi = 1/2^-$), que se encuentra a $E_x = 320.04(10)$ keV por encima del estado fundamental ($S_n = 181.6$ keV),

$$|{}^{11}\text{Be}^*\rangle_{1/2^-} = |{}^{10}\text{Be}(0^+)\rangle \otimes \nu(p_{1/2})\rangle_{1/2^-}. \quad (\text{D.2})$$

Es posible poblar este estado a través de una transición dipolar eléctrica $E1$ desde el estado fundamental, y siendo destacable que la probabilidad de transición dipolar entre estos dos estados, $\mathcal{B}(E1) = 0.116 \pm 0.012 e^2 fm^2$ [Mil83], es la mayor $\mathcal{B}(E1)$ medida hasta la fecha entre estados ligados.

La descripción puramente monoparticular de ${}^{11}\text{Be}$, dada por las ecuaciones (D.1) y eq. (D.2) es útil en un gran número de contextos, pero es una simplificación funcional de un sistema subyacente más complicado. Estudios experimentales y teóricos han puesto de manifiesto que los estados de baja energía de ${}^{11}\text{Be}$ contienen contribuciones significativas del del core de ${}^{10}\text{Be}$ en estados excitados. Manteniendo una descripción en términos de un *core* de ${}^{10}\text{Be}$ y un neutrón de valencia, y teniendo en cuenta estas excitaciones, el estado fundamental

de ^{11}Be puede escribirse de la siguiente forma

$$\begin{aligned}
 |^{11}\text{Be}(\text{g.s.})\rangle_{1/2^+} &= \alpha |^{10}\text{Be}(0^+) \otimes \nu(s1/2)\rangle_{1/2^+} \\
 &+ \beta |^{10}\text{Be}(2^+) \otimes \nu(d5/2)\rangle_{1/2^+} \\
 &+ \gamma |^{10}\text{Be}(2^+) \otimes \nu(d3/2)\rangle_{1/2^+} \\
 &+ \dots
 \end{aligned} \tag{D.3}$$

con pesos $\alpha^2 \sim 0.86$, $\beta^2 \sim 0.12$ y $\gamma^2 \sim 0.02$ extraídos de [Lay12b] (usando el modelo partícula-rotor descrito en [Nun96], y consistente con los resultados experimentales obtenidos en [Zwi79, For99, Win01, Sch12]. Análogamente, el único estado excitado ligado queda mejor descrito del siguiente modo:

$$\begin{aligned}
 |^{11}\text{Be}^*\rangle_{1/2^-} &= a |^{10}\text{Be}(0^+) \otimes \nu(p1/2)\rangle_{1/2^-} \\
 &+ b |^{10}\text{Be}(2^+) \otimes \nu(f5/2)\rangle_{1/2^-} \\
 &+ c |^{10}\text{Be}(2^+) \otimes \nu(p3/2)\rangle_{1/2^-} \\
 &+ \dots
 \end{aligned} \tag{D.4}$$

con pesos $a^2 \sim 0.79$, $b^2 \sim 0.21$ y $c^2 \sim 0.004$ extraídos de [Lay12a], y compatibles con los valores experimentales medidos por Schmitt [Sch12]. En [Nun96], las configuraciones extra resultantes de acoplamiento del neutrón de valencia a estados excitados del *core* han sido interpretados en un modelo de partícula-rotor, suponiendo una deformación permanente del núcleo de ^{10}Be ($\beta = 0.67$). En las configuraciones extra consideradas en las ecuaciones (D.1) y (D.2) el neutrón se encuentra en una órbita *d* y, además, la energía de separación efectiva del neutrón es mayor (debido a la energía del core). Ambos factores hacen que en dichas configuraciones no se manifieste la estructura de halo.

Por encima de la energía de separación del último neutrón, muchos otros estados han sido identificados (véase [Kel12] para una revisión reciente). Un ejemplo de ello son las dos resonancias estrechas observadas en el experimento de Fukuda y colaboradores, una a 1.78 MeV ($J^\pi = 5/2^+$) y otra a 3.41 MeV ($J^\pi = 3/2^+$) [Fuk04].

Existen numerosos estudios de reacciones de ^{11}Be con diferentes núcleos y a diversas energías. Los experimentos más similares al nuestro se enumeran a continuación:

- $^{208}\text{Pb}(^{11}\text{Be}, ^{10}\text{Be}+n)^{208}\text{Pb}$: Medidas exclusivas de breakup, en las que se medían el neutrón y el ^{10}Be producidos en coincidencia, fueron realizados en RIKEN a energías ~ 70 MeV/u [Nak97, Fuk04] y en GSI a energías ~ 520 MeV/u [Pal03]. Para ángulos de dispersión suficientemente pequeños, las secciones eficaces de ruptura medidas en estas reacciones están dominadas por la interacción dipolar eléctrica ($E1$), hecho que permite extraer la probabilidad de transición eléctrica reducida $d\mathcal{B}(E1)/dE$ mediante la comparación de dichas secciones eficaces con un modelo de reacción adecuado. A pesar de que las distribuciones de la $\mathcal{B}(E1)$ obtenidas difieren entre ellas significativamente, las tres medidas citadas predicen valores grandes de $\mathcal{B}(E1)$ para energías próximas al umbral de ruptura, como se espera para los núcleos halo. Estos experimentos también ofrecieron estimaciones del factor espectroscópico de la configuración $\nu 2s_{1/2} \otimes ^{10}\text{Be}(0^+)$ en la función de onda del estado fundamental del ^{11}Be : $S = 0.61 \pm 0.05$ [Pal03] y $S = 0.72 \pm 0.04$ [Fuk04].

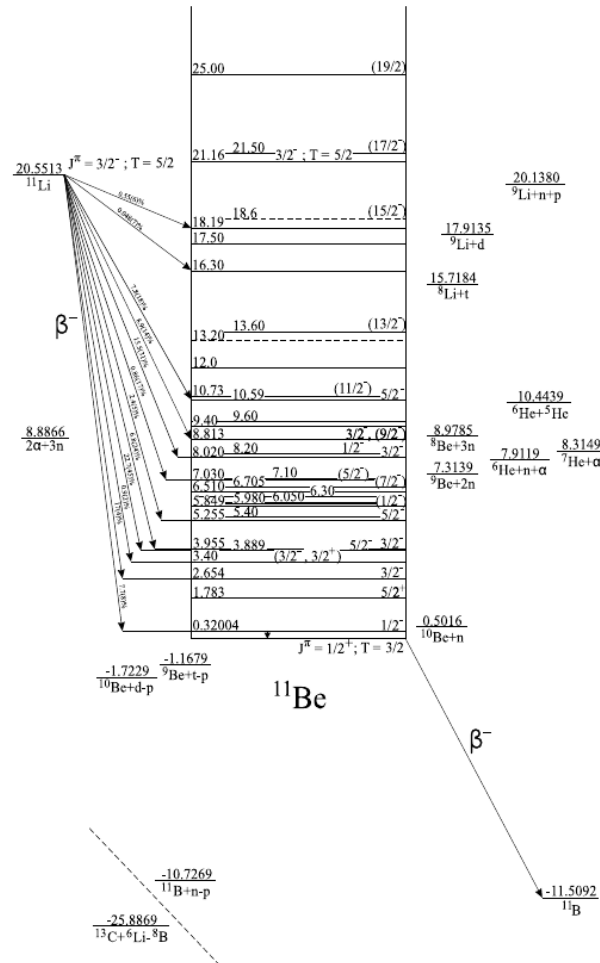


Figure D.2: Esquema de niveles del ^{11}Be obtenido a partir de la desintegración beta y el estudio de reacciones [Kel12].

- $^{12}\text{C}(^{11}\text{Be}, ^{10}\text{Be}+n)^{12}\text{C}$: Medidas de breakup con blancos ligeros (por ejemplo ^{12}C), en las que los efectos nucleares son dominantes, permitieron la identificación de resonancias a bajas energías y asignarles spin y paridad. En [Fuk04] se observaron dos resonancias, una a $E_x = 1.78$ MeV ($J^\pi = 5/2^+$) y una $E_x = 3.41$ MeV ($J^\pi = 3/2^+$).
- $^{64}\text{Zn}(^{11}\text{Be}, ^{11}\text{Be})^{64}\text{Zn}$ [Pie13] y $^{120}\text{Sn}(^{11}\text{Be}, ^{11}\text{Be})^{120}\text{Sn}$ [Aco11]: Estos experimentos, realizados en CERN-ISOLDE evidenciaron las diferencias de las reacciones usando diferentes isótopos de Be ($^9,^{10},^{11}\text{Be}$) contra blancos de masas intermedias a energías alrededor de la barrera de Coulomb. Para el canal elástico, se observó una gran absorción a todos los ángulos medidos ($10^\circ < \theta_{cm} < 120^\circ$). Esta absorción también produce la desaparición del patrón de difracción característico al ángulo de trayectoria rasante. Este ángulo, clásicamente, se corresponde con trayectorias del proyectil en las que la distancia de máxima aproximación es similar al radio de interacción, en el que los potenciales de Coulomb y nuclear son del mismo orden. En el experimento con el blanco de Zn, la resolución en los ángulos hacia adelante fue suficiente para separar los fragmentos de ruptura, para los que estimaron una sección eficaz de breakup integrada de $\sigma = 1.100 \pm 150$ mb.

El experimento analizado en este trabajo se realizó a energías alrededor de la barrera de Coulomb. La barrera de Coulomb se puede definir como el valor máximo positivo del potencial real, obtenido sumando el potencial electrostático y el potencial nuclear. La barrera surge de forma natural debido al largo alcance de la interacción electromagnética en comparación con el de corto alcance de la fuerza nuclear. A medida que la distancia entre los núcleos aumenta, el potencial nuclear tiende a cero en unos pocos fermi (10^{-15} m), donde el potencial de Coulomb de repulsión todavía tiene valores no despreciables, convirtiéndose en la fuerza dominante. Esto crea un máximo (positivo) en el potencial a un radio determinado. Clásicamente, si la energía de la reacción está por debajo de este umbral, el proyectil no puede penetrar en el potencial y la interacción sería puramente electromagnética. Dentro de este marco, una estimación razonable del valor de la barrera de Coulomb está dada por

$$V_b = \frac{1}{4\pi\epsilon_0} \frac{Z_p Z_t e^2}{R_b} \quad (\text{D.5})$$

donde R_b es una estimación de la distancia a la cual se encuentra el máximo de la barrera, dada por $R_b = 1.44 \times (A_t^{1/3} + A_p^{1/3})$ fm, donde A es el número másico.

Como se menciona arriba, se han realizado experimentos similares con otros núcleos halo en el marco de esta colaboración, como son ^6He [Esc07, Sá08] y ^{11}Li [Cub12, Fer13]. El conocimiento adquirido en esos trabajos componen la piedra angular del presente trabajo y se realizará un análisis que permita identificar los puntos comunes y las diferencias, lo que ayudará a entender la dinámica de las reacciones con núcleos halo y las particularidades del caso de ^{11}Be .

D.2 Objetivos

La motivación para llevar a cabo este estudio proviene de diferentes frentes. Principalmente, existía una línea de investigación de reacciones con núcleos halo en el grupo de Física Nuclear Experimental del IEM-CSIC junto con nuestros colaboradores, dentro de la cual se habían realizado estudios de ^{11}Li y ^6He contra blancos de ^{208}Pb a energías cercanas a la barrera coulombiana. Además, no había datos disponibles a estas energías para reacciones de ^{11}Be con blancos pesados. El experimento más similar, la reacción $^{11}\text{Be} + ^{120}\text{Sn}$, fue medida por esta colaboración en ISOLDE [Aco11], experimentó varios problemas que impidieron una separación clara de los sucesos de breakup respecto de los elásticos e inelásticos. En este caso, no solamente se obtuvo una clara separación entre ellos, sino que las contribuciones elásticas e inelásticas pudieron separarse utilizando coincidencias gamma.

El objetivo final de este trabajo, como se mencionó anteriormente, es contribuir a entender cómo la estructura de halo influye en la dinámica de las reacciones nucleares. Tal propósito se puede abordar de diferentes maneras, por lo que una explicación del alcance de este enfoque en particular, puede ayudar a que el lector tenga una idea más concreta del contenido de esta tesis.

La información experimental extraída más directamente es la energía y el ángulo a los que los eyectiles de Be son detectados después de la dispersión en el blanco de ^{197}Au , identificando y extrayendo los canales elástico, inelástico y breakup. De este modo, la sección eficaz

en función del ángulo y de la energía para cada uno de estos tres canales puede ser obtenida y comparada con diferentes cálculos.

Este trabajo se centra en el estudio simultáneo de todos estos canales. Usando detectores de silicio y germanio con alta granularidad, se puede realizar espectroscopía gamma y de partículas cargadas de alta resolución. Las distribuciones angulares extraídas proporcionaron nuevos datos experimentales que motivaron avances en algunos cálculos teóricos.

La energía del haz de ^{11}Be utilizado en este trabajo es 20 veces menor que los estudios anteriores de $^{11}\text{Be}+^{208}\text{Pb}$, por lo que el mecanismo de interacción es completamente diferente. A energías altas, el tiempo de interacción es considerablemente más corto que el tiempo característico de la interacción electromagnética (el dominante), por lo que la excitación puede tratarse perturbativamente. En ese marco, los cálculos de primer orden son una buena aproximación al problema. Esta aproximación también se conoce como *sudden* (repentina), ya que más allá de este primer *paso*, no hay una reorganización del sistema.

El tiempo de interacción puede ser calculado aproximadamente como el tiempo en el que el proyectil recorre la distancia de máxima aproximación, $2 a_0$. En nuestro caso, esto equivale a $t_i \sim 1.21 \times 10^{-21}$ s y $t_i \sim 0.87 \times 10^{-21}$ s, a 2.9 y 3.6 MeV/u, respectivamente (la distancia de máxima aproximación es 14.3 fm para la energía baja y 11.5 fm para la alta). Estos tiempos son del mismo orden que el tiempo característico de los procesos electromagnéticos, por lo que incluir procesos de orden superior resulta esencial para una descripción correcta de los datos. La importancia de los procesos de orden superior da información sobre cómo el sistema minimiza su energía a través de la dinámica de reacción.

D.3 Teoría de reacciones directas

El objetivo de la teoría de reacciones directas o de dispersión es el desarrollo de modelos que, a partir de alguna información referente a los núcleos involucrados en la reacción y las condiciones de la misma, sean capaces de generar resultados comparables a los observables medidos. En este experimento, los observables medidos son las secciones eficaces diferenciales para la dispersión elástica, inelástica y de ruptura (^{10}Be), en función del ángulo y energía del fragmento detectado.

Considerando la baja energía de la reacción y las características de los núcleos involucrados en la misma, los datos experimentales se compararon con varios modelos teóricos, que se describen brevemente a continuación:

- modelo óptico: El modelo óptico es el formalismo de dispersión cuántica entre sistemas compuestos más simple, en el que solamente la dispersión elástica se considera explícitamente. Esto significa que los grados de libertad internos del proyectil y del blanco solo se consideran a nivel efectivo, y la interacción es descrita a través de un potencial efectivo que depende solo de su distancia relativa. Este potencial de interacción se construye habitualmente como suma del potencial coulombiano y un potencial nuclear complejo (complejo queriendo decir que tiene una componente imaginaria). La parte imaginaria da cuenta de la pérdida de flujo en el canal elástico, que es redistribuido entre otros

canales como excitaciones, transferencia de nucleones o fusión.

- Equivalent Photon Method (cálculo semiclásico).

El Equivalent Photon Method, es una teoría para describir las reacciones dominadas por la interacción coulombiana partiendo de un punto de vista semiclásico. Este formalismo trata el movimiento relativo entre el proyectil y el target en términos de trayectorias coulombianas, mientras que la excitación del proyectil es tratada cuánticamente.

- Canales acoplados con discretización del continuo (CDCC).

El método de canales acoplados con discretización del continuo es una extensión del formalismo de canales acoplados, en el que además de los estados ligados (discretos y normalizables), estados del continuo son explícitamente incluidos. Llamamos continuo de un núcleo a todos los estados por encima de la energía de separación, en los que un nucleón o más tienen suficiente energía para escapar de la ligadura del resto. Nos centraremos en el caso de breakup del proyectil en un *core* (^{10}Be) y una partícula de *valencia* (neutrón) debido a la interacción con un blanco de (^{197}Au). Cada uno de estos tres cuerpos se considera inerte, por lo que los estados internos que se consideran del proyectil, son aquellos que resultan del movimiento relativo entre la partícula de valencia y el *core*. Físicamente, una vez el proyectil se ha fragmentado, todos los valores de energía relativa entre el core y la partícula de valencia (ε) permitidos por conservación de energía pueden ser poblados, y cada ε corresponde a un estado, por lo que el número de estados con energía positiva es, de hecho, infinito. Estos estados son agrupados, bien utilizando bins de energía, bien utilizando pseudo-estados, resultando en estados discretos y normalizables. La función de onda del sistema se desarrolla en una base de estados internos del proyectil, que contiene los estados ligados y la representación del continuo discretizado. Cada uno de estos estados, aparece multiplicado por una función de la coordenada relativa proyectil-blanco. Para obtener estas funciones radiales, se sustituye la función de onda del sistema en la ecuación de Schrodinger, dando lugar a un conjunto de ecuaciones diferenciales acopladas.

- Canales acoplados con discretización del continuo incluyendo excitaciones del core (XCDCC).

El formalismo XCDCC [Sum06, dDALA14], es una aproximación al problema basada en el método CDCC, en la que se tienen en cuenta excitaciones de uno o de los dos fragmentos del proyectil. Estas excitaciones afectan a la estructura del proyectil, dando cabida a contribuciones en las que el *core* se encuentra en un estado excitado, así como a la dinámica de la reacción, permitiendo excitaciones y desexcitaciones de este fragmento durante la colisión.

- Transferencia de un neutrón a estados ligados y no ligados del blanco (TC) [Mor06].

El cálculo TC es otra aproximación para calcular la sección eficaz de ruptura. En esta aproximación, en lugar de describir los estados de la partícula de valencia respecto al *core*, se describen respecto al blanco. En general, el método TC incluye tanto estados ligados como no ligados del sistema blanco+n que pueden ser poblados, con lo que, además

de considerar los canales de ruptura, permite describir también los canales de transferencia.

D.4 Experimento y montaje

El experimento fue llevado a cabo en TRIUMF (Vancouver, Canada). En esta instalación se encuentra el mayor ciclotrón del mundo, capaz de acelerar iones H^- a energías entre 475 y 520 MeV con intensidades tan altas como $100 \mu A$. Una vez los iones alcanzan la energía deseada, se le arrancan los dos electrones, quedando un haz de protones. En ISAC-I el haz de protones incide en un blanco primario y el haz radioactivo se produce utilizando el método ISOL. Un haz de iones ligeros de alta energía, en general un haz de protones, golpea un blanco de un espesor alrededor de los ~ 20 cm. Los núcleos del blanco primario se rompen y los productos se extraen por difusión hacia una fuente de iones. En la fuente de iones los productos se seleccionan, se extraen y se aceleran. La intensidad del haz de ^{11}Be , una vez separado y post-acelerado, era de 10^5 pps en nuestra cámara.

Table D.1: Resumen de los haces de iones producidos para el experimento S1202 en TRIUMF y los blancos utilizados.

2012			2013		
Isótopo	Blanco	Energía (MeV/u)	Isótopo	Blanco	Energía (MeV/u)
^{10}Be	^{208}Pb	3.6	^{12}C	^{197}Au	5.04
^{11}Be	^{208}Pb	3.6	^{11}Be	^{197}Au	3.6
^{11}Be	^{208}Pb	3.1	^{11}Be	^{197}Au	2.9
^{11}Be	^{208}Pb	2.9			

El haz era conducido hasta nuestra cámara de reacción, donde el blanco de ^{197}Au y los detectores estaban posicionados en la configuración especificada en la tabla D.2. Los detectores se montaron en una placa de circuito impreso (*Printed Circuit Board, PCB*). La PCB se diseñó para cumplir una doble función: Mantener una configuración estable y permanente para los detectores, y proporcionar la circuitería que permitió un cableado cómodo de los detectores.

La cámara de reacción fue específicamente diseñada para este experimento. Las restricciones geométricas del experimento dieron lugar al desarrollo de un diseño específico, capaz de cumplir los requerimientos, que básicamente eran:

- Mantener la PCB y los detectores en su posición.
- Dejar suficiente espacio para el cableado de la PCB a la tapa de la cámara.
- Proveer de una estructura en la que montar una rueda de blancos. Diferentes blancos se montarán en la rueda para poder cambiar entre ellos sin necesidad de abrir la cámara.
- Dejar suficiente espacio para mover la rueda de blancos sin tocar ningún detector.

Table D.2: Detectores de silicio usados en el experimento S1202 para la detección de partículas cargadas, junto con sus especificaciones técnicas y la configuración en la que estuvieron dispuestos durante el experimento.

L : Distancia nominal del centro del detector al blanco.

th : Espesor.

DL: Capa muerta.

θ : Angulo entre la dirección del haz y la dirección al centro del detector.

*: Número de serie proporcionada en el catálogo por la empresa productora Micron Electronics Ltd. catalog.

	Telescopio	tipo	θ, L	No. de serie*	Det. th (μm)	DL frontal th. (nm)	DL trasera th. (nm)
ΔE	1	DSSSD	28°, 80 mm	2449-7	42	50+4%(300)	800
	2	DSSSD	45°, 60 mm	2449-10	40	50+4%(300)	800
	3	DSSSD	76°, 60 mm	2561-6	41	50+4%(300)	800
	4	SSSSD	130°, 55 mm	2752-7	20	800	800
E	1	PAD	45°, 60 mm	2712-8	500	800	800
	2	PAD	28°, 80 mm	2331-4	500	800	800
	3	PAD	76°, 60 mm	2712-11	505	800	800
	4	DSSSD	130°, 55 mm	2851-20	295	800	800

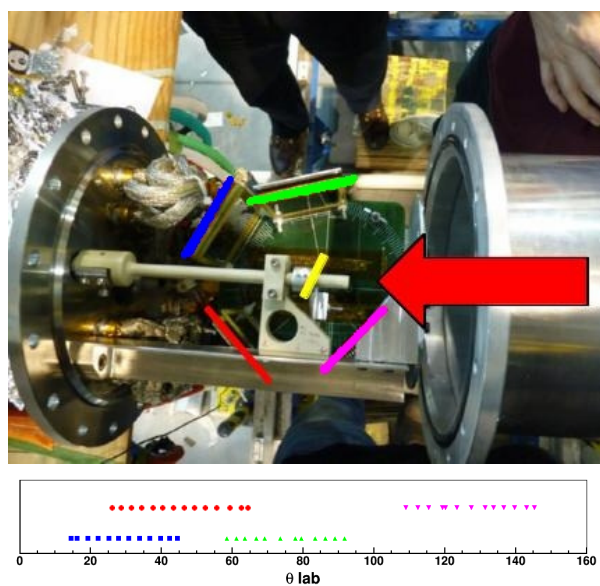


Figure D.3: Posición de los detectores en la cámara y rango angular cubierto por cada uno de ellos.

- Permitir que los clovers de TIGRESS, posicionados rodeando la cámara, estén lo más próximos posible al blanco.

Los detectores colocados dentro de la cámara eran detectores de silicio en configuración de telescopio, lo que permitió la identificación de los diferentes fragmentos. Básicamente, los telescopios consisten en dos detectores en serie. En el primer detector, los iones dejan sólo una parte de su energía, y en el segundo dejan el resto. La identificación de los iones que llegan al detector se puede hacer teniendo en cuenta que la energía depositada por unidad de longitud por un ion depende de su carga Z y su velocidad (v). El primer detector (ΔE) tenía un espesor de 40 μm en todos los telescopios excepto en telescopio 4, que está en ángulos de dispersión

más grandes, en el que el ΔE tenía un espesor de $20 \mu\text{m}$.

Se utilizaron detectores segmentados en todos los telescopios para obtener información precisa de la dirección en la que los fragmentos eran dispersados. Utilizando Double Sided Silicon Strip Detectors (DSSSDs), el ángulo subtendido por un pixel era de 3° .

La cámara de reacción tenía situados alrededor los detectores de TIGRESS. TIGRESS [Bal07] es un *array* de detectores de germanio de alta pureza. Está compuesto por 16 *clovers*, cada *clover* por 4 cristales y, a su vez, cada cristal está segmentado en 8 volúmenes. Los *clovers* están distribuidos cubriendo una importante parte del ángulo sólido alrededor de la cámara de reacción. Cuatro de los *clovers* se encuentran formando un anillo a $\theta_{lab} = 45^\circ$, otros cuatro en otro anillo a 135° y los ocho restantes en otro a 90° . En la figura D.4 puede verse la cámara de reacción con el anillo a 90° alrededor.



Figure D.4: Array de detectores TIGRESS cerrado alrededor de la cámara de reacción. En esta imagen pueden verse los clovers formando el anillo a 90° , rodeados por los cristales BGO para la supresión Compton.

En nuestro experimento el anillo a 45° no pudo usarse, ya que nuestra cámara de reacción era demasiado grande como para permitir que se cerrara toda la bola de TIGRESS a su alrededor. La cámara tenía forma de bala, con una semiesfera que encajaba con 12 de los *clovers* de TIGRESS, y una extensión cilíndrica en la dirección del haz hacia una tapa circular donde se perforaron los conductos para cablear los detectores. Estos conductos permiten la conexión de cables sin perjudicar el vacío necesario dentro de la cámara.

D.4.1 Calibraciones

Las principales calibraciones llevadas a cabo son tres:

- Calibración de energía de los detectores de silicio.
- Optimización de la posición de los detectores de silicio.

- Calibración de eficiencia de TIGRESS.
- Caracterización del espesor de un SSSSD de 20 μm .

La calibración en energía de los detectores de silicio se realizó utilizando una fuente triple-alfa y los iones de ^{12}C dispersados elásticamente en un blanco de ^{197}Au . Para el SSSSD en el telescopio 4, se realiza con una fuente de ^{148}Gd y el pico más bajo de la triple-alfa ($E = 5.15 \text{ MeV}$) en los casos en los que esta última se para. En el resto de casos se realiza con la fuente de Gd y la señal generada por un pulser.

La optimización de la posición de los detectores se realizó integrando el número de cuentas por píxel obtenidos en la dispersión de ^{12}C , y comparándolo con el número de cuentas obtenidos a partir de la sección eficaz diferencial de Rutherford considerando nuestra intensidad de haz, tiempo de medida y espesor de nuestro blanco. La mejora obtenida en el posicionamiento puede ser apreciada en la figura D.5.

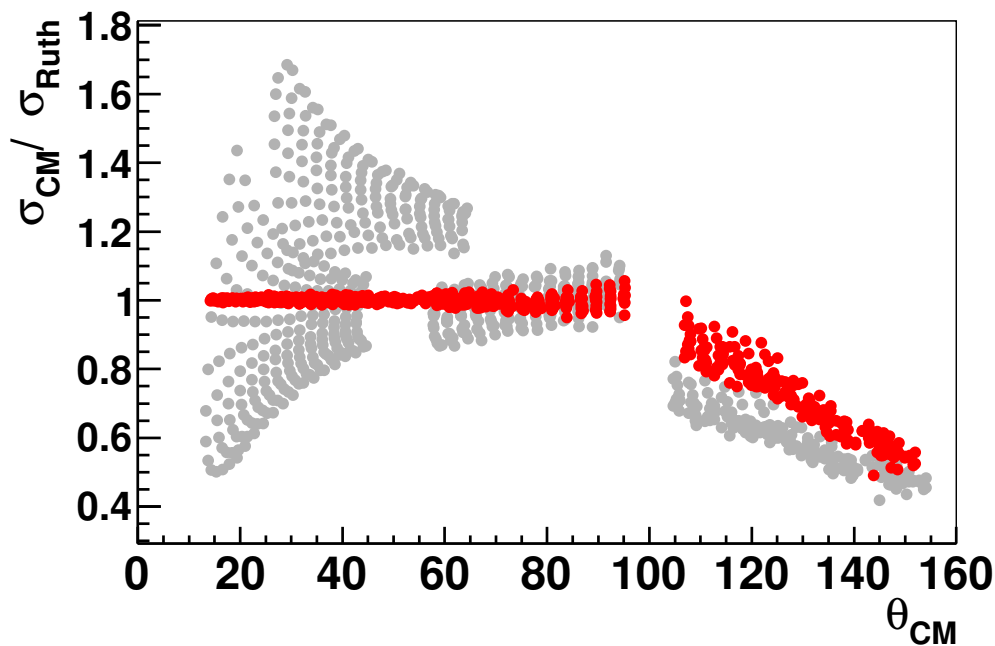


Figure D.5: Sección eficaz diferencial de la dispersión elástica de ^{12}C - ^{197}Au respecto a Rutherford a energías alrededor de la barrera de Coulomb, obtenidas antes (gris) y después de la optimización de la posición de los detectores.

La eficiencia de calibración de los detectores de TIGRESS se realizó utilizando dos fuentes de radiación gamma, una de ^{60}Co y otra de ^{152}Eu . La fuente de ^{60}Co utilizada tenía una actividad conocida con mucha precisión, lo que proporciona una muy buena estimación de la eficiencia absoluta a las dos energías a las que emite radiación. La fuente de ^{152}Eu está caracterizada por una gran variedad de picos. Comparando las tasas de ramificación de cada pico con la intensidad detectada se puede obtener la dependencia de la eficiencia con la energía. Utilizando ambas fuentes, es posible determinar la eficiencia absoluta de TIGRESS en un amplio rango de energías. La eficiencia de detección de radiación gamma a 320 keV, que es la que

nos interesa para identificar los procesos inelásticos, es de $\text{Eff} = 0.121(5)$.

Además de las calibraciones, se impusieron condiciones sobre los datos antes de incluirlos en el análisis. La condición más restrictiva consistía en coincidencias entre la señal proveniente de ambos lados de los DSSSDs, restringiendo una diferencia de energía entre ellos $E_{diff} < 200$ keV. Para evaluar la calidad de los datos, la anchura a media altura (FWHM) de los picos de la triple alfa tras calibraciones y condiciones, era de 32 ± 1 keV. Puede verse que el valor de corte para la E_{diff} elegido es significativamente mayor que la FWHM. Se eligió este valor debido a que la diferencia de energía $p-n$ en algunos casos puntuales era significativa y se decidió hacer un corte que mejorara el espectro pero que no introdujese un error adicional por contar para unos píxeles más proporción de sucesos que para otros.

D.5 Resultados

En las representaciones bidimensionales $\Delta E - E_b$, se pueden identificar dos regiones principales. Observando la figura D.6, la región con más estadística y (en la mayoría de casos) a mayor energía total ($\Delta E + E_b$) corresponde a la dispersión *cuasielástica* (elástica + inelástica) del ^{11}Be , mientras que la región a menor energía corresponde al canal de ruptura. Esto ofrece información por píxel de los canales de reacción. La información más directa que puede extraerse es:

- Cantidad de fragmentos de ^{10}Be detectados en un píxel, calculada integrando el número de cuentas dentro del corte que delimita la región de ruptura.
- Cantidad de fragmentos de ^{11}Be detectados en un píxel, calculada integrando el número de cuentas dentro del corte que delimita la región del cuasielástico.
- Probabilidad de breakup, calculada a partir del cociente entre fragmentos de ^{10}Be y ^{11}Be ,

$$P_{bu} = \frac{N_{bu}}{N_{bu} + N_{qe}}. \quad (\text{D.6})$$

La ventaja de trabajar con probabilidades es que se minimizan los efectos de algunos errores experimentales. Cualquier particularidad en la detección, amplificación, calibración o selección de los eventos afectará homogéneamente a todos los eventos detectados en el mismo píxel. Si, por ejemplo, los iones detectados sufren mucho *struggling* en el blanco porque se encuentran en una zona sombreada del detector, el número de cuentas en el píxel se reducirá y lo mismo ocurriría si calculásemos la sección eficaz directamente a partir de este número. En cambio, la reducción se produciría tanto en el canal elástico como en el de ruptura, por lo que el cociente no se verá afectado y puede ser utilizado para dar información con menos incertidumbre del proceso de reacción. En esta misma dirección, la estadística de los píxeles a ángulos similares se sumada, presentando la información de las probabilidades en bins angulares de 3° .

El canal inelástico no puede ser separado del canal elástico usando espectroscopía de partículas cargadas solamente. El array de detectores de germanio de alta pureza TIGRESS se usa para detectar, en coincidencia con los fragmentos, la radiación gamma emitida tras la

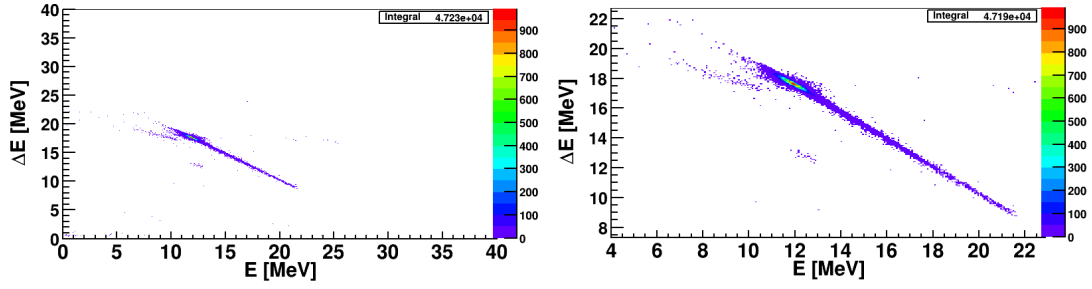


Figure D.6: Gráficos bidimensionales $\Delta E - E$ de la dispersión de ^{11}Be en ^{197}Au a energías por debajo de la barrera de Coulomb. En el eje Y se representa la energía perdida en el detector ΔE , y la energía depositada en el detector trasero, E , en el eje X. Se observa que las contribuciones del cuasielástico y del breakup están bien separadas y son identificables. En este gráfico se muestra toda la estadística acumulada por un píxel durante el experimento a la energía $E_{\text{lab}} = 2.9 \text{ MeV/u}$.

desexcitación del ^{11}Be . Para el uso detectores gamma en coincidencia, se hace indispensable corregir por la eficiencia del conjunto de detectores. Este hecho, junto con la baja probabilidad de excitación, y el consiguiente bajo número de cuentas, suponen un incremento de la incertidumbre con respecto al cálculo de breakup.

En este caso, la probabilidad de dispersión inelástica se define como:

$$P_{\text{inel}} = \frac{N_{\text{in}}}{\varepsilon_{\gamma} N_{\text{Be}}}, \quad (\text{D.7})$$

donde N_{in} es el número de fragmentos detectados en coincidencia con una gamma a 320 keV en TIGRESS, ε_{γ} es la eficiencia de TIGRESS a esta energía, y N_{Be} es el número de cuentas de fragmentos de Be. Las coincidencias se muestran en la figura D.7. La probabilidad de dispersión inelástica se calcula sustrayendo el inelástico del cuasielástico,

$$\begin{aligned} P_{\text{el}} &= \frac{N_{\text{qel}} - \frac{N_{\text{in}}}{\varepsilon_{\gamma}}}{N_{\text{Be}}} \\ &= \left(\frac{N_{\text{qel}}}{N_{\text{Be}}} \right) - \left(\frac{N_{\text{in}}}{\varepsilon_{\gamma} N_{\text{Be}}} \right) \\ &= (1 - P_{\text{bu}}) - (P_{\text{in}}). \end{aligned} \quad (\text{D.8})$$

D.5.1 Discusión

Los resultados obtenidos se han comparado con diferentes cálculos realizados a partir de varios formalismos teóricos. Los diferentes cálculos de centran en diferentes aspectos de la reacción, por lo que se considera oportuno explicar qué lectura podemos extraer de los datos con cada enfoque particular.

La primera evidencia experimental de la estructura de halo en el ^{11}Be es un comportamiento inusual de la dispersión elástica, donde se observa la desaparición del pico de interacción Coulomb-nuclear, y una desviación sustancial respecto a la sección eficaz de Rutherford a partir de ángulos relativamente pequeños. Esto se materializa, dentro de una descrip-

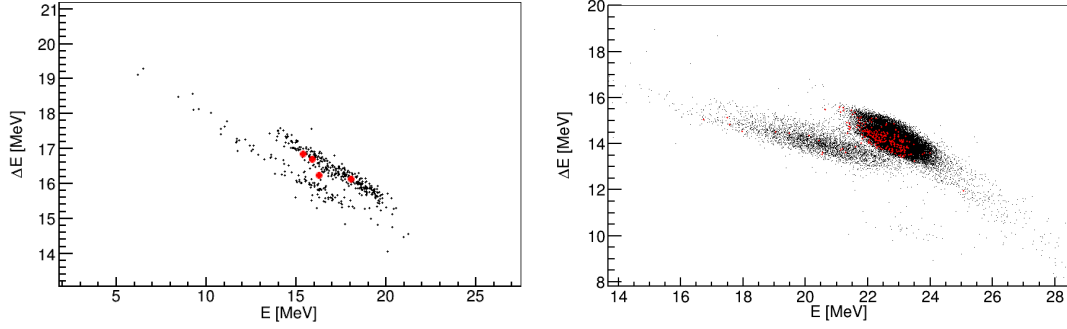


Figure D.7: Gráfico bidimensional $\Delta E - E$ en coincidencia con una gamma a 320 keV (puntos rojos) representados sobre el gráfico $\Delta E - E$ sin coincidencia. A la izquierda se muestra el caso para un solo píxel, donde se observa el pobre conteaje. A la derecha se mejora la estadística y se reduce el error sumando las cuentas de los píxeles correspondientes a un mismo bin angular de 3° .

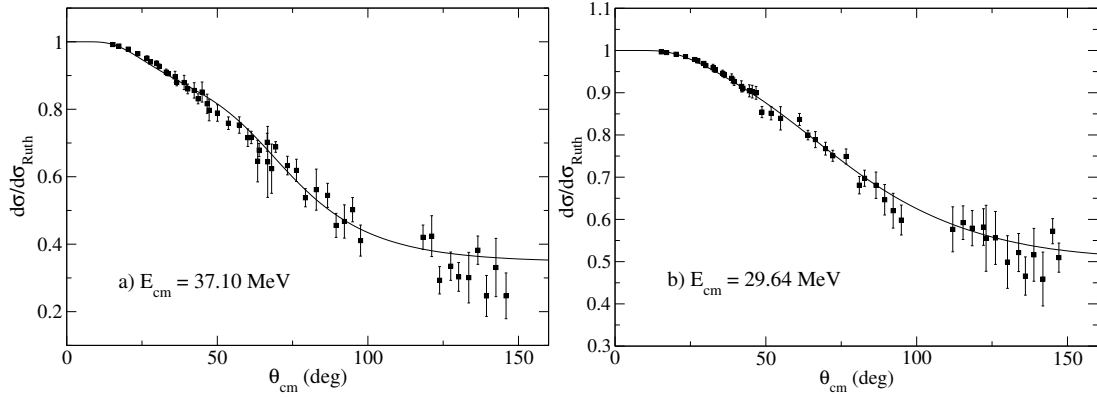


Figure D.8: Dispersión elástica relativa a la sección eficaz de Rutherford. Datos experimentales y ajuste dentro del modelo óptico, usando un factor de forma de Woods-Saxon para la parte real e imaginaria. Las medidas se realizaron a: 3.6 MeV/u (39.6 MeV) y 2.9 MeV/u (31.9 MeV). Para los cálculos se ha utilizado la energía del haz en el centro del blanco, $E_{lab} = 39.17$ MeV ($E_{cm} = 37.09$ MeV) y $E_{lab} = 31.30$ MeV ($E_{cm} = 29.64$ MeV), que están respectivamente, alrededor y por debajo de la barrera de Coulomb ($V_b \sim 40$ MeV).

ción de modelo óptico (ajuste en la figura D.8), en el valor extremadamente grande de la difusividad del potencial imaginario, $a_i = 8.6$ fm. El radio de sensibilidad se encuentra a $r_{sens} = 35-40$ fm que, comparado con la suma de los radios de ^{11}Be y ^{197}Au ($R = 14.3$ fm), demuestra la importancia de los acoplamientos de largo alcance y cómo la repulsión coulombiana domina la dinámica de la reacción.

Un cálculo a primer orden utilizando el método de fotones equivalentes (en inglés Equivalent Photon Method, EPM) es capaz de explicar la dispersión inelástica a ángulos hacia adelante (hasta $\sim 50^\circ$), pero subestima claramente la probabilidad de ruptura en el mismo rango angular, donde se espera que esta sea una buena aproximación al mecanismo (ver figura D.9). Esto difiere significativamente del caso de la reacción $^{11}\text{Li} + ^{208}\text{Pb}$, donde la probabilidad de breakup a ángulos pequeños pudo ser bien reproducida con un cálculo a primer orden.

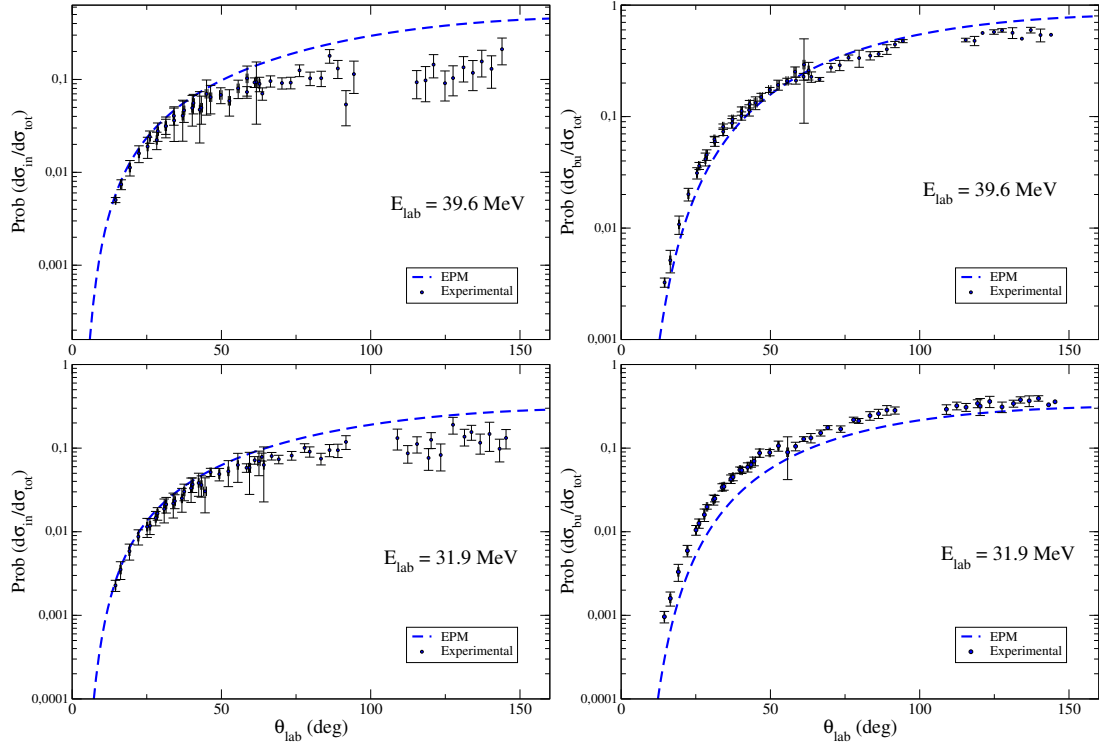


Figure D.9: Izquierda: Probabilidad de dispersión inelástica experimental comparada con un cálculo semiclásico a primer orden (EPM), suponiendo que la excitación es puramente dipolar coulombiana. Para el cálculo se utilizó el valor experimental aceptado, $\mathcal{B}(E1; 1/2^+ \rightarrow 1/2^-) = 0.116 e^2 fm^2$ [Mil83]. Los cálculos muestran un buen acuerdo con los datos a ángulos hacia adelante a ambas energías. Derecha: Probabilidad de breakup experimental comparada con cálculos EPM. La $\mathcal{B}(E1)$ usada para el cálculo es la que se obtiene con un modelo de partícula-rotor, usando los parámetros de la tabla 5.4 (presentados en el texto y extraídos de [Sum07]), que proporciona una distribución $d\mathcal{B}(E1)/dE$ en acuerdo con la extraída a partir del experimento de disociación coulombiana de Fukuda et al [Fuk04]. Este tratamiento se espera que sea adecuado donde la interacción coulombiana es dominante, es decir, a ángulos hacia adelante. En cambio, observamos que el cálculo subestima los resultados, demostrando la importancia de otros efectos, tales como acoplamiento en varios pasos, importancia de multipolos superiores de la interacción coulombiana o efectos nucleares.

Se realizaron cálculos CDCC incluyendo estados del continuo del sistema ^{10}Be -n hasta $E_{max} = 10$ MeV y $\ell_{max} = 10$. Estos cálculos reproducen los datos de breakup (como se ve en la figura D.10) utilizando la misma $\mathcal{B}(E1)$ que se extrajo de experimentos a energías considerablemente mayores, incluyendo espacios modelo considerablemente grandes y resolviendo las ecuaciones acopladas a todos los ordenes. Estos resultados muestran una relevancia inesperada de efectos de orden superior a ángulos hacia adelante. A pesar de que el parámetro de adiabaticidad es del orden de la unidad, lo que implica que la probabilidad de interaccionar en más de un paso no es despreciable, la dispersión hacia ángulos delanteros se corresponde con trayectorias distantes, donde normalmente los potenciales no son muy intensos, por lo que se esperaba que el breakup en ese rango angular fuese explicado por un cálculo a primer orden.

El cálculo CDCC convergido, como se muestra en la figura C.10, es capaz de explicar la

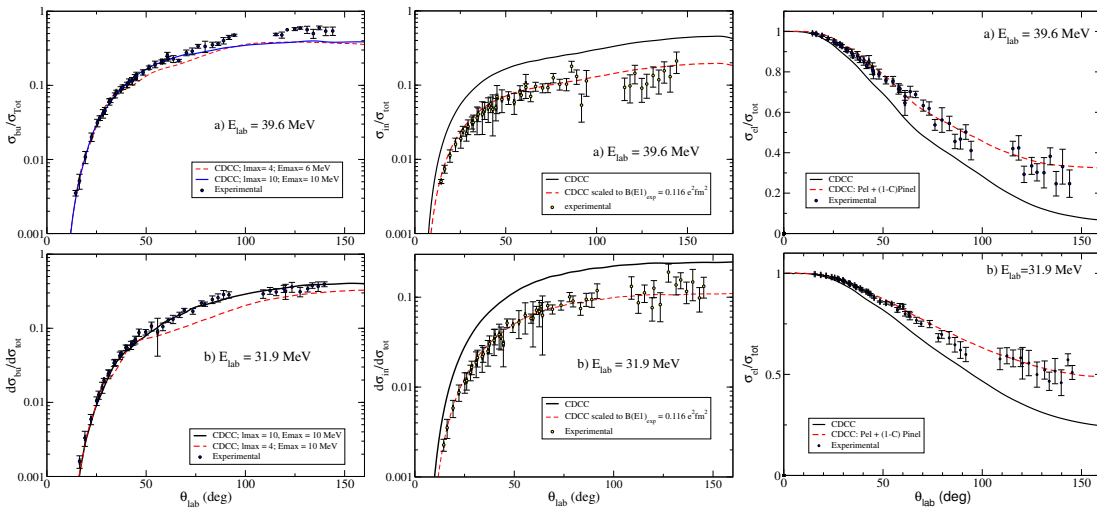


Figure D.10: Izquierda: probabilidad experimental de breakup comparada con cálculos del CDCC a energías alrededor y por debajo de la barrera de Coulomb. Se observa que el cálculo explica los datos por debajo de la barrera. Alrededor de la barrera, subestima los datos para ángulos mayores que 80° . Ángulos grandes y alta energía se corresponden con los casos en los que el neutrón del halo penetra más en el blanco y es más probable que pobleemos estados de $^{197}\text{Au}+n$, que son difíciles de describir dentro del enfoque del CDCC. Centro: se muestra la probabilidad de dispersión inelástica para ambas energías. El cálculo sobreestima los datos, pero escalando la $\mathcal{B}(E1)$ que nos da el modelo de estructura de dos cuerpos que estamos utilizando al valor experimental $\mathcal{B}(E1)$, los cálculos reproducen los datos. Derecha: probabilidad de dispersión elástica a ambas energías. Para que el cálculo reproduzca los datos, hay que añadir al elástico la cantidad sustraída al inelástico.

probabilidad de ruptura, pero falla en dar correctamente la sección eficaz correspondiente a los estados ligados, sobrestimando el inelástico y subestimando el elástico en la misma medida. Además, para los ángulos grandes, donde la partícula de valencia penetra más en el potencial del blanco y es de esperar una mayor influencia de los efectos nucleares, el cálculo subestima la sección eficaz de ruptura.

Los cálculos XCDCC (ver figura D.11) muestran una clara mejora sobre los otros formalismos, al ser capaces de describir los datos de todos los canales de reacción de manera simultánea. La mejora se atribuye al hecho de que se utiliza un modelo de partícula-rotor para describir el sistema ^{10}Be -n, teniendo así en cuenta la deformación del ^{10}Be e incluyendo una función de onda más realista para los estados del ^{11}Be , más que a una excitación dinámica del *core* durante la interacción. Vemos por tanto, cómo la influencia sutil de la función de onda

completa del ^{11}Be en la dinámica de reacción se pone de manifiesto en un experimento de dispersión de baja energía en un objetivo pesado.

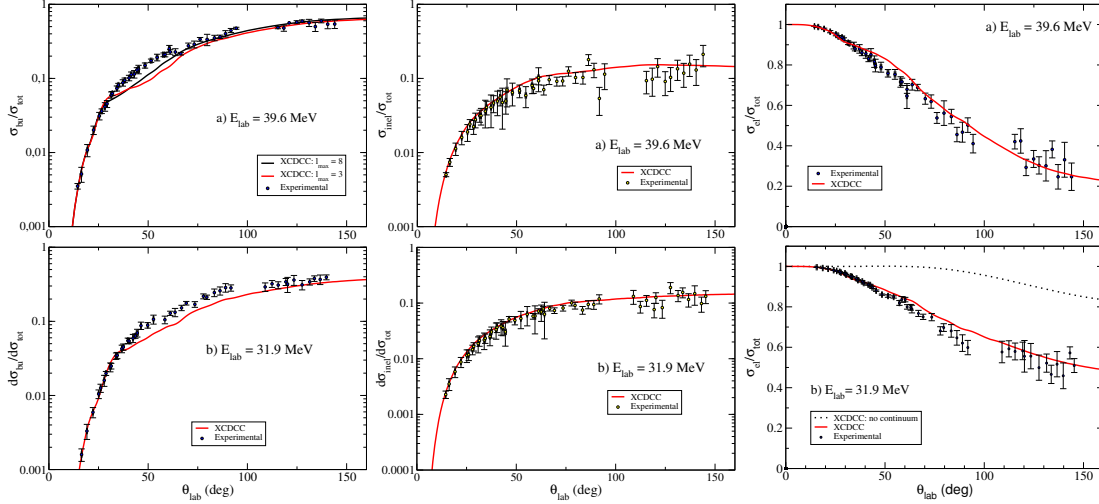


Figure D.11: Izquierda: datos experimentales de probabilidad de breakup a energías alrededor y por debajo de la barrera de Coulomb en comparación con los cálculos preliminares XCDCC. A ambas energías, el cálculo explica los datos a ángulos de dispersión de pequeños y grandes. A ángulos intermedios, se evidencian problemas de convergencia. Se espera que, a medida que mejoremos nuestra capacidad para hacer frente a las limitaciones computacionales, seamos capaces de describir el breakup del mismo modo que con el cálculo CDCC. Centro: la probabilidad de dispersión inelástica calculada explica los datos sin necesidad de escalarlos. Derecha: la dispersión elástica obtenida con el cálculo también está en buen acuerdo con los datos, excepto en ángulos intermedios, donde los problemas de convergencia son más evidentes.

Para cuantificar la contribución de la transferencia de un neutrón a estados del blanco de ^{197}Au a energías alrededor de la barrera de Coulomb se realizaron cálculos usando el método de TC, en el que la ruptura se trata como un mecanismo de transferencia del neutrón a estados no ligados del blanco. Asimismo, en estos cálculos se incluyeron también estados ligados del sistema $n+^{197}\text{Au}$ que pueden contribuir también a las secciones eficaces inclusivas de ^{10}Be . El cálculo evidencia que este proceso es dominante, precisamente, en el caso en el que el cálculo CDCC fallaba, a ángulos mayores que $\theta = 75^\circ$ (ver figura D.12).

D.6 Conclusiones

En este trabajo, hemos realizado un análisis detallado de la reacción $^{11}\text{Be}+^{197}\text{Au}$ medida en 2013 en TRIUMF (Vancouver, Canada), en el marco de una colaboración internacional liderada por los grupos de física nuclear del IEM-CSIC y de las Universidades de Sevilla y Huelva. Los datos obtenidos consisten en las distribuciones angulares elástica, inelástica (poblando el único estado ligado del ^{11}Be) y breakup inclusivo. Estos datos han sido comparados con diversos modelos teóricos, de los que se ha extraído información de interés de la estructura del ^{11}Be y de la dinámica de la reacción. Las conclusiones principales, son:

- El montaje experimental, específicamente diseñado para este experimento, junto con el uso del array de detectores de germanio de alta pureza TIGRESS, ha sido adecuado para

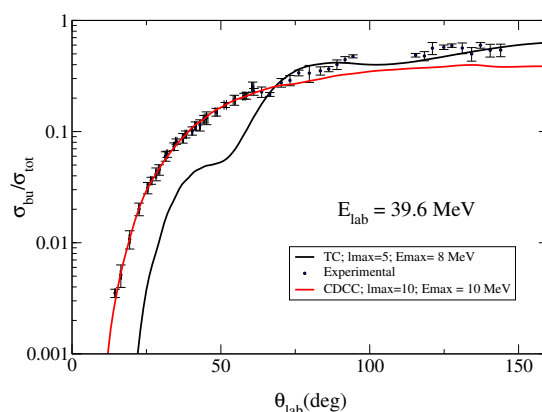


Figure D.12: Probabilidad de breakup experimental comparada con un cálculo de transferencia al continuo (TC) a energías alrededor de la barrera de Coulomb. Se observa que los datos a energía alta y ángulos de dispersión grandes, condiciones en las que el neutrón penetra más en el potencial del blanco, están bien descritos por este cálculo.

la obtención de los datos deseados, identificando los principales canales de reacción entre los ángulos $13^\circ < \theta < 150^\circ$.

- TRIUMF y ISAC-II han proporcionado un haz continuo de ^{11}Be con alta producción, baja contaminación, y alta resolución energética.
- Hay claras evidencias del rol jugado por los acoplamientos de largo alcance. Experimentalmente, esto puede extraerse de la desviación de la sección eficaz elástica respecto a la de Rutherford a partir de ángulos pequeños, y del gran número de ondas parciales que se necesitan en el cálculo CDCC para reproducir los datos. A energías cercanas a la barrera, un enfoque de transfer ha resultado más efectivo que el del CDCC, mostrando que el neutrón puebla, en esos casos, estados del ^{198}Au .
- La estructura particular del ^{11}Be , con un *core* de ^{10}Be deformado que puede rotar, juega un papel apreciable en el proceso de reacción, como puede inferirse del hecho de necesitar un cálculo XCDCC para explicar todos los observables medidos, contrastando con el cálculo CDCC de tres cuerpos que usa una descripción de dos cuerpos inertes para describir el proyectil de ^{11}Be .
- El objetivo en el futuro próximo es continuar con el análisis de los datos de la reacción $^{11}\text{Be} + ^{208}\text{Pb}$, medidos en 2012 durante el experimento S1202, y continuar trabajando en la convergencia de los cálculos XCDCC y TC para este caso.

El trabajo presentado aquí ha conseguido cumplir sus objetivos iniciales: estudiar las distribuciones angulares elástica, inelástica y de breakup del ^{11}Be , un núcleo halo de un neutrón, en el campo electrostático intenso creado por un blanco pesado a energías alrededor y por debajo de la barrera de Coulomb. Datos experimentales valiosos y originales han sido recopilados y han contribuido a una mejor comprensión de las reacciones a bajas energías involucrando núcleos halo y blancos pesados.

Bibliography

- [Aco11] L. Acosta et al., Phys. Rev. C **84** (2011), 044604.
- [Ald75] K. Alder, A. Winther, Electromagnetic excitation, North Holland, Amsterdam, 1975.
- [Ame13] F. Ames et al, Rev. of Scientific Inst. **85** (2013), 02B912.
- [Aum00] T. Aumann, et al., Phys. Rev. Lett. **84** (2000), 35.
- [Aus87] N. Austern et al, Physics Reports **153** (1987), 125.
- [Aut70] D.L. Auton, Nucl. Phys. A **157** (1970), 305.
- [AV87] N. Austern and C.M. Vincent, Phys. Rev. C **23** (1987), no. 5, 1847.
- [Bal07] G.C. Ball et al, Nucl. Phys. A **787** (2007), 118c.
- [Bay82a] W.E. Baylis and S.J. Peel, Comp. Physics Commun. **25** (1982), 21.
- [Bay82b] W.E. Baylis and S.J. Peel, Comp. Physics Commun. **25** (1982), 7.
- [BB88] C.A. Bertulani and G. Baur, Phys. Rep. **163** (1988), 299.
- [Bri12] P.G. Bricault et al, Rev. of Scientific Inst. **83** (2012), 02A914.
- [Bru07] R. Brun et al., Root user's guide, 2007.
- [Cap04a] P. Capel et al., Phys. Rev. C **70** (2004), 064605.
- [Cap04b] F. Cappuzzello et al., Nucl. Phys. A **739** (2004), 30.
- [Cub12] M.A. Cubero, et al., Phys. Rev. Lett. **109** (2012), 262701.
- [Dai98] I. Daito et al., Phys. Lett. B **418** (1998), 27.
- [dDALA14] R de Diego, J.M. Arias, J.A. Lay, and Moro A.M., Phys. Rev. C **89** (2014), 064609.
- [Des97] P. Descouvemont, Nucl. Phys. A **615** (1997), 261–276.

- [Esc07] D. Escrig et al., Nucl. Phys. A **792** (2007), 2.
- [Fer13] J.P. Fernández-García et al, Phys. Rev. Lett. **110** (2013), 142701.
- [For99] S. Fortier et al., Phys. Lett. B **461** (1999), 22.
- [Fuk04] N. Fukuda et al., Phys. Rev. C **70** (2004), 054606.
- [GEA] GEANT4-CERN international collaboration, <http://geant4.cern.ch/>.
- [Gle04] N.K. Glendenning, Direct nuclear reactions (2nd edition), World Scientific Pub Co Inc/Mc Graw-Hill, 2004.
- [Gor04] G. Gori et al., Phys. Rev. C **69** (2004), 041302.
- [Han87] P.G. Hansen, B. Jonson, Europhys. Lett. **4** (1987), 409.
- [Han01] P.G. Hansen, Nucl. Phys. **A682** (2001), 310c–319c.
- [Jä87] B. Jäckel et al., Nucl. Inst. and Methods A **261** (1987), 547.
- [Kel03] J.H. Kelley et al., Nucl. Phys. A **728** (2003), 339.
- [Kel12] J.H. Kelley et al., Nucl. Phys. A **88** (2012), 880.
- [Kle73] D. Kleppner, R.J. Kolenkow, An introduction to mechanics (2nd edition), p. 498, Mc Graw-Hill, 1973.
- [Kno89] G.F. Knoll, Radiation detection and measurement, John Wiley & Sons, Inc., 1989.
- [Kol07] J.J. Kolata et al., Phys. Rev. C **69** (2007), 047601.
- [Kon03] A.J. Koning and J.P. Delaroche, Nucl. Phys. A **713** (2003), 231.
- [Lay12a] J.A. Lay, Descripción de la estructura y reacciones de núcleos exóticos en una base de oscilador armónico transformado, Ph.D. thesis, U. Sevilla, 2012.
- [Lay12b] J.A. Lay et al., Phys. Rev. C **85** (2012), 054618.
- [Luk15] V.K. Lukyanov et al., Nucl. Phys. A **615** (2015), 261–276.
- [Mil83] D.J. Millener et al., Phys. Rev. C **28** (1983), 497.
- [Mor06] A.M. Moro, F.M. Nunes, Nucl. Phys. A **767** (2006), 138–154.
- [Nak97] T. Nakamura et al., Phys. Lett. B **394B** (1997), 11.
- [Nak06] T. Nakamura et al., Phys. Rev. Lett. **96** (2006), 252502.
- [Nun96] F. Nunes et al., Nucl. Phys. A **596** (1996), 171.
- [Pal03] R. Palit et al., Phys. Rev. C **68** (2003), 4318.
- [Pie13] A. di Pietro, et al., Phys. Rev. C **87** (2013), 064614.
- [RGM11] M. Rodríguez-Gallardo and A.M. Moro, Int.J.Mod.Phys. **E20** (2011), 947.

- [Rib15] G. Ribeiro et al., JPS Conf. Proc. **6** (2015), 030098.
- [Rod08] M. Rodríguez-Gallardo et al., Phys. Rev. C **77** (2008), 064609.
- [Rod09] M. Rodríguez-Gallardo et al., Phys. Rev. C **80** (2009), 051601.
- [Rus09a] K. Rusek et al., Eur. Phys. J. A **42** (2009), 461.
- [Rus09b] K. Rusek et al., Eur. Phys. J. A **42** (2009), 623.
- [San01] S. Santra et al., Phys. Rev. C **64** (2001), 024602.
- [San05] A.M. Sanchez-Benítez et al., J.Phys.(London) **G31** (2005), S1953.
- [Sat80] G.R. Satchler, Introduction to nuclear reactions, The Macmillan Press LTD, 1980.
- [Sat83] G.R. Satchler, Direct nuclear reactions, Oxford University Press, New York, 1983.
- [Sch12] K.T. Schmitt et al., Phys. Rev. Lett. **108** (2012), 192701.
- [Shr04] A. Shrivastava et al., Phys. Lett. B **596** (2004), 54.
- [Sum06] N.C. Summers et al., Phys. Rev. C **73** (2006), 031603.
- [Sum07] N.C. Summers et al., Phys. Lett. B **650** (2007), 127.
- [Sá08] A.M. Sánchez-Benítez et al., Nucl. Phys. A **803** (2008), 30.
- [Tan85] I. Tanihata et al., Phys. Rev. Lett. **55** (1985), 2676.
- [Tan88] I. Tanihata et al., Phys. Lett. B **206** (1988), 592.
- [Tho88] I.J. Thompson, Comput. Phys. Rep. **7** (1988), 167.
- [Tol86] L.D. Tolsma, G.W. Veltkamp, Comp. Physics Commun. **40** (1986), 233–262.
- [Vin95] N. Vinh Mau, Nucl. Phys. A **592** (1995), 33.
- [Win01] J.S. Winfield et al., Nucl. Phys. A **683** (2001), 48.
- [Zie84] J.F. Ziegler et al., "the stopping and range of ions in solids," vol. 1 of series "stopping and ranges of ions in matter", Pergamon Press, New York, 1984.
- [Zwi79] B. Zwieglinski et al, Nucl. Phys. A **315** (1979), 124.

